Autonomous Airborne Refueling: Relative State Estimation

by

Anton Johan Runhaar

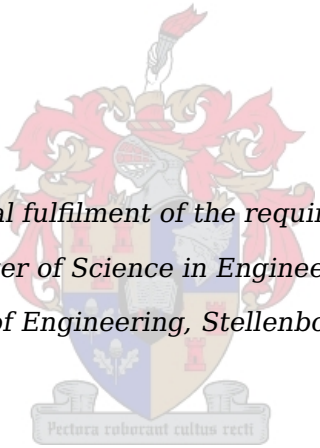

Thesis presented in partial fulfilment of the requirements for the degree of

Master of Science in Engineering

at the Faculty of Engineering, Stellenbosch University

Supervisor: Dr I.K. Peddle

Department Electrical and Electronic Engineering

December 2011

Declaration

By submitting this thesis electronically, I declare that the entirety of the work contained therein is my own, original work, that I am the sole author thereof (save to the extent explicitly otherwise stated), that reproduction and publication thereof by Stellenbosch University will not infringe any third party rights and that I have not previously in its entirety or in part submitted it for obtaining any qualification.

December 2011

Abstract

This thesis presents the development of a state estimation system for use in an Autonomous Airborne Refueling (AAR) operation through the simulated implementation of GPS, monocular and stereoscopic vision, inertial measurement sensors and boom parameter measurement in combination with the Extended Kalman Filter (EKF) and Unscented Kalman Filter (UKF).

A set of functional criteria for the estimation system was developed through an analysis of the control system input requirements and associated constraints. The estimation system is further developed by integrating the sensor configurations into the estimation algorithm structures through the derivation of the applicable mathematical models. Final sensor configurations are set based on a sensitivity analysis in which the effect of parameters such as sensor noise, placement and quantity are related to the accuracy with which the states are estimated.

Uncertainty in the process noise, which is typically approximated, is overcome by adding an adaptive element to the estimation algorithms in which the current process noise is estimated allowing compensation for unmodeled process noise uncertainty.

Finally twelve practical sensor configurations are established utilising unique combinations of the five sensors. Each configuration is simulated using both estimation algorithms after which all results are evaluated with respect to one another as well as to the minimum state accuracy criteria. Conclusions are presented based on the evaluation of the results followed by recommendation for future development.

Opsomming

Die ontwikkeling van ’n toestandafskattingstelsel, spesifiek toegepas op outonome brandstofhervulling, word voorgelê in hierdie tesis. Hierdie ontwikkeling behels die implementering van GPS, monukulêre- en stereo-visie sensors, inersiële sensor eenhede en verbindingsarmsensors wat gebruik word in ’n Uitgebruide Kalman Filter (Extended Kalman Filter) en Geurlose Kalman Filter (Unscented Kalman Filter).

’n Volledige ontleding van die beheerstelsel se toevoervereistes en geassosieerde beperkings is gebruik om ’n stel beoordelingsmaatstawwe vir die toestandafskatting-stelsel te bepaal. Die stelsel is verder ontwikkel deur verskillende sensorkonfigurasies met die afskattingsalgoritmes te kombineer deur die afleiding van toepaslike wiskundinge modelle. Hierdie konfigurasies is verfyn deur ’n sensitiwiteitsanalise, waar die verwantskap tussen die effekte van sensorruis, sensorligging, hoeveelheid sensors ondersoek is met betrekking tot afskattingsakkuraatheid.

Onsekerheid in die stelsel se prosesruis is deur ’n aanpassings substelsel hanteer, wat kompensasie vir ongemodeleerde onsekerheid moontlik maak. Twaalf praktiese sensorkonfigurasies is opgestel vanuit unieke kombinasies van die vyf sensore behartig in die projek. Hierdie konfigurasies is deur beide afskattingsalgoritmes gebruik om sodoende die akkuraatheid van die konfigurasies asook die afskattingsalgoritmes te evalueer met betrekking tot mekaar en aan die hand van die beoordelingsmaatstawwe vir die beheerstelsel. Die tesis is afgesluit deur gevolgtrekkings asook aanbevelings vir toekomstige navorsing.

Contents

List of Figures

List of Tables

Nomenclature

Vectors

$\boldsymbol{p}$	Position
$\boldsymbol{v}$	Velocity
$\boldsymbol{a}$	Acceleration
$\boldsymbol{\omega}$	Angular velocity
$\boldsymbol{e}$	Vector of Euler angles
$\boldsymbol{q}$	Quaternion
$\boldsymbol{\alpha}$	Vector of Modified Rodrigues Parameters
$\boldsymbol{x}$	The state vector
$\mathbf{X}$	Sigma point vector
$\mathbf{Y}$	Measurement sigma point vector
$\mathbf{e}$	Quaternion axis of rotation also known as the Euler Axis
φ	Three Component vector for error quaternion representation
$S(\cdot)$	Relative Likelihood used in the Particle Filter

Scalars

x, y, z	Coordinates of vector $\boldsymbol{p}$
V_x, V_y, V_z	Coordinates of $\boldsymbol{v}$
ϕ, θ, ψ	Euler angles corresponding to roll pitch and yaw
P, Q, R	Body roll, pitch and yaw rates
τ	Relative pitch angle between boom and tanker reference frame
l	Boom length
σ	Boom universal joint pitch angle
χ	Boom universal joint roll angle
ϑ	Quaternion rotation angle
n	State vector size for use in the UKF
N	Number of particles for use in the PF
f	Optical sensor focal distance

Matrices

$F(\cdot)$	Continuous time process Jacobian
$F_k(\cdot)$	Discrete time process Jacobian
$L(\cdot)$	Process noise Jacobian
$Q(t)$	Process noise spectral density matrix
Q_k	Discrete process noise covariance
H_k	Measurement Jacobian
M_k	Measurement noise Jacobian
$\boldsymbol{T}(\cdot)$	Coordinate transformation matrix
$\boldsymbol{\Omega}(\cdot)$	Quaternion propagation matrix

Reference frames

F_t	Tanker body reference frame with origin T
F_r	Receiver body reference frame with origin R
F_b	Boom reference frame with origin B
F_{bj}	Boom reference frame with origin BJ
F_i	Inertial reference frame with origin I
F_e	Earth centered Earth Foxed reference frame with origin E
F_l	Local NED reference frame with origin L

Acronyms

AAR	Autonomous Airborne Refueling
EKF	Extended Kalman Filter
UKF	Unscented Kalman Filter
PF	Particle Filter
GPS	Global Positioning System
GNSS	Global Navigation Satellite System
CG	Center of Gravity
SBAS	Satellite Based Augmentation System
FOV	Field Of View
LOS	Line Of Sight
MRP	Modified Rodrigues parameters
RTK	Real Time Kinematic

Relevant Shorthand

RR	Roaming GPS Receiver
RB	Roaming GPS Base
FR	Fuel Receptacle
C	Camera
B	Beacon
N_0	Center of the control envelope

Vector Notations

$\boldsymbol{x}_k^+$	An *a postiori* state at time k
$\boldsymbol{x}_k^-$	An *a priori* state at time k
$\boldsymbol{x}^{a/b}$	Vector of a relative (or with respect to) b
$\boldsymbol{x}_b^{a/b}$	Vector of a relative (or with respect to) b coordinated in b
$\frac{d}{dt}\left(\boldsymbol{x}\right)\big\vert_a$	Time derivative of vector x with respect to reference frame a
$\dot{\boldsymbol{x}}$	Time derivative
$\hat{\boldsymbol{x}}$	Estimated value
$\tilde{\boldsymbol{x}}$	Measured value
$\delta\boldsymbol{x}$	Error vector indicating the difference in the true and estimated value
	Also used to indicate the vector of error-MRP

Math Operators

$[(\cdot)\times]$	Skew-Symmetric matrix operator
$\otimes$	Quaternion multiplier

Acknowledgments

I would like to extend my gratitude to the following people/organisations for their contributions towards this thesis,

- My study leader Dr. Iain Peddle as well as Prof. Tomas Jones and Mr. Japie Engelbrecht for their invaluable guidance, advice and patience through the course of this project.
- My colleague, A.M de Jager, for the hours he spent proof reading and the valuable advice that ensued.
- My girlfriend Sunette for her love and support throughout the good and rough days.
- My parents for their endless support and the opportunities they have afforded me.
- My fellow students, especially Righardt, who made some of the long office hours bearable.
- The UAV research funding partner Airbus, for the opportunity to work on this project.

Chapter 1

Introduction

With the success of unmanned flight in recent years there has been an increased demand to provide autonomous capabilities to piloted and unmanned systems for use in close proximity operations of which the most noteworthy include airborne refueling and formation flight. The automation of such processes aim to extend the capabilities of Unmanned Aerial Vehicles (UAVs), enabling them to perform tasks similar to that of piloted craft resulting in increased operational usefulness.

Typically, the addition of a refueling capability to an aircraft, piloted or otherwise, aims to extend the range of the aircraft without compromising the aircraft payload through the addition of large reserve fuel tanks. This is especially advantageous in military applications, where an aircraft can stay airborne for extended periods of time while still maintaining operational functionality. Similar to airborne refueling, with respect to close proximity flight operations, formation flying serves to reduces drag which increases fuel efficiency extending aircraft range in long distance flights. Currently such operations are still limited to piloted aircraft, with the aim of current research in the field to provide unmanned aircraft with the same capabilities.

In addition to the improvement to UAVs, conventional piloted aircraft also benefit from autonomous capabilities, where close proximity flight for extended periods of time can prove to be tedious and dangerous. The addition of autonomous functionality will serve as a pilot aid during such operations allowing the pilot to focus on other aspects of the particular flight operation.

1.1 Airbus and Autonomous Airborne Refueling

The focus of this thesis is directed at Autonomous Airborne Refueling (AAR) as proposed by Airbus through the initial work presented by *Gauvain* [2]. The initial report introduces the use of the Airbus A330 Multi Role Tanker Transport (MRTT) aircraft with the capability to

refuel other aircraft (Tanker phase) and to be refueled in flight (Receiver phase) through the implementation of a boom and receptacle refueling configuration as seen in Figure 1.1.

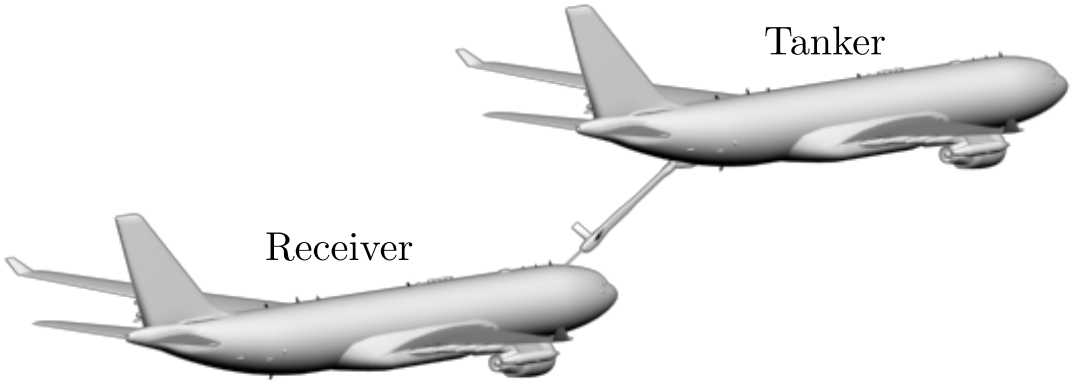

Figure 1.1 – AAR tanker and receiver aircraft with flying boom refueling configuration

The need for the automation of this procedure arose from discussions with fighter and transport pilots, pointing out the increased difficulty in the refueling procedure of a transport aircraft, as opposed to a fighter aircraft, due to their increased size and slow dynamic behaviour. The higher level of difficulty in controlling a large receiver aircraft within a narrow window coupled with the extended period of time required for large aircraft fuel transfer necessitated the development of an autonomous system to aid the pilot during the refueling procedure.

The goal of an autonomous refueling system is thus to assist the pilot by replacing the tedious task of close proximity aircraft control with an automated process. This allows for more focus to be placed on other flight operations where possible hazardous scenarios potentially introduced by the high risk nature of proximity flight can be avoided .

Research into the automation of an airborne refueling procedure is divided into the development of the control system responsible for controlling the various states of the aircraft, and the development of an estimation system tasked with providing the required relative state information to the control system.

1.1.1 Control Research

The initial AAR control research presented in *Gauvain* [2] was tasked with developing the *AAR Mode* which would be engaged once both aircraft where connected, relinquishing control from the pilot to the control system. The main objective of the project was to design a flight control law that could, once the connection between aircraft is established, maintain the receiver aircraft fuel receptacle within a specified control envelope, defined by the allowable range of boom motion.

This connection is to be maintained while the tanker enters any one of three modes of flight:

- Tanker straight and level flight: Maintain airspeed, altitude and attitude
- Tanker bank mode: Maintain a constant specified bank angle
- Tanker toboggan mode: Maintain a constant specified rate of descent

In addition to maintaining the fuel receptacle within the appropriate envelope during any of the three tanker modes the additional requirements of the receiver aircraft control system where to facilitate:

- Autonomous approach: Control the receiver to manoeuvre from an observation position, to a pre-contact position and then into a connect position in which the receiver fuel receptacle must be maintained in a connect envelope while the boom operator completes the connection.
- Automatic Break-Away: If the fuel receptacle strays beyond the range of safe fuel transfer which is governed by the allowable boom motion, the boom will automatically disconnect. The receiver must then immediately deploy spoiler and reduce thrust until a safe following distance has been reached.

Gauvain continues to develop a functional control system for all the required processes using fuel receptacle position error feedback and successive loop closure techniques in the design of the receiver aircraft lateral and longitudinal control laws. There are, however, various aspects of the control system derivation that require improvement and further investigation in order to improve the performance and the fidelity of an AAR operation in simulation. As such the control system aspect of AAR has been subdivided into three projects, each focusing on a unique aspect of aircraft control. The titles of these projects are:

- A comparative study of control strategies
- An in-depth control analysis including modeling and control of refuel point kinematics
- Frequency domain analysis and disturbance rejection

These projects aim to investigate all aspects of relative aircraft control in turbulent conditions through direct manipulation of the aircraft control surfaces as well as applied control through existing fly-by-wire configurations in order to design feasible control architectures for practical implementation in conditions ranging from light to medium turbulence as seen in [2].

The second category of research is that of state estimation, the task of which is to provide the control system with sufficiently accurate state information allowing the applicable control strategies to be applied effectively. In the original report, as well as subsequent control projects, the assumption is made that the relative and absolute states required by the control algorithms are exactly known and readily available. Addressing this assumption through the development of a state estimation system is the focus of this thesis.

1.1.2 Estimation Research

In a control system a reference state is set as an input parameter, and the task of the control system is to match its internal state with that of the reference input, effectively driving the error to zero.

In an ideal AAR scenario the receiver aircraft fuel receptacle must be maintained at the center of the applicable control envelope. The position error between the current fuel receptacle position and the control envelope center acts as the control system error input which is provided by th estimation system.

In addition to the relative position, the velocity of the envelope center relative to the fuel receptacle also serves to improve the performance of the control system by adding damping and allowing for more stable control.

The original AAR state estimation strategy relies on measuring the rotation angles of the boom joint as well as the boom length. Measuring these parameters allows the position of the fuel receptacle relative to the envelope center to be calculated, which subsequently acts as the control system error input. This approach however has its limitations:

- It requires that the aircraft be connected, and as such cannot be used during the approach, connect and break-away procedures.
- The control system inputs are limited to position errors, where the advantages of using relative velocity are not considered.
- Additional information, such as the tanker flight path and roll angle, which cannot be calculated using only the boom parameters, are also control system input requirements.

In addition to the limitations of this approach it was also assumed that the applicable sensors provided perfect measurements without noise. Since no formal approach for AAR state estimation has been defined this project was proposed in order to investigate possible state estimation architectures and sensor technologies to provide the control system with accurate state estimates for use in AAR control modes.

1.2 Literature Study

In the development of an estimation system there are two main aspects that require consideration,

- Sensors: Measurements obtained from the various sensor in the sensor array provide inputs to an estimation algorithm. The consideration of aspects such as the choice of sensors, sensor accuracy and noise, placement and configuration, and relevance to the estimated states, will have a direct effect on the estimation accuracy as well as the resultant effectiveness of the estimation system.
- Estimation Algorithm: The estimation algorithm utilizes a mathematical model of the system dynamics in combination with measurements obtained from the sensor array to produce an estimate of the state vector. The choice of estimation algorithm, especially in the case of a non-linear system, affects the accuracy with which the states can be estimated.

Autonomous refelling as well as various other close proximity operations, such as formation flight and satellite docking, have been researched extensively, some of which have also been implemented in practice. The choice of a suitable sensor configuration as well as accompanying estimation algorithm is universal to all state estimation problems and as such this study will consider the work done in each of these aspects separately.

1.2.1 Sensors

Using a conventional non-differential Global Positioning System (GPS) [1] provides an absolute position measurement of the GPS receiver relative to a corrected Earth Centered Earth Fixed (ECEF) reference frame by measuring the pseudo-range signals from at least four satellites and comparing them using an estimator. The velocity of the GPS receiver can also be obtained by either taking the difference in position over time, or by using the Doppler measurement from the satellites directly as proposed in [3]. By transmitting these measurements from a lead vehicle to a trailing vehicle, in combination with the trailing vehicle's own position and velocity measurements, the relative aircraft position and velocity can be obtained. These measurements are however of a relatively low accuracy, with conventional non-differential GPS position accuracy around $\pm$2.5m in the horizontal plane, $\pm$3m in altitude and approximately $2\frac{m}{s}$ in velocity, rendering it unsuitable for close proximity operations.

[1] GPS is used in popular reference to Global Navigation Satellite Systems (GNSS) which encompasses Galileo, GLONASS and NAVSTAR GPS.

Various improvements in position and velocity measurement accuracy have been proposed in recent years, with the most applicable being the addition of the satellite carrier phase signals to the measured GPS parameters, as well as the development of differential GPS techniques.

One such a method, referred to as Real Time Kinematic (RTK), can produce position and velocity measurements of a roaming GPS module relative to a base station with accuracies in the order of $0.02m$ and $0.03\frac{m}{s}$ RMS respectively [4] . This is achieved by transmitting the position estimate as well as the carrier and code phase measurements received by the bases station to the rover modules. These values, along with the satellite signals received by the roaming GPS module, are combined with the constraint that the roaming GPS modules are in close proximity to the base station in an internal estimator to produce high accuracy position and velocity estimates.

Typically the GPS base station is used as a stationary reference point, but since a moving base is required for relative navigation, the roaming base differential GPS (RB-DGPS) system was developed which has been used in various navigation applications from relative aircraft navigation to ship heading estimation [3; 5; 6; 7]. Alternatives to RB-DGPS are also available, where systems generally referred to as Satellite-Based Augmentation Systems (SBAS) use multiple base stations located at accurately surveyed fixed points to send correction messages to geostationary satellites. These corrections are in turn transmitted to the GPS receiver modules for increased accurate in their position and velocity measurements [8].

The high accuracy measurements from DGPS systems are a big advantage in relative navigation but the disadvantages lie within their complexity with issues such as integer ambiguity, ephemeris errors, multipath effects, satellite drop-out and cycle slip all affecting the system performance [3]. Systems that can be reliably implemented in relative navigation application also tend to be expensive where the systems are heavily dependent on the a communication link between the GPS receiver and base, which can be susceptible to interference.

Due to the complexity and variable accuracy of differential GPS systems, many research papers have introduced the addition of vision-based sensors to the state estimation systems allowing high accuracy relative measurements at close range. Vision sensors have been used in various close proximity state estimation scenarios including airborne refueling [9; 10; 11; 12], navigation navigation and terrain avoidance [13], autonomous landing [14; 15] and spacecraft formation control and docking [16; 17].

The fundamental concept of a vision-based sensor lies in the two dimensional (2D) projection of a three dimensional (3D) object onto the sensor's image plane. For the vision sensor to be useful, some form of 3D mapping must be applied, where measurements are obtained in reference to known features on the object in view.

Pattern recognition systems developed in [18; 19; 20] require cameras fitted with recognition software to be placed on the tanker. The software can identify aspects on the target vehicles

such as a fuel receptacle and provide a relative position measurement for operations such as boom docking control. Pattern recognition methods have been shown to not be sufficiently reliable in all lighting conditions and require large amounts of processing power to converge on position measurements of sufficient accuracy. Addressing these problems, systems utilising feature extraction and corner detection methods as well as systems using deformable contour algorithms aim to make receptacle position estimation more accurate, robust and produced at a higher frequency [21]. The limiting factor to these systems is that they only provide a measure to single aspects such as the fuel receptacle position relative to the tanker, with no information about any other relative states such as attitude or velocity, which limits their use.

An alternative to full image processing techniques serves to reduce the amount of information that requires processing by creating a created contrast between points of interest and background noise. In such cases optical markers are placed at know locations on the feature object which allow adequate 3D mapping without the use of complex algorithms. A sensor configuration applied in the autonomous landing of an RC helicopter [14] implements an infra-red LED beacon array placed at know locations on a landing target, with a single downward facing optical sensor fitted to the helicopter. The optical sensor is equipped with a passive bandpass filter which allows visible light to be filtered from the image leaving only the infra-red light from the beacon array to be captured and processed yielding a small vector of two dimensional (2D) measurements. Two dimensional measurements of at least four points on the target vehicle allows for the relative position and attitude to be estimated, with the optical filtering allowing for implementations in a variety of lighting conditions and an increased measurement rate as there is less information to process when compared to an unfiltered image.

These 2D measurements along with the high measurement accuracy and data availability attained by applying an optical filter allows for high accuracy position and attitude estimation. The added advantage to this configuration is in its simplicity. Beacons are not constrained to specific quantity or location on the tanker, and can thus be placed purposefully to increase the estimation accuracy of certain states. The one challenge to overcome when using this measurement method is the possible marker ambiguity. While the 2D data of each marker can be successfully measured, one does not necessarily know which measurements correspond to which beacons. Differentiating between them is a case of least squares matching, where an initial marker configuration and sufficiently small measurement updates will allow marker correspondence between time steps.

A commercially available product utilising this method is called VisNav [9], developed by Texas A&M University. The basic principle is the same as [14] but solves the beacon ambiguity problem by using sequenced infra-red LED beacons. Known as an active optical sensor, a controller on the receiver orchestrates the sequence and timing of an active marker array on

the tanker through a wireless data link which ensures marker correspondence.

Least squares matching, which is computationally more complex is a simpler and quicker solution than creating an entire modulation and demodulation system to accommodate sequenced beacons. It is also left to be seen if the computational burden of least squares matching is more time consuming than an entire marker sequencing process.

An alternative to GPS and vision-based proposed in the initial Airbus AAR report [2], makes use of the physical connection between the tanker and receiver via the boom in the refuel phase of flight. The boom is attached to the tanker by way of a universal joint. If the boom is assumed to be rigid and of that of fixed or measurable length, and the angular deflection of the universal joint can be measured the relative position and attitude between aircraft can be calculated. This measurement approach can however not be used on its own as the boom parameter measurement are not enough to facilitate estimation of a six degree of freedom (6DOF) model and can only provide measurements once the aircraft are connected.

The use on an Inertial Measurement Unit (IMU) is also very common in autonomous flight, with the specific force and angular rate measurements used in the propagation of the aircraft position, velocity and attitude states. Primarily shown to be used in the derivations of the relative velocity and attitude kinematic equations of satellite control [22; 23], the IMU measurement of the lead aircraft can be transmitted to the trailing aircraft and used in combination with its own IMU as inputs to the estimation algorithm.

Naturally none of the sensors discussed provide a direct measure of all of the relative states. For this reason estimation algorithms are used to fuse measurements, resulting in the estimation of the required states.

1.2.2 Estimation Algorithms

Estimation algorithms are used to estimate the state vector given a set of noisy measurements, a mathematical representation of the system dynamics and the measurement model which relates measurement to the state vector.

Various estimation algorithms exist in literature, none more popular than the Extended Kalman filter (EKF). Based on the Kalman filter for optimal estimation of linear systems, the EKF compensates for the presence of non-linearities in the system model through model linearisation using a Taylor series expansion. Model linearisation can be highly effective in cases where the models are simple, but can become increasingly complex and inaccurate with increased non-linearities, potentially causing the state estimate to diverge.

This method of sensor and process model fusion has been used in numerous cases throughout the literature. Most predominantly the EKF is used where vision-based sensors are used as the sole measurement device [10; 24; 17; 22], cases where vision sensors are fused with

traditional IMU/GPS configurations for relative state estimation [9; 25], or cases where they are used primarily in relative state estimation using differential GPS [3].

An alternate variation of the Kalman filter has been used in autonomous close proximity operations for state estimation of non-linear systems. This algorithm, known as the Unscented Kalman Filter (UKF), uses a set of deterministically chosen particles, referred to as *sigma points* to capture the state probability distribution more accurately than the model linearisation of the EKF, resulting in faster convergence to inaccurate initial conditions and a more stable solution for highly non-linear systems. The UKF estimation algorithm has been compared to the EKF in obstacle avoidance as well as various spacecraft autonomous docking simulations where GPS, IMU and vision sensors fusion is required [13][26][27].

The Particle Filter (PF) is a practical solution for applying the optimal non-linear estimation algorithm, or Bayesian filter, but is generally discarded for real time applications due to the amount of processing power required. In a PF an arbitrary amount of particles are used to represent the state statistics. Increasing the number of particles will increase the optimal nature of the state estimate. This approach has been introduced in select cases for estimation of the relative attitude between spacecraft [28]. Examples of the use of such an estimation algorithm are featured in specific examples in [13][29] to illustrate optimal estimation and the deviation of the EKF and UKF from it.

Various papers also introduce an adaptive component to the estimation algorithms typically allowing the process or measurement noise models to be estimated, compensating for modeling errors and uncertainty and varying conditions such as turbulence [24; 30; 31; 32; 33].

Though many sensor end estimation algorithms have been theorised for use in autonomous close proximity operation only a few have been practically implemented. As such the sensors and algorithms used in these projects are afforded special consideration.

1.2.3 Practical Implementation

Close formation control with the aim of simulating an autonomous refueling procedure was first achieved by the Air Force Institute of Technology (AFIT) using a Beechcraft C-12 Hurion as the leader aircraft and a Learjet LJ-25 as the follower [34]. Both lead and follower aircraft were equipped with carrier phase differential AFIT Relative Navigation Global Positioning System (GPS) providing high accuracy relative position measurements. The lead aircraft was also fitted with a small Micro-Electrical Mechanical System Inertial Measurement Unit (MEMS IMU) providing axial specific force and angular rate measurements, used to aid the GPS in position estimation and also allow attitude estimation. A wireless data link allowed communication between aircraft with state estimation being facilitated by an unknown estimation algorithm.

The first autonomous refueling manoeuvre was executed using a Boeing B-707-300 tanker aircraft and NASA's F/A-18 as the receiver aircraft [35]. Relative state estimation was achieved in two parts. Similar to [34], a relative GPS/IMU sensor package in combination with a wireless data link was used to estimate relative aircraft states. Refueling was achieved through the use of a probe and drogue configuration, and as such an additional measurement providing information of the drogue relative to the receptacle was required. The solution was to fit the receiver with a single camera with an off-the-shelf video tracking processor providing relative camera-to-drogue azimuth, elevation and range measurements to the control system.

In 2007 Williamson *et al.* [36] introduced the use of a Formation Flight Instrumentation System (FFIS) developed specifically for state estimation between aircraft in close proximity. The FFIS provides precise estimation of relative position, velocity and attitude between aircraft in formation through the use of differential carried phase GPS and an inertial navigations system (INS), where again communication was facilitated through the use of a wireless data link. An extended Kalman filter is used to fuse the measurements in order to maximise the accuracy of the state estimates.

1.3 Proposed Approach

From the literature it is clear that there is no unified solution to the state estimation problem. Practically, each sensor configuration poses its own advantages and disadvantages in terms of noise, complexity and measurement relevance. Similarly, the choice of estimation algorithm also suffers from indecision, where the three algorithms considered vary in terms of processing power required, complexity of implementation and the stability and accuracy to which states can be estimated.

For this reason the idea of developing a single state estimation solution was replaced with one that considers all applicable sensor technologies and estimation algorithms. Evaluating multiple sensor configurations in conjunction with any of the three estimation algorithms does not change any of the project goals, it merely requires that the analysis of a single configuration be expanded to an analysis of multiple configurations. Analysing multiple configurations serves to provide a more comprehensive analysis of the state estimation problem, which allows for broader insight into the effect of variable sensors and estimation algorithms on the state estimate accuracy.

In light of the multiple estimation configuration approach the project goals and proposed approach are set to be:

- Define the estimation system functional requirements and performance specifications.

  - Establish the estimation state vector by introducing the AAR scenario and evaluating the input requirements of the control system.
  - Define the accuracy requirements to which the state vector must be estimated based on the performance requirement imposed by the control system .

- Select applicable state estimation algorithm for simulation.
  - Evaluate all applicable state estimation algorithms.
  - Conduct a study to determine which algorithms are more practically suited for implementation in terms of robustness, ease of implementation and accuracy of the resultant state estimates.

- Establish sensor configurations for simulation
  - Evaluate all applicable sensors for use in the sensor array
  - Decide on various sensor combinations to simulate the options available in practice
  - Conduct a study to determine the effect of varying sensor parameters such as sensor noise, sensor positioning and number of measurements will have on the estimation accuracy
  - Based on the conclusions, suggest a final set of seonsor configurations to be evaluated in simulation

- Simulate an AAR procedure with the applicable sensor configurations and estimation algorithms
  - Simulate all sensor configurations using each of the estimation algorithms
  - Compare state estimate accuracies to the performance requirements
  - Draw conclusions based on the relative accuracy of the resulting state estimation accuracies

The following section provides a functional breakdown of the rest of the document a brief outline of each chapter.

1.4 Thesis layout

Chapter 2 provides an overview of the project, creating the AAR scenario and parametrising the state estimation problem allowing the subsequent chapters to solve the aspects of estimation mentioned. Initially the the AAR scenario is defined, accompanied by an evaluation of the control system input requirements. This leads to a definition of the estimation system

requirements in the form of a state vector and subsequent estimation accuracy requirements. Finally the sensors and estimation algorithms that will be considered are introduced along with the motivation of the choice of sensor configurations used throughout this thesis.

Chapter 3 and Chapter 4 form the basis of the state estimation system, where the three estimation algorithm are derived with generic equations after which the process and measurement models are derived as they will be used in simulation.

Chapter 5 conducts a sensitivity analysis which evaluates the effect a change in system parameters will have on the state estimates, which serves to increase the insight into how the state estimates can be improved. The system parameters include the process and measurement noise as well as the particular setup of the sensors, such as a varied sensor position and number of measurements. After the sensitivity analysis has been performed the configurations proposed in Chapter 2 are fixed to provide the practically optimal state estimation solution.

The final simulation is outlined in Chapter 6 , where each sensor configuration discussed in Chapter 2 and subsequently finalised in Chapter 5 is implemented using the estimation algorithms introduced in Chapter 3, with their respective state estimation accuracies being the desired output. These accuracies are compared to the state estimation accuracy requirements also shown in Chapter 2, with sensor configurations being ranked on how well state estimation is achieved. Suggestions for state estimate accuracy improvements for the configurations that do not meet the minimum criteria are provided based on the insight gained in Chapter 5.

Finally, Chapter 7 provides a conclusion on the work presented and provides final recommendations on possible future work related to the project.

Chapter 2

AAR State Estimation

Following the conceptual introduction of the AAR project as well as an overview of the aspects that require attention in the development of a state estimation system, the aim of this chapter is to parameterise the state estimation problem within an AAR specific scenario. By doing so all of the aspects of AAR estimation that required further evaluation are brought to light, some of which are considered in this chapter, with others the object of the subsequent chapters.

In the process of developing a state estimation system it is first necessary to define the output requirements. Since the estimation system is tasked with providing the inputs to the control system an evaluation on the control system input requirements result in the definition of an estimation state vector and a set of minimum accuracy requirements.

With a full definition of the system requirements the means with which state estimates are obtained are presented in the form of sensor and estimation algorithms. An overview of each of the sensors and algorithms is given, after which the sensor configurations that will be tested in simulation are outlined. Subsequent chapters will serve to derive the particulars of the sensors models, estimation algorithms, configuration optimisation and final simulation.

Note that the vector notation and coordinate system definitions used in the mathematical representation of the physical system can be found in Appendix A.

2.1 The AAR Scenario

In order to have a better understanding of the the interaction between the aircraft, the tanker and receiver aircraft configurations are presented. Each aircraft is reduced to a body-fixed coordinate frame with additional relevant body-fixed or body-carried coordinate frames. Points of interest are also indicated and defined followed by a description of the stages of operation in an AAR scenario.

2.1.1 Aircraft Configurations

Considering the tanker aircraft first, the coordinate system representation can bee seen in Figures 2.1 and 2.2.

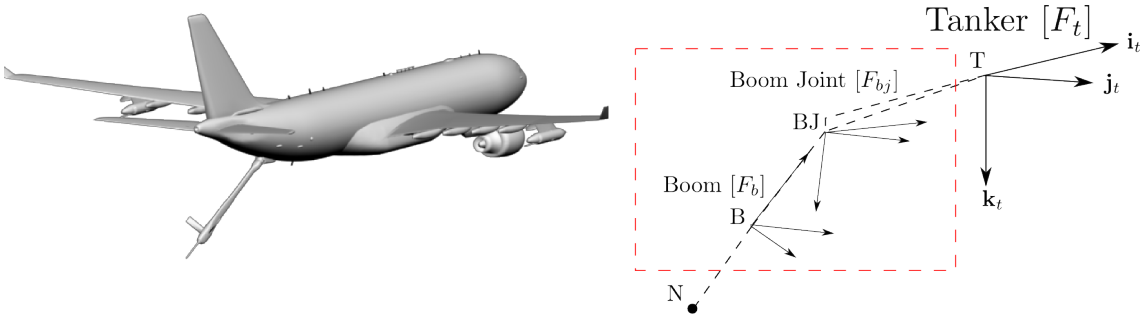

Figure 2.1 – Tanker Configuration

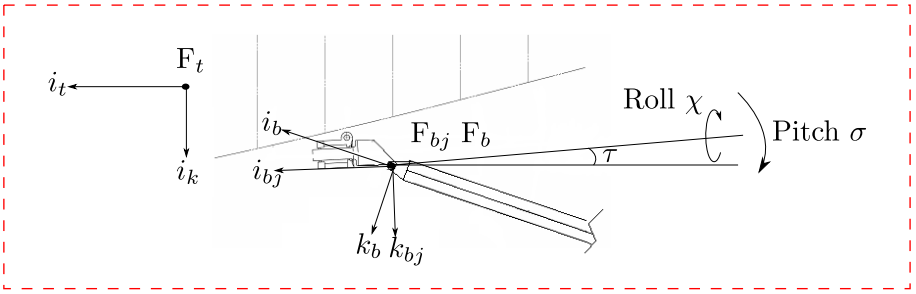

Figure 2.2 – Boom Joint Configuration

The aspects of interest are:

- F_t : Tanker reference frame in accordance with a body-fixed reference frame with origin T at the tanker center of mass (CM) which coincides with its center of gravity (CG). This CG position is generally an estimate and can move significantly in large aircraft, especially due to the transfer of fuel. Evaluating this additional uncertainty associated with the CG position estimates does not fall within the scope of this projects and as such is assumed negligible.
- F_{bj} : The boom joint body-fixed reference frame with origin BJ where the boom is attached to the tanker fuselage. The orientation of this reference frame is fixed relative to that of the tanker with base vector $\mathbf{j}_{bj}$ parallel to the tanker lateral axis $\mathbf{j}_t$ and base vectors $\mathbf{i}_{bj}$ and $\mathbf{k}_{bj}$ in the tanker plane of symmetry, pitched about $\mathbf{j}_{bj}$ by the angle τ as seen in Figure 2.2.

- F_b : The boom reference frame is a body-carried reference frame with origin, B, at the same point as the boom joint on the tanker fuselage. Note that this is not apparent in Figure 2.1, where the origins are shown to be different to avoid confusion between the reference frame axes. The orientation of the boom reference frame is independent of that on the tanker. At its nominal position $\mathbf{i}_b$ aligns with the length of the boom, $\mathbf{j}_b$ runs parallel to the tanker lateral axis $\mathbf{j}_t$ and $\mathbf{k}_b$ completes the right handed axis system. The angular offset from the tanker reference frame is achieved through a roll angle χ about $\mathbf{i}_{bj}$ and a pitch angle σ about $\mathbf{j}_b$ also shown in Figure 2.2.

- N : Nozzle situated at the end of the boom has a known fixed position in the boom reference frame but a variable position in the tanker reference frame due to the variable orientation of the boom reference frame relative to the tanker reference frame. This point is the connection point between the tanker and the receiver aircraft fuel receptacle.

In comparison to the tanker aircraft the receiver is much less complicated. A receiver aircraft model along with its coordinate frame representation is shown in Figure 2.3.

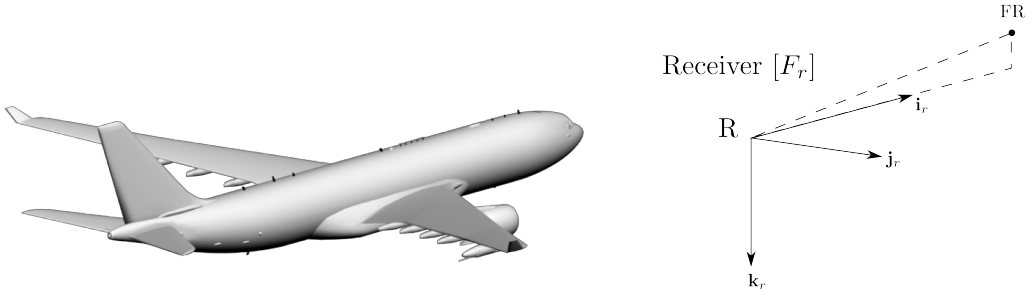

Figure 2.3 – Receiver Configuration

The aspects of interest are:

- F_r : Receiver reference frame in accordance with the body-fixed coordinate system with origin R at the receiver CM which is assumed to be at a known and fixed location. The same consideration in terms of the estimated CM position is made as with the tanker aircraft.

- FR : Fuel receptacle point at fixed known location in the receiver reference frame. This is the connection point between the receiver aircraft and the nozzle in the tanker reference frame.

Having introduced the tanker and receiver configurations as they appear within the AAR scenario it is necessary to put the actions of the aircraft into perspective by introducing the modes of flight and stages of operation encountered during the refueling procedure.

2.1.2 Stages of operation

The tanker aircraft follows an independent trajectory which implies that the control modes that dictate the tanker's flight path are independent to the motion of the receiver aircraft. The possible tanker modes of flight are given as:

- Straight and Level Mode: The tanker is set to maintain a constant air speed, altitude and attitude. This is the only flight mode in which the tanker and receiver can connect via the boom-receptacle configuration.
- Bank mode : The tanker enters a constant pre-defined bank angle in order to change heading as the required flight path is typically an oval shape. The receiver aircraft is not required to connect to the tanker in this phase, but once connected must be able to maintain the connection during the bank mode.
- Toboggan Mode : The tanker engages in a constant rate of descent. When the receiver aircraft becomes too heavy and has difficulty maintaining its longitudinal position due to limited engine power, a constant descent mode aims to improve longitudinal control response. Similar to the bank mode the receiver is not required to connect to the tanker in this mode, but once connected in the straight and level mode must be able to maintain the connection.

While the tanker is engaged in straight and level flight the receiver is tasked with performing the refueling procedure. The five stages of refueling are given as:

- Rendezvous : The receiver joins with the tanker and puts itself in position 300m behind, and 300m to starboard of the tanker known as the observation position .
- Pre-contact : The receiver leaves the observation position to approach to tanker and settles in a position 10m behind the tanker known as the pre-contact position ready to engage the contact phase.
- Contact: Approach from the pre-contact position until contact between the boom and fuel receptacle is made. The pilot, or control system, must maintain the fuel receptacle of the aircraft within a connect envelope for roughly 30s which is the time required by the boom operator to dock the nozzle in the fuel receptacle.

- Refueling phase: The fuel receptacle must be maintained within a disconnect envelope. During this stage the boom is no longer controlled by the boom operator but follows the evolution of the receiver as seen in the tanker coordinate frame. This stage can take up to 20 minutes.
- Breakaway: If the fuel receptacle violates the constraints of the disconnect envelope the receiver aircraft must break away by deploying spoilers and reducing thrust, returning to the observation position.

Note that the pre-contact and contact phases of operations can only be performed while the tanker is in a straight and level flight mode, with the refueling phase maintained throughout all tanker mode of operation. The task of the control system is to allow the receiver aircraft to perform each of these tasks autonomously. In order to establish a set of estimation system requirements it is necessary to first evaluate the control system's functional requirements and control strategy.

2.2 The Control System Specifications

The control system is tasked with maneuvering the receiver aircraft in all five stages of an AAR operation. The critical stages in terms of control are the contact and refueling stages as they result in the smallest distance between aircraft and by extension require the tightest control. In the following section the control constraints are defined first after which the control input parameter requirements are presented.

2.2.1 Control Envelopes

The control constrains that apply to each of the refueling stages correspond to control envelopes that define the boundaries within which the receiver's fuel receptacle must be maintained. These envelopes are defined as follows:

- Connect Envelope: The range in which the boom can be controlled when the aircraft are in the connect phase of flight, allowing the connection between the nozzle and the fuel receptacle to be made. The receiver pilot must maintain the receiver aircraft within this envelope until the boom is successfully to the fuel receptacle.
- Disconnect Envelope: The range in which the boom can manoeuvre, with an allowable safety margin, when both aircraft are connected. If the receiver's receptacle leaves this envelope the boom disconnects and stows automatically and the receiver's pilot is ordered to break away to ensure the safety of both aircraft, ending the refueling procedure.

From Figure 2.4 it is clear that the control limits originate from the allowable range of deflection of the three boom parameters $\{\sigma, \chi, l\}$.

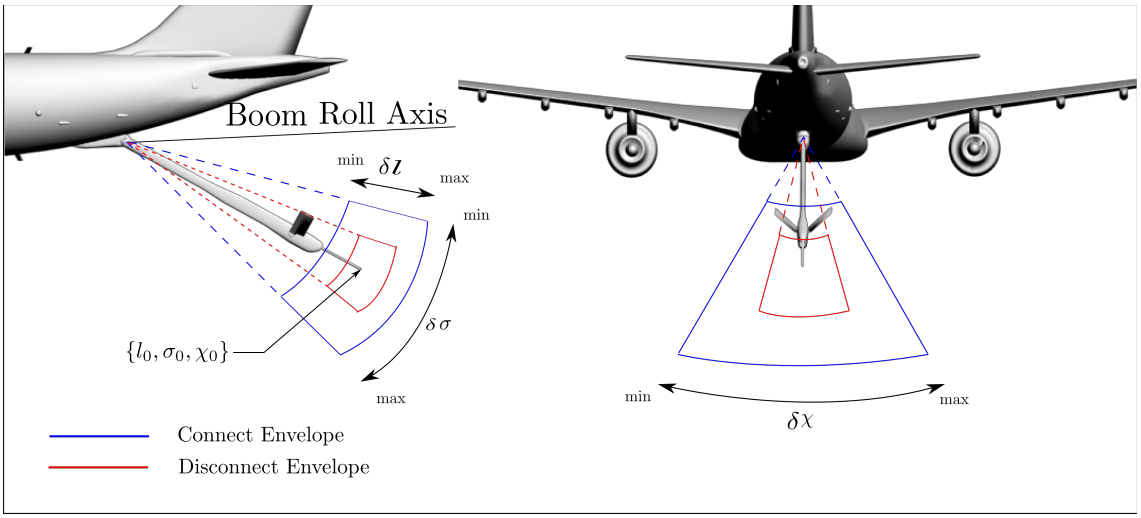

Figure 2.4 – Control Envelopes as a function of the allowable boom parameter deflection

Note that the center point of these envelopes corresponds to the nozzle position when the boom parameters assume their nominal values. These values along with the applicable deflection limits are given in Appendix D . The position of the envelope center relative to the tanker CM is fixed and known, expressed by the coordinate vector $\boldsymbol{p}_t^{N_0/T}$. This point signifies the center point of the envelope, furthest away from all control envelope boundaries and as such holds significance for control purposes.

The goal of the control system will be to control the fuel receptacle to this envelope center point through the manipulation of the receiver aircraft control surfaces in response to the position error input which is to be driven to zero.

As the internal function of the control system is not the focus of this thesis, the manner in which the control system attempts to minimise the error state is not of importance, however, providing the control system with the relevant control input states is the purpose of the estimation system and as such warrants significant attention. The first step to designing a state estimation system is identifying the system outputs, which requires an evaluation of the control system inputs.

2.2.2 Control Inputs

As the main goal of the control system is to maintain the fuel receptacle within the applicable envelope it stands to reason that the control system must attempt to minimise the distance between the fuel receptacle and the control envelope center. From the concurrent AAR control

systems projects it is known that it is this relative position vector that acts as the control input parameter. A visual representation of this vector is shown in Figure 2.5, where the true value of the control input vector is given by $\boldsymbol{p}_t^{FR/N_0}$.

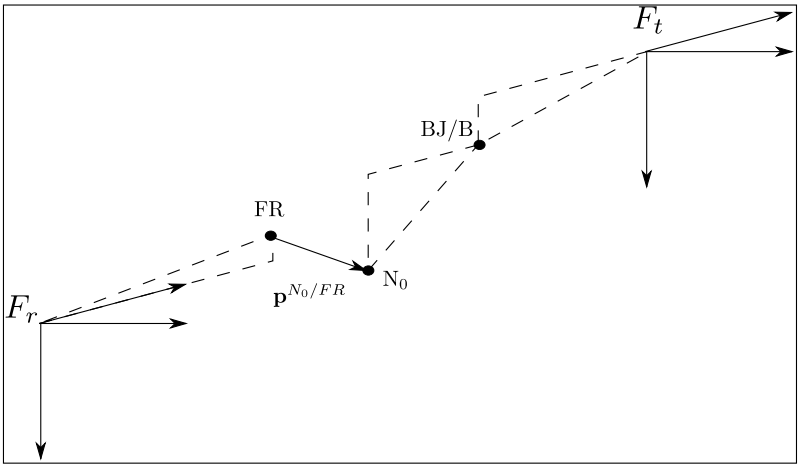

Figure 2.5 – Position Control Input

In addition to the position control input, the control system also utilises the velocity of the envelope center relative to the fuel receptacle to allow predictive control to be applied which serves to improve the control response by adding damping. This control input velocity is shown in Figure 2.6 and given by $\boldsymbol{v}_t^{FR/N_0}$. Note that both the control input position and velocity are of the fuel receptacle relative to the envelope center and coordinated in the tanker reference frame. The vectors are chosen as such for easy comparison to the control envelope boundaries.

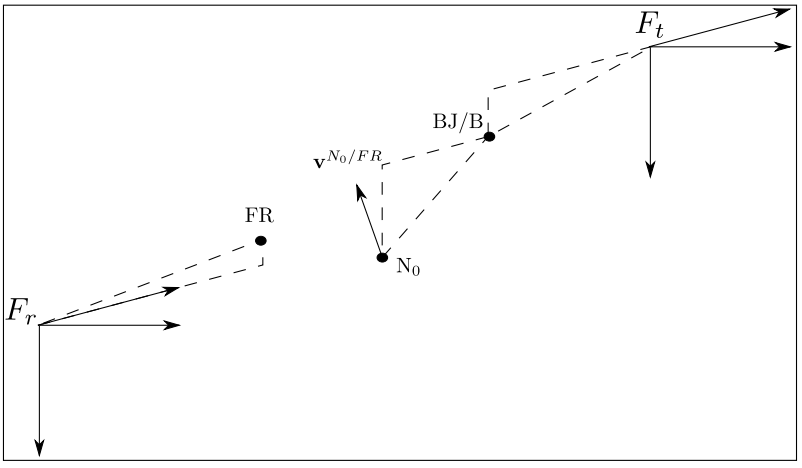

Figure 2.6 – Velocity Control Input

In practice the state estimates are accompanied by a degree of uncertainty. An error in the estimated value of either of the input parameters would provide false reference commands to the receiver aircraft control system, resulting in the fuel receptacle not being controlled to the

desired point. Uncertainty in the state estimate can be tolerated up to a degree, after which the performance of the control system diminishes. This limit is referred to as the minimum control input accuracy.

2.2.3 Minimum control input accuracy

The assumption is made that the control system can maintain the fuel receptacle within the desired control envelope given the true values of the control inputs. The minimum control input accuracy is obtained by establishing the maximum input parameter error that will still allow the fuel receptacle to be maintained within the control envelope.

The error in the control inputs are defined as the difference between the true and estimated values,

$$\delta \boldsymbol{p}_t^{FR/N_0} = \boldsymbol{p}_t^{FR/N_0} - \hat{\boldsymbol{p}}_t^{FR/N_0} \tag{2.2.1}$$

$$\delta \boldsymbol{v}_t^{FR/N_0} = \boldsymbol{v}_t^{FR/N_0} - \hat{\boldsymbol{v}}_t^{FR/N_0} \tag{2.2.2}$$

When evaluating the effect of an error in the the control input position, consider the scenario where the fuel receptacle FR is being controlled to the control envelope center N_0. The position of the fuel receptacle is, however, an estimated position, where the uncertainty associated with the position is a function of the control input position estimate error, $\delta \boldsymbol{p}_t^{FR/N_0}$. If the error is small, the control system is responsive to changed in the relative position of the fuel receptacle. On the other hand, if the control input error is large, the uncertainty in the true position of thefuel receptacle is large, which makes the control of the fuel receptacle insensitive to changes in the control envelope center. Given a large enough uncertainly the fuel receptacle cannot be maintained within the control envelope.

The assumption is made that if the 3σ uncertainty in the control position error is known to within 10% of the control envelope, that the control system will be sufficiently responsive to maintain the fuel receptacle within that control envelope. This concepts is visualised in Figure 2.7. Note that this scaling is achieved by moving the boundaries of the envelope towards the center by the specified fraction. It is also important to note that that the 10% value is an approximation and subject to a more detailed analysis of the control system capabilities.

The same logic can be applied in the evaluation of the control input velocity error. The control input velocity is essential for a quick response to the change the position of the control envelope. If the uncertainty in this input velocity is small, the control system is responsive to quick changes in the control input position. On the other hand, a large uncertainty in velocity will result in less responsive control of the fuel receptacle as it relies mostly on the position control. If a sufficiently large true velocity is encountered the control system will not

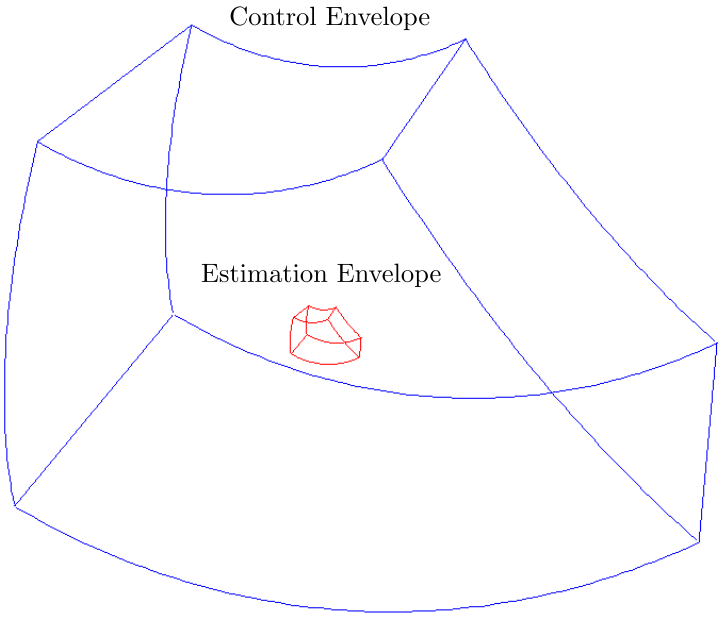

Figure 2.7 – Estimation envelope chosen to be 10% of the control envelope

be responsive enough to follow the control envelope center. For this reason it is assumed that if the velocity input can be estimated in such a way that the associated 3σ error integrated over 5 seconds does not violate the control envelope constraints, that sufficient control can be applied in that envelope. This corresponds to an allowable velocity uncertainty envelope 20% that of the control envelope.

As with the allowable position estimate error, the margin for the allowable control input velocity error is an approximate value chosen based on the assumed capabilities of the aircraft and control system and is subject to a more detailed analysis of the control system capabilities

Having introduced the control aspect of AAR the estimation system requirements are presented. The estimation system will use the control input vector and accompanying accuracy requirements as output requirements, where the subsequent sections define the state vector, as well as a suitable method of evaluating the resultant state estimate accuracies.

2.3 State Estimation System Specifications

The state estimation system is tasked with estimating the control input parameters by using measurements obtained from a sensor array. The control envelope center does not correspond to a physical point to which sensors can be attached. It is however possible to attach sensors to the tanker and receiver fuselages in which case the measurement can be easily related to the relative aircraft states which can also be used to construct the control input position and velocity vectors.

2.3.1 The State Vector

The correct choice of states is arguably one of the most important aspects of the estimation process. Firstly, the states must be chosen as to fulfill the requirements set by the control system, i.e provide the necessary information to allow the control inputs to be calculated, and secondly, the choice of states will affect the complexity of the non-linear measurement and process models derived in Chapter 4. It is thus necessary to choose states that are applicable in terms of control, yet have sufficiently simple dynamic and measurement models.

The equation relating the relative position between the control envelope center and fuel receptacle is given by:

$$\boldsymbol{p}^{FR/N_0} = \boldsymbol{p}^{T/N_0} + \boldsymbol{p}^{R/T} + \boldsymbol{p}^{FR/R} \tag{2.3.1}$$

To find the expression for the relative velocity, the time derivative of the relative potion vector is taken with respect to the receiver tanker frame:

$$\begin{aligned} \frac{d}{dt}\left(\boldsymbol{p}^{FR/N_0}\right)\Big|_t &= \frac{d}{dt}\left(\boldsymbol{p}^{T/N_0}\right)\Big|_t + \frac{d}{dt}\left(\boldsymbol{p}^{R/T}\right)\Big|_t + \frac{d}{dt}\left(\boldsymbol{p}^{FR/R}\right)\Big|_t \\ \boldsymbol{v}^{FR/N_0} &= \boldsymbol{v}^{R/T} + \boldsymbol{\omega}^{r/t} \times \boldsymbol{p}^{FR/R} \end{aligned} \tag{2.3.2}$$

Note that the time derivative of the position vector between the tanker body axis, T, and the and the control envelope center , N_0, is zero and as such is omitted in the subsequent equation.

Coordinating this equations into the applicable reference frames yields:

$$\boldsymbol{p}_t^{FR/N_0} = -\boldsymbol{p}_t^{N_0/T} + \boldsymbol{T}\left(\boldsymbol{e}^{t/r}\right)\left(-\boldsymbol{p}_r^{T/R} + \boldsymbol{p}_r^{FR/R}\right) \tag{2.3.3}$$

$$\boldsymbol{v}_t^{FR/N_0} = -\boldsymbol{T}\left(\boldsymbol{e}^{t/r}\right)^T \boldsymbol{v}_r^{T/R} + [\boldsymbol{\omega}_t^{t/r}\times]\boldsymbol{T}\left(\boldsymbol{e}^{t/r}\right)^T \boldsymbol{p}_r^{FR/R} \tag{2.3.4}$$

with $\boldsymbol{T}\left(\boldsymbol{e}^{r/t}\right)$ the coordinate transformation matrix as a function of the relative Euler angles. From Equations 2.3.3 and 2.3.4 the resulting states required to allow the control input position and velocity to be calculated are:

- $\boldsymbol{p}_r^{T/R}$ and $\boldsymbol{v}_r^{T/R}$: Position and velocity of the tanker CG relative to the receiver CG coordinated in the receiver reference frame
- $\{\boldsymbol{e}^{t/r}/\boldsymbol{q}^{t/r}\}$: The attitude of the tanker reference frame relative to the receiver reference frame given in term of either Euler angles or quaternions, the definitions of which can be found in Appendix B

- $\boldsymbol{\omega}_t^{t/r}$: The angular velocity of the tanker reference frame relative to the receiver reference frame coordinated in the tanker reference frame. Coordinating this vector in the tanker reference frame simplifies attitude kinematics equations which are shown in Chapter 4.

As a result the estimation state vector is shown to be:

$$\boldsymbol{x} = \begin{bmatrix} \boldsymbol{p}_r^{T/R} \\ \boldsymbol{v}_r^{T/R} \\ \{\boldsymbol{e}^{t/r}/\boldsymbol{q}^{t/r}\} \\ \boldsymbol{\omega}_t^{t/r} \end{bmatrix} \tag{2.3.5}$$

Note that the attitude vector is given as both Euler angles and a quaternion. The quaternion is preferred to the Euler angle representation for use in simulation due to the simplicity with which successive rotations and relative quaternions can be represented. Quaternions also do not suffer the limitation of a singularity, which in the case of AAR is not critical, but allows the research to be more general in its application. The measurement and process model derivations of Chapter 4 will utilise this quaternion attitude representation.

The Euler angles are used in scenarios where the explanation of a concept requires the visualisation of the attitude. This is especially useful when evaluating the accuracy requirements of each state, where an effect of an error in relative roll, pitch or yaw is much easier understood than errors in the quaternion estimate.

With this newly defined state vector it is also necessary to relate the accuracy requirements of the control input parameters to that of the state vector and introduce a method with which the accuracies resulting from simulation in Chapter 6 can be evaluated.

2.3.2 State estimate accuracy

An error in the position and velocity control inputs, $\delta\boldsymbol{p}_t^{FR/N_0}$ and $\delta\boldsymbol{v}_t^{FR/N_0}$, will cause the fuel receptacle to be controlled to an incorrect control envelope center, hampering the ability of the control system to maintain the fuel receptacle within the specified envelope.

In order to evaluate the required state estimation accuracy it is necessary to derive the error vector equations relating the errors in state estimates to errors in the control input position and velocity. With the true position and velocity of the control envelope center relative to the fuel receptacle is give by Equations 2.3.3 and 2.3.4, the estimated values are given by:

$$\hat{\boldsymbol{p}}_t^{FR/N_0} = -\boldsymbol{p}_t^{N_0/T} + \boldsymbol{T}\left(\hat{\boldsymbol{e}}^{t/r}\right)\left(-\hat{\boldsymbol{p}}_r^{T/R} + \boldsymbol{p}_r^{FR/R}\right) \tag{2.3.6}$$

$$\hat{\boldsymbol{v}}_t^{FR/N_0} = -\boldsymbol{T}\left(\hat{\boldsymbol{e}}^{t/r}\right)^T \hat{\boldsymbol{v}}_r^{T/R} + [\hat{\boldsymbol{\omega}}_t^{t/r}\times]\boldsymbol{T}\left(\hat{\boldsymbol{e}}^{t/r}\right)^T \boldsymbol{p}_r^{FR/R} \tag{2.3.7}$$

Subtracting this from the true value and making the assumption that the true relative attitude, velocity and angular velocity is zero,

$$\begin{aligned} \boldsymbol{e}^{t/r} &= [0\ 0\ 0]^T \\ \boldsymbol{v}_r^{t/r} &= [0\ 0\ 0]^T \\ \boldsymbol{\omega}_t^{t/r} &= [0\ 0\ 0]^T \end{aligned}$$

yields an equation for the error in control input position and velocity as a function of the error states:

$$\delta \boldsymbol{p}_t^{FR/N_0} = \left(\boldsymbol{T}\left(\boldsymbol{\delta e}^{t/r}\right) - I\right)\boldsymbol{p}_r^{T/R} - \boldsymbol{T}\left(\boldsymbol{\delta e}^{t/r}\right)\delta \boldsymbol{p}_r^{T/R} + \left(\boldsymbol{T}\left(\boldsymbol{\delta e}^{t/r}\right) - I\right)\boldsymbol{p}_r^{FR/R} \quad (2.3.8)$$

$$\delta \boldsymbol{v}_t^{FR/N_0} = -\boldsymbol{T}\left(\boldsymbol{\delta e}^{t/r}\right)^T \delta \boldsymbol{v}_r^{T/R} + [\delta \boldsymbol{\omega}_t^{t/r}\times]\boldsymbol{T}\left(\boldsymbol{\delta e}^{t/r}\right)^T \boldsymbol{p}_r^{FR/R} \quad (2.3.9)$$

Increasing the errors in the states will increase the error in the control inputs, which are then related to the constraints of the position and velocity estimation envelopes. Note in the error equations that if the state errors are zero, the resultant control input error is also zero.

From these equations the state estimation accuracy will be evaluated in one of two ways, through either the upstream or downstream analysis.

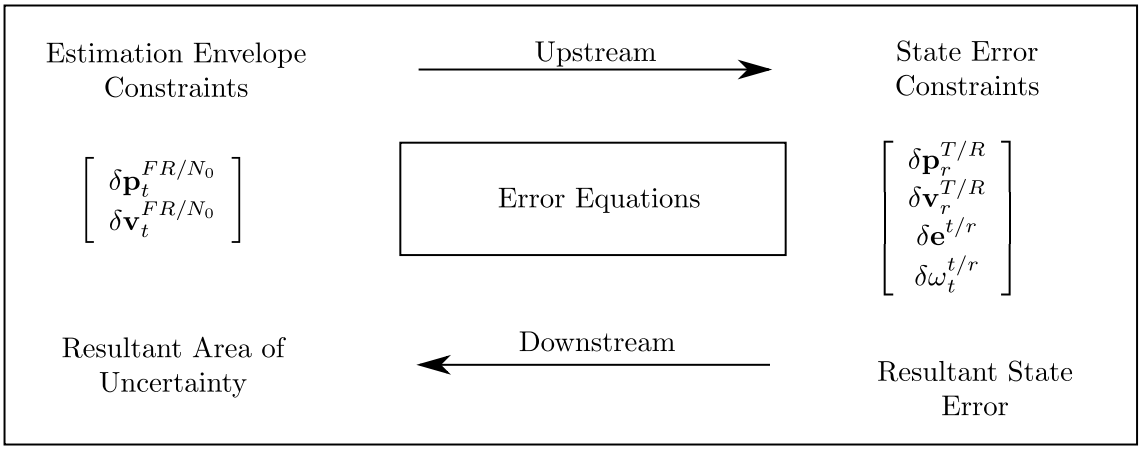

The upstream method uses control envelope constraints to constrain the allowable error in each state as shown in Figure 2.8, where each of the states, position, attitude states are perturbed from the nominal value whilst the other states remain fixed, until the estimation envelope constraint is violated.

This is particularly useful in indicating the coupling between an error in a selected state and an error in the control input parameter. An error in the relative pitch for instance, will have

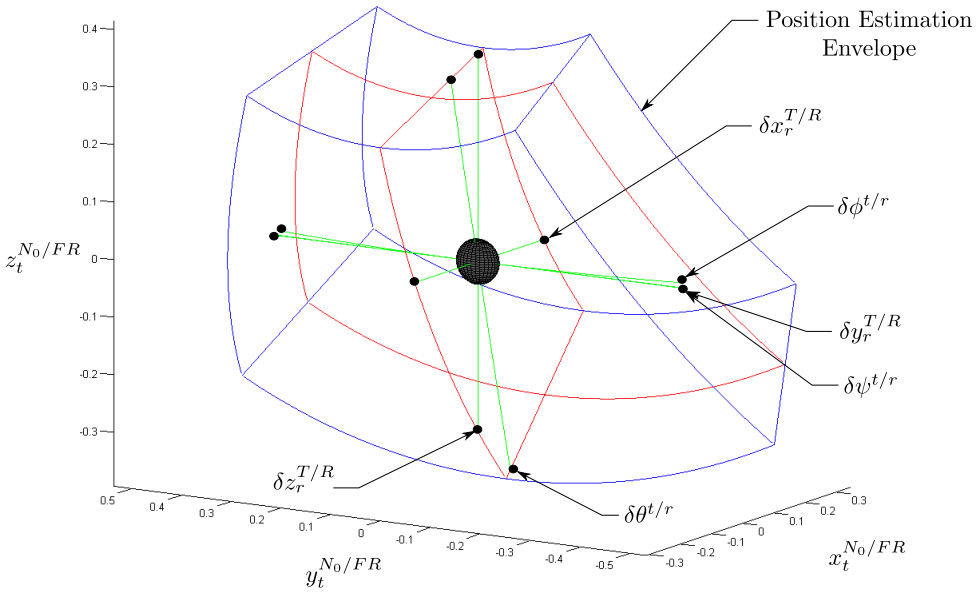

Figure 2.8 – Estimation envelope and the results of the upstream error analysis

a much larger effect on the control input position than an error in relative roll, due to the much longer distance of the boom nozzle from the pitch axis. This allows specific states to be identified as states that require more accurate estimation, for which the estimation system can be designed. Since all of the states cannot be evaluated simultaneously the error in each state is increased whilst the remaining states are assumed to be exact. The minimum state error resulting in the estimation envelope boundary being violated corresponds to the state accuracy limit.

Following a similar analysis for the relative translational and angular velocity state the resultant state error tolerances are shown to be:

State Estimate Error 3σ bound		
Vectors		state limit
$\delta \boldsymbol{p}_r^{T/R}$	δx	0.09 m
	δy	0.24 m
	δz	0.15 m
$\delta \boldsymbol{v}_r^{T/R}$	δV_x	0.18 $\frac{m}{s}$
	δV_y	0.48 $\frac{m}{s}$
	δV_z	0.03 $\frac{m}{s}$
$\delta \boldsymbol{e}^{t/r}$	$\delta \phi$	1.54^o
	$\delta \theta$	0.35^o
	$\delta \psi$	0.41^o
$\delta \boldsymbol{\omega}_t^{t/r}$	δP	3.1 $\frac{deg}{s}$
	δQ	0.7 $\frac{deg}{s}$
	δR	0.82 $\frac{deg}{s}$

Since each state is evaluated individually, it is possible that the combined errors of states can violate the estimation envelope limits. The effect of this is captured in the downstream analysis, with the piece-wise analysis deemed sufficient for initial use in identifying individual state estimate accuracy limits.

The downstream method for evaluating the accuracy of the state estimates uses the state error standard deviation to create an area of uncertainty in the control input position and velocity visualised in Figure 2.9.

The use of this method is, however, only applicable after the state estimation accuracies are evaluated in Chapter 6. This evaluation does not provide any insight in the particular contribution of each state, but does allow the full effect of the combined state uncertainty to be included in the analysis which makes the method more suited for evaluating the final results.

Having shown two methods for evaluating the state estimate accuracies the focus of the estimation system development moves to the introduction of the sensors and estimation algorithms that will be considered.

2.4 Sensors

A sensor input can either be classified as a driving input $\boldsymbol{u}$ or an observation input $\boldsymbol{y}$, where driving input are used in the propagation of the state vector, and observations have relevance to the current value of the state vector facilitating the correction of states and covariances. The sensors discussed will form part of the sensor array and may be used in conjunction with one another in various sensor configurations to be tested in simulation.

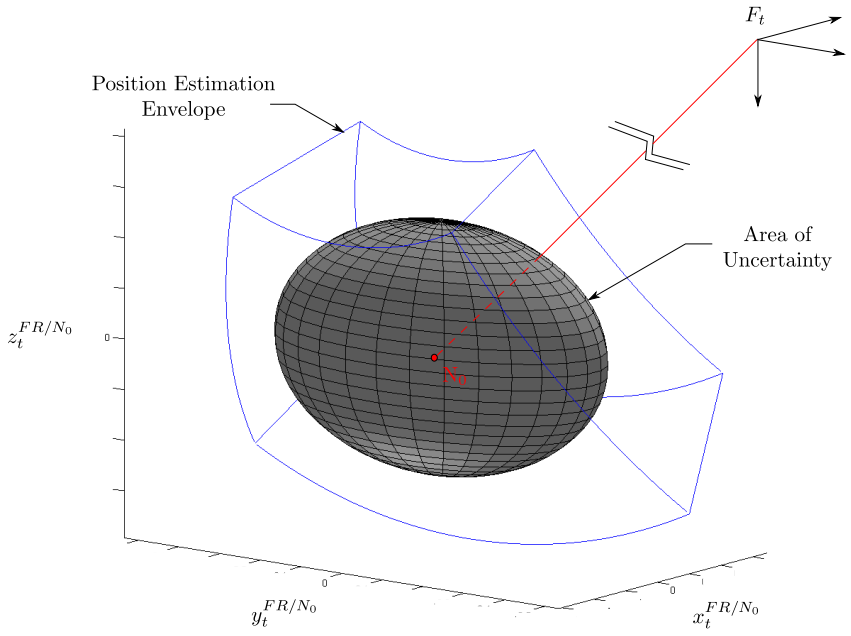

Figure 2.9 – Estimation envelope and area of position control input uncertainty due to state estimate uncertainty

2.4.1 Inertial Measurement Unit

An inertial measurement unit (IMU) is a device typically containing a three axis accelerometer and three axis angular rate gyroscope which provides a measure of the specific force and the angular velocity experienced by the IMU reference frame, respectively. IMUs are often used for inertial navigation allowing the position, velocity and attitude states of a vehicle to be propagated, with sensors such as GPS providing position and velocity corrections.

By fitting both the aircraft with IMUs and transmitting the measurements from the tanker to the receiver, the specific force and angular velocity measurements from both sensors can be used as driving inputs to the relative velocity and attitude quaternion kinematic equations.

There are however a few points to consider when implementing an IMU. In addition to white noise corrupting the measured specific force and angular velocity, the measurements can also contain a bias which can lead to drift in the estimated states due to integration over time. To combat this, additional bias stats are typically added to the state vector and estimated allowing a corrected IMU measurement to be used in state propagation. The IMU is also unlikely to be placed exactly on the aircraft center of gravity (CG) and as such the specific force measurement will include an additional force due to the aircraft's rotational velocity and acceleration.

In the AAR scenario obtaining aircraft accelerations and angular velocities is simplified as each aircraft already has an inertial measurement system, where the bias states and specific force projection of the IMU are corrected in an internal estimator. As a result the output

obtained from the aircraft will be highly accurate unbiased aircraft acceleration and angular velocity. Though this is the case, for the sake of a thorough analysis, the estimation of the IMU bias as well as CG offset compensation will be discussed in further detail in the derivation of the IMU measurement model in Chapter 4.

2.4.2 Roaming Base Differential GPS

GPS devices have long been used for navigation purposes, where code phase signals from at least four satellites allow the position of the GPS receiver to be calculated in the Earth Centered Earth Fixed (ECEF) reference frame.

Such devices, though useful, are not sufficiently accurate to facilitate autonomous close proximity operations. For this reason differential GPS techniques were developed which require an additional GPS receiver, known as a base receiver at a fixed locations on the Earth's surface. Over time the base receiver position estimate will converge to its true position allowing the measured pseudoranges to be compared to the expected pseudoranges, after which corrections are sent to roaming GPS receivers which correct their pseudoranges by the same amount. This, in combination with the additional use of the satellite carrier phase signal dramatically increases the accuracy of conventional GPS, potentially to centimeter level.

As the base receiver is stationary, the implementation of this form of GPS is limited to applications performed in an acceptable range from the base receiver. As AAR occurs over a large range this basic form of DGPS cannot be implemented, but the basic principle of GPS base station and rover communication has been applied in the development of a roaming base differential GPS (RB-DGPS) system.

In accordance with the theory presented in [3], the satellite signals received by a roaming GPS receiver are relayed to the roaming base receiver where the differences in carrier phase, code phase and Doppler shift signals are used as inputs to an estimator, which produces and estimate of the position and velocity of the roaming receiver module relative to the roaming base module. Various sources of GPS uncertainty such as the difference in atmospheric distortion of the satellite signals are negated due to the close proximity of the GPS receivers. This, in combination with the accuracy associated with the use of the carrier phase signal results in centimeter and centimeter per second accuracies in position and velocity [4]. Note that as mentioned in Chapter 1 there are alternative solutions to the RB-DGPS, such as SBAS, that are not considered in this project as they will serve the same purpose.

From Figure 2.10 it can be seen that a single GPS roaming base receiver RB_j can be placed on the receiver aircraft with multiple GPS roaming receivers RR_i attached to the tanker fuselage. The satellite signals received by a roaming receiver i are relayed to the roaming base j and

combined in the internal estimator to produce the relative position and velocity estimates used as measurement to the relative state estimator.

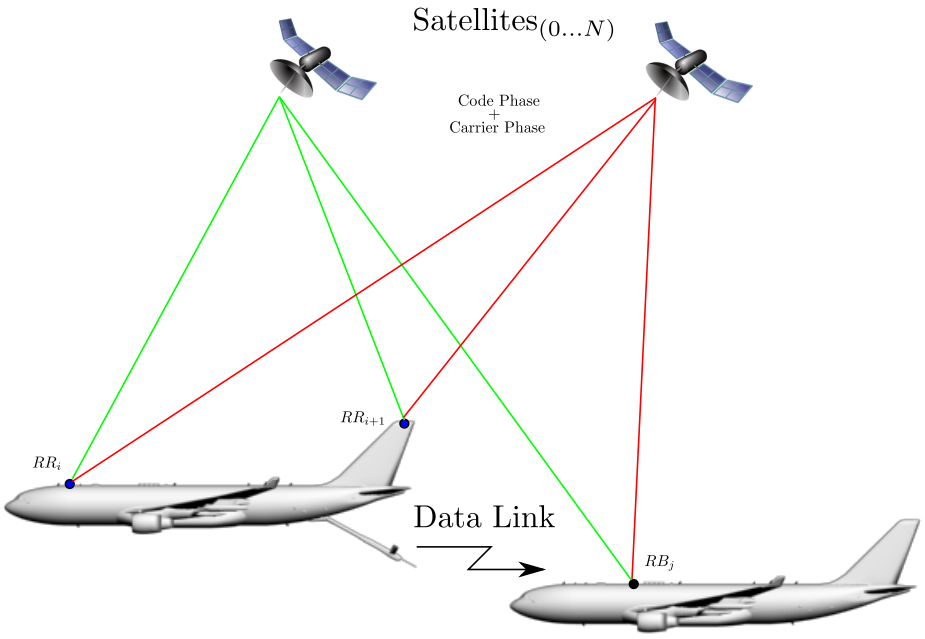

Figure 2.10 – Roaming Base Differential GPS as it applied to the AAR scenario

The development of the internal GPS estimator falls beyond the scope of this project. Various aspects such as integer ambiguity, ephemeris errors, multipath effects, satellite drop out and cycle slip must be considered and there are numerous papers dedicated to the optimisation of such as system. For the purposes of this thesis this system will be seen as a black box subsystem where the satellite signals are received as inputs and relative positions and velocities of the GPS receiver pairs are obtained as outputs, allowing them to be used as measurement in the estimation algorithm. Details on the development of such a RB-GPS system can be found in [3].

Similar to the use of the IMUs, the RB-DGPS system also requires inter-aircraft communication, as the satellite signals from each roaming GPS receiver must be be relayed from the tanker to the receiver aircraft. Commercial products exist where this communication is provided, or alternatively a single aircraft communication link can be developed for all necessary data transfer.

2.4.3 Optical sensors

As discussed in the literature study, there are various ways in which optical sensors can be used to provide measurements of features of interest in the sensor's view. The approach used throughout this thesis is developed in full in [14] where an autonomous helicopter is set to

land unassisted by using an optical sensor and infra red beacon array. The optical sensor is fitted with a passive light filter allowing only light from the beacons to pass, with ambient light filtered out. After filtering, the image is thresholded which differentiates between pixels having a certain light intensity, allowing any ambient light and edge effects that might have filtered through to be ignored. The result, as seen in Figure 2.11, is an array of pixels that correspond to the 2D projection of the infra red light from a particular beacon. These pixels are averaged and the center point used as the 2D measurement of the corresponding beacon.

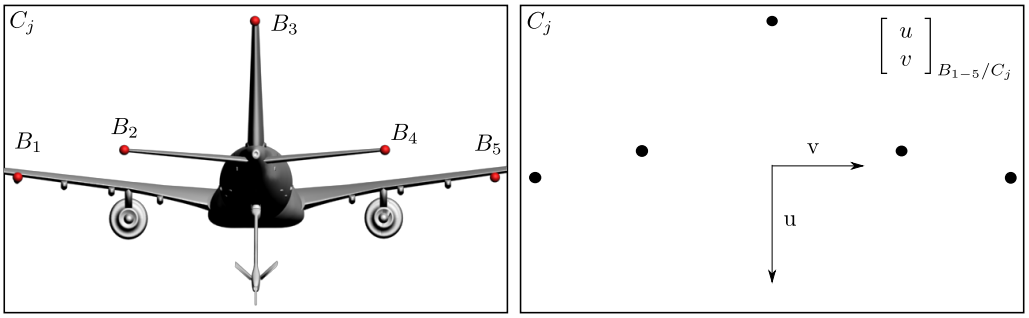

Figure 2.11 – IR Beacon array view vs. filtered measurement point array of optical sensor C_j

In the application of this technique in AAR the image sensor is placed on the receiver fuselage with the infra-red emitting beacons placed at known fixed locations on the tanker fuselage. The image sensor can either be set at a fixed orientation, in which case the IR beacon array must be in the correct field of view during the contact and refueling stages, or the sensor can be set to follow the light pattern, in which case its orientation relative to the receiver body frame will be varied.

The image is captured in accordance with the ideal pinhole camera model, which relates the 2D measurement of the beacons to their real world coordinates. The measurement obtained from the optical sensor can be used in the estimation algorithm in one of two ways depending on the sensor configuration, referred to as the monocular and stereoscopic configurations respectively.

2.4.3.1 Monocular

In the monocular configuration all the sensors are seen as independent measurement devices, each producing the 2D measurements of the markers in its particular field of view. The advantage of such a configuration is in its configurability, where a single sensor can be used to view all beacons, or multiple sensors can be used to view subsets of beacons, based on limitations such as the allowable sensor field of view. For state estimation of relative position and

attitude to be applied using monocular vision only, at least four measurement are required for a unique solution.

2.4.3.2 Stereoscopic

In stereoscopic vision, two monocular sensors with know relative position are used in combination to construct the real world coordinates of the beacons from the combined 2D measurements. Whereas the monocular sensor measurements are directly used in the estimation algorithm, the stereoscopic configuration requires an additional step where coordinate conversion occurs. Two sets of 2D measurements to a particular beacon are converted to relative 3D coordinates and used as measurement inputs to the estimation system. The added measure of accuracy provided by the known sensor offset allows for increased accuracy and robust estimation further discussed in the derivation of the sensor models in Chapter 4.

2.4.4 Boom parameters

The boom is connected to the tanker fuselage by means of a universal joint as seen in Figures 2.2 and 2.4. Once the nozzle at the end of the boom is connected to the fuel receptacle on the receiver aircraft the roll and pitch angular deflections allowed by the boom's universal joint as well as the variable length of the boom can me measured and relayed via a data link to the estimation algorithm on the receiver aircraft. The advantage of using these parameters is the high degree of measurement accuracy associated with modern angular and linear displacement sensors.

The obvious disadvantage is that the use of these measurements are restricted to the phases of operation where the aircraft are connected. Additionally, the boom parameter measurements on their own do not provide sufficient information to allow the relative states to be estimated. For this reason, the boom parameters can never be used as the sole measurement strategy, but will act as a complementary measurement device.

2.5 Proposed Configurations

Following the introduction of each sensor it is possible to set apart various configurations in which unique combinations of sensors are proposed for simulation. The configurations chosen to showcase the capabilities of each sensor in the AAR state estimation environment and are shown to be,

- **Configuration 1** : Roaming Base Differential GPS Only - Using three or more roaming GPS receivers placed on the tanker in combination with a single roaming GPS base

placed on the receiver allows all states to be estimated. This configuration will showcase the effectiveness with which DGPS can be used in relative state estimation.

- **Configuration 2** : Optical (Monocular) Only - Using three or more IR beacons placed on the tanker in combination with a single optical sensor placed on the receiver allows estimation of the position and attitude states. This minimalist configuration will showcase what can be achieved with a simple optical sensor configuration.

- **Configuration 3** : Optical (Stereoscopic) Only - Using three or more IR beacons placed on the tanker, in combination with a two optical sensor with known offset placed on the receiver allows estimation of the position and attitude states. Slightly more intricate that monocular vision, the configuration will highlight what effect a varied optical configuration will have, and if any improvements on the state estimates are observed as a result.

- **Configuration 4,5 and 6** : Roaming Base DGPS, Optical (Monocular) and Optical (Stereoscopic) only configurations with the addition of the boom parameter measurements. The boom serves as an addition measurement in stages where the aircraft are connected. This configuration will show if the addition of the accurate boom measurement have a significant effect on the state estimates.

- **Configuration 7,8 and 9** : Roaming Base DGPS, Optical (Monocular) and Optical (Stereoscopic) only configurations with the addition of the IMU measurements. The addition of the IMU will highlight the gain in estimation accuracy due to the addition of driving input measurement.

- **Configuration 10,11 and 12** : Roaming Base DGPS, Optical (Monocular) and Optical (Stereoscopic) only configurations with the addition of the boom and IMU measurements. The final three configurations showcase what is expected to be the most accurate state estimates that can be obtained through the addition of driving inputs as well as high accuracy boom measurement to the original three configurations

These configurations will be implemented in the AAR state estimation simulations of Chapter 6 after which the resultant state estimate accuracies can be compare to one another as well as to the minimum accuracy criteria. The configurations are implemented in simulation through the use of an estimation algorithm.

2.6 Estimation Algorithms

Having defined the state vector as well as introduced the sensors, the final aspect of the estimation system design is the choice of estimation algorithm, which aims to combine the

driving input and the observation vector inputs using the process and measurement equations to form an estimate of the state vector.

Optimal estimation of any linear or non-linear system can be achieved through so called Bayesian estimation which forms a conceptual solution to the estimation problem through a recursive expression for the posterior probability density function[37]. In practice this optimal solution is usually impossible to compute since it involves several integrals that lack analytical solutions.

Various sub-optimal solutions to the non-linear state estimation problem have been developed, with the three most popular being the Particle Filter (PF), Extended Kalman Filter (EKF) and the Unscented Kalman Filter (UKF). Each filter approaches the estimation problem in a unique way, where the basic function of each algorithms is given as:

- **Particle Filter**: Considered a method for practically implementing Bayesian estimation, the PF substitutes an analytical representation of the state probability density functions with an arbitrary number of particles to represent the state probability distribution. The multitude of particles are propagated through the non-linear process equations after which each particle is then used to calculate a measurement estimate, and assigned a weight based the proximity the measurement estimate to the actual measurement. These weights are the used to resample the particles and evaluate the new state mean and covariance.

- **Kalman Filter**: Arguably the most popular state estimation technique, the Kalman filter is a recursive estimation algorithm aimed at using the system dynamic and measurement equations to find an optimal state estimate by minimising the mean-square-error. The Kalman filter, however, is in optimal solution for a state estimation problem with linear process and measurement equations and as such approximations must be made in order to apply its structure to non-linear systems. Two popular variations exist in the form of the Extended Kalman Filter and the Unscented Kalman Filter:

  - **Extended Kalman Filter**: The assumption is made that the non-linear process and measurement equations can be sufficiently linearised about the current state estimate using a first order Taylor series expansion, which allows the general Kalman Filter Structure to be applied.
  - **Unscented Kalman Filter**: The UKF is founded on the intuition that it is easier to approximate a probability distribution of the state vector than than it is to approximate the linear behaviour of the non-linear transformation equations through linearisation about a conditional mean. The UKF represents the state mean and covariance through a deterministically chosen set of *sigma points*, which are used

to transform the mean and covariances through the equation non-linearities. Similar to the EKF, this approximation, allowing the transformation of the means and covariances allows the Kalman Filter structure to be applied.

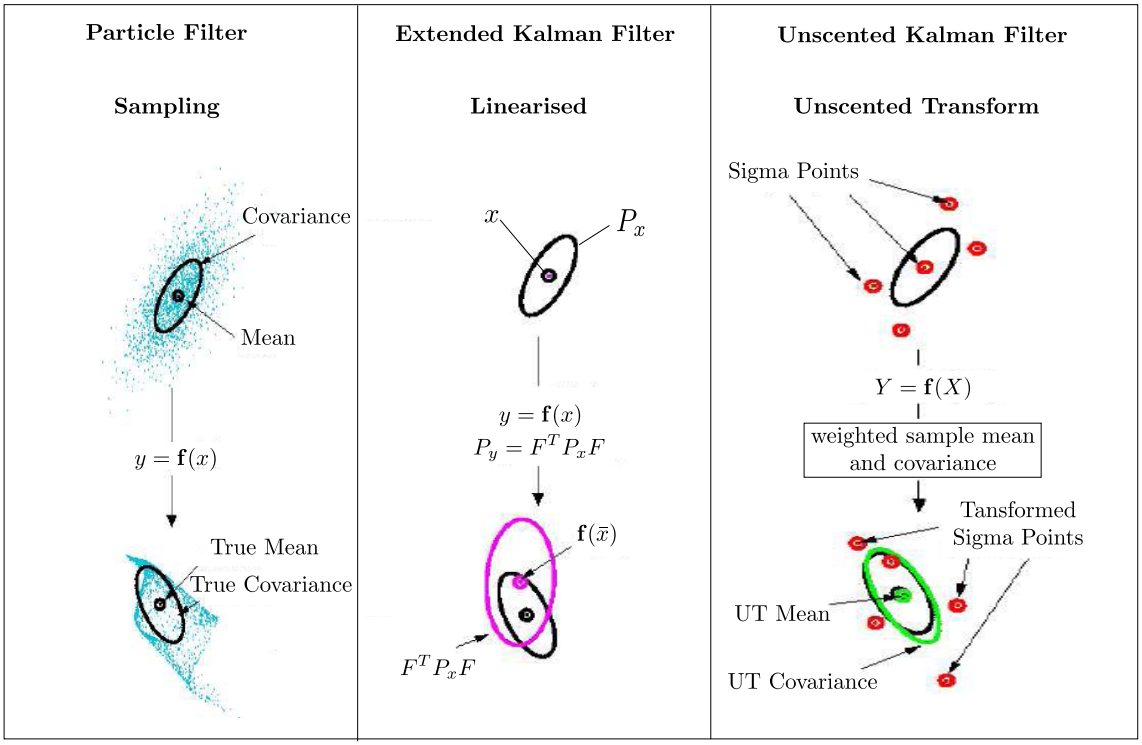

Figure 2.12 – Estimation algorithm flow adapted from [1]

These three estimation algorithms will be considered in simulation in order to evaluate the effectiveness of their respective state estimation approaches. The derivation of each algorithm is shown in Chapter 3.

2.7 Summary

This chapter provided a overview of the AAR scenario as is relevant to the operation of the estimation system. A set of estimation requirements in the form of a state vector definition as well as minimum accuracy requirements were derived through an analysis of the control system requirements and constraints.

In addition to the functional criteria of the estimation system,the aspects that will facilitate estimation, such as the estimation algorithms and sensors where introduced along with 12 sensor configurations to be evaluated in simulated. The estimation algorithms are discussed in detail in the next chapter, with the process measurement model derivations are given in Chapter 4.

Chapter 3

State Estimation Algorithms

Arguably the most fundamental aspect of state estimation, the state estimation algorithm provides a method with which a set of states can be recursively estimated given the knowledge of the dynamics of a state vector in combination with sufficiently relevant measurements.

Various forms of estimation algorithms exist, with their particular strategies dependent on the system to which estimation is applied. In the case of the AAR scenario the system in which estimation is applied is inherently non-linear, and as such, a non-linear state estimation algorithm must be considered.

By far the most popular estimation algorithm the Extended Kalman Filter, a derivative of the popular Kalman filter, is a likely choice to facilitate state estimation. The EKF has been utilised in solving numerous relative state estimation problems, with the most applicable cases addressing the problem of relative spacecraft attitude and position estimation [22; 23]. Though very popular the EKF and its adopted linearisation approach has its limitations, with estimate convergence is not guaranteed, especially in the face of large non-linearities.

Several alternatives to the EKF have been introduced in relative navigation, where algorithms such as the Unscented Kalman Filter and the Particle Filter have come in to light with the potential to outperform the EKF in terms of estimate convergence and stability. These algorithms have also been applied to similar non-linear relative spacecraft attitude and position estimation problems [28; 27; 38].

With the multitude of applicable estimation algorithms, the particular strategy of each estimation algorithm warrants further investigation. Through a thorough investigation, the advantages of each method can be weighed against the potential pitfalls in order to differentiate between their suitability for the AAR estimation problem.

The aim of this chapter is to introduce the fundamentals of non-linear state estimation as well as to elaborate on the implementation of the three algorithms for potential use in AAR. The differences in algorithms are highlighted with the advantages and potential pitfalls of each

factoring into the consideration of whether the algorithm will be implemented fully in simulation. The final section focuses on a variation in the estimation algorithm allowing adaptive estimation to be implemented, where uncertain parameters are adapted to improve the state estimates.

3.1 The non-linear system model

The non-linear system model is comprised of two sections, namely the process model and the measurement model. The process model is a set of equations that describe the time evolution of the state vector, whereas the measurement model describes the relation of the state vector to the measurement obtained from a sensor array.

The system model can be represented in either continuous or discrete time, depending on the implementation purpose. Since the physical process occurs in continuous time, the process model is derived accordingly resulting in a set of non-linear differential equations. Measurement are obtained at discrete intervals and as such the measurement equations are related to the states in discrete time. As a result the system model is represented by the the non-linear continuous-discrete representation:

$$\dot{\boldsymbol{x}}(t) = f\left(\boldsymbol{x}(t), \boldsymbol{u}(t), \boldsymbol{w}(t)\right), \quad \boldsymbol{w}(t) \sim (\boldsymbol{0}, Q(t)) \tag{3.1.1}$$

$$\boldsymbol{y}_k = h\left(\boldsymbol{x}_k, \boldsymbol{v}_k\right), \quad \boldsymbol{v}_k \sim (\boldsymbol{0}, R_k) \tag{3.1.2}$$

with $\boldsymbol{x} \in \Re^n$, $\boldsymbol{y} \in \Re^m$ representing the state and measurement vectors and corresponding vector mutation,

$$f(\,\cdot\,) : \Re^n \to \Re^n$$

$$h(\,\cdot\,) : \Re^n \to \Re^m$$

where the process and measurement noise, $\boldsymbol{w}(t)$ and $\boldsymbol{v}_k$, are uncorrelated zero-mean Gaussians with $Q(t)$ and R_k representing the spectral noise density of the continuous process and measurement covariances, respectively.

The representation of the process model in continuous time facilitates easy equation derivations, but due to the implementation requirements it is often necessary to use a discrete process model representation. The corresponding discrete process model is given by the non-linear stochastic difference equation,

$$\boldsymbol{x}_{k+1} = f_k\left(\boldsymbol{x}_k, \boldsymbol{u}_k, \boldsymbol{w}_k\right) \quad \boldsymbol{w}_k \sim (0, Q_k) \tag{3.1.3}$$

where the propagation model $f(\cdot)$ and process noise spectral density matrix $Q(t)$ have been discretised to form the discrete propagation equation $f_k(\cdot)$ and process covariance matrix Q_k.

With this generalised representation of the non-linear system model, the fundamentals of optimal non-linear estimation as well as the implementation of the PF, EKF and UKF can be presented.

3.2 Particle Filter

Optimal estimation of any linear or non-linear system can be achieved through Bayesian estimation. This algorithm forms a conceptual solution to the estimation problem through a recursive expression for the posterior probability density function of the state vector conditioned on the observed measurements [37]. In practice this optimal solution is usually impossible to compute since it involves several integrals that lack analytical solutions. Following the work presented in [28] the Particle Filter is introduced as a method for practically implementing the Bayesian estimator.

Due to the lack of an analytical representation for the state probability distributions, the Particle filter utilises an arbitrary amount of particles randomly sampled to represent the state probability distribution. The larger the amount of particles, the more accurately the true probability distribution can be represented, resulting in a more optimal state estimate.

As with most estimation algorithms the particle filter has a prediction and correction step where the states, or particles associated with the states, are propagated forward in time according to the discrete process model equations and corrected at intervals when measurements are present. In the correction step each particle is used to create a measurement estimate and assigned a weight based on the proximity of the measurement estimate to the actual measurement. These weights are then used to resample the particles and determine the new state statistics from which the state mean and covariance can be calculated.

A summary of the algorithm is presented in Table 3.1. An overview of the filter operation is given as follows.

1. Generate an initial set of N particles $\boldsymbol{x}_{0,i}^{+}(i = 1, \cdots, N)$ based on the known initial probability density function (PDF) of the state $p(\boldsymbol{x}_0)$ each with an initial weight $W_{0,i}$ of $\frac{1}{N}$.

2. Propagation for k = 1,2,$\cdots$:

   a) Generate N random process noise partices $\boldsymbol{w}_{k-1}^{i}$ on the basis of the known process noise PDF

b) Propagate each *a postiori* particle forward in time using the non-linear process equations, driving inputs, process noise particles in order to obtain the *a priori* particles $\boldsymbol{x}_{k,i}^{-}$,

$$\boldsymbol{x}_{k,i}^{-} = f_k\left(\boldsymbol{x}_{k-1,i}^{+}, \boldsymbol{u}_{k-1}, \boldsymbol{w}_{k-1}^{i}\right) \qquad (i = 1, \cdots, N)$$

whilst maintaining the particles weights.

3. Correction for k = 1,2,$\cdots$:

a) Use the propagated particles and the non-linear measurement equations to generate a set of measurement estimate particles

$$\boldsymbol{y}_{k,i} = h\left(\boldsymbol{x}_{k-1,i}^{-}, \boldsymbol{v}_{k-1}^{i}\right) \qquad (i = 1, \cdots, N)$$

b) Evaluate a new set of particle weights based on the relative likelihood of each propagated particle $L(\boldsymbol{x}_{k,i}^{-})$ conditioned on the measurement $\boldsymbol{y}_k$. This is done by evaluating the conditional probability function $p(\boldsymbol{y}_k|\boldsymbol{x}_{k,i}^{-})$ which, in [28], is shown to be

$$S(\boldsymbol{x}_{k,i}^{-}) = p(\boldsymbol{y}_k|\boldsymbol{x}_{k,i}^{-}) \propto \exp\left[-\frac{1}{2}(\tilde{\boldsymbol{y}}_k - \boldsymbol{y}_{k,i})^T R^{-1}(\tilde{\boldsymbol{y}}_k - \boldsymbol{y}_{k,i})\right]$$

where $\boldsymbol{y}_{k,i}$ is the estimated measurement produced by each particle. Note that similar equations are also derived in [39].

c) As a result the particle weights are updates accordingly

$$W_{k,i} = W_{k-1,i} S(\boldsymbol{x}_{k,i}^{-})$$

and normalised

$$W_{k,i} = \frac{W_{k-1,i}}{\sum_{j=1}^{N} W_{k-1,j}}$$

with the resultant sum equal to one.

d) The *a postiori* state mean and covariance can now be evaluated using the updated particle weights by evaluating the first two moments of the particle cloud, the mean and covariance respectively

$$\hat{\boldsymbol{x}}_k^{+} = E[\boldsymbol{x}_k|\tilde{\boldsymbol{y}}_{\boldsymbol{k}}] \approx \sum_{i=1}^{N} W_{k,i}\boldsymbol{x}_{k,i}^{-}$$

$$P_k^{+} = E[(\boldsymbol{x}_k - \hat{\boldsymbol{x}}_k^{+})(\boldsymbol{x}_k - \hat{\boldsymbol{x}}_k^{+})^T|\tilde{\boldsymbol{y}}_{\boldsymbol{k}}] \approx \sum_{i=1}^{N} W_{k,i}\left(\boldsymbol{x}_k^{+} - \boldsymbol{x}_{k,i}^{-}\right)\left(\boldsymbol{x}_k^{+} - \boldsymbol{x}_{k,i}^{-}\right)^T$$

4. The variance associated with the particle weights can only increase with time eventually resulting in all particles but one having negligible weight [39]. Typically a process called resampling is performed to counteract this by discarding particles with negligible weights and duplicating particles with large weights.Multiple methods for resampling

have been derived, but for simplicity sake the method used in [39] is used where resampled particles are drawn from the existing state particles, based on the distribution of $W_{k,i}$ after which the weights of the particles are again set to $\frac{1}{N}$,

$$\boldsymbol{x}_{k,i}^{+} = \boldsymbol{x}_{k,i}^{-} \text{ with probability } W_{k,i}$$

5. In the resampling process it often occurs that many of the particles are duplicated, effectively reducing the number of unique particles. This is referred to as sample impoverishment, which is why resampling is often followed by a regularisation step. In the regularisation step a small amount of noise $\boldsymbol{s}_{k,i}$ is added to the resampled particles in order to increase their diversity,

$$\boldsymbol{x}_{k,i}^{+} = \boldsymbol{x}_{k,i}^{+} + \boldsymbol{s}_{k,i}$$

where one method for calculating this optimal regularisation noise variance can be found in [28].

Initial Particles	$\boldsymbol{x}_{0,i}^{+}(i = 1, \cdots, N)$ $P_0^{+} = E[(\boldsymbol{x}_0 - x_{0,i}^{+})(\boldsymbol{x}_0 - x_{0,i}^{+})^T]$ $W_{0,i} = \frac{1}{N}$
Propagation	$\boldsymbol{x}_{k,i}^{-} = f\left(\boldsymbol{x}_{k-1,i}^{+}, \boldsymbol{u}_{k-1}, \boldsymbol{w}_{k-1}^{i}\right) \quad (i = 1, \cdots, N)$
Relativel Likeleyhood	$\boldsymbol{y}_{k,i} = h\left(\boldsymbol{x}_{k-1,i}^{-}, \boldsymbol{v}_{k-1}^{i}\right) \quad (i = 1, \cdots, N)$ $S(\boldsymbol{x}_{k,i}^{-}) = p(\boldsymbol{y}_k \vert \boldsymbol{x}_{k,i}^{-}) \propto \exp\left[-\frac{1}{2}(\tilde{\boldsymbol{y}}_k - \boldsymbol{y}_{k,i})^T R^{-1}(\tilde{\boldsymbol{y}}_k - \boldsymbol{y}_{k,i})\right]$ $W_{k,i} = W_{k-1,i} L(\boldsymbol{x}_{k,i}^{-})$ $W_{k,i} = \frac{W_{k-1,i}}{\sum_{j=1}^{N} W_{k-1,j}}$
Correction	$\boldsymbol{x}_k^{+} = E[\cdots] \approx \sum_{i=1}^{N} W_{k,i} \boldsymbol{x}_{k,i}^{-}$ $P_k^{+} = E[\cdots] \approx \sum_{i=1}^{N} W_{k,i} \left(\boldsymbol{x}_k^{+} - \boldsymbol{x}_{k,i}^{-}\right)\left(\boldsymbol{x}_k^{+} - \boldsymbol{x}_{k,i}^{-}\right)^T$

Table 3.1 – Particle Filter Summary

The running example used to demonstrate the differences in the basic function of each algorithm is shown in Figure 3.1. The example, most notably shown in [13], represents the transformation of the state mean and covariance through the non-linear function $y = f(x) = -sin(x)$. The state x with mean at 265^o and covariance of 10^o is represented by $N = 1000$ particles, where it is assumed that the distribution is Gaussian. Each particle is propagated through the transformation equation to form a set of transformed points. Unlike the EKF and UKF, the transformed points are not assumed to have a Gaussian distribution and as such any applicable method of statistical analysis can be used to evaluated the resultant mean and covariance. Note that the particles distributions have been scaled for visual effect.

The PF is the clear choice of estimation algorithm when near-optimal estimates are required when dealing with highly non-linear systems with non-Gaussian noise. The number of particles

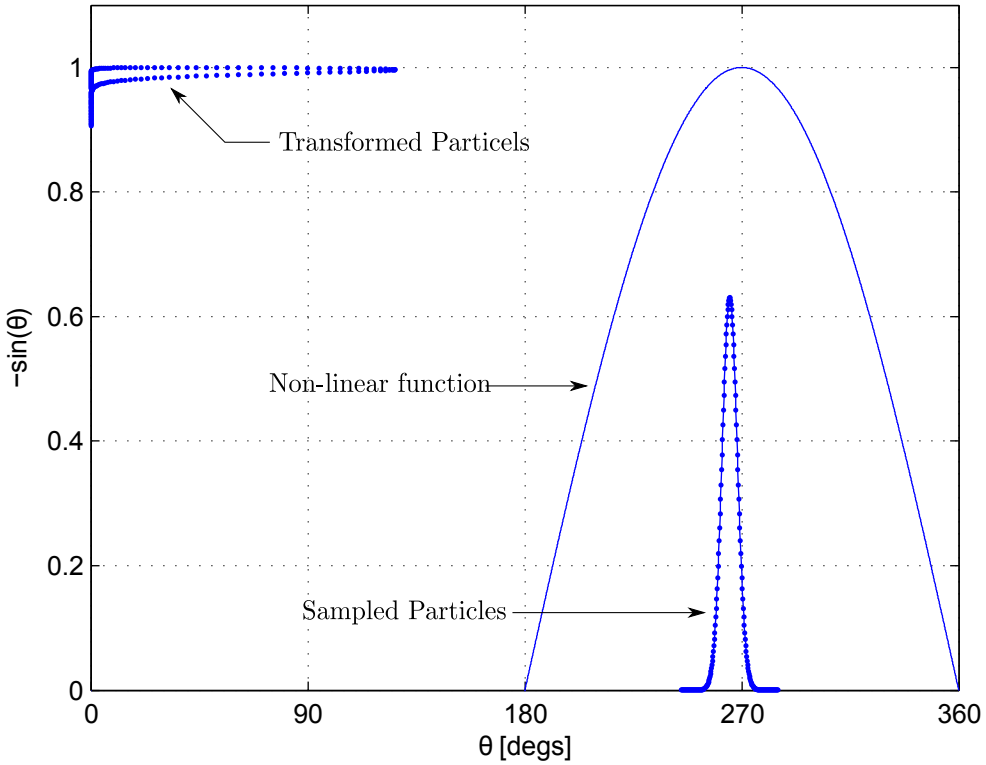

Figure 3.1 – Propagation of Particle Filter particles through a non-linear function

increases the optimal nature of the state estimates, where the choice of N becomes a trade-off between the allowable computational burden and required optimality of the solution. Considering the complexity of the particle filter, its implementation seems relatively straight forward, but as a result of steps such as resampling as well as regularisation the estimation problem becomes increasingly complex. The prevalent concern is the computational power required to perform real time estimation.

3.3 Extended Kalman Filter

The Extended Kalman Filter is arguably the most popular and most widely used non-linear state estimation algorithm for real time applications. Fundamentally it is a derivative of the popular Kalman Filter which provides optimal state estimation for linear systems. Similar to implementation of Bayesian estimation through the Particle Filter the Extended Kalman Filter must implement an approximation allowing the structure of its parent to be utilised. In this case, in order to implement the structure of a linear estimation algorithm to a non-linear problem, the non-linear system equations are linearised about the current states estimate using a Taylor series expansion.

With the equations linearised, the Kalman Filter sequence can be applied. The states are propagated using the non-linear equations, with covariance propagation a function of the

process Jacobian and the process noise covariance. When measurements are available the states and covariances are corrected in order to minimise the mean-square-error. As a result the correction is based on the difference between the true and estimated measurement as well as the relationship between the measurement and process Jacobians as well as the process and measurement noise covariances.

A summary of the algorithm is presented in Table 3.2. An overview of the filter operation is given as follows.

1. Initialisation of the estimation algorithm involves an estimate of the initial state vector as well as the initial error covariance.

$$\hat{\boldsymbol{x}}(t_0) = \hat{\boldsymbol{x}}_0^+$$

$$P_0^+ = E[(\boldsymbol{x}_0 - \hat{\boldsymbol{x}}_0^+)(\boldsymbol{x}_0 - \hat{\boldsymbol{x}}_0^+)^T]$$

2. Propagation for k = 1,2,$\cdots$:

   a) The *a postiori* state estimate is propagated forward in time using the discrete non-linear process equations and the driving inputs in order to obtain the *a priori* state estimates.

$$\hat{\boldsymbol{x}}_k^- = f_k\left(\hat{\boldsymbol{x}}_{k-1}^+, \boldsymbol{u}_{k-1}, \boldsymbol{0}\right)$$

   Note that the noise estimate input is zero as the process noise is zero mean Gaussian.

   b) As with the propagation of the estimated states the process covariance is also propagated in order to find its *a priori* state. The Kalman Filter, however, requires the process covariance to be linearly scaled based on the linear propagation of states. As the process equations are non-linear they are linearised about the current state estimate (conditional mean) using a Taylor series expansion. The Taylor series expansion of the continuous system is given as,

$$f(\boldsymbol{x}(t), \boldsymbol{u}(t), \boldsymbol{w}(t), t) = f(\hat{\boldsymbol{x}}(t), \boldsymbol{u}(t), \boldsymbol{w}(t), t) + \left.\frac{\partial f}{\partial \boldsymbol{x}}\right|_{\hat{\boldsymbol{x}}, \boldsymbol{u}} (\boldsymbol{x} - \hat{\boldsymbol{x}}) + \left.\frac{\partial f}{\partial \boldsymbol{w}}\right|_{\hat{\boldsymbol{x}}, \boldsymbol{u}} (\boldsymbol{x}) + h.o.t$$

   where h.o.t is short for higher order terms. In the EKF, the assumption is made that the error state term $(\boldsymbol{x} - \hat{\boldsymbol{x}})$ is sufficiently small that the h.o.t can be ignored. Since $f(\boldsymbol{x}(t), \boldsymbol{u}(t), \boldsymbol{w}(t), t)$ is also assumed to be continuously differentiable the following partial derivatives are defined:

$$F(\hat{\boldsymbol{x}}(t), \boldsymbol{u}(t), t) \equiv \left.\frac{\partial f}{\partial \boldsymbol{x}}\right|_{\hat{\boldsymbol{x}}, u}$$

$$L(\hat{\boldsymbol{x}}(t), \boldsymbol{u}(t), t) \equiv \left.\frac{\partial f}{\partial \boldsymbol{w}}\right|_{\hat{x},u}$$

Following the derivations of a continuous-time process model the propagation of the process covariance is given as,

$$\dot{P}(t) = F(\hat{\boldsymbol{x}}(t), \boldsymbol{u}(t), t)P(t) + P(t)F(\hat{\boldsymbol{x}}(t), \boldsymbol{u}(t), t)^T + L(\hat{\boldsymbol{x}}(t), \boldsymbol{u}(t), t)Q(t)L(\hat{\boldsymbol{x}}(t), \boldsymbol{u}(t), t)$$

where Q(t) is typically given as the spectral density matrix. Since the algorithm is implemented in its discrete form the continuous propagation of the process covariance must be discretised in order to fit the following discrete propagation equation ,

$$P_k^- = F(\hat{\boldsymbol{x}}_{k-1}^+, \boldsymbol{u}_{k-1})P_{k-1}^+F(\hat{\boldsymbol{x}}_{k-1}^+, \boldsymbol{u}_{k-1})^T + Q_k$$

where $F(\hat{x}_{k-1}^+, u_{k-1})$ is the discrete process Jacobian shown to be,

$$F(\hat{\boldsymbol{x}}_{k-1}^+, \boldsymbol{u}_{k-1}) \equiv \left.\frac{\partial f}{\partial \boldsymbol{x}}\right|_{\hat{\boldsymbol{x}}_{k-1}^+, \boldsymbol{u}_{k-1}}$$

and Q_k is the discrete process covariance matrices. As stated in [23], if the sampling period Δt is *small* enough, then a good approximation for the discretization of the process covariance is given by,

$$Q_k = L(\hat{\boldsymbol{x}}_{k-1}^+, \boldsymbol{u}_{k-1})Q(t)L(\hat{\boldsymbol{x}}_{k-1}^+, \boldsymbol{u}_{k-1})^T\Delta t$$

3. Following the state and covariance propagation, at the instance when measurements are available, the *a postiori* state estimates and covariance are determined in the correction step:

   a) As with the propagation step, the non-linear measurement equations must be linearised using a Taylor series expansion about he current state estimate (conditional mean),

$$h(x_k, v_k) = h(\hat{\boldsymbol{x}}_k, \boldsymbol{0}) + \left.\frac{\partial h}{\partial \boldsymbol{x}}\right|_{\hat{\boldsymbol{x}}_k^-} \left(\boldsymbol{x} - \hat{\boldsymbol{x}}_k^-\right) + \left.\frac{\partial h}{\partial \boldsymbol{v}}\right|_{\hat{\boldsymbol{x}}_k^-} (\boldsymbol{v}_k) + h.o.t$$

   Again with the error state term $(\boldsymbol{x} - \hat{\boldsymbol{x}})$ assumed to be sufficiently small and $h\left(\boldsymbol{x}_k, \boldsymbol{v}_k\right)$ assumed to be continuously differentiable the partial derivatives are defined as,

$$H(\hat{\boldsymbol{x}}_k^-) \equiv \left.\frac{\partial h}{\partial \boldsymbol{x}}\right|_{\hat{\boldsymbol{x}}_k^-} \tag{3.3.1}$$

$$M(\hat{\boldsymbol{x}}_k^-) \equiv \left.\frac{\partial h}{\partial \boldsymbol{v}}\right|_{\hat{\boldsymbol{x}}_k^-} \tag{3.3.2}$$

b) With this, the *a postiori* states are calculated using the the Kalman Filter discrete correction step equation,

$$\boldsymbol{x}_k^+ = \boldsymbol{x}_k^- + K_k \left(\boldsymbol{y}_k - h(\boldsymbol{x}_k^-, 0)\right)$$
$$P_k^+ = \left(I - K_k H(\boldsymbol{x}_k^-)\right) P_k^-$$

with K_k given as the discrete Kalman Gain,

$$K_k = P_k^- H(\hat{\boldsymbol{x}}_k^-) \left[H(\hat{\boldsymbol{x}}_k^-) P_k^- H(\hat{\boldsymbol{x}}_k^-) + M(\hat{\boldsymbol{x}}_k^-) R_k M(\hat{\boldsymbol{x}}_k^-)^T\right]^{-1}$$

which is obtained by minimising the mean-square-error (MSE), which is achieved through minimising the trace of the error covariance matrix. The Kalman filter equation and the resultant continuous and discrete state propagation, correction and gain equitions are well established. For this reason only a summary is provided with some elaboration where necessary. The full derivation of the filter can be found in [39].

Initialisation	$\hat{\boldsymbol{x}}(t_0) = \hat{\boldsymbol{x}}_0$ $P_0^+ = E[(\boldsymbol{x}_0 - \hat{\boldsymbol{x}}_0^+)(\boldsymbol{x}_0 - \hat{\boldsymbol{x}}_0^+)^T]$
Propagation	$\hat{\boldsymbol{x}}_k^- = f\left(\hat{\boldsymbol{x}}_{k-1}^+, \boldsymbol{u}_{k-1}, \boldsymbol{0}\right)$ $P_k^- = F(\hat{\boldsymbol{x}}_{k-1}^+, \boldsymbol{u}_{k-1}) P_{k-1}^+ F(\hat{\boldsymbol{x}}_{k-1}^+, \boldsymbol{u}_{k-1})^T + Q_k$ $F(\hat{\boldsymbol{x}}_{k-1}^+, \boldsymbol{u}_{k-1}) \equiv \left.\frac{\partial f}{\partial \boldsymbol{x}}\right\|_{\hat{\boldsymbol{x}}_{k-1}^+, \boldsymbol{u}_{k-1}}$ $Q_k = L(\hat{\boldsymbol{x}}_{k-1}^+, \boldsymbol{u}_{k-1}) Q(t) L(\hat{\boldsymbol{x}}_{k-1}^+, \boldsymbol{u}_{k-1})^T \Delta t$
Gain	$K_k = P_k^- H(\hat{\boldsymbol{x}}_k^-) \left[H(\hat{\boldsymbol{x}}_k^-) P_k^- H(\hat{\boldsymbol{x}}_k^-) + M(\hat{\boldsymbol{x}}_k^-) R_k M(\hat{\boldsymbol{x}}_k^-)^T\right]^{-1}$ $H(\hat{\boldsymbol{x}}_k^-) \equiv \left.\frac{\partial h}{\partial \boldsymbol{x}}\right\|_{\hat{\boldsymbol{x}}_k^-}$ $M(\hat{\boldsymbol{x}}_k^-) \equiv \left.\frac{\partial h}{\partial \boldsymbol{v}}\right\|_{\hat{\boldsymbol{x}}_k^-}$
Correction	$\hat{\boldsymbol{x}}_k^+ = \hat{\boldsymbol{x}}_k^- + K_k \left(\tilde{\boldsymbol{y}}_k - h(\hat{\boldsymbol{x}}_k^-, 0)\right)$ $P_k^+ = \left(I - K_k H(\hat{\boldsymbol{x}}_k^-)\right) P_k^-$

Table 3.2 – Extended Kalman Filter Summary

The same example used to describe the function of the PF is shown again in Figure 3.2, with the effects of the linearisation assumption being highlighted. In this example the non-linear function is linearised about the conditional mean $x = 265^o$. The state is transformed through the non-linear function, with the Gaussian state variance of 10^o propagated through the linearised transform resulting in a scaled Gaussian variance. In comparison to the PF approach, resultant transformed state distribution does not accurately represent the state statistics.

FThe success of the EKF has been due to its relative simplicity as well as the minimal computational power required to implement the algorithm in real time applications. The significant

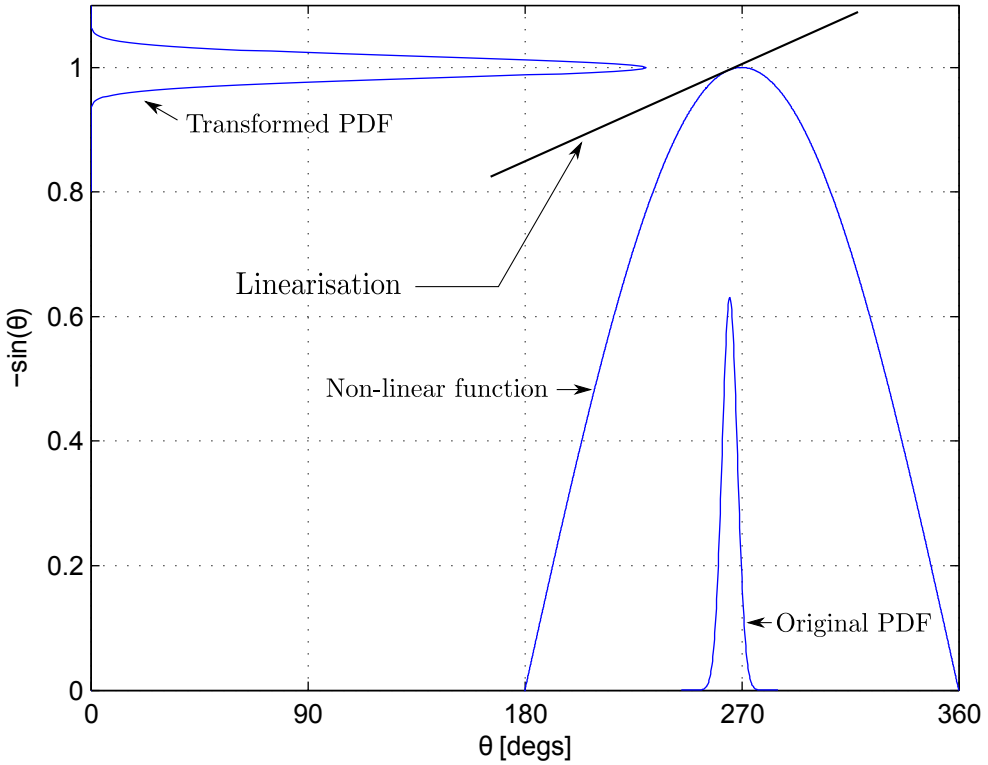

Figure 3.2 – The propagation of the state mean and covariance based on function linearisation in the EKF

drawback to the implementation of the EKF is its performance when confronted with highly non-linear process or measurement models. A large uncertainty between estimation intervals could invalidate the linearisation assumption, creating the potential for estimator divergence. Another disadvantage unique to the EKF, is the requirement to evaluate the partial derivatives of the system equations which can proves to be tedious in highly non-linear systems, and in some cases the derivatives cannot even be evaluated. Fortunately the derivatives of the process and measurement model equations in the AAR scenario can all be evaluated.

3.4 Unscented Kalman Filter

According to [40] the Unscented Kalman Filter uses statistical linearisation techniques and falls under a larger set of filters called Sigma-Point Kalman Filter or Linear Regression Kalman Filter. As opposed to the Extended Kalman filter, where the mean and covariance of the states are propagated through a first Taylor series linearisation, the Unscented Kalman Filter linearises the non-linear process and measurement models through the linear regression between n points drawn from prior distributions of the state variables.

The UKF is founded on the intuition that it is easier to approximate a probability distribution than it is to approximate a arbitrary function of transformation [41].

Similar to the PF and EKF, the UKF has a prediction and correction stage. A point cloud is generated for each state, referred to as *Sigma Points*, which are deterministically chosen to have the same mean and covariance as the state vector. These points are then transformed by the non-linear process equations to yield a new set of propagated points, the mean and covariance of which are determined thought the distribution statistics. The propagated particles are used to generate a set of estimated measurements which are compared to the true measurement, where the states and covariances are corrected based on the theory of minimising the mean-square-error, similar to that of the EKF.

This filter has a superficial resemblance to the Particle Filter, but differs in the sense that these sigma points are not drawn at random, but are deterministically chosen to represent the state mean and covariance. This process of determining sigma points and passing them through the non-linear functions is called the Unscented Transform (UT).

A summary of the algorithm is presented in Table 3.3. An overview of the filter operation is given as follows.

1. As with the EKF the UKF initialisation of the estimation algorithm involves an estimate of the initial state vector as well as the initial error covariance.

$$\hat{\boldsymbol{x}}(t_0) = \hat{\boldsymbol{x}}_0^+$$

$$P_0^+ = E[(\boldsymbol{x}_0^+ - \hat{\boldsymbol{x}}_0^+)(\boldsymbol{x}_0^+ - \hat{\boldsymbol{x}}_0^+)^T]$$

2. Before state and covariance propagation a set of 2n *sigma points* are generated from the current state estimate and error covariance,

$$\mathbf{X}_k = \left[\begin{array}{ccc} \hat{\boldsymbol{x}}_{k-1}^a & \vdots & \hat{\boldsymbol{x}}_{k-1}^a + \sqrt{(n+\lambda)P_{k-1}^a} \quad \vdots \quad \hat{\boldsymbol{x}}_{k-1}^a - \sqrt{(n+\lambda)P_{k-1}^a} \end{array} \right]$$

where n is the length of the state vector λ is a composite scaling factor and $\hat{\boldsymbol{x}}_{k-1}^a$ and P_{k-1}^a are the augmented state vector and error covariance respectively.

The augmented state vector is given as

$$\boldsymbol{x}_{k-1}^a = \begin{bmatrix} \boldsymbol{x}_{k-1} \\ \boldsymbol{w}_{k-1} \\ \boldsymbol{v}_{k-1} \end{bmatrix}, \quad \hat{\boldsymbol{x}}_{k-1}^a = \begin{bmatrix} \hat{\boldsymbol{x}}_{k-1}^+ \\ \mathbf{0} \\ \mathbf{0} \end{bmatrix}$$

and the augmented error covariance matrix is given as

$$P_{k-1}^a = \begin{bmatrix} P_{k-1}^+ & P_{k-1}^{xw} & P_{k-1}^{xv} \\ P_{k-1}^{wx} & Q_{k-1} & P_{k-1}^{wv} \\ P_{k-1}^{vx} & P_{k-1}^{vw} & R_{k-1} \end{bmatrix}$$

with λ given by

$$\lambda = \alpha^2(n - \kappa) - n$$

The spread of the sigma points around the state estimate $\hat{x}_k$ is governed by the constant α, usually set to a small positive value $(0 \leq \alpha \leq 1)$. The constant κ provides an extra degree of freedom for fine tuning of higher order moments (if available) but in this case is set to zero ($\kappa = 0$).

3. With the *sigma points* matrix of vectors established, the propagation step can be undergone

   a) The sigma point are propagated through the non-linear process equations to form a set of propagated *sigma points*,

   $$\mathbf{X}_k(i) = f(\mathbf{X}^x_{k-1}(i), \mathbf{X}^w_{k-1}(i), \boldsymbol{u}_{k-1}), \quad i = 0, 1, 2, \cdots, 2n$$

   where $\mathbf{X}^x_k(i)$ and $\mathbf{X}^w_k(i)$ are subsets of the *sigma points* matrix shown to be

   $$\mathbf{X}^a_k(i) = \begin{bmatrix} \mathbf{X}^x_k(i) \\ \mathbf{X}^w_k(i) \\ \mathbf{X}^v_k(i) \end{bmatrix}$$

   b) The propagated *sigma points* are used to calculate the propagated *a priori* state estimate as well as error covariance,

   $$\hat{\boldsymbol{x}}^-_k = \sum_{j=0}^{2n+1} W^j_m \mathbf{X}^x_k(j)$$

   $$P^{xx}_k = \sum_{j=0}^{2n+1} W^j_c (\mathbf{X}^x_k(j) - \hat{x}^-_k)(\mathbf{X}^x_k(j) - \hat{x}^-_k)^T$$

   with the weighted factors for both the state and error covariance calculation given by,

   $$W^0_m = \frac{\lambda}{(n + \lambda)}$$

   $$W^0_c = \frac{\lambda}{(n + \lambda)} - (1 - \alpha^2 + \beta)$$

   $$W^i_m = W^i_c = \frac{1}{2(n + \lambda)}, \quad i = 1, 2, \cdots, 2n$$

4. With the *sigma points* propagated and *a priori* state and error covariance estimate evaluated, the available measurements are used to determine the *a postiori* states in the corrections step.

   a) Each of the propagated sigma points is used to calculate a measurement estimate

   $$\mathbf{Y}_k(i) = h(\mathbf{X}_k^x, \mathbf{X}_k^v), \quad i = 0, 1, 2, \cdots, 2n$$

   b) From this the mean estimated measurement as well as the innovation covariance it determined through a weighted average,

   $$\hat{\boldsymbol{x}}_k^- = \sum_{j=0}^{2n} W_m^j \mathbf{Y}_k(i) \tag{3.4.1}$$

   $$P_k^{yy} = \sum_{j=0}^{2n} W_c^j (\mathbf{Y}_k(i) - \hat{\boldsymbol{x}}_k^-)(\mathbf{Y}_k(i) - \hat{\boldsymbol{y}}_k)^T \tag{3.4.2}$$

   c) Finally, the cross covariance between propagated states and estimated measurements is calculated,

   $$P_k^{xy} = \sum_{j=0}^{2n} W_c^j (\mathbf{X}_k(i) - \hat{\boldsymbol{x}}_k^-)(\mathbf{Y}_k(i) - \hat{y}_k)^T \tag{3.4.3}$$

   which allows for the Kalman gain to be calculated,

   $$K_k = P_k^{xy}(P_k^{yy})^{-1}$$

   and the correction to the state estimate and error covariance can be applied

   $$\boldsymbol{x}_k^+ = \boldsymbol{x}_k^- + K_k\left(\tilde{\boldsymbol{y}}_k - \hat{\boldsymbol{x}}_k\right)$$
   $$P_k^+ = P_k^{xx} - K_k P_k^{yy} K_k^T$$

The non-linear mean and covariance transformation example for the UKF is shown in Figure 3.3. Similar to the PF, the state vector is represented as a set of particles, which in this case are specifically chosen *sigma points*. Each sigma point is transformed by non-linear function resulting in a set of transformed particles. The UKF does ,however, make the same Gaussian assumption on the distribution of the transformed particles that the EKF makes, but the UKF transformed mean and covariance is much closer to the true transformation represented by the PF.

The UKF provides a good approximation of the non-linear transform, without the burden of a large number of particles or the risk of an inaccurate linearisation assumption. It is clear that the more complex the system in which estimation must be applied, i.e, the size of state vector,

Initialisation	$\hat{\boldsymbol{x}}(t_0) = \hat{\boldsymbol{x}}_0$ $P_0^+ = E[(\boldsymbol{x}_0 - \hat{\boldsymbol{x}}_0^+)(\boldsymbol{x}_0 - \hat{\boldsymbol{x}}_0^+)^T]$
Sigma Points	$\mathbf{X}_k = \left[\hat{\boldsymbol{x}}^a_{k-1} \;\vdots\; \hat{\boldsymbol{x}}^a_{k-1} + \sqrt{(n+\lambda)P^a_{k-1}} \;\vdots\; \hat{\boldsymbol{x}}^a_{k-1} - \sqrt{(n+\lambda)P^a_{k-1}} \right]$
Propagation	$\mathbf{X}_k(i) = f(\mathbf{X}^x_{k-1}(i), \mathbf{X}^w_{k-1}(i), u_{k-1})$ $\hat{\boldsymbol{x}}_k^- = \sum_{j=0}^{2n+1} W_m^j \mathbf{X}_k^x(j)$ $P_k^{xx} = \sum_{j=0}^{2n+1} W_c^j (\mathbf{X}_k^x(j) - \hat{\boldsymbol{x}}_k^-)(\mathbf{X}_k^x(j) - \hat{\boldsymbol{x}}_k^-)^T$
Gain	$\mathbf{Y}_k(i) = h(\mathbf{X}_k^x, \mathbf{X}_k^v)$ $P_k^{yy} = \sum_{j=0}^{2n} W_c^j (\mathbf{Y}_k(i) - \hat{\boldsymbol{y}}_k^-)(\mathbf{Y}_k(i) - \hat{\boldsymbol{y}}_k^-)^T$ $P_k^{xy} = \sum_{j=0}^{2n} W_c^j (\mathbf{X}_k(i) - \hat{\boldsymbol{x}}_k^-)(\mathbf{Y}_k(i) - \hat{\boldsymbol{y}}_k^-)^T$ $K_k = P_k^{xy}(P_k^{yy})^{-1}$
Correction	$\hat{\boldsymbol{y}}_k^- = \sum_{j=0}^{2n} W_m^j \mathbf{Y}_k(i)$ $\boldsymbol{x}_k^+ = \boldsymbol{x}_k^- + K_k\left(\tilde{\boldsymbol{y}}_k - h(\hat{\boldsymbol{x}}_k^-)\right)$ $P_k^+ = P_k^{xx} - K_k P_k^{yy} K_k^T$

Table 3.3 – Unscented Kalman Filter Summary

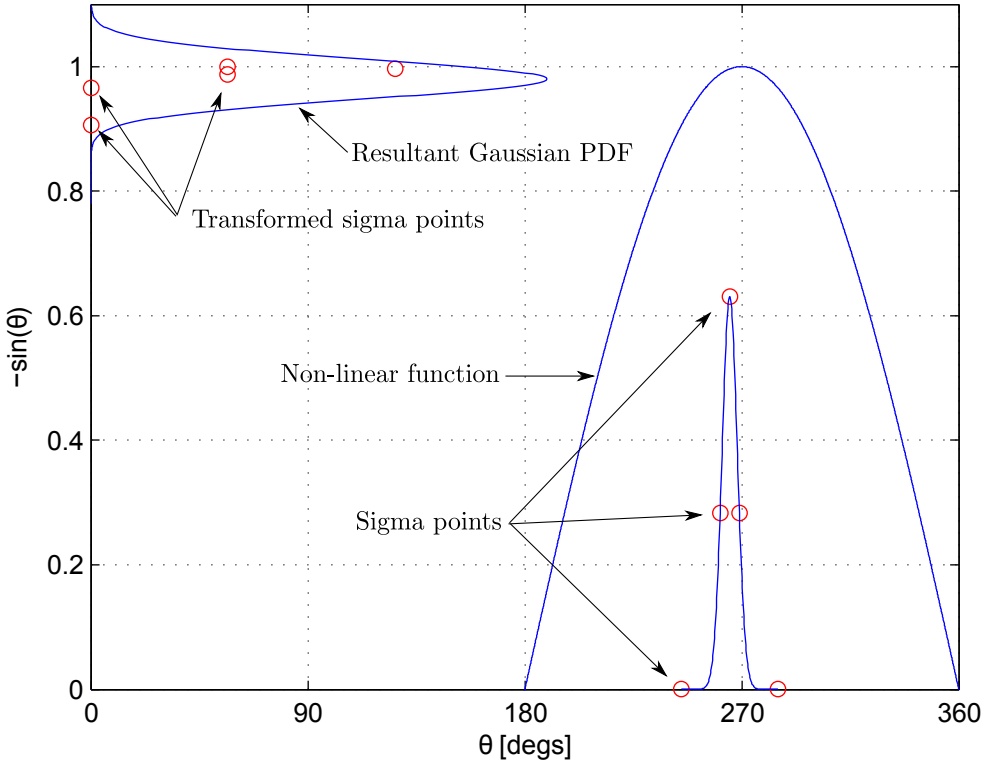

Figure 3.3 – Unscented Kalman Filter

as well as the size of the process and measurement noise vector, the larger the computational burden will become. In this derivation the state vector and covariance matrix are augmented to include the noise term due to the assumption that the noise terms enter the process and measurement models through the non-linear equations. This is often not the case, especially with measurement, which allows the augmented state vector and covariance matrix to be simplified. These simplifications are shown in Chapter 4 after the process and measurement equations have been evaluated.

3.5 Algorithm Comparison

Each of the three algorithms follows a slightly different approach when tasked with state estimation of a non-linear system. This unique approach, typically in the way the state statistics are represented, propagated and corrected, has a large impact on the function of the estimation algorithm as well as its effectiveness. In order to highlight these differences the non-linear propagation of a simplified inertial navigation scenario is shown. This particular illustration is adapted from [13] as it illustrates the point most clearly.

Consider the states of the aircraft x and y to be its position North and East relative to a stationary runway point, and its heading angle ψ relative to North as seen in Figure 3.4.

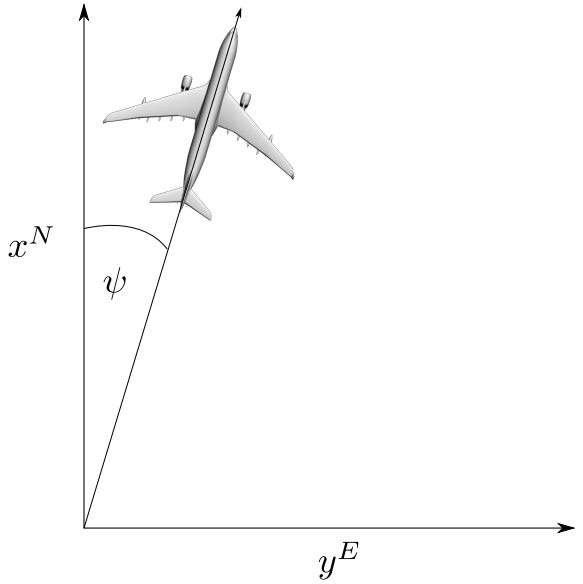

Figure 3.4 – Mean and Covariance propagation example

The kinematic equations are given as

$$\begin{bmatrix} x^N_{k+1} \\ y^E_{k+1} \\ \psi_{k+1} \end{bmatrix} = \begin{bmatrix} x^N_k + u\Delta t\cos(\psi) \\ y^E_k + u\Delta t\sin(\psi) \\ \psi + \dot{\psi}\Delta t \end{bmatrix}$$

It is also assumed that the driving input velocity is known to be exactly $u = 100\frac{m}{s}$ and that the sampling rate is 10 Hz. Figure 3.5 shows the propagation of means and covariances associated with the x and y position of the aircraft based on the fundamentals of each of the algorithms.

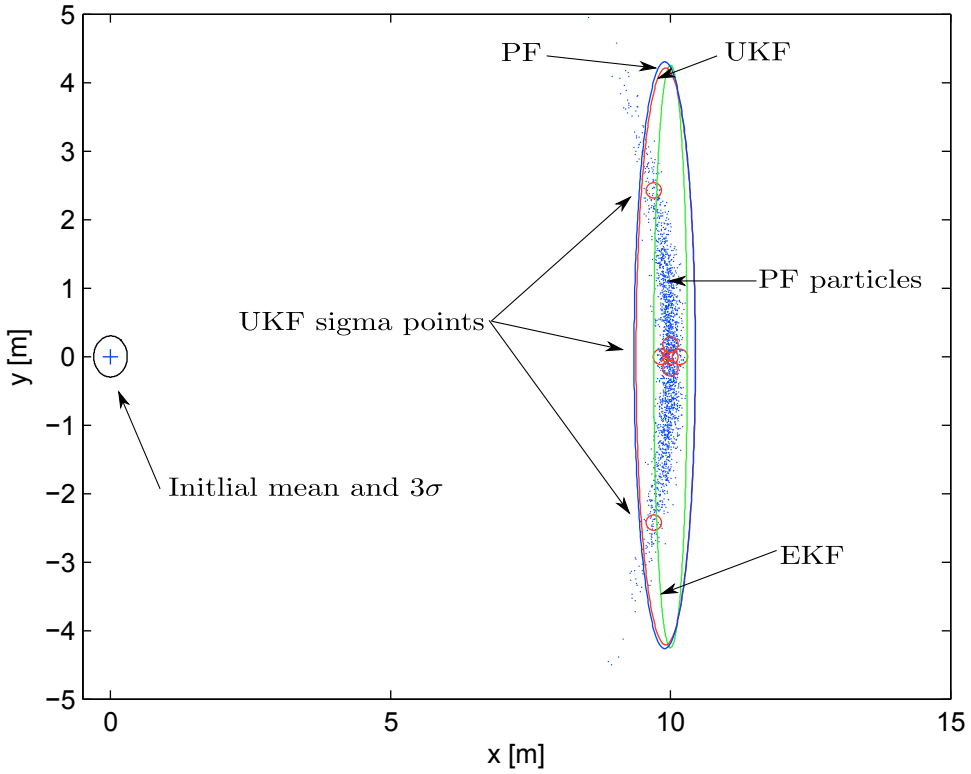

Figure 3.5 – Propagation of means and covariances in a simplified 2D aircraft kinematics example

In the case of the Particle Filter, $N = 1000$ particles were initially generated and propagated through the non-linear kinematic equation to form the distinct arc shape of propagated particles. A Gaussian distribution is fitted to the resultant particles, bearing in mind that other distributions can be selected. The PF provides the closest approximation of true non-linear propagation.

As expected the EKF linearisation assumption merely scales the initial error covariance based on the size of the process model Jacobian, and the propagated mean is obtained though the propagation of the old mean, which results in a propagated state with an incorrect mean and a underestimated variance.

The effectiveness of the UKF sigma points can be clearly seen in Figure 3.5, where the propagated mean and covariance is very similar to that of the PF at a fraction of required amount of transformations. The UKF provides a good compromise between the optimal nature of the state estimate and the resultant computational burden.

With the high degree of similarity between the results obtained from the PF and the UKF in this example it is reasoned that it is unnecessary to implement both in simulation, at least initially. Even though the PF proves to produce the more optimal state estimate, the advantages of the UKF in its simplicity as well as significantly lower computational requirements, which outweigh the slight increase in state estimate optimality resulting from the PF. For this reason the PF will be omitted from further implementation, with conditional return if the non-linearities in state estimation prove to degrade the function of the UKF significantly.

With the popularity of the EKF, its ease of implementation, low computational requirements, and the fact that it is a benchmark estimation algorithm for most state estimation applications the EKF must also be tested in simulation, with the results obtained compared to that of the UKF.

3.6 Process covariance adaptation

The noise statistics in both the EKF and UKF, but also applicable to the PF, are encapsulated in the constant values of the process and measurement noise covariance matrices Q_k and R_k respectively. If these parameters are chosen to be correct the non-linear estimation algorithms will perform to the maximum of their respective abilities, based on their particular approximation. If, on the other hand, the noise statistics are incorrectly specified due to inaccurate models or unmodeled non-linearities, the performance of the estimation algorithms could be compromised.

Traditionally, in order to combat such problems when implementing the estimation algorithms, the process and measurement covariance matrices are carefully chosen, typically with iterative tuning until near optimal estimation is achieved. This ,however, is very tedious and will not account for any changes in the process or measurement statistics during operation. For a more rounded solution to the problem it is proposed that the noise statistics be adaptively estimated in order to mitigate the unknown effects of unmodeled uncertainty.

Much of the prevalent research undergone in adaptive estimation is thoroughly summarised in [42]. From this research it is known that even though in theory it is possible to estimate the errors in both the process and measurement noise covariances Q_k and R_k, filters that attempt to adapt both these parameters are not robust as it is hard to differentiate between an error introduced by inaccurate process covariance or an inaccurate measurement covariance. For this reason only one of the noise parameters is adapted, and since it is assumed that the measurement covariance R_k can be fairly accurately modeled from the sensor noise models, only process covariance Q_k remains to be adapted.

From [42] numerous adaptive approaches are discussed in the formulation of the process covariance adaptation algorithm. Subsequently, a variation of the maximum likelihood estimation

approach, originally developed in [43] for linear systems, is proposed for use in the current non-linear application. The fundamental concept of this adaptation method uses the measurement and state residual to correct the current process noise estimate, where the modification is based on a window scale factor which is chosen through iterative simulation.

The equation that evaluates the new process covariance estimate is shown to be,

$$\hat{Q}_k = \hat{Q}_{k-1} + \frac{1}{\lambda}\left(Q^* - \hat{Q}_{k-1}\right) \tag{3.6.1}$$

where $\hat{Q}_{k-1}$ is the previous estimate of the process covariance, λ is a gain dictating how much of an effect Q^* will have on the change in process covariance, and Q^* is given by,

$$Q^* = \Delta \boldsymbol{x}_i \Delta \boldsymbol{x}_i^T - \left[P_k^+ - \left(P_k^- - \hat{Q}_{k-1}\right)\right] \tag{3.6.2}$$

where state residual $\Delta \boldsymbol{x}_k$ is given as the difference between the state estimate before and after correction,

$$\Delta \boldsymbol{x}_k = \boldsymbol{x}_k^+ - \boldsymbol{x}_k^- \tag{3.6.3}$$

It is this Q^* that will effect a change in the process covariance and as such requires finer analysis. The size of the process covariance correction term is a function of the difference in the state residual covariance $\Delta x_i \Delta x_i^T$ and the expected change in error covariance $P_k^+ - \left(P_k^- - \hat{Q}_{k-1}\right)$. This expected change in error covariance is coupled to the previous process covariance estimate. A state residual covariance larger than what is expected indicates that a larger state correction was necessary than expected. This in turn indicates inaccurate state propagation which serves to increase the process covariance, increasing the expected change in covariance due to correction. Essentially, when propagation is inaccurate, large corrections are required, which decreases the confidence in propagation increasing the covariance.

The integration of process covariance adaptation into the estimation algorithms is fairly straight forward, where Eq. 3.6.1 must be executed after each state correction step. The addition of this adaptation concludes the general derivation of the estimation algorithms.

3.7 Summary

This chapter set out to introduce the theory of three popular state estimation algorithms for consideration in the AAR state estimation system. Having initially introduced the fundamental non-linear system model, each estimation algorithm is discussed, with particular focus on the complexity of the algorithm, practicality in term of processing requirements, and optimal nature of the resultant state estimates.

After evaluation is was found that the negative nature of the large processing power and complexity associated with the Particle Filter outweighed the potential gain in performance optimality, since the UKF has the potential of also producing near optimal estimates with significantly less processing power requirements. As a result the EKF and UKF will be considered for implementation. In addition to the algorithm evaluation, a method for continuously adapting the process covariance is also provided which adds to the sequence of the standard estimation algorithms and aims to improve the state estimates through a more accurate estimate of the process noise.

In order to implement the estimation algorithms in the AAR scenario the non-linear process and measurement equations and accompanying sensor models are covered in the next section.

Chapter 4

Process and Measurement Model Derivation

In Chapter 3 the state estimation algorithms were derived using a generic non-linear representation for the system dynamic and measurement model. In order to implement the estimation algorithms, the equation specific to the AAR state estimation problem must be derived. This task is approached in two distinct sections corresponding to the equation derivations for the process and measurement models respectively.

In the process model equations the time derivatives of the states are derived factoring in that the IMU accelerations and angular rates of both the tanker and receiver aircraft are available as driving inputs. Aspects particular to the IMU such as its offset from the aircraft CG, as well as an IMU noise model which includes white noise, bias and drift are considered.

In the second section the measurement models are derived in which the state vector is related to the measurement vector and the uncertainty coupled with the sensor is modeled. Some of the sensors also have additional considerations when implemented, which will also be discussed

4.1 Process Model

The function of the process model in state estimation is to utilise the equations that govern the dynamics of the state vector to propagate the states and their respective error covariances from one measurement instance to the next. These kinematic equations are functions of the state vector, the driving inputs to the system, and the accompanying process noise as shown by the continuous-time non-linear process model:

$$\dot{\boldsymbol{x}}(t) = f\left(\boldsymbol{x}(t), \boldsymbol{u}(t), \boldsymbol{w}(t)\right), \quad \boldsymbol{w}(t) \sim (\boldsymbol{0}, Q(t))$$

Where $\boldsymbol{w}(t)$ is zero mean Gaussian noise and $Q(t)$ is the spectral density process covariance matrix. Typically the equations are derived in continuous time and then discretized for implementation in a digital format as shown in the EKF derivation in Chapter 3.

From Chapter 2 the true states are given by:

$$x = \begin{bmatrix} \boldsymbol{p}_r^{T/R} & \boldsymbol{v}_r^{T/R} & \boldsymbol{q}^{t/r} & \boldsymbol{\omega}_t^{t/r} \end{bmatrix} \tag{4.1.1}$$

with the driving inputs vector given as

$$u = \begin{bmatrix} \boldsymbol{a}_t^{T/I} & \boldsymbol{a}_r^{R/I} & \boldsymbol{\omega}_t^{t/i} & \boldsymbol{\omega}_r^{r/i} \end{bmatrix}^T \tag{4.1.2}$$

These driving inputs are obtained from IMU modules attached to both the tanker and receiver aircraft. The measurements obtained from these sensors are not the true accelerations and angular rates experienced by the aircraft but are measurements of the IMU acceleration and angular rates corrupted by noise. For this reason the measurement model of the IMU is introduced first, followed by the derivation of the angular rate and quaternion kinematics after which the position and velocity kinematic equations are evaluated.

4.1.1 Accelerometer and Rate Gyroscope Measurement Models

4.1.1.1 Measured vector, noise and bias

As with all sensors the values measured by the IMU are not the true specific forces and angular rates experienced by the IMU reference frame, but are corrupted by uncertainty. Typically this uncertainty comes in the form of additive white noise and in the case of IMU measurement there are additional bias terms that must be considered.

Accelerometers provide a measure of specific force experienced by the IMU reference frame, whereas the rate gyroscope provides a measured of the angular velocity of IMU reference frame relative to inertial space. Note that a generic axis system F_x will be used to represent the IMU as to avoid repetition for the sensors on each aircraft.

The specific force can be related to the inertial acceleration of the IMU unit through,

$$\boldsymbol{a}_x^{sf} = \boldsymbol{a}_x^{X/I} - \boldsymbol{g}_x \tag{4.1.3}$$

where $\boldsymbol{a}^{sf}$ is the true specific force, also referred to as the proper acceleration, $\boldsymbol{a}_x^{X/I}$ is the acceleration of the IMU relative to inertial space and $\boldsymbol{g}_x$ is the gravity vector coordinated in the IMU reference frame. The true inertial acceleration experienced by the IMU is then related to the measured value through the measurement model

$$\boldsymbol{a}_x^{X/I} = \left(\tilde{\boldsymbol{a}}^{sf} + \boldsymbol{g}_x\right) - \boldsymbol{\beta}_{\boldsymbol{a}_x^{X/I}} - \boldsymbol{\eta}_{\boldsymbol{a}_x^{X/I}} \tag{4.1.4}$$

$$= \tilde{\boldsymbol{a}}_x^{X/I} - \boldsymbol{\beta}_{\boldsymbol{a}_x^{X/I}} - \boldsymbol{\eta}_{\boldsymbol{a}_x^{X/I}} \tag{4.1.5}$$

where $\boldsymbol{\beta}_{\boldsymbol{a}_x^{X/I}}$ and $\boldsymbol{\eta}_{\boldsymbol{a}_x^{X/I}}$ are the accelerometer bias and white noise terms respectively. The true angular velocity experienced by the IMU reference frame is related to the measured value through the measurement model,

$$\boldsymbol{\omega}_x^{x/i} = \tilde{\boldsymbol{\omega}}_x^{x/i} - \boldsymbol{\beta}_{\boldsymbol{\omega}_x^{x/i}} - \boldsymbol{\eta}_{\boldsymbol{\omega}_x^{x/i}} \tag{4.1.6}$$

with $\beta_{\boldsymbol{\omega}_x^{x/i}}$ and $\eta_{\boldsymbol{\omega}_x^{x/i}}$ the gyroscope bias and white noise terms.

The noise terms is zero-mean Gaussian and as such its expected value is zero, but the bias terms can in fact be estimated. Where typical sensor measurements are directly input into the relevant equations the IMU measurements are first corrected by the bias estimate, where the estimated driving input acceleration and angular velocity are given as,

$$\hat{\boldsymbol{a}}_x^{X/I} = \tilde{\boldsymbol{a}}_x^{X/I} - \hat{\boldsymbol{\beta}}_{\boldsymbol{a}_x^{X/I}} \tag{4.1.7}$$

$$\hat{\boldsymbol{\omega}}_x^{x/i} = \tilde{\boldsymbol{\omega}}_x^{x/i} - \hat{\boldsymbol{\beta}}_{\boldsymbol{\omega}_x^{x/i}} \tag{4.1.8}$$

In light of this the state vector is amended to include the tanker and receiver IMU bias terms, which becomes

$$X = \begin{bmatrix} \boldsymbol{p}_r^{T/R} & \boldsymbol{v}_r^{T/R} & \boldsymbol{q}^{t/r} & \boldsymbol{\omega}_t^{t/r} & \boldsymbol{\beta}_{\boldsymbol{a}_t^{T/I}} & \boldsymbol{\beta}_{\boldsymbol{a}_r^{R/I}} & \boldsymbol{\beta}_{\boldsymbol{\omega}_t^{t/i}} & \boldsymbol{\beta}_{\boldsymbol{\omega}_r^{r/i}} \end{bmatrix}^T \tag{4.1.9}$$

The true bias kinematics can be described as white noise,

$$\dot{\boldsymbol{\beta}}_{\boldsymbol{a}_x^{X/I}} = \boldsymbol{\eta}_{\dot{\boldsymbol{\beta}}_{\boldsymbol{a}_x^{X/I}}} \tag{4.1.10}$$

$$\dot{\boldsymbol{\beta}}_{\boldsymbol{\omega}_x^{x/i}} = \boldsymbol{\eta}_{\dot{\boldsymbol{\beta}}_{\boldsymbol{\omega}_x^{x/i}}} \tag{4.1.11}$$

with the estimated value of white noise assumed to be zero.

In some cases the bias terms are deemed negligibly small and are omitted from the state vector and the IMU measurement model. In such cases the uncertainty in the accelerations and angular velocity measurements only stems from the white noise terms. In addition to the omission of the bias terms, the nature of this thesis also allows for scenarios where there are no IMU measurements present in which case the measurement term in the acceleration and angular rate representations also reduces to zero. This results in cases where the driving input equations simply reduce to the noise terms. This is further shown later in the section where the simplified measurement model is discussed.

4.1.1.2 IMU offset from aircraft CG

The accelerometer measurement $\tilde{\boldsymbol{a}}_x^{X/I}$ is based on the acceleration perceived by the IMU reference frame. This inertial acceleration of the IMU does not, however, necessarily coincide with that of the aircraft body axis. As the dynamic equations derivations are typically dependent on acceleration of the aircraft CG, the induced acceleration resulting from the IMU offset must be compensated for.

An expression for the resultant acceleration due to IMU offset can be found by taking the second time derivative of the relative position vector,

$$\frac{d^2}{dt^2}\left(\boldsymbol{p}^{X/I}\right) = \frac{d^2}{dt^2}\left(\boldsymbol{p}^{R/I} + \boldsymbol{p}^{X/R}\right) \tag{4.1.12}$$

where the receiver is used as the applicable aircraft. Rearranging the resulting equation and coordinating the vectors in the applicable reference frames yields an expression for the aircraft CG acceleration as a function of the IMU acceleration,

$$\boldsymbol{a}_r^{R/I} = \boldsymbol{a}_x^{X/I} - \left[\dot{\boldsymbol{\omega}}_r^{r/i}\times\right]\boldsymbol{p}_r^{X/R} - \left[\boldsymbol{\omega}_r^{r/i}\times\right]\left[\boldsymbol{\omega}_r^{r/i}\times\right]\boldsymbol{p}_r^{X/R} \tag{4.1.13}$$

Notice that this expression requires the angular acceleration measurement of the IMU, which is not typically avaiable. It can eather be assumed that the angular acceleration can be sufficiently represented by zero mean white noise, in which case the measured value would be assumed as zero. Alternatively, the discrete time derivative of the angular velocity measurements in combination with a low pass fliter could prove an improvement on a zero mean noise assumption, but is left to be inverstigated in future developments.

This, when combined with the IMU bias and noise measurement model, forms a full representation for the aircraft acceleration and angular rate driving inputs as a function of the IMU measurements. For ease of implementation, however, a few assumptions can be made to simplify the models.

4.1.1.3 Simplifications

In the AAR scenario it is assumed that each aircraft is fitted with a sophisticated array of inertial measurement sensors that provide specific force and angular rate measurement into an estimation algorithm which compensates for sensor measurement biases and IMU acceleration due the to IMU offset from the aircraft CG. The net result is an unbiased body acceleration and angular velocity output which can be used as the driving inputs to the AAR state estimation system. This allows the bias terms in Equations 4.1.5 and 4.1.6 and the acceleration compensation of Eq. 4.1.13 to be omitted from further analysis in which case the state vector reverts to the original representation.

With this new simplified model the measured aircraft acceleration and angular velocity measurement model is shown to be,

$$\boldsymbol{a}_x^{X/I} = \tilde{\boldsymbol{a}}_x^{X/I} - \boldsymbol{\eta}_{\boldsymbol{a}_x^{X/I}} \tag{4.1.14}$$

$$\boldsymbol{\omega}_x^{x/i} = \tilde{\boldsymbol{\omega}}_x^{x/i} - \boldsymbol{\eta}_{\boldsymbol{\omega}_x^{x/i}} \tag{4.1.15}$$

where $\tilde{\boldsymbol{a}}_x^{X/I}$ and $\tilde{\boldsymbol{\omega}}_x^{x/i}$ are the measured outputs of the aircraft estimators and $\boldsymbol{\eta}_{\boldsymbol{a}_x^{X/I}}$ and $\boldsymbol{\eta}_{\boldsymbol{\omega}_x^{x/i}}$ are zero-mean white noise. The expected value the reverts to being the measured value,

$$\hat{\boldsymbol{a}}_x^{X/I} = \tilde{\boldsymbol{a}}_x^{X/I} \tag{4.1.16}$$

$$\hat{\boldsymbol{\omega}}_x^{x/i} = \tilde{\boldsymbol{\omega}}_x^{x/i} \tag{4.1.17}$$

For Chapter 2 it can be recalled that there are configurations in which IMU are not used. In such cases the aircraft body acceleration and angular rate measurement in these models merely become zero causing the driving inputs to the system to be white noise.

$$\boldsymbol{a}_x^{X/I} = -\boldsymbol{\eta}_{\boldsymbol{a}_x^{X/I}} \tag{4.1.18}$$

$$\boldsymbol{\omega}_x^{x/i} = -\boldsymbol{\eta}_{\boldsymbol{\omega}_x^{x/i}} \tag{4.1.19}$$

With the driving input sensor models defined the attitude and angular rate kinematics are derived after which the position and linear velocity kinematics are evaluated.

4.1.2 Relative Angular Rate and Attitude Kinematics

The relative angular rate $\boldsymbol{\omega}_t^{t/r}$ is not typically added to the state vector due to the fact that it can be sufficiently represented by the angular rate driving inputs and attitude state through,

$$\boldsymbol{\omega}_t^{t/r} = \boldsymbol{\omega}_t^{t/i} - \boldsymbol{T}\left(\boldsymbol{q}^{t/r}\right)\boldsymbol{\omega}_r^{r/i} \tag{4.1.20}$$

In the scenario presented by this thesis however, there are cases in which the IMU will not be included in the sensor array. In such cases the relative angular rate cannot be directly calculated but can be estimated using velocity measurements obtained from the RB-DGPS and as such must be added to the state vector.

The relative angular rate time derivative equation is a complex function of the aircraft inertias, applied torque and current angular rates. It is assumed that little is known regarding the forces and moments applied to each aircraft, especially that of the tanker and as such the

time derivative of the relative angular velocity is simplistically represented by zero mean white noise,

$$\dot{\boldsymbol{\omega}}_t^{t/r} = \boldsymbol{\eta}_{\dot{\boldsymbol{\omega}}_t^{t/r}} \tag{4.1.21}$$

This assumption implies that the realtive angular rate has a constant value, which is valid for the flight scenarios considered in this thesis. As a result there is no discrete propagation of the relative angular rate, as it merely holds its old value in the case when the IMU angular velocity driving inputs are absent and in cases where the IMU measurements are present, the estimated relative angular rate is obtained from the Eq. 4.1.20.

Relative quaternions in attitude estimation have been most notably used in relative spacecraft navigation in the work presented in [28; 38; 23; 44]. As a result, this section follows the same general derivations, with specific alterations for implementation in AAR. A general introduction to quaternions and quaternion kinematics is given in Appendix B.

The relative attitude quaternion between aircraft, denoted as $\boldsymbol{q}^{t/r}$, is used to map vectors in the tanker reference frame to vectors in the receiver reference frame. The symbol $\otimes$ is known as the quaternion multiplication operator.

The continuous time relative quaternion kinematic equation is known to be,

$$\dot{\boldsymbol{q}}^{t/r} = \frac{1}{2}\begin{bmatrix} \boldsymbol{\omega}_t^{t/r} \\ 0 \end{bmatrix} \otimes \boldsymbol{q}^{t/r} \tag{4.1.22}$$

which can be represented in matrix format to be,

$$\dot{\boldsymbol{q}}^{t/r} = \frac{1}{2}\Xi(\boldsymbol{q}^{t/r})\boldsymbol{\omega}_t^{t/r} \tag{4.1.23}$$

$$= \frac{1}{2}\Omega(\boldsymbol{\omega}_t^{t/r})\boldsymbol{q}^{t/r} \tag{4.1.24}$$

with the transformation matrices are given as

$$\Xi(\boldsymbol{q}^{t/r}) = \begin{bmatrix} q_4^{t/r} I_{3\times 3} + [\boldsymbol{q}_{13}^{t/r}\times] \\ -\left(\boldsymbol{q}_{13}^{t/r}\right)^T \end{bmatrix} \quad , \quad \Omega(\boldsymbol{\omega}_t^{t/r}) = \begin{bmatrix} [\boldsymbol{\omega}_t^{t/r}\times] & \boldsymbol{\omega}_t^{t/r} \\ -(\boldsymbol{\omega}_t^{t/r})^T & 0 \end{bmatrix}$$

The discrete equivalent for the quaternion propagation can be found in a similar way as in [23] which yields,

$$\boldsymbol{q}_{k+1}^{t/r} = \exp\left[\frac{1}{2}\Omega(\boldsymbol{\omega}_t^{t/r})\Delta t\right]\boldsymbol{q}_k^{t/r} \tag{4.1.25}$$

$$= \begin{bmatrix} \cos\left(\frac{1}{2}\left\|\boldsymbol{\omega}_t^{t/r}\right\|\Delta t\right) I_{3\times 3} - [\psi_k\times] & \psi_k \\ -\psi_k^T & \cos\left(\frac{1}{2}\left\|\boldsymbol{\omega}_t^{t/r}\right\|\Delta t\right) \end{bmatrix}\boldsymbol{q}_k^{t/r} \tag{4.1.26}$$

where

$$\psi_k = \frac{\sin\left(\frac{1}{2}\left\|\boldsymbol{\omega}_t^{t/r}\right\|\Delta t\right)\boldsymbol{\omega}_t^{t/r}}{\left\|\boldsymbol{\omega}_t^{t/r}\right\|} \tag{4.1.27}$$

There are however a few limitations in the implementation of quaternions in the current EKF and UKF algorithms. In the UKF, the propagated state mean is derived from an averaged sum of state sigma points, in which case no guarantees can be made that the unit quaternion constraint will be maintained. In the correction step of both the EKF and UKF, the state correction is achieved through the addition of an error correction term, in which ,again, no guarantee can be made that the unity constraint of the quaternion will be maintained.

In order to overcome the constraints imposed by the quaternion attitude representation the use of an error attitude representation as seen in [45; 46] was adopted. This approach implements an error-quaternion in combination with a reference quaternion where the error-quaternion is represented by an unconstrained three-component vector. This allows an unconstrained error state to be estimated whilst maintaining a non-singular global attitude representation.

4.1.2.1 Error Attitude Representations

Following the theory of quaternion rotations in Appendix B and the work presented in [45; 46] the true attitude quaternion can be represented by sequential quaternion rotations,

$$\boldsymbol{q}^{t/r} = \delta\boldsymbol{q}^{t/r}(\varphi) \otimes \hat{\boldsymbol{q}}^{t/r} \tag{4.1.28}$$

where the true attitude quaternion $\boldsymbol{q}^{t/r}$ is represented by an error rotation $\delta\boldsymbol{q}^{t/r}(\varphi)$ from a quaternion estimate $\hat{\boldsymbol{q}}^{t/r}$. Note that the error quaternion $\delta\boldsymbol{q}^{t/r}(\varphi)$ is a function of an unconstrained three-component vector. The basic premise of using this representation is that the three-component vector φ is used in the function of the estimation algorithms, where unconstrained vectors can be averaged and corrected as required. Once estimated, φ is used to calculate the error quaternion which is used to update the correctly normalized four-component global quaternion estimate.

If the quaternion estimate is chosen such that the expected value of the $\hat{\varphi} \equiv E(\varphi)$ is zero once all the dynamic and measurement information is available it can be shown that the new quaternion estimate is given as a rotation of the error quaternion about the old estimate,

$$\hat{\boldsymbol{q}}^{t/r} = \delta\boldsymbol{q}^{t/r}(\hat{\varphi}) \otimes \hat{\boldsymbol{q}}^{t/r} \tag{4.1.29}$$

The main advantages of this approach is the fact that the global attitude quaternion has unity norm by definition, the covariance has minimum dimensionality and the three-component error vector φ never approaches a singularity as it only represents small attitude errors. Following the most popular implementations the use of Modified Rodrigues Parameters (MRP) is proposed as implemented in [44; 28].

4.1.2.2 Modified Rodrigues Parameters

From the introduction of the quaternion attitude representation in Appendix B it is known that the quaternion is comprised of a vector component and a scalar component as $q = [q_{13} \quad q_4]$ with $q_{13} = [q_1 \quad q_2 \quad q_3] = \mathbf{e}\sin(\vartheta/2)$, and $q_4 = \cos(\vartheta/2)$, with $\mathbf{e}$ representing the Euler axis of rotation and ϑ the angle of rotation. The vector of Modified Rodrigues Parameters is represented by $\boldsymbol{\alpha}^{t/r}$ and is related to these parameters through the following

$$\boldsymbol{\alpha}^{t/r} \equiv \mathbf{e}\tan(\vartheta/2) \tag{4.1.30}$$

Rearranging Eq. 4.1.29 the error quaternion is shown to be the difference in rotation between the true and estimated attitude quaternions,

$$\delta\boldsymbol{q}^{t/r}(\varphi) = \boldsymbol{q}^{t/r} \otimes \hat{\boldsymbol{q}}^{t/r\,-1} = \begin{bmatrix} \delta\boldsymbol{q}_{\mathbf{13}}^{t/r} \\ \delta q_4^{t/r} \end{bmatrix} \tag{4.1.31}$$

The error Modified Rodrigues Parameters (error-MRP) is shown to be related to the local error quaternion through,

$$\varphi = \delta\boldsymbol{\alpha}^{t/r} = f\frac{\delta\boldsymbol{q}_{\mathbf{13}}^{t/r}}{a + \delta q_4^{t/r}} \tag{4.1.32}$$

where a is chosen to be 1 and f chosen to be 4 so that $\boldsymbol{q}_{\mathbf{13}}^{t/r}$ is equal to physically intuitive roll pitch an yaw angles for small errors [28]. The inverse relation between the error quaternion and the error-MRP is given by

$$\begin{aligned} \delta q_4^{t/r} &= \frac{-a\left\|\delta\boldsymbol{\alpha}^{t/r}\right\| + f\sqrt{f^2 + (1-a^2)\left\|\delta\boldsymbol{\alpha}^{t/r}\right\|}}{f^2 + \left\|\delta\boldsymbol{\alpha}^{t/r}\right\|} \\ &= \frac{16 - \left\|\delta\boldsymbol{\alpha}^{t/r}\right\|}{16 + \left\|\delta\boldsymbol{\alpha}^{t/r}\right\|} \qquad (4.1.33) \\ \delta\boldsymbol{q}_{\mathbf{13}}^{t/r} &= f^{-1}(1+\delta q_4)\delta\boldsymbol{\alpha}^{t/r} \\ &= \frac{1}{4}(1+\delta q_4)\delta\boldsymbol{\alpha}^{t/r} \qquad (4.1.34) \end{aligned}$$

With this new attitude representation the quaternion in the state vector is replaced by the error-MRP, with the quaternion estimate used as a global attitude presentation. The new state vector is shown to be,

$$\boldsymbol{x} = \begin{bmatrix} \boldsymbol{p}_r^{T/R} & \boldsymbol{v}_r^{T/R} & \delta\boldsymbol{\alpha}^{t/r} & \boldsymbol{\omega}_t^{t/r} \end{bmatrix} \tag{4.1.35}$$

This new attitude representation allows for seamless transition between attitude representations which is especially useful in the UKF. The value of this new representation is shown in its integration into the current estimation algorithm structures in Table 4.1 and Table 4.2.

Initialisation	$\hat{\boldsymbol{x}}(t_0) = \hat{\boldsymbol{x}}_0, \quad \hat{\boldsymbol{q}}(t_0) = \hat{\boldsymbol{q}}_0$ $\hat{P}_0 = E[(\tilde{\boldsymbol{x}}_0)(\tilde{\boldsymbol{x}}_0)^T]$
Propagation	$\hat{\boldsymbol{x}}_k^- = f\left(\hat{\boldsymbol{x}}_{k-1}^+, \boldsymbol{u}_{k-1}, \boldsymbol{0}\right)$ $\hat{\boldsymbol{q}}_k^- = \frac{1}{2}\begin{bmatrix} \boldsymbol{\omega}_{k-1}^+ \\ 0 \end{bmatrix} \hat{\boldsymbol{q}}_{k-1}^+$ $P_k^- = F(\hat{\boldsymbol{x}}_{k-1}^+, \boldsymbol{u}_{k-1}) P_{k-1}^+ F(\hat{\boldsymbol{x}}_{k-1}^+, \boldsymbol{u}_{k-1})^T + Q_k$ $F(\hat{\boldsymbol{x}}_{k-1}^+, \boldsymbol{u}_{k-1}) \equiv \left.\frac{\partial f}{\partial \boldsymbol{x}}\right\|_{\hat{\boldsymbol{x}}_{k-1}^+, \boldsymbol{u}_{k-1}}$
Gain	$K_k = P_k^- H(\hat{\boldsymbol{x}}_k^-)\left[H(\hat{\boldsymbol{x}}_k^-) P_k^- H(\hat{\boldsymbol{x}}_k^-) + M(\hat{\boldsymbol{x}}_k^-) R_k M(\hat{\boldsymbol{x}}_k^-)^T\right]^{-1}$ $H(\hat{\boldsymbol{x}}_k^-) \equiv \left.\frac{\partial h}{\partial \boldsymbol{x}}\right\|_{\hat{\boldsymbol{x}}_k^-}$ $M(\hat{\boldsymbol{x}}_k^-) \equiv \left.\frac{\partial h}{\partial \boldsymbol{v}}\right\|_{\hat{\boldsymbol{x}}_k^-}$
Correction	$\hat{\boldsymbol{x}}_k^+ = \hat{\boldsymbol{x}}_k^- + K_k\left(y_k - h(\hat{\boldsymbol{x}}_k^-, \boldsymbol{0})\right)$ $\delta\hat{q}_{4k}^+ = \frac{16 - \left\|\delta\hat{\boldsymbol{\alpha}}_k^-\right\|}{16 + \left\|\delta\hat{\boldsymbol{\alpha}}_k^-\right\|}, \quad \delta\hat{\boldsymbol{q}}_{13k}^+ = \frac{1}{4}(1 + \delta\hat{q}_{4k}^+)\delta\hat{\boldsymbol{\alpha}}_k^-$ $\hat{\boldsymbol{q}}_k^+ = \delta\hat{\boldsymbol{q}}_k^+ \otimes \hat{\boldsymbol{q}}_{k-1}^+$ $P_k^+ = \left(I - K_k H(\hat{\boldsymbol{x}}_k^-)\right) P_k^-$

Table 4.1 – Extended Kalman Filter Summary

In the case of the UKF there are no additional derivations required, but in the case of the EKF it is necessary that the new error-MRP state kinematic equation be evaluated to allow the partial derivative to be calculated for covariance propagation.

Initialisation	$\hat{\boldsymbol{x}}(t_0) = \hat{\boldsymbol{x}}_0, \quad \hat{\boldsymbol{q}}(t_0) = \hat{\boldsymbol{q}}_0$ $\hat{P}_0 = E[(\tilde{\boldsymbol{x}}_0)(\tilde{\boldsymbol{x}}_0)^T]$
Sigma Points	$\mathbf{X}_k = \left[\hat{\boldsymbol{x}}_{k-1}^{+a} \;\vdots\; \hat{\boldsymbol{x}}_{k-1}^{+a} + \sqrt{(n+\lambda)P_{k-1}^{a}} \;\vdots\; \hat{\boldsymbol{x}}_{k-1}^{+a} - \sqrt{(n+\lambda)P_{k-1}^{a}} \right]$
Propagation	$\delta\hat{q}_{4k-1}^{+}(i) = \frac{16-\left\|\delta\hat{\boldsymbol{\alpha}}_{k-1}^{-}(i)\right\|}{16+\left\|\delta\hat{\boldsymbol{\alpha}}_{k-1}^{-}(i)\right\|}, \quad \delta\hat{\boldsymbol{q}}_{13k-1}^{+}(i) = \frac{1}{4}(1+\delta\hat{q}_{4k-1}^{+}(i))\delta\hat{\boldsymbol{\alpha}}_{k-1}^{-}(i)$ $\hat{\boldsymbol{q}}_{k-1}^{+}(i) = \delta\hat{\boldsymbol{q}}_{k-1}^{+}(i) \otimes \hat{\boldsymbol{q}}_{k-1}^{+}$ $\mathbf{X}_k^{p,v,\omega}(i) = f(\mathbf{X}_{k-1}^{p,v,\omega}(i), \hat{\boldsymbol{q}}_{k-1}^{+}(i), \mathbf{X}_{k-1}^{w}(i), \boldsymbol{u}_{k-1})$ $\hat{\boldsymbol{q}}_k^{-}(i) = \frac{1}{2}\begin{bmatrix} \boldsymbol{\omega}_{k-1}^{+}(i) \\ 0 \end{bmatrix} \hat{\boldsymbol{q}}_{k-1}^{+}(i)$ $\mathbf{X}_k^{\delta\alpha}(i) = 4\frac{\hat{\boldsymbol{q}}_{13k}^{-}(i)}{1+\hat{q}_{4k}^{-}(i)}$ $\hat{\boldsymbol{x}}_k^{-} = \sum_{j=0}^{2n+1} W_m^j \mathbf{X}_k^x(j)$ $P_k^{xx} = \sum_{j=0}^{2n+1} W_c^j (\mathbf{X}_k^x(j) - \hat{\boldsymbol{x}}_k^{-})(\mathbf{X}_k^x(j) - \hat{\boldsymbol{x}}_k^{-})^T$
Gain	$\mathbf{Y}_k(i) = h(\mathbf{X}_k^{p,v,\omega}, \hat{\boldsymbol{q}}_k^{-}(i), \mathbf{X}_k^{v})$ $P_k^{yy} = \sum_{j=0}^{2n} W_c^j (\mathbf{Y}_k(i) - \hat{\boldsymbol{y}}_k^{-})(\mathbf{Y}_k(i) - \hat{\boldsymbol{y}}_k^{-})^T$ $P_k^{xy} = \sum_{j=0}^{2n} W_c^j (\mathbf{X}_k(i) - \hat{\boldsymbol{y}}_k^{-})(\mathbf{Y}_k(i) - \hat{\boldsymbol{y}}_k^{-})^T$ $K_k = P_k^{xy}(P_k^{yy})^{-1}$
Correction	$\hat{y}_k^{-} = \sum_{j=0}^{2n} W_m^j \mathbf{Y}_k(i)$ $\hat{\boldsymbol{x}}_k^{+} = \hat{\boldsymbol{x}}_k^{-} + K_k\left(\boldsymbol{y}_k - \hat{\boldsymbol{y}}_k^{-}\right)$ $\delta\hat{q}_{4k-1}^{+} = \frac{16-\left\|\delta\hat{\boldsymbol{\alpha}}_{k-1}^{-}\right\|}{16+\left\|\delta\hat{\boldsymbol{\alpha}}_{k-1}^{-}(i)\right\|}, \quad \delta\hat{\boldsymbol{q}}_{13k}^{+} = \frac{1}{4}(1+\delta\hat{q}_{4k}^{+})\delta\hat{\boldsymbol{\alpha}}_k^{-}$ $\hat{\boldsymbol{q}}_k^{+} = \delta\hat{\boldsymbol{q}}_k^{+} \otimes \hat{\boldsymbol{q}}_k^{-}$ $P_k^{+} = P_k^{xx} - K_k P_k^{yy} K_k^T$

Table 4.2 – Unscented Kalman Filter Summary

4.1.2.3 Error MRP kinematic equation

In order to derive an equation for the error-MRP kinematics it is first necessary to evaluate the error quaternion kinematic equations. A similar approach as presented in [23] was followed in the derivation of error-MRP the kinematic equation.

The time derivative of the error quaternion in Eq. 4.1.31 is given by,

$$\delta\dot{\boldsymbol{q}}^{t/r} = \dot{\boldsymbol{q}}^{t/r} \otimes \hat{\boldsymbol{q}}^{t/r\,-1} + \boldsymbol{q}^{t/r} \otimes \dot{\hat{\boldsymbol{q}}}^{t/r\,-1} \tag{4.1.36}$$

The quaternion time derivative is given by Eq. 4.1.22, where an expression for the time derivative of the inverse quaternion estimate can be evaluated by using the known relation $\dot{\boldsymbol{q}}^{t/r} \otimes \hat{\boldsymbol{q}}^{t/r\,-1} = [0 \;\; 0 \;\; 0 \;\; 1]^T$. The derivative can be evaluated to yield,

$$\dot{\hat{\boldsymbol{q}}}^{t/r\,-1} = \frac{1}{2}\,\hat{\boldsymbol{q}}^{t/r\,-1} \otimes \begin{bmatrix} \hat{\boldsymbol{\omega}}_t^{t/r} \\ 0 \end{bmatrix} \tag{4.1.37}$$

where the estimated relative angular velocity is given by,

$$\hat{\boldsymbol{\omega}}_r^{t/r} = \hat{\boldsymbol{\omega}}_t^{t/i} - \boldsymbol{T}\left(\hat{\boldsymbol{q}}^{t/r}\right)\hat{\boldsymbol{\omega}}_r^{r/i} \tag{4.1.38}$$

Substituting Eq. 4.1.22 and Eq. 4.1.37 into Eq. 4.1.36 leads to an expression for the error quaternion time derivative,

$$\delta\dot{\boldsymbol{q}}^{t/r} = \frac{1}{2}\begin{bmatrix} \boldsymbol{\omega}_t^{t/r} \\ 0 \end{bmatrix} \otimes \delta\boldsymbol{q}^{t/r} - \frac{1}{2}\delta\boldsymbol{q}^{t/r} \otimes \begin{bmatrix} \hat{\boldsymbol{\omega}}_t^{t/r} \\ 0 \end{bmatrix} \tag{4.1.39}$$

As this derivation is intended for using the EKF the small angle approximation is applied which results in the error quaternion being represented by a vector of half angles,

$$\boldsymbol{\delta q}^{t/r} = \begin{bmatrix} \frac{1}{2}\boldsymbol{\delta\alpha}^{t/r} \\ 1 \end{bmatrix} \tag{4.1.40}$$

Combining Equations 4.1.39 and 4.1.40 yields an expression which includes the error MRP time derivative,

$$\boldsymbol{\delta}\dot{\boldsymbol{q}}^{t/r} = \frac{d}{dt}\left(\begin{bmatrix} \frac{1}{2}\boldsymbol{\delta\alpha}^{t/r} \\ 1 \end{bmatrix}\right) = \frac{1}{2}\begin{bmatrix} \boldsymbol{\omega}_t^{t/r} \\ 0 \end{bmatrix} \otimes \begin{bmatrix} \frac{1}{2}\boldsymbol{\delta\alpha}^{t/r} \\ 1 \end{bmatrix} - \frac{1}{2}\begin{bmatrix} \frac{1}{2}\boldsymbol{\delta\alpha}^{t/r} \\ 1 \end{bmatrix} \otimes \begin{bmatrix} \hat{\boldsymbol{\omega}}_t^{t/r} \\ 0 \end{bmatrix} \tag{4.1.41}$$

Employing quaternion multiplication as well as isolating the vector part of the equations results in an expression for the error-MRP kinematics,

$$\begin{aligned} \delta\dot{\boldsymbol{\alpha}}^{t/r} &= \boldsymbol{\omega}_t^{t/r} + \frac{1}{2}\left[\boldsymbol{\omega}_t^{t/r}\times\right]\delta\boldsymbol{\alpha}^{t/r} - \hat{\boldsymbol{\omega}}_t^{t/r} - \frac{1}{2}\left[\boldsymbol{\delta\alpha}^{t/r}\times\right]\hat{\boldsymbol{\omega}}_t^{t/r} && (4.1.42) \\ &= \delta\boldsymbol{\omega}_t^{t/r} + \left[\hat{\boldsymbol{\omega}}_t^{t/r}\times\right]\delta\boldsymbol{\alpha}^{t/r} + \frac{1}{2}\left[\delta\boldsymbol{\omega}_t^{t/r}\times\right]\delta\boldsymbol{\alpha}^{t/r} && (4.1.43) \end{aligned}$$

where the error in relative angular velocity is given as

$$\delta\boldsymbol{\omega}_t^{t/r} = \boldsymbol{\omega}_t^{t/r} - \hat{\boldsymbol{\omega}}_t^{t/r} \tag{4.1.44}$$

Substituting Equations 4.1.20 and 4.1.38 into Eq. 4.1.43 and applying the transformation matrix linearisation approximation

$$\boldsymbol{T}\left(\boldsymbol{q}^{t/r}\right) \approx \left(I_{3\times3} - \left[\delta\boldsymbol{\alpha}^{t/r}\times\right]\right)\boldsymbol{T}\left(\hat{\boldsymbol{q}}^{t/r}\right) \tag{4.1.45}$$

yields an expression for the error-MRP kinematics as a function of the angular rate driving inputs and associated noise vectors,

$$\begin{aligned} \delta\dot{\alpha} &= \boldsymbol{\delta\omega}_t^{t/i} - \boldsymbol{T}\left(\hat{\boldsymbol{q}}^{t/r}\right)\boldsymbol{\delta\omega}_r^{r/i} + \left[\hat{\boldsymbol{\omega}}_t^{t/i}\times\right]\boldsymbol{\delta\alpha}^{t/r} && (4.1.46) \\ &= -\eta_{\boldsymbol{\omega}_t^{t/i}} + \boldsymbol{T}\left(\hat{\boldsymbol{q}}^{t/r}\right)\eta_{\boldsymbol{\delta\omega}_r^{r/i}} + \left[\hat{\boldsymbol{\omega}}_t^{t/i}\times\right]\boldsymbol{\delta\alpha}^{t/r} && (4.1.47) \end{aligned}$$

Note that this simplification is not shown, but higher order terms are omitted due to the linearisation assumption of the EKF.

The position and velocity kinematics can now be derived using new attitude representation allowing the UKF and PF to propagate their particles and the process model Jacobian to be evaluated for use in the EKF.

4.1.3 Relative Position and Velocity Kinematics

Evaluating the relative position kinematics is fairly straight forward. The time derivative of the relative position taken with respect to the receiver reference frame simply becomes the relative velocity state,

$$\frac{d}{dt}\left(\boldsymbol{p}^{T/R}\right)\Big|_r = \boldsymbol{v}^{T/R} \tag{4.1.48}$$

Evaluating the time derivative of the relative velocity vector is more intricate, as the derivative must contain the driving input acceleration vectors. To achieve this, the time derivative of the relative position equation is initially evaluated with respect to the inertial reference frame,

$$\begin{aligned}
\boldsymbol{p}^{T/I} &= \boldsymbol{p}^{R/I} + \boldsymbol{p}^{T/R} && (4.1.49)\\
\frac{d}{dt}\left(\boldsymbol{p}^{T/I}\right)\Big|_i &= \frac{d}{dt}\left(\boldsymbol{p}^{R/I}\right)\Big|_i + \frac{d}{dt}\left(\boldsymbol{p}^{T/R}\right)\Big|_i && (4.1.50)\\
\frac{d}{dt}\left(\boldsymbol{p}^{T/I}\right)\Big|_i &= \frac{d}{dt}\left(\boldsymbol{p}^{R/I}\right)\Big|_i + \frac{d}{dt}\left(\boldsymbol{p}^{T/R}\right)\Big|_r + \boldsymbol{\omega}^{r/i}\times\boldsymbol{p}^{T/R} && (4.1.51)\\
\boldsymbol{v}^{T/I} &= \boldsymbol{v}^{R/I} + \boldsymbol{v}^{T/R} + \boldsymbol{\omega}^{r/i}\times\boldsymbol{p}^{T/R} && (4.1.52)
\end{aligned}$$

Taking the time derivative of the resultant velocity equation, again with respect to the inertial reference frame leads to the required acceleration equation,

$$\begin{aligned}
\boldsymbol{v}^{T/I} &= \boldsymbol{v}^{R/I} + \boldsymbol{v}^{T/R} + \boldsymbol{\omega}^{r/i}\times\boldsymbol{p}^{T/R} && (4.1.53)\\
\frac{d}{dt}\left(\boldsymbol{v}^{T/I}\right)\Big|_i &= \frac{d}{dt}\left(\boldsymbol{v}^{R/I}\right)\Big|_i + \frac{d}{dt}\left(\boldsymbol{v}^{T/R}\right)\Big|_i + \frac{d}{dt}\left(\boldsymbol{\omega}^{r/i}\right)\Big|_i \times \boldsymbol{p}^{T/R} && (4.1.54)\\
&\quad + \boldsymbol{\omega}^{r/i}\times\frac{d}{dt}\left(\boldsymbol{p}^{T/R}\right)\Big|_i && (4.1.55)\\
\boldsymbol{a}^{T/I} &= \boldsymbol{a}^{R/I} + \boldsymbol{a}^{T/R} + \dot{\boldsymbol{\omega}}^{r/i}\times\boldsymbol{p}^{T/R} + 2\boldsymbol{\omega}^{r/i}\times\boldsymbol{v}^{T/R} + \boldsymbol{\omega}^{r/i}\times\boldsymbol{\omega}^{r/i}\times\boldsymbol{p}^{T/R} && (4.1.56)
\end{aligned}$$

with the velocity kinematic equation obtained from the rearranged expression with the relative angular acceleration as the subject coordinated in the relevant reference frames,

$$\begin{aligned} \boldsymbol{a}_r^{T/R} &= \boldsymbol{T}\left(\boldsymbol{q}^{t/r}\right)^T \boldsymbol{a}_t^{T/I} - \boldsymbol{a}_r^{R/I} - \left[\dot{\boldsymbol{\omega}}_r^{r/i}\times\right]\boldsymbol{p}_r^{T/R} - 2\left[\boldsymbol{\omega}_r^{r/i}\times\right]\boldsymbol{v}_r^{T/R} - \\ &\quad \left[\boldsymbol{\omega}_r^{r/i}\times\right]\left[\boldsymbol{\omega}_r^{r/i}\times\right]\boldsymbol{p}_r^{T/R} \qquad (4.1.57) \\ &= \left(I_{3\times 3} - [\boldsymbol{\delta\alpha}^{t/r}\times]\right)\boldsymbol{T}\left(\hat{\boldsymbol{q}}^{r/t}\right)\boldsymbol{a}_t^{T/I} - \boldsymbol{a}_r^{R/I} - \left[\dot{\boldsymbol{\omega}}_r^{r/i}\times\right]\boldsymbol{p}_r^{T/R} \\ &\quad -2\left[\boldsymbol{\omega}_r^{r/i}\times\right]\boldsymbol{v}_r^{T/R} - \left[\boldsymbol{\omega}_r^{r/i}\times\right]\left[\boldsymbol{\omega}_r^{r/i}\times\right]\boldsymbol{p}_r^{T/R} \qquad (4.1.58) \end{aligned}$$

These kinematic equations will be used in combination with the attitude and angular rate kinematics in the process model of the estimation algorithms. The implentation of the EKF requires the linearisation of the process model equations for use in the propagation of the state covariance.

4.1.4 Process Model Linearisation

Having derived the kinematic equation of the process model it is also necessary to evaluate the partial derivatives of the kinematic equations with respect to the state vector and the noise vector for use in the EKF shown in Chapter 3. A summary of the state process model equations with error-MRP attitude representation is shown to be,

$$\begin{bmatrix} \dot{\boldsymbol{p}}_r^{T/R} \\ \dot{\boldsymbol{v}}_r^{T/R} \\ \boldsymbol{\delta\dot{\alpha}}^{t/r} \\ \dot{\boldsymbol{\omega}}_t^{t/r} \end{bmatrix} =$$

$$\begin{bmatrix} \boldsymbol{v}_r^{T/R} \\ \left(I_{3\times 3} + [\boldsymbol{\delta\alpha}^{t/r}\times]\right)\boldsymbol{T}\left(\hat{\boldsymbol{q}}^{t/r}\right)^T\boldsymbol{a}_t^{T/I} - \boldsymbol{a}_r^{R/I} - \left[\dot{\boldsymbol{\omega}}_r^{r/i}\times\right]\boldsymbol{p}_r^{T/R} - 2\left[\boldsymbol{\omega}_r^{r/i}\times\right]\boldsymbol{v}_r^{T/R} - \left[\boldsymbol{\omega}_r^{r/i}\times\right]\left[\boldsymbol{\omega}_r^{r/i}\times\right]\boldsymbol{p}_r^{T/R} \\ -\eta_{\boldsymbol{\omega}_t^{t/i}} + \boldsymbol{T}\left(\hat{\boldsymbol{q}}^{t/r}\right)\eta_{\boldsymbol{\omega}_r^{r/i}} + \left[\hat{\boldsymbol{\omega}}_t^{t/i}\times\right]\boldsymbol{\delta\alpha}^{t/r} \\ -\eta_{\dot{\boldsymbol{\omega}}_t^{t/r}} \end{bmatrix} \qquad (4.1.59)$$

The partial derivative of the non-linear equations with respect to the state vector

$$x = \begin{bmatrix} \boldsymbol{p}_r^{T/R} & \boldsymbol{v}_r^{T/R} & \delta\boldsymbol{\alpha}^{t/r} & \boldsymbol{\omega}_r^{t/r} \end{bmatrix}^T$$

evaluated at the current state estimates is given as,

$$F(\cdot) = \begin{bmatrix} 0_{3\times 3} & I_{3\times 3} & 0_{3\times 3} & 0_{3\times 3} \\ -\left[\tilde{\boldsymbol{\omega}}_r^{r/i}\times\right]\left[\tilde{\boldsymbol{\omega}}_r^{r/i}\times\right] & -2\left[\tilde{\boldsymbol{\omega}}_r^{r/i}\times\right] & \left[\boldsymbol{T}\left(\hat{\boldsymbol{q}}^{t/r}\right)^{-1}\tilde{\boldsymbol{a}}_t^{T/I}\times\right] & 0_{3\times 3} \\ 0_{3\times 3} & 0_{3\times 3} & \left[\tilde{\boldsymbol{\omega}}_t^{t/i}\times\right] & I_{3\times 3} \\ 0_{3\times 3} & 0_{3\times 3} & 0_{3\times 3} & 0_{3\times 3} \end{bmatrix} \qquad (4.1.60)$$

The partial derivative of the process model taken with respect to the noise vector

$$w = \begin{bmatrix} \eta_{\boldsymbol{a}_t^{T/I}} & \eta_{\boldsymbol{a}_r^{R/I}} & \eta_{\boldsymbol{\omega}_t^{t/i}} & \eta_{\boldsymbol{\omega}_r^{r/i}} & \eta_{\dot{\boldsymbol{\omega}}_r^{r/i}} & \eta_{\dot{\boldsymbol{\omega}}_t^{t/r}} \end{bmatrix}^T$$

evaluated at the current state estimate is given as,

$$L(\cdot) = \begin{bmatrix} 0_{3\times3} & 0_{3\times3} & 0_{3\times3} & 0_{3\times3} & 0_{3\times3} & 0_{3\times3} \\ -\boldsymbol{T}\left(\hat{\boldsymbol{q}}^{t/r}\right)^{-1} & I_{3\times3} & 0_{3\times3} & -2\left[\boldsymbol{v}_r^{T/R}\times\right] & -\left[\boldsymbol{p}_r^{T/R}\times\right] & 0_{3\times3} \\ 0_{3\times3} & 0_{3\times3} & -I_{3\times3} & \boldsymbol{T}\left(\hat{\boldsymbol{q}}^{t/r}\right) & 0_{3\times3} & 0_{3\times3} \\ 0_{3\times3} & 0_{3\times3} & 0_{3\times3} & 0_{3\times3} & 0_{3\times3} & -I_{3\times3} \end{bmatrix} \tag{4.1.61}$$

These matrices are used in the discretisation of the EKF process model in Chapter 3. Having derived the equations necessary to implement the propagation step of the estimation algorithms leads to the derivation of the sensor measurement models.

4.2 Measurement Model

The basic function of each of the sensors has been introduced in Chapter 2, where the goal of this chapter is to integrate each sensor into the estimation algorithm structure. This is done by deriving the equations that relate the measured value to the states and noise vectors.

As a reminder, the discrete non-linear measurement model is given as,

$$\boldsymbol{y}_k = h\left(\boldsymbol{x}_k, v_k\right), \quad \boldsymbol{v}_k \sim (\boldsymbol{0}, R_k) \tag{4.2.1}$$

where the newly defined modified state vector is given by

$$\boldsymbol{x} = \begin{bmatrix} \boldsymbol{p}_r^{T/R} & \boldsymbol{v}_r^{T/R} & \boldsymbol{\delta\alpha}^{t/r} & \boldsymbol{\omega}_t^{t/r} \end{bmatrix}^T \tag{4.2.2}$$

Given this generalized measurement model, the measurement equations are shown in the subsequent subsections. Note that the integration of a sensor into the estimation algorithm structure often requires additional considerations, which are also discussed in the evaluation of each sensor.

4.2.1 Roaming Base Differential GPS

Building on the RB-DGPS theory introduced in Chapter 2 and referring to Figure 4.1 it is shown that the measured vector resulting from this sensor configuration is the relative position and velocity of the Roaming GPS Receiver RR_i, relative to the Roaming GPS Base RB_j. The measured value along with its relation to the true value is given by the measurement model

$$y_{GPS}^{ij} = \begin{bmatrix} \tilde{\boldsymbol{p}}_{RB_j}^{RR_i/RB_j} \\ \tilde{\boldsymbol{v}}_{RB_j}^{RR_i/RB_j} \end{bmatrix} = \begin{bmatrix} \boldsymbol{p}_{RB_j}^{RR_i/RB_j} \\ \boldsymbol{v}_{RB_j}^{RR_i/RB_j} \end{bmatrix} + \begin{bmatrix} \boldsymbol{v}_p \\ \boldsymbol{v}_v \end{bmatrix} \tag{4.2.3}$$

where the noise vector $[\boldsymbol{v}_p \quad \boldsymbol{v}_v]^T$ is assumed to be zero mean Gaussian.

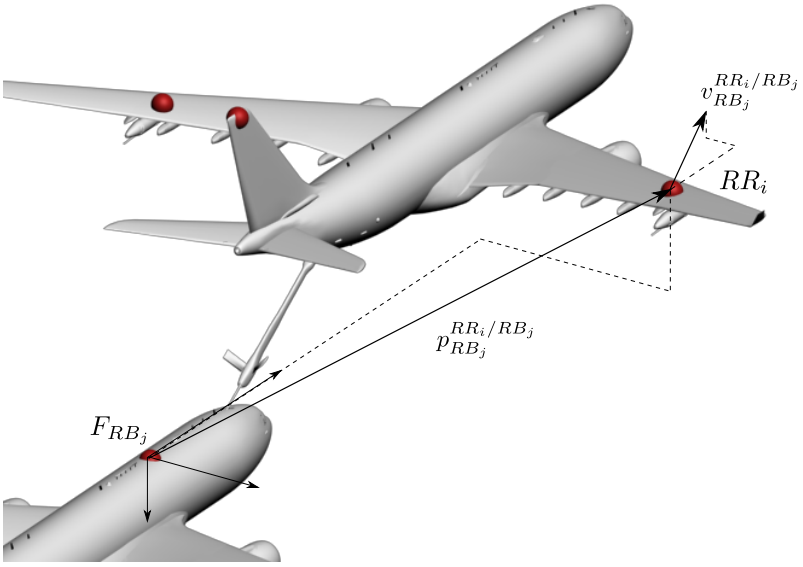

Figure 4.1 – Roaming Base Differential GPS measurement vectors

Note that the measurement model requires the measurements to be coordinated in the sensor reference frame, RB_j. In the method of calculating the relative position and velocity using DGPS, outlined by [3], the relative position and velocity measurements obtained from the DGPS system are typically given with reference to the ECEF reference frame. In order to represent the measurements in the sensor reference frame the relevant coordinate transformation from ECEF to sensor frame must be undergone. It is assumed that this can be done to such an accuracy as to not affect the accuracy of the resulting relative position and velocity measurement, with further investigation on the effects of the transformation to be undergone in the development of the RB-DGPS system. As the orientation of the RB-DGPS sensor reference frame is arbitrary, it is chosen to coincide with the receiver aircraft body axis, with all future RB-DGPS measurement vectors coordinated accordingly.

In order to relate the measured vector to the state vector, the true relative measurement vector is expanded to,

$$\boldsymbol{p}^{RR_i/RB_j} = \boldsymbol{p}^{R/RB_j} + \boldsymbol{p}^{T/R} + \boldsymbol{p}^{RR_i/T} \tag{4.2.4}$$

which , when coordinated in the appropriate reference frames provides relation between the measurement and the state vector,

$$\boldsymbol{p}_r^{RR_i/RB_j} = -\boldsymbol{p}_r^{RB_j/R} + \boldsymbol{p}_r^{T/R} + \boldsymbol{T}\left(\boldsymbol{q}^{t/r}\right)\boldsymbol{p}_t^{RR_i/T} \tag{4.2.5}$$

The velocity measurement vector can also be related to the state vector by taking the time derivative of the position measurement vector with respect to the receiver body axis reference frame,

$$\frac{d}{dt}\left(\boldsymbol{p}^{RR_i/RB_j}\right)\Big|_r = \frac{d}{dt}\left(\boldsymbol{p}^{R/RB_j} + \boldsymbol{p}^{T/R} + \boldsymbol{p}^{RR_i/T}\right)\Big|_r \tag{4.2.6}$$

$$= \frac{d}{dt}\left(\boldsymbol{p}^{R/RB_j}\right)\Big|_r + \frac{d}{dt}\left(\boldsymbol{p}^{T/R}\right)\Big|_r + \frac{d}{dt}\left(\boldsymbol{p}^{RR_i/T}\right)\Big|_t + \boldsymbol{\omega}^{t/r} \times \boldsymbol{p}^{RR_i/T} \tag{4.2.7}$$

and coordinating the vector into the applicable reference frame,

$$\boldsymbol{v}_r^{RR_i/RB_j} = \boldsymbol{v}_r^{T/R} + \boldsymbol{T}\left(\boldsymbol{q}^{t/r}\right)\left[\boldsymbol{\omega}_t^{t/r}\times\right]\boldsymbol{p}_t^{RR_i/T} \tag{4.2.8}$$

For the process model derivations an alternate attitude representation was introduced that allow the estimation algorithms to utilize the global quaternion attitude representation. The current representation is sufficient for use in the UKF, but the EKF uses the linearisation assumption of Eq. 4.1.40 and the approximate value for the coordinate transformation matrix in Eq. 4.1.45. As a result the measurement equation must also be written in terms of the vector of error-MRP and the quaternion estimate,

$$\boldsymbol{p}_r^{RR_i/RB_j} = -\boldsymbol{p}_r^{RB_j/R} + \boldsymbol{p}_r^{T/R} + \left(I_{3\times3} + \left[\boldsymbol{\delta\alpha}^{t/r}\times\right]\right)\boldsymbol{T}\left(\hat{\boldsymbol{q}}^{t/r}\right)^T\boldsymbol{p}_t^{RR_i/T} \tag{4.2.9a}$$

$$\boldsymbol{v}_r^{RR_i/RB_j} = \boldsymbol{v}_r^{T/R} + \left(I_{3\times3} + \left[\boldsymbol{\delta\alpha}^{t/r}\times\right]\right)\boldsymbol{T}\left(\hat{\boldsymbol{q}}^{t/r}\right)^T\left[\boldsymbol{\omega}_t^{t/r}\times\right]\boldsymbol{p}_t^{RR_i/T} \tag{4.2.9b}$$

It is important to note that these equations, even though derived for relative GPS, can describe the relative position and velocity of any point on the tanker relative to another point on the receiver. As a result they will be encountered in other measurement model derivations as most other measurements are functions of the relative position between the sensor and the measured point.

The linearised measurement equations for use in the EKF are shown to be,

$$H = \begin{bmatrix} I_{3\times3} & 0_{3\times3} & -\left[\left(\boldsymbol{T}\left(\hat{\boldsymbol{q}}^{t/r}\right)^T\boldsymbol{p}_t^{RR_i/T}\right)\times\right] & 0_{3\times3} \\ 0_{3\times3} & I_{3\times3} & -\left[\left(\boldsymbol{T}\left(\hat{\boldsymbol{q}}^{t/r}\right)^T\left[\boldsymbol{\omega}_t^{t/r}\times\right]\boldsymbol{p}_t^{RR_i/T}\right)\times\right] & -\left[\left(\boldsymbol{T}\left(\hat{\boldsymbol{q}}^{t/r}\right)^T\boldsymbol{p}_t^{RR_i/T}\right)\times\right] \end{bmatrix} \tag{4.2.10}$$

4.2.2 Monocular Vision

Monocular vision utilizes an IR light beacon array, a single optical sensor and a passive light filter to capture the 2D coordinates of known points on the tanker aircraft. Conceptually introduced in Chapter 2 and shown in Figure 4.2 the measurement vector produced by a single monocular sensor as well as its relation to the true value is given by,

$$\boldsymbol{y}_{Mono}^{ij} = \begin{bmatrix} \tilde{\boldsymbol{u}}^{B_i/C_j} \\ \tilde{\boldsymbol{v}}^{B_i/C_j} \end{bmatrix} = \begin{bmatrix} \boldsymbol{u}^{B_i/C_j} \\ \boldsymbol{v}^{B_i/C_j} \end{bmatrix} + \begin{bmatrix} \boldsymbol{v}_u \\ \boldsymbol{v}_v \end{bmatrix} \tag{4.2.11}$$

where C_j and B_i refer to the applicable cameras and beacons within the optical sensor configuration and $[\boldsymbol{v}_u \;\; \boldsymbol{v}_v]^T$ is zero-mean Gaussian noise. The true value of the measured 2D vector can be related to the relative 3D position through the ideal pinhole camera model.

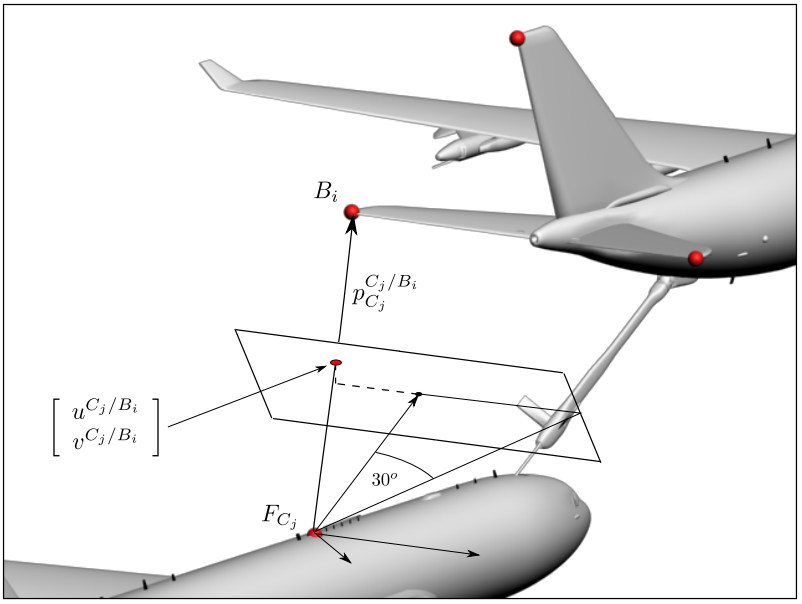

Figure 4.2 – Monocular vision measurement vector and coordinate projection

The pinhole camera model describes the geometric relationship between a 3D coordinate's projection in a 2D plane. The mapping of the 3D point in 2D is referred to as perspective projections with the center of the projection called the optical center. The optical axis extends from the optical center perpendicular to the focal plane and intersects it at the principle point as seen in Figure 4.3.

The equation relating the true projection to the real world coordinates is given by:

$$\begin{bmatrix} \boldsymbol{u}^{B_i/C_j} \\ \boldsymbol{v}^{B_i/C_j} \end{bmatrix} = \frac{f}{x_{C_j}^{B_i/C_j}} \begin{bmatrix} z_{C_j}^{B_i/C_j} \\ y_{C_j}^{B_i/C_j} \end{bmatrix} \tag{4.2.12}$$

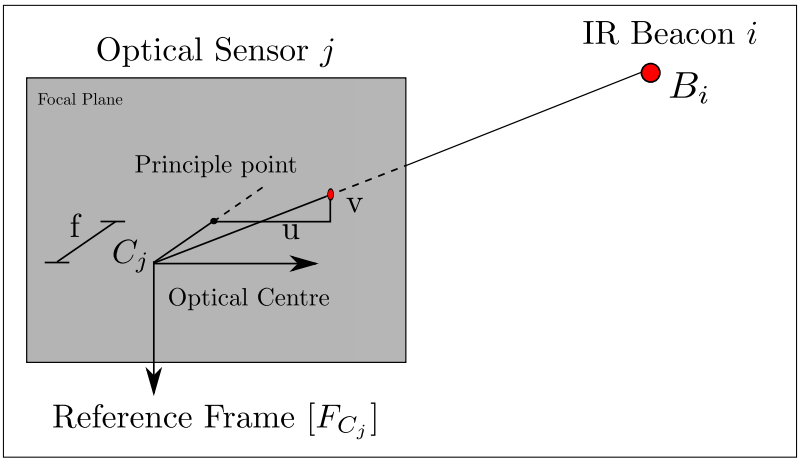

Figure 4.3 – Pinhole Camera Model

The 3D coordinates of the beacon relative to the camera coordinated in the camera reference frame can be obtained from the relative position vector obtained through a similar derivation to that of the RB-DGPS in Eq. 4.2.9a and is shown to be,

$$\boldsymbol{p}_{C_j}^{B_i/C_j} = \boldsymbol{T}\left(\boldsymbol{q}^{C_j/r}\right)\left(-\boldsymbol{p}_r^{C_j/R} + \boldsymbol{p}_r^{T/R} + \boldsymbol{T}\left(\boldsymbol{q}^{t/r}\right)^T \boldsymbol{p}_t^{B_i/T}\right) \tag{4.2.13}$$

$$= \boldsymbol{T}\left(\boldsymbol{q}^{C_j/r}\right)\left(-\boldsymbol{p}_r^{C_j/R} + \boldsymbol{p}_r^{T/R} + \left(I_{3\times 3} + \left[\boldsymbol{\delta\alpha}^{t/r}\times\right]\right)\boldsymbol{T}\left(\hat{\boldsymbol{q}}^{t/r}\right)^T \boldsymbol{p}_t^{B_i/T}\right) \tag{4.2.14}$$

where the matrix $\boldsymbol{T}\left(\boldsymbol{q}^{C_j/r}\right)$ transforms the vectors coordinated in the receiver body reference frame to the camera reference frame. This is an important transformation as it is crucial in directing the optical sensor field of view towards the beacon array. For optimal use the beacon array must be centered in the image frame, where the sensor orientation can be controlled to maintain a centered beacon array, or chosen to have a centered beacon array in the intended stage the measurements are to be used. This fixed orientation method will be adopted, where it assumed that the image sensor has a 30^o horizontal and vertical field of view and is pitched relative to the receiver body axis as seen in Figure 4.2. The exact placement of the beacons, as well as sensor placement and pitch angle is further discussed in the Sensitivity Analysis of Chapter 5.

The current sensor model is however a simplification of what is encountered in practice where the ideal pinhole camera model does not sufficiently represent the relation between the 2D measurements and the relative position vector. The deviation in a specific sensor from the ideal model is rectified through calibrations, where the following aspects are typically considered,

- Barrel distortion: Due to imperfections in the sensor lens straight line aspects in the world frame tend to have a curved projection in the image frame.

- Optical center alignment: Due to an offset in the true optical center the principle point will not be in the center of the image
- Focal distance calibration: The exact focal distance must be experimentally determined where the focal distance in simulation is assumed to be one, and the measurement adjusted accordingly. This will be referred to as the normalized measurement approach.

As the development of the state estimation system at this point is purely conceptual, these practical considerations are very hard to model and can vary greatly depending on the particular hardware chosen. For these reasons the uncertainty introduced by barrel distortion, optical center misalignment and an error in focal distance are not further investigated as it is assumed that the additive Gaussian noise parameters sufficiently encapsulates the uncertainty introduced by errors in calibration.

The final aspect of this form of vision sensing that has not yet been discussed is the problem of marker ambiguity and recognition. For the estimation algorithms to use the measurements it is crucial to know which 2D measurement corresponds to which beacon. A Least Squares Estimate (LSE) algorithm is proposed in [14]. In this algorithm the state estimates are used to generate a set of 2D measurement estimates which correspond to what is expected from the sensors. The measurement which most closely relates the expected measurement is associated with the corresponding beacon.

The linearisation of the monocular vision measurement model for use in the EKF is given by,

$$\mathbf{H}_{Mono} = \begin{bmatrix} \frac{-z}{x^2} & 0 & \frac{1}{x} & 0_{1\times 3} & \frac{-y}{x} & \frac{x^2+z^2}{x^2} & \frac{zy}{x^2} & 0_{1\times 3} \\ \frac{-y}{x^2} & \frac{1}{x} & 0 & 0_{1\times 3} & \frac{z}{x} & \frac{yz}{x^2} & \frac{-x^2-y^2}{x^2} & 0_{1\times 3} \end{bmatrix} \tag{4.2.15}$$

where the coordinates $[x \quad y \quad z]^T$ are the components of $\boldsymbol{p}_{C_j}^{B_i/C_j}$, with the designators omitted for a simplified representation.

4.2.3 Stereoscopic Vision

The derivation of a sensor model for stereoscopic vision is very similar to that of monocular vision as the fundamental concept of obtaining measurement of IR beacons through optical sensors is shared by both. In the case of monocular vision the measurement obtained from the sensors are directly used by the estimation algorithms. In stereoscopic vision however, using the monocular measurement of a single beacon from two sensors along with the known sensor offset allows the relative real world coordinates to be constructed. The added measurement and known position constraint allow for higher accuracy measurement that are ultimately less non-linear than the monocular counterpart.

In the case of a single IR marker in full view of two optical sensors, two sets of monocular measurements are obtained,

$$\boldsymbol{y}^{ij}_{Stereo2D} = \begin{bmatrix} \tilde{u}^{B_i/C_j} \\ \tilde{v}^{B_i/C_j} \end{bmatrix} = \begin{bmatrix} u^{B_i/C_j} \\ v^{B_i/C_j} \end{bmatrix} + \begin{bmatrix} v_u \\ v_v \end{bmatrix} \tag{4.2.16}$$

with $j = 1$ and $j = 2$ designating each optical sensor respectively as seen in Figure 4.4.

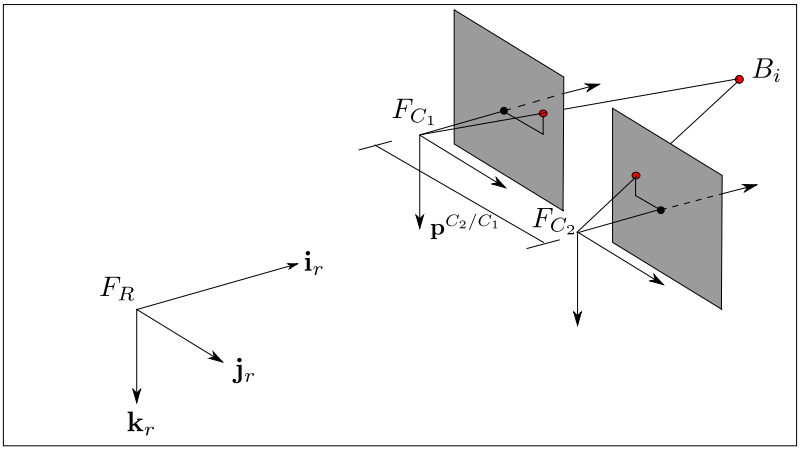

Figure 4.4 – Stereoscopic vision configuration with two measurements of a particular beacon, each obtained via the ideal pinhole camera model

These measurements must be used to construct the 3D position of the beacon relative to a reference point, which in this case is chosen to be the receiver body axis origin. From the ideal pinhole camera model the true value of the measured parameters are related to the relative position state through,

$$\begin{bmatrix} \boldsymbol{u}^{B_i/C_1} \\ \boldsymbol{v}^{B_i/C_1} \end{bmatrix} = \frac{f_{C_1}}{\boldsymbol{X}_r^{B_i/C_1}} \begin{bmatrix} \boldsymbol{Z}_r^{B_i/C_1} \\ \boldsymbol{Y}_r^{B_i/C_1} \end{bmatrix} \quad \text{and} \quad \begin{bmatrix} \boldsymbol{u}^{B_i/C_2} \\ \boldsymbol{v}^{B_i/C_2} \end{bmatrix} = \frac{f_{C_2}}{\boldsymbol{X}_r^{B_i/C_2}} \begin{bmatrix} \boldsymbol{Z}_r^{B_i/C_2} \\ \boldsymbol{Y}_r^{B_i/C_2} \end{bmatrix} \tag{4.2.17}$$

where the relative position vectors are shown to be the same as in monocular vision,

$$\boldsymbol{p}_{C_j}^{B_i/C_j} = \boldsymbol{T}\left(\boldsymbol{q}^{C_j/r}\right)\left(-\boldsymbol{p}_r^{C_j/R} + \boldsymbol{p}_r^{T/R} + \boldsymbol{T}\left(\boldsymbol{q}^{t/r}\right)\boldsymbol{p}_t^{B_i/T}\right) \tag{4.2.18}$$

Using this relation as well as the known relations,

$$\boldsymbol{p}_r^{B_i/C_1} = \boldsymbol{p}_r^{B_i/C_2} + \boldsymbol{p}_r^{C_2/C_1} \tag{4.2.19}$$

$$\boldsymbol{p}_r^{B_i/R} = \boldsymbol{p}_r^{B_i/C_1} + \boldsymbol{p}_r^{C_1/R} \tag{4.2.20}$$

the position of beacon B_i relative to the receiver body axis origin can be given by either,

$$z_r^{B_i/R} = z_r^{B_i/C_1} + z_r^{C_1/R} = \frac{1}{\frac{f^{C_1}}{u^{B_i/C_1}} - \frac{f^{C_1}}{u^{B_i/C_1}}} \left(x_r^{C_1/C_2} - \frac{f^{C_1} z_r^{C_1/C_2}}{u^{B_i/C_1}} \right) + z_r^{C_1/R} \tag{4.2.21}$$

$$y_r^{B_i/R} = y_r^{B_i/C_1} + y_r^{C_1/R} = \frac{1}{\frac{f^{C_1}}{v^{B_i/C_1}} - \frac{f^{C_1}}{v^{B_i/C_1}}} \left(x_r^{C_1/C_2} - \frac{f^{C_1} y_r^{C_1/C_2}}{v^{B_i/C_1}} \right) + y_r^{C_1/R} \tag{4.2.22}$$

$$x_r^{B_i/R} = x_r^{B_i/C_1} + x_r^{C_1/R} = \frac{1}{2} \left(\frac{f^{C_1} z_r^{B_i/C_1}}{u^{B_i/C_1}} + \frac{f^{C_1} y_r^{B_i/C_1}}{v^{B_i/C_1}} \right) + x_r^{C_1/R} \tag{4.2.23}$$

or

$$z_r^{B_i/R} = z_r^{B_i/C_2} + z_r^{C_2/R} = \frac{1}{\frac{f^{C_2}}{u^{B_i/C_2}} - \frac{f^{C_2}}{u^{B_i/C_2}}} \left(x_r^{C_2/C_1} - \frac{f^{C_2} z_r^{C_2/C_1}}{u^{B_i/C_2}} \right) + z_r^{C_2/R} \tag{4.2.24}$$

$$y_r^{B_i/R} = y_r^{B_i/C_2} + y_r^{C_2/R} = \frac{1}{\frac{f^{C_2}}{v^{B_i/C_2}} - \frac{f^{C_2}}{v^{B_i/C_2}}} \left(x_r^{C_2/C_1} - \frac{f^{C_2} y_r^{C_2/C_1}}{v^{B_i/C_2}} \right) + y_r^{C_2/R} \tag{4.2.25}$$

$$x_r^{B_i/R} = x_r^{B_i/C_2} + x_r^{C_2/R} = \frac{1}{2} \left(\frac{f^{C_2} z_r^{B_i/C_2}}{u^{B_i/C_2}} + \frac{f^{C_2} y_r^{B_i/C_2}}{v^{B_i/C_2}} \right) + x_r^{C_2/R} \tag{4.2.26}$$

Using the true sensor values in either of these equation sets will accurately calculate the required 3D coordinates. In practice however, the measured values are corrupted by white noise consistent with the monocular vision measurement model. In addition to the relative position vector of beacon B_i the corresponding measurement covariance is also required. As a result the now familiar Unscented Transform (UT) can be utilised to transform the measured 2D vectors and measurement covariance to an estimate of the 3D coordinate vector and corresponding measurement covariance.

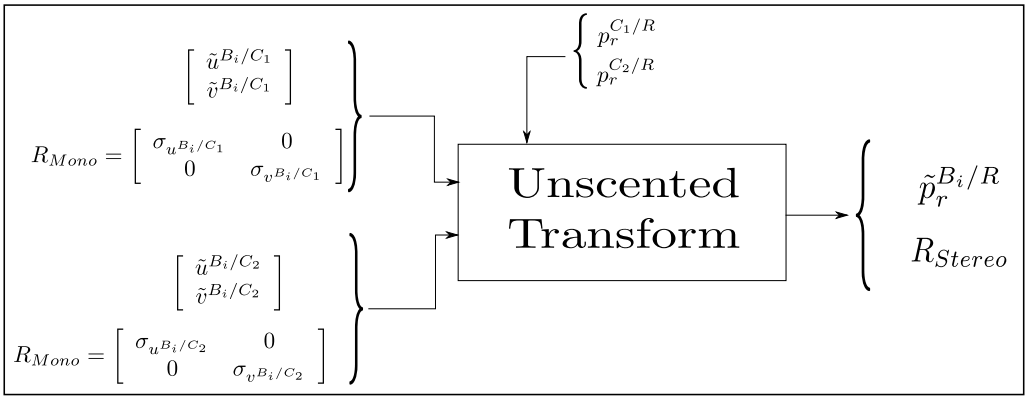

Figure 4.5 – Stereoscopic vision subsystem for converting two 2D measurements and covariances to a 3D coordinate measurement and associated covariance

The details of this derivation are shown in detail in Appendix C.

The new measurement is the position measurement of the beacon B_j relative to the receiver body axis center, which can be related to the true value though the measurement model,

$$\boldsymbol{y}^{ij}_{Stereo3D} = \begin{bmatrix} \tilde{\boldsymbol{p}}_r^{B_i/R} \end{bmatrix} = \begin{bmatrix} \boldsymbol{p}_r^{B_i/R} \end{bmatrix} + \begin{bmatrix} \boldsymbol{v}_p \end{bmatrix} \tag{4.2.27}$$

where the true value of the measured vector can be related to the relative aircraft state through,

$$\begin{aligned} \boldsymbol{p}_r^{B_i/R} &= \boldsymbol{p}_r^{T/R} + \boldsymbol{T}\left(\boldsymbol{q}^{t/r}\right)^T \boldsymbol{p}_t^{B_i/T} && (4.2.28) \\ &= \boldsymbol{p}_r^{T/R} + \left(I_{3\times 3} + \left[\boldsymbol{\delta\alpha}^{t/r}\times\right]\right)\boldsymbol{T}\left(\hat{\boldsymbol{q}}^{t/r}\right)^T \boldsymbol{p}_t^{B_i/T} && (4.2.29) \end{aligned}$$

The noise vector in this case is not the same as the additive white noise term from the RB-DGPS model. The new noise term is dependent on the 2D noise terms of each of the monocular vision models used to construct the 3D value. Thus in addition to the 2D to 3D coordinate transformation, the associated measurement covariance must also be transformed. Luckily an effective method for non-linear covariance transformation in the form of the Unscented Transform has been discussed in Chapter 3.

The linearisation of the stereoscopic vision measurement model is similar to that of the RB-DGPS position measurements resulting in the stereoscopic vision measurement Jacobian,

$$H_{Stereo} = \begin{bmatrix} I_{3\times 3} & 0_{3\times 3} & -\left[\left(\boldsymbol{T}\left(\hat{\boldsymbol{q}}^{t/r}\right)^T \boldsymbol{p}_t^{B_i/T}\right)\times\right] & 0_{3\times 3} \end{bmatrix} \tag{4.2.30}$$

4.2.4 Boom

The final measurement model to be derived is that of the boom parameter measurements. Once the aircraft are connected via the boom in the connect and refuel phases of operation a physical link between the aircraft is created. From Figure 4.6 it can be seen that the three parameters that can be measured are the two universal join angular deflections and the length variation of the boom.

The measurements are related to the true value through the measurement model,

$$\boldsymbol{y}^{ij}_{Boom} = \begin{bmatrix} \tilde{l} \\ \tilde{\sigma} \\ \tilde{\chi} \end{bmatrix} = \begin{bmatrix} l \\ \sigma \\ \chi \end{bmatrix} + \begin{bmatrix} v_l \\ v_\sigma \\ v_\chi \end{bmatrix} \tag{4.2.31}$$

Typically, as with the other sensors, the measurements are related to the state vector through the position vector of the measured point relative to the base of measurement. This case is no different except that the base of measurement is now situated on the tanker at the boom joint, and the measured point is on the receiver at the fuel receptacle. The measurement for

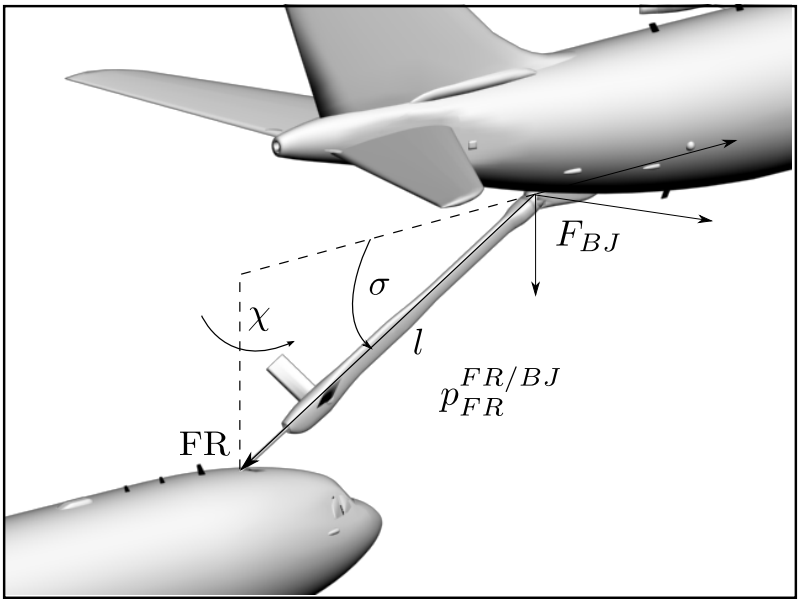

Figure 4.6 – Measured boom parameters and the relative position vector

a deflection in length δl, roll $\delta\chi$ and pitch $\delta\sigma$ are related to the position of the fuel receptacle relative to the boom joint through,

$$l = \|\boldsymbol{p}_t^{FR/BJ}\| \tag{4.2.32}$$

$$\sigma = \sin^{-1}\left(\frac{\sqrt{(z_T^{FR/BJ})^2 + (y_T^{FR/BJ})^2}}{\|\boldsymbol{p}_t^{FR/BJ}\|}\right) \tag{4.2.33}$$

$$\chi = \cos^{-1}\left(\frac{z_T^{FR/BJ}}{\sqrt{(z_T^{FR/BJ})^2 + (y_T^{FR/BJ})^2}}\right) \tag{4.2.34}$$

with nominal boom parameter values $\{l_0, \sigma_0, \chi_0\}$ given in the AAR configuration specifics in Appendix D. The relative position vector can be written in terms of the relative aircraft states,

$$\boldsymbol{p}^{FR/BJ} = \boldsymbol{p}^{T/BJ} + \boldsymbol{p}^{R/T} + \boldsymbol{p}^{FR/R} \tag{4.2.35}$$

Coordinating the vectors in their applicable reference frames yields,

$$\boldsymbol{p}_t^{FR/BJ} = -\boldsymbol{p}_t^{BJ/T} + \boldsymbol{T}\left(\boldsymbol{q}^{r/t}\right)\left(-\boldsymbol{p}_r^{T/R} + \boldsymbol{p}_r^{FR/R}\right) \tag{4.2.36}$$

$$= -\boldsymbol{p}_t^{BJ/T} + \left(I_{3\times 3} - \left[\boldsymbol{\delta\alpha}^{t/r}\right]\right)\boldsymbol{T}\left(\hat{\boldsymbol{q}}^{r/t}\right)\left(-\boldsymbol{p}_r^{T/R} + \boldsymbol{p}_r^{FR/R}\right) \tag{4.2.37}$$

The partial derivative of the measurement equation with respect to the state vector yields the required measurement Jacobian,

$$\boldsymbol{H}_{Boom} = \begin{bmatrix} \frac{1}{2l}\left(2x\frac{\partial x}{\partial \boldsymbol{x}} + 2y\frac{\partial y}{\partial \boldsymbol{x}} + 2z\frac{\partial z}{\partial \boldsymbol{x}}\right) \\ \frac{-1}{l^2\sqrt{1-\frac{z^2+y^2}{l^2}}}\left(\frac{1}{2}l\left(z^2+y^2\right)^{-\frac{1}{2}}\left(2z\frac{\partial z}{\partial \boldsymbol{x}}\right) - \sqrt{z^2+y^2}\frac{\partial l}{\partial \boldsymbol{x}}\right) \\ \frac{-1}{(z^2+y^2)\sqrt{1-\frac{z^2}{z^2+y^2}}}\left(\sqrt{z^2+y^2}\frac{\partial z}{\partial \boldsymbol{x}} - \frac{1}{2}z(z^2+y^2)^{-\frac{1}{2}}(2z\frac{\partial z}{\partial \boldsymbol{x}} + 2y\frac{\partial y}{\partial \boldsymbol{x}})\right) \end{bmatrix} \tag{4.2.38}$$

where the coordinates $[x \;\; y \;\; z]^T$ are the components of $\boldsymbol{p}_t^{FR/BJ}$, with the designators omitted for a simplified representation. The partial derivative of the relative position vector with respect to the state vector is shown to be,

$$\frac{\partial}{\partial \boldsymbol{x}}\left(\boldsymbol{p}_t^{FR/BJ}\right) = \begin{bmatrix} -\boldsymbol{T}\left(\hat{\boldsymbol{q}}^{t/r}\right) & 0_{3\times 3} & \left[\left(\boldsymbol{T}\left(\hat{\boldsymbol{q}}^{r/t}\right)\left(-\boldsymbol{p}_r^{T/R} + \boldsymbol{p}_r^{FR/R}\right)\right)\times\right] & 0_{3\times 3} \end{bmatrix} \tag{4.2.39}$$

4.3 Summary

With the introduction of the sensors in Chapter 2 and the estimation algorithm derivations of Chapter 3 the goal of this chapter was to derive the applicable process and measurement equations to allow AAR state estimation to be implemented in simulation.

The measurement model coupled with the use of IMUs as driving inputs to the process equations are derived. Special consideration is given to the addition of the bias terms to the state vector as well as the effect of an offset in IMU position from the aircraft CG. Some simplifications are suggested based on the AAR scenario, where it assumed that the sensor biases and offset compensation are performed by an estimators local to each aircraft.

The process model equations for the states are derived, where an alternate attitude representation to the standard quaternion is introduced. The use of error Modified Rodrigues Parameters allows for seamless interaction between constrained and unconstrained attitude representations which in turn allows for the correct implementation of the estimation algorithms.

The measurement models for each of the remaining sensors are shown, where the measurement vector are related to the standard, and newly defined state vector. In addition to the equations the aspects that require consideration when implementing the sensors are also discussed. This will be the focus of Chapter 5.

With all the applicable equations derived it is necessary to evaluate the parameters that have an effect on the accuracy and *optimal* nature of the state estimate by performing a sensitivity analysis.

Chapter 5

Sensitivity Analysis

At this point all the aspects necessary for the implementation of an AAR estimation system in simulation have been evaluated, which includes the derivation of the EKF and UKF algorithms as well as the process and measurement models applicable for use in AAR.

With the non-linear nature of the estimation problem the estimation algorithms offer solutions to the estimation problem by making assumptions on the nature of the non-linear functions and applying their respective sub-optimal estimation strategies. There are however other factors that can affect the *optimal* nature of the state estimate. The goal of the sensitivity analysis is to identify these parameters and evaluate what effect a change will have on the accuracy with which the states can be estimated. Note that the state error covariance is used to evaluate the accuracy of the state estimate, with an increase in the error covariance indicating an increase in the uncertainty associated with state estimate.

First it is necessary to identify the parameters that affect the magnitude of the error covariance. This is done by evaluating the equations in the estimation algorithms that alter the error covariance value in the prediction and correction steps respectively. Once this has been done focus can be shifted to how the magnitude of these parameters affect the the propagation and correction of the error covariance and how they can be changed to improve on the results.

All evaluations are made qualitatively after which the analysis is substantiated through simple simulation. This simulation configuration is similar to that of the AAR scenario, but simplified in order to illustrate the various points that are discussed in the respective sections. The details of the simulation scenario can be found in Appendix D.

5.1 Error Covariance Analysis

The goal of the sensitivity analysis is to investigate parameters that effect a change in error covariance. The equations that facilitate these changes are presented in the propagation and correction steps of both the EKF and UKF where each algorithm has a unique approach but

performing the sensitivity analysis with either will yield the same conclusions. As a result the EKF structure is chosen for the analysis as the linearised equations can provide some insight into the coupling between state, state kinematics and measurements.

From Chapter 3 the propagation and correction steps are shown to be,

	EKF
Propagation	$P_k^- = F_k(\cdot)P_{k-1}^+ + P_{k-1}^+ F_k(\cdot)^T + Q_k$ $F_k(\cdot) \approx \exp(F(\cdot)\Delta t), \;\; Q_k = L(\cdot)Q_c L(\cdot)^T \Delta t$ $F(\cdot) \equiv \frac{\partial f}{\partial x}\Big\vert_{\hat{\boldsymbol{x}}(t),\boldsymbol{u}(t)}$ $L(\cdot) \equiv \frac{\partial f}{\partial w}\Big\vert_{\hat{\boldsymbol{x}}(t),\boldsymbol{uu}(t)}$
Correction	$P_k^+ = P_k^- - P_k^- H(\hat{x}_k^-)\left[H(\hat{x}_k^-)P_k^- H(\hat{x}_k^-) + M(\hat{x}_k^-)R_k M(\hat{x}_k^-)^T\right]^{-1} H(x_k^-)P_k^-$ $H(\hat{x}_k^-) \equiv \frac{\partial h}{\partial x}\Big\vert_{\hat{\boldsymbol{x}}_k^-}$ $M(\hat{x}_k^-) \equiv \frac{\partial h}{\partial v}\Big\vert_{\hat{\boldsymbol{x}}_k^-}$

Table 5.1 – Propagation and correction steps of the Extended Kalman Filter

From these equations it is clear that there are particular matrices that influence the magnitude of change in error covariance in each of these steps. These are known to be,

- Propagation:
  - Q_c : The continuous time process covariance matrix, which provides a measure of the noise associated with each of the driving inputs to the state kinematic equations. This matrix in combination with the process noise Jacobian $L(\cdot)$ which provides a measure of the uncertainty in the propagation of each state as a function of the input noise.
  - $L(\cdot)$: The process noise Jacobian obtained through the partial derivative of the state kinematic equations with respect to the noise vector and evaluating them at the current state estimate. This matrix provides the coupling between the state kinematics and the input noise.
  - $F(\cdot)$: The process Jacobian is obtained through the partial derivative of the state kinematics with respect to the state vector evaluated at the current state estimate. It is used in the propagation of the state error covariance as it provides a linearised relationship between each state and the kinematic equations.
- Correction:
  - R_k : The measurement covariance matrix contains the measurement noise covariance associated with each sensor.

- $M(\cdot)$: In cases where the measurement noise associates with a sensor is dependant on the state vector this matrix provides coupling between the noise and the measurement vector. Typically this matrix is unity as most measurement noise is additive.
- $H(\cdot)$: The measurement Jacobian is obtained by taking the derivative of the measurement equation with respect the the state vector. This linearized relationship is intricate in the evaluation of the gain used to update the states based on an error in the estimates measurement.

Each of these matrices are either functions of user defined parameters such as the sensor noise and sensor positioning, or functions of controllable parameters such as the state vector. By evaluating the role of these parameters within the respective matrices and evaluating the effect of the matrices in the covariance propagation and correction steps it is possible to map the change in parameters to a change in state estimate accuracy.

5.2 Error Covariance Propagation

At any particular time an estimate of the true state vector is available accompanied by a degree of uncertainty represented in the current error covariance. Through propagation the future state is estimated using the kinematic equations where the uncertainty associated with the state is also propagated. By propagating the states, and the associated covariances, using the current states and driving inputs each with their own inherent uncertainty serves to increase the state error covariance. As a result the error covariance will increase during state propagation, with the rate of increase being a function of the uncertainty associated with the propagation input parameters.

From the discrete propagation step in Table 5.1 it is clear that the propagated *a priori* error covariance P_{k-1}^{-} is obtained by scaling the current *a postiori* error covariance P_{k-1}^{+} by the discrete process Jacobian F_k and adding the discrete process covariance Q_k which is obtained through the discretization of $L(\cdot)Q_cL(\cdot)^T$ where Q_c is the the process spectral density matrix and $L(\cdot)$ the process noise Jacobian. Form Chapter 4 these parameters are given by,

$$F(\cdot) = \begin{bmatrix} 0_{3\times3} & I_{3\times3} & 0_{3\times3} & 0_{3\times3} \\ -\left[\tilde{\boldsymbol{\omega}}_r^{r/i}\times\right]\left[\tilde{\boldsymbol{\omega}}_r^{r/i}\times\right] & -2\left[\tilde{\boldsymbol{\omega}}_r^{r/i}\times\right] & \left[\boldsymbol{T}\left(\hat{\boldsymbol{q}}^{t/r}\right)^{-1}\tilde{\boldsymbol{a}}_t^{t/i}\times\right] & 0_{3\times3} \\ 0_{3\times3} & 0_{3\times3} & \left[\tilde{\boldsymbol{\omega}}_t^{t/i}\times\right] & 0_{3\times3} \\ 0_{3\times3} & 0_{3\times3} & 0_{3\times3} & 0_{3\times3} \end{bmatrix} \tag{5.2.1}$$

$$L(\cdot) = \begin{bmatrix} 0_{3\times3} & 0_{3\times3} & 0_{3\times3} & 0_{3\times3} & 0_{3\times3} & 0_{3\times3} \\ -\boldsymbol{T}\left(\hat{\boldsymbol{q}}^{t/r}\right)^{-1} & I_{3\times3} & 0_{3\times3} & -2\left[\boldsymbol{v}_r^{T/R}\times\right] & -\left[\boldsymbol{p}_r^{T/R}\times\right] & 0_{3\times3} \\ 0_{3\times3} & 0_{3\times3} & -I_{3\times3} & \boldsymbol{T}\left(\hat{\boldsymbol{q}}^{t/r}\right) & 0_{3\times3} & 0_{3\times3} \\ 0_{3\times3} & 0_{3\times3} & 0_{3\times3} & 0_{3\times3} & 0_{3\times3} & -I_{3\times3} \end{bmatrix} \tag{5.2.2}$$

$$Q_c = \text{diag}\left(\sigma_{\boldsymbol{a}_t^{T/I}} \quad \sigma_{\boldsymbol{a}_r^{R/I}} \quad \sigma_{\boldsymbol{\omega}_t^{t/i}} \quad \sigma_{\boldsymbol{\omega}_r^{r/i}} \quad \sigma_{\dot{\boldsymbol{\omega}}_r^{r/i}} \quad \sigma_{\dot{\boldsymbol{\omega}}_t^{t/r}}\right) \tag{5.2.3}$$

The propagation of each of the state error covariances are evaluated as follows,

- Relative position: The relative position time derivative is equal to the relative velocity and independent of all other states or driving input noise parameters. As such the position error covariance is propagated based on the velocity state error covariance. As the relation between the state suggest, the resultant position error covariance will be the integral of the velocity error covariance.
- Relative Velocity: The relative velocity kinematic equation is a function of three of the four driving inputs as well as three of the four states. As such the error covariance propagation is highly dependent on the noise associated with the driving inputs as well as the growing state error covariance. A change in the magnitude of each of the applicable states as well as the driving inputs is discussed. Evaluating the partial derivatives of the velocity kinematic equation with respect to the state and noise vectors yields the following conclusions in relation to the propagation of the velocity error covariance.
  - $\frac{\partial}{\partial \boldsymbol{p}_r^{T/R}}(\cdot)$: An increase in the true receiver angular rate or associated noise will serve to increase the contribution of the position error covariance to the growth in velocity error covariance.
  - $\frac{\partial}{\partial \boldsymbol{v}_r^{T/R}}(\cdot)$: An increase in the true receiver angular rate or associated noise will serve to increase the contribution of the velocity error covariance to its own propagation.
  - $\frac{\partial}{\partial \boldsymbol{\delta\alpha}^{t/r}}(\cdot)$: An increase in the true tanker acceleration of associated noise serve to increase the contribution of the attitude error covariance to the relative velocity error covariance propagation.
  - $\frac{\partial}{\partial \eta_{\boldsymbol{a}_t^{T/I}}}(\cdot)\&\frac{\partial}{\partial \eta_{\boldsymbol{a}_r^{R/I}}}(\cdot)$: The tanker acceleration noise is coupled via the the coordinate transformation matrix which is typically very close to a unity matrix. An increase in these noise parameters directly and significantly affect the rate of velocity covariance propagation.
  - $\frac{\partial}{\partial \eta_{\boldsymbol{\omega}_r^{r/i}}}(\cdot)$: The contribution of this term directly affects the velocity covariance propagation which can be minimized by reducing the measurement noise and relative velocity.

  - $\frac{\partial}{\partial \eta_{\boldsymbol{\omega}_r^{r/i}}}(\cdot)$: The receiver angular acceleration is typically not measured and as such the value of the associated noise is not known and must be approximated. Reducing the relative position between the aircraft limits the contribution of this parameter to the velocity covariance propagation

- Error attitude : The error attitude error covariance propagation is a function of both the measured tanker and receiver relative angular velocities and associated noise. Evaluating the partial derivatives of the error attitude kinematic equation with respect to the state and noise vectors yields the following conclusions in relation to the propagation of the attitude error covariance.

  - $\frac{\partial}{\partial \eta_{\boldsymbol{\omega}_t^{t/i}}}(\cdot)\&\frac{\partial}{\partial \eta_{\boldsymbol{\omega}_r^{r/i}}}(\cdot)$: An increase in the noise associated with the the tanker and receiver angular rate measurements serves to increase the rate of attitude error covariance propagation. The same can be said for a decrease in respective noise terms resulting in diminished rate of error attitude covariance propagation.

- Relative angular velocity: Form the considerations of Chapter 4 the relative angular velocity estimate is obtained using the driving inputs. As a result the state error covariance is a function of the noise covariances of both the tanker and receiver angular rate measurement. An increase in the measurement noise values or increase in the attitude error covariance will increase the relative angular velocity error covariance.

The propagation of the relative velocity error covariance is shown in Figure 5.1 where each of the six relevant parameters have been varied from a nominal configuration to illustrate their respective affect on the rate of error covariance propagation.

- Nominal : The covariance propagation of the relative velocity error covariance. The states, driving inputs and associated noise values as indicated in Appendix D.

- Case a & b: The tanker and receiver body acceleration measurement noises are increased to ten times their nominal values respectively, $10 \times \eta_{\boldsymbol{a}_t^{T/I}}$ and $10 \times \eta_{\boldsymbol{a}_t^{T/I}}$. The effect of the increase in noise in each parameters has roughly the same effect on the increase in the rate of covariance growth. One would expect the tanker noise to have a larger effect due to its presence in the process Jacobian, but due to the fairly small covariance and input measurement noise the covariance scaling $F(\cdot)P_{k-1}^{+}F(\cdot)^T$ has a far smaller effect than the addition of noise through $L(\cdot)Q_cL(\cdot)^T$.

- Case c : The receiver angular velocity measurement noise is increased to ten times it nominal value $10 \times \eta_{\boldsymbol{\omega}_r^{r/i}}$. It is clear that an increase in this noise parameter does not have a noticeable impact on the increase in velocity covariance propagation. This is to be expected since this value couples into the scaling of P_{k-1}^{+} which in this case is

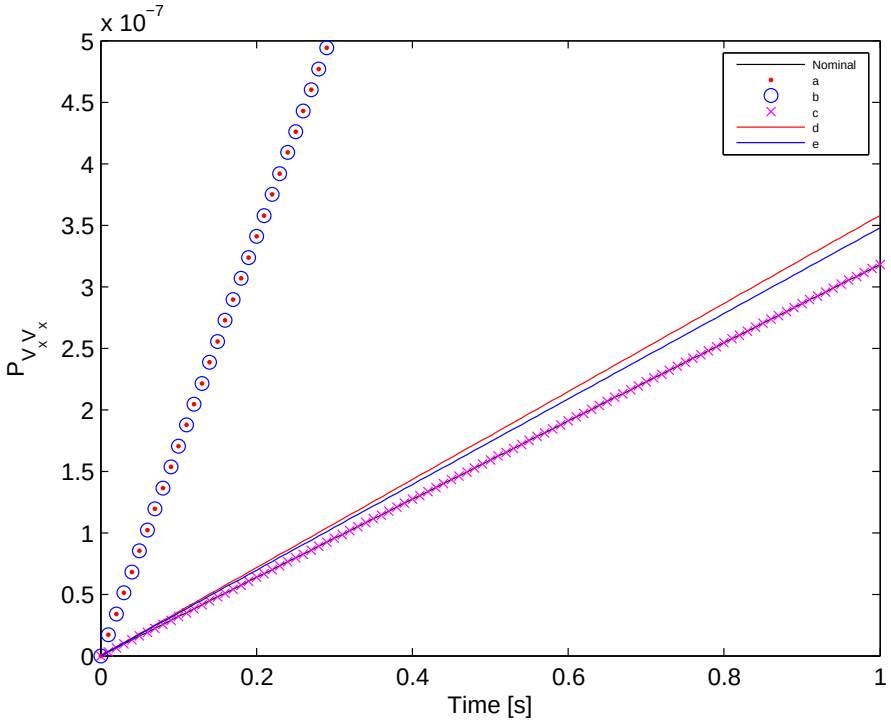

Figure 5.1 – Velocity error covariance propagation

relatively small. As the process covariance increases so will the effect of the receiver angular rate measurement noise.

- Case d : Changing the relative position vector changes the influence of the uncertainty associated with the receiver angular velocity. In this case the relative position is changed from $\boldsymbol{p}_r^{T/R} = [50 \quad 0 \quad -10]^T$ to $\boldsymbol{p}_r^{T/R} = [60 \quad 10 \quad -10]^T$ which will increase the rate of covariance propagation in all three velocity states.

- Case e : The magnitude of the relative velocity is changed from the nominal $\boldsymbol{v}_r^{T/R} = [0 \quad 0 \quad 0]^T$ to $\boldsymbol{p}_r^{T/R} = [1 \quad 1 \quad 1]^T$ which increases the contribution of the receiver angular velocity noise to the propagation. For a fairly large relative velocity this effect is shown to be small in comparison to the other effects.

From this it is clear that the magnitude of the tanker and receiver accelerations and associated noise terms effect the largest change in the propagation rate of the velocity error covariance. As such, minimising the accelerometer noise as well as limiting the true accelerations will serve to improve the accuracy with which the velocity and position states can be estimated. Note that only the the error covariance of V_x is shown as the analysis indicates a similar response in the other states.

Additionally the propagation of the attitude error covariance, or relative roll angle, is shown in Figure 5.2. Each of the variations show a change in the propagation of the relative velocity error covariance due to a change in one of the applicable parameters.

- Nominal : The covariance propagation of the relative velocity error covariance. The states, driving inputs and associated noise values as indicated in Appendix D.
- Case f & g : The tanker and receiver angular velocity measurement noises are increased to twice their nominal values respectively, $2 \times \eta_{\omega_t^{t/i}}$ and $2 \times \eta_{\omega_t^{t/i}}$. The effect of the increase in noise in each parameters has roughly the same effect on the increase in the rate of covariance growth. One would expect the tanker noise to have a larger effect due to its presence in the process Jacobian, but due to the fairly small covariance and input measurement noise the covariance scaling $F_k(\cdot)P_{k-1}^{+}F_k(\cdot)^T$ has a far smaller effect than the addition of noise through $L(\cdot)Q_cL(\cdot)^T\Delta t$.

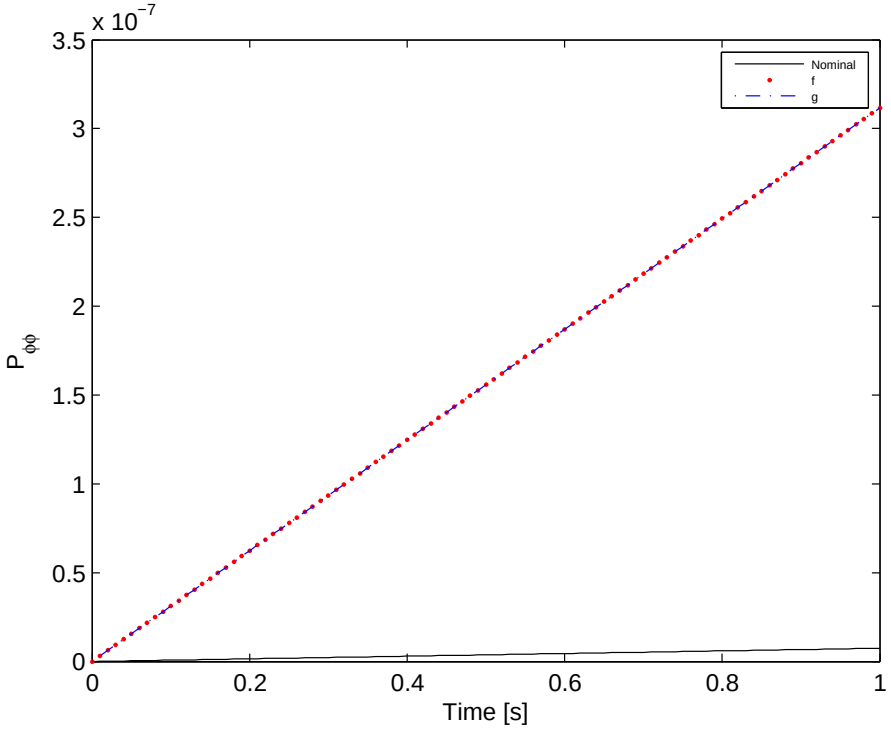

Figure 5.2 – Attitude error covariance propagation

From this it is clear that the attitude error covariance propagation is severely dependent on the aircraft angular rate measurement and associated noise covariances. Reducing the noise will serve to improve the overall accuracy if the attitude estimates.

The next step is to evaluate the parameters that correct the error when sensor measurements become available. This, along with the propagation considerations, will allow sensors to be chosen and placed in such a way as to *optimize* the accuracy of the state estimates.

5.3 Error Covariance Correction

Periodically sensor measurements enter the estimation algorithms in which case the states and corresponding error covariances are corrected based on the accuracy of the measurements and the relevance of the states to the measurements. Adding measurements to the estimation process serves to provide more information on the true value of the state vector and as such will improve the state estimate and the corresponding state error covariance.

Extremely inaccurate measurements with a large amount of noise will have a large covariance matrix R_k and will have little effect on the change in state and error covariance. Extremely accurate measurements, on the other hand, provide a good measure of the true state value and will reduce the error covariance by improving the confidence in the value of the state estimate with respect to the true states. In theory, a system with infinitely accurate and continuous measurements can exactly estimate the true states and, as a result, does not require a propagation step.

This effect can be substantiated through an evaluation of the EKF error covariance update step, where the subtracting term converges to zero as the magnitude of R_k increases, which leaves the propagated error covariance unchanged. By gradually reducing the magnitude of R_k to zero, the subtracting term reduces to P_k^-, resulting in a corrected error covariance of zero.

The magnitude of the measurement Jacobian H_k affects the relative contribution of the measurement covariance R_k to the covariance correction equation. As the magnitude of H_k increases, the relative effect of R_k in diminishes, which makes the state estimates less sensitive to noise, but also less sensitive to a change in the measurements as the gain is decreased. Similarly, a decrease in the magnitude of H_k will increase the relative effect of R_k effectively increasing the sensitivity of the state estimate to changes in measurements through a larger gain, making them more susceptible to the accompanying sensor noise. As a result it is required that the measurement Jacobian H_k be as large as possible resulting in a state vector insensitive to sensor noise which is ideal for AAR applications.

Evaluating the linearised measurement matrix H_k requires the partial derivative of the non-linear measurement equations to be taken with respect to the state vector, $\frac{\partial h}{\partial x}$. This evaluation will be conducted separately for each of the sensors.

5.3.1 Roaming Base DGPS

The measurement equations and resulting Jacobian can be evaluated as follows,

$$\begin{bmatrix} \boldsymbol{p}_r^{RR_i/RB_j} \\ \boldsymbol{v}_r^{RR_i/RB_j} \end{bmatrix} = \begin{bmatrix} -\boldsymbol{p}_r^{RR_i/R} + \boldsymbol{p}_r^{T/R} + \left(I_{3\times 3} + \left[\delta\boldsymbol{\alpha}^{t/r}\times\right]\right)\boldsymbol{T}\left(\hat{\boldsymbol{q}}^{t/r}\right)^T \boldsymbol{p}_t^{RB_j/T} \\ \boldsymbol{v}_r^{T/R} + \left(I_{3\times 3} + \left[\delta\boldsymbol{\alpha}^{t/r}\times\right]\right)\boldsymbol{T}\left(\hat{\boldsymbol{q}}^{t/r}\right)^T \left[\boldsymbol{\omega}_t^{t/r}\times\right]\boldsymbol{p}_t^{RB_j/T} \end{bmatrix} \tag{5.3.1}$$

$$H_{RB-GPS} = \begin{bmatrix} I_{3\times3} & 0_{3\times3} & -\left[\left(\boldsymbol{T}\left(\hat{\boldsymbol{q}}^{t/r}\right)^{T}\boldsymbol{p}_t^{RR_i/T}\right)\times\right] & 0_{3\times3} \\ 0_{3\times3} & I_{3\times3} & -\left[\left(\boldsymbol{T}\left(\hat{\boldsymbol{q}}^{t/r}\right)^{T}\left[\hat{\boldsymbol{\omega}}_t^{t/r}\times\right]\boldsymbol{p}_t^{RR_i/T}\right)\times\right] & -\boldsymbol{T}\left(\hat{\boldsymbol{q}}^{t/r}\right)^{T}\left[\boldsymbol{p}_t^{RR_i/T}\times\right] \end{bmatrix} \tag{5.3.2}$$

Evaluating the partial derivatives of the position measurement with respect to each state results in the following analysis,

- $\frac{\partial}{\partial \boldsymbol{p}_r^{T/R}}(\cdot)$: The relative position measurement is directly related to a change in relative aircraft position.
- $\frac{\partial}{\partial \boldsymbol{\delta\alpha}^{t/r}}(\cdot)$: The relative position measurement is related to the error attitude state through the position vector of the roaming receiver relative to the tanker CG coordinated in the receiver reference frame. The further the marker position from the tanker CG, the larger the applicable derivative will become. From the argument on the relative magnitude of H_k and R_k it can be seen seen that an increase in the magnitude of the components of the measurement matrix will effectively reduce the significance of the measurement noise. Thus, for a constant amount of noise, a marker further away from the tanker CM would produce a larger H_k, resulting in a larger covariance reducing term. Intuitively this makes sense as the noisy position measurement of a point close to the tanker CG would cause more uncertainty in the relative attitude as the same measurement of a point on the aircraft extremes. This effect leads to the conclusion that sensor markers on the tanker should ideally be placed on the wing tips as well as elevator and rudder tips, to improve on the estimates of the error-MRP and its associated covariance. Note that in Chapter 3 where the use of the error-MRP is introduced it is stated that the components of the $\boldsymbol{\delta\alpha}^{t/r}$ are physically intuitive to small Euler angles ϕ, θ and ψ corresponding to roll, pitch and yaw and as such an improvement in the associated error covariance is directly related to to an improvement of the Euler angles error covariance.

To illustrate the effect of a varied marker position, the simulation scenario in Appendix D is shown in Figure 5.3 where three roaming receivers are initially placed close to the tanker CG and systematically moved further from the tanker CG to the aircraft extremities.

The effects of the change in roaming GPS receiver position can be seen in Figure 5.4 where the change in average error covariance of each state is given as a percentage of the error covariance associated with the initial sensor configuration. Additionally two extra curves represent the results of the same simulation performed with half and double the nominal measurement noise. From this the following conclusions can be drawn,

- According to the derivative analysis the error covariance associated with the X and Y states should stay constant as the roaming receiver is moved but from simulation it

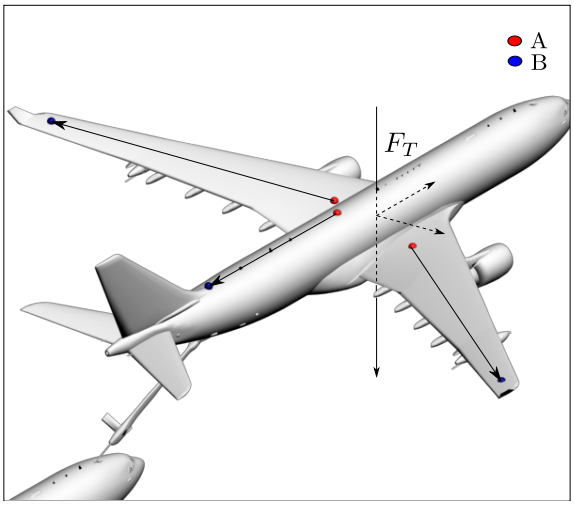

Figure 5.3 – Variation in the roaming GPS receiver position on the tanker fuselage from configuration positions A to B

can be seen that there is a slight improvement estimated accuracy which is a result of the large increase in attitude accuracy. The error covariance in the relative Z position increases with GPS receiver distance however, due to the increased induced uncertainty in the Z position of the GPS receiver resulting from attitude uncertainty.

- All of the attitude state improve as a result of the GPS receiver position position change. The yaw and roll states improve more than the pitch state due to the particular configuration, where only the marker moving towards the aircraft tail has significant relevance to the relative pitch.

Showing the effects of a change in the measurement noise on the error covariance provides an indication of the relative effect of noise versus sensor positioning. As a result it can be seen that by positioning the GPS receiver 10m from the CG is equivalent to using a sensor with double the accuracy placed 1m from the CG in estimating the attitude.

Evaluating the partial derivatives of the velocity measurement with respect to each state results in the following analysis.

- $\frac{\partial}{\partial \boldsymbol{v}_r^{T/R}}(\cdot)$: The relative velocity measurement is directly coupled to a change in relative aircraft velocity.
- $\frac{\partial}{\partial \boldsymbol{\delta\alpha}^{t/r}}(\cdot)$: The relative velocity measurement coupling to the error attitude is again dependent on the marker location coordinated in the receiver reference frame with an addition factor in the form of the measured relative angular rate. This angular rate term is significant in the contribution of the term where a large angular rate serves to improve the attitude estimates through the velocity measurements. This relative angular rate is typically very small rendering the velocity measurements insignificant in attitude estimation.

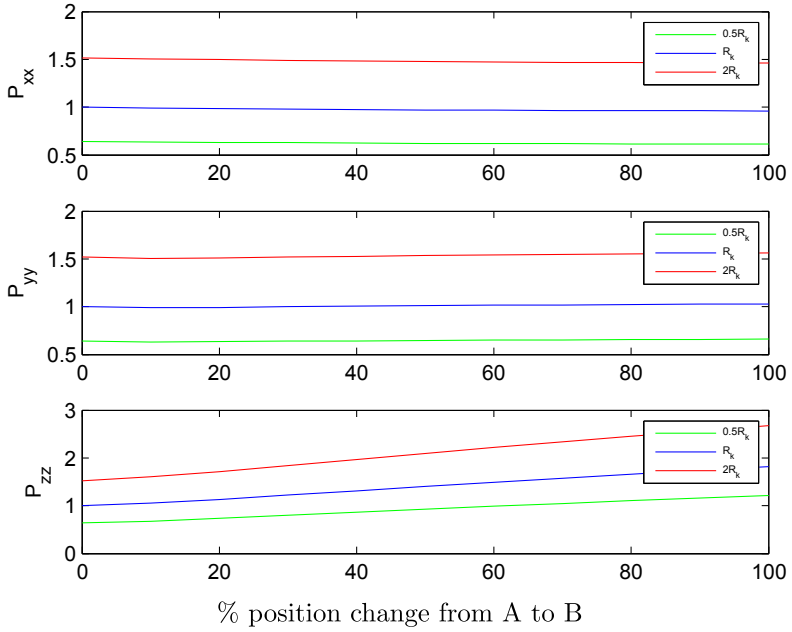

(a) Position error covariance fractional change

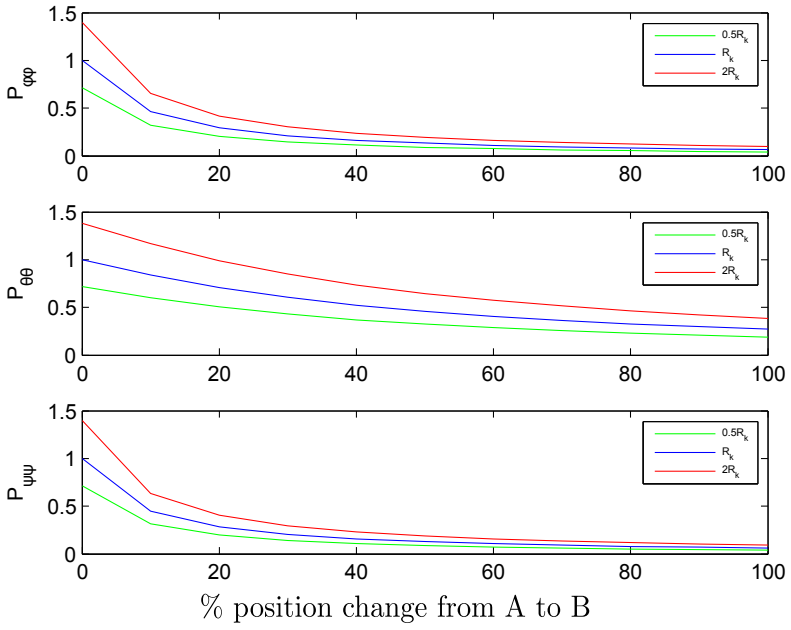

(b) Attitude error covariance fractional change

Figure 5.4 – The change in error covariance as a function of the % distance moved from configuration A to B as a fraction of the nominal error covariance at configuration A [Non Dimentional]

- $\frac{\partial}{\partial \boldsymbol{\omega}_t^{t/r}}(\cdot)$: A change in relative velocity measurement couples to a change in the relative angular velocity in much the same way as position measurements to the error attitude. An increase in the distance of the roaming receiver relative to the tanker CG, $\boldsymbol{p}_t^{RR_i/T}$, increases the magnitude of the derivative which in turn makes the relative angular rate estimate less sensitive to noise, reducing the associated error covariance.

The same simulation is performed, this time with focus on the relative velocity and angular

velocity states yielding very similar results. From the derivative analysis it is shown that the relative linear and angular velocities are related to the velocity measurements in a similar way as the position and attitude states are related to the position measurements. This is confirmed in simulation and shown in Figure 5.5 where the error covariance in relative linear and angular velocities show similar improvement in accuracy as a function of the GPS receiver position.

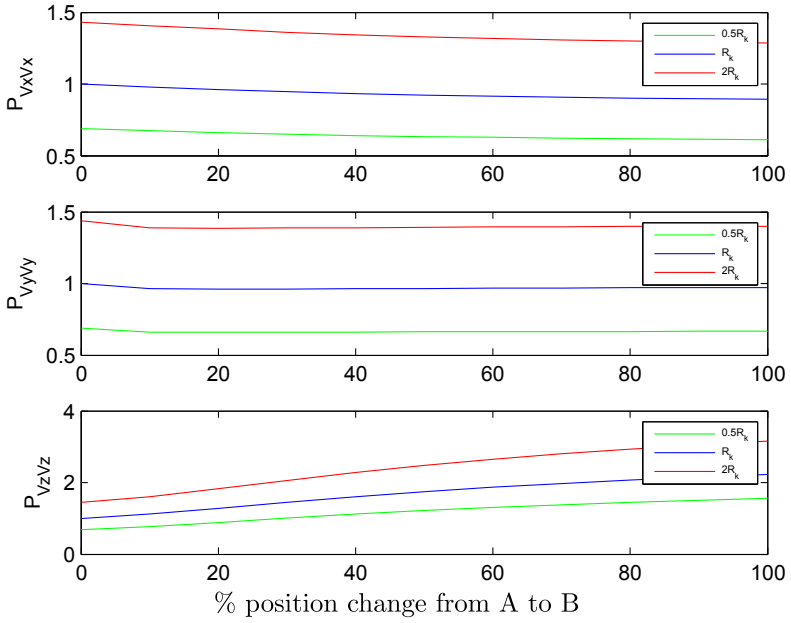

(a) Velocity error covariance fractional change

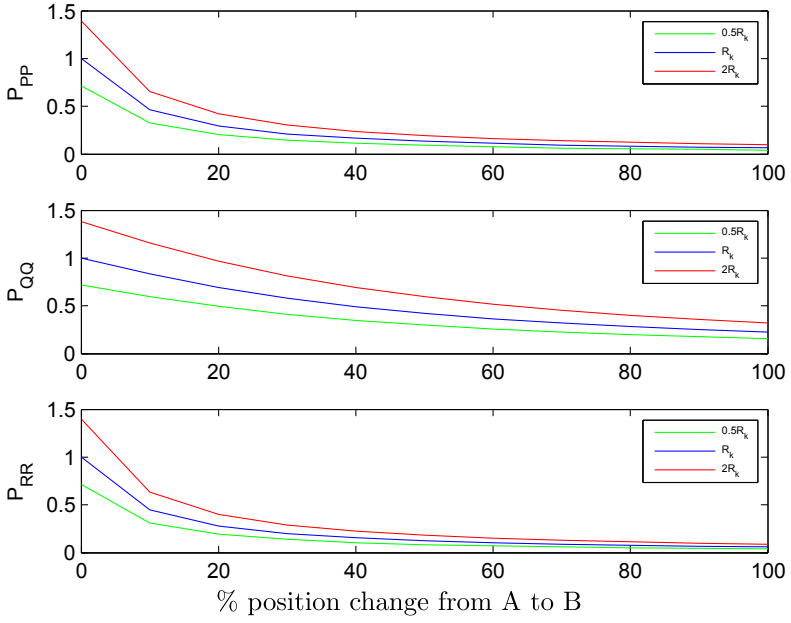

(b) Angular velocity error covariance fractional change

Figure 5.5 – The change in error covariance as a function of the % distance moved from configuration A to B as a fraction of the nominal error covariance at configuration A [Non Dimentional]

5.3.2 Optical - Monocular

The measurement equations and resultant Jacobian can be evaluated as follows,

$$\begin{bmatrix} \boldsymbol{u}^{B_i/C_j} \\ \boldsymbol{v}^{B_i/C_j} \end{bmatrix} = \frac{f}{\boldsymbol{X}_{C_j}^{B_i/C_j}} \begin{bmatrix} \boldsymbol{Z}_{C_j}^{B_i/C_j} \\ \boldsymbol{Y}_{C_j}^{B_i/C_j} \end{bmatrix} \tag{5.3.3}$$

where

$$\begin{aligned} \boldsymbol{p}_{C_j}^{B_i/C_j} &= \boldsymbol{T}\left(\boldsymbol{q}^{C_j/r}\right)\left(-\boldsymbol{p}_r^{C_j/R} + \boldsymbol{p}_r^{T/R} + \boldsymbol{T}\left(\boldsymbol{q}^{t/r}\right)\boldsymbol{p}_t^{B_i/T}\right) && (5.3.4) \\ &= \boldsymbol{T}\left(\boldsymbol{q}^{C_j/r}\right)\left(-\boldsymbol{p}_r^{C_j/R} + \boldsymbol{p}_r^{T/R} + \left(I_{3\times 3} - \left[\boldsymbol{\delta\alpha}^{t/r}\times\right]\right)\boldsymbol{T}\left(\hat{\boldsymbol{q}}^{t/r}\right)\boldsymbol{p}_t^{B_i/T}\right) && (5.3.5) \end{aligned}$$

and

$$H_k^{Mono} = \begin{bmatrix} \frac{-Z}{X^2} & 0 & \frac{1}{X} & 0_{1\times 3} & \frac{-Y}{X} & \frac{X^2+Z^2}{X^2} & \frac{ZY}{X^2} & 0_{1\times 3} \\ \frac{-Y}{X^2} & \frac{1}{X} & 0 & 0_{1\times 3} & \frac{Z}{X} & \frac{YZ}{X^2} & \frac{-X^2-Y^2}{X^2} & 0_{1\times 3} \end{bmatrix} \tag{5.3.6}$$

The measurements themselves are functions of the relative position vector between an IR beacon on the tanker and the optical sensor on the receiver aircraft. As such the measurement Jacobian is also a function of the relative position vector.

Evaluating the partial derivatives of the velocity measurement with respect to each state results in the following analysis.

- $\frac{\partial}{\partial \boldsymbol{p}_r^{t/r}}(\cdot)$ - From H_k^{Mono} it is clear that the magnitude of the components are dependent on the relative position vector between the IR marker on the tanker and the optical sensor on the receiver, which is comprised of the components of the relative beacon to camera position vector, which is a function of camera position, beacon position, relative attitude and relative aircraft position. It can be seen that the vertical pixel measurement u is independent of $y_{C_j}^{B_i/C_j}$, and that the horizontal pixel measurement v is independent of $z_{C_j}^{B_i/C_j}$, which is to be expected. Considering the partial derivative of each vector component separately,
  - $\frac{\partial}{\partial x_r^{T/R}}(\cdot)$: The magnitude of the derivatives are dependent directly on the relative beacon-camera Y and Z values, respectively, and importantly inversely related to the square of the relative X distance. This implies that, similar to the GPS measurement analysis, a large Y and Z offset of the beacon relative to the camera will cause a larger derivative, resulting in better estimation of the relative aircraft position given constant noise. Secondly, with an increase in the X distance between sensors and beacons, comes an exponential decrease in the derivative magnitude, resulting in a increased sensitivity to sensor noise.

  - $\frac{\partial}{\partial y_r^{T/R}}(\cdot)\&\frac{\partial}{\partial z_r^{T/R}}(\cdot)$: The magnitude of the derivatives are inversely related to the relative sensor beacon X distance and as a result an increase in the distance of the beacon relative to camera will decrease the coupling between the measurements and the states.

  As a result the design consideration is to have the beacon as close to the sensor as possible, and have the beacon placed as far to the aircraft periphery as possible whilst maintaining the beacon in the camera field of view.

- $\frac{\partial}{\partial \boldsymbol{\delta\alpha}^{t/r}}(\cdot)$ - The measurement derivatives in terms of the error MRP vectors are more complex than that of the previous analysis but the same deductions can be made. From the derivatives it is clear that an increase in the Y and Z coordinates of the beacon relative to the camera yields larger derivatives which serves to improve the attitude estimates. An increase in X distance however, decreases the the derivative magnitude diminishing the coupling between the measurements and the error attitude.

Similar to the analysis of the RB-DGPS the IR beacons can also be moved from position close to the tanker CG to those at the extremities of the aircraft as seen in Figure 5.6. Note that the beacon placement is limited to positions visible from the receiver aircraft.

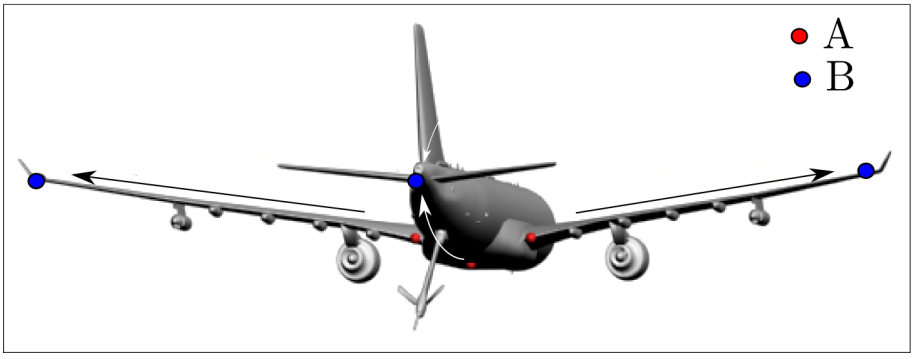

Figure 5.6 – Variation in the IR beacon position on the tanker fuselage from configuration positions A to B

The effect on the relative position error covariance as a function of marker position is shown in Figure 5.7 where the following conclusions can be drawn,

- Moving the IR beacons to the tanker extremities drastically improves the accuracy with which all the relative position and attitude states can be estimated.
- From the derivative analysis an increase in the relative Y and Z positions of the beacons serve to improve the relative X position accuracy as well as the accuracy of all the attitude states. The additional reduction in relative X distance between the beacon and the sensor also increases the relative magnitude of all derivatives which can be most clearly seen in the reduction of the relative Y and Z error covariance.

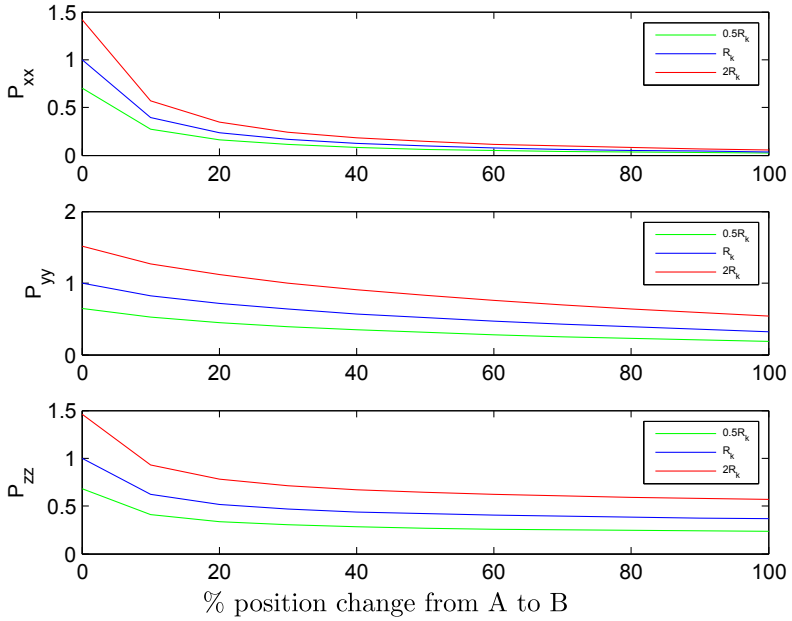

(a) Position error covariance fractional change

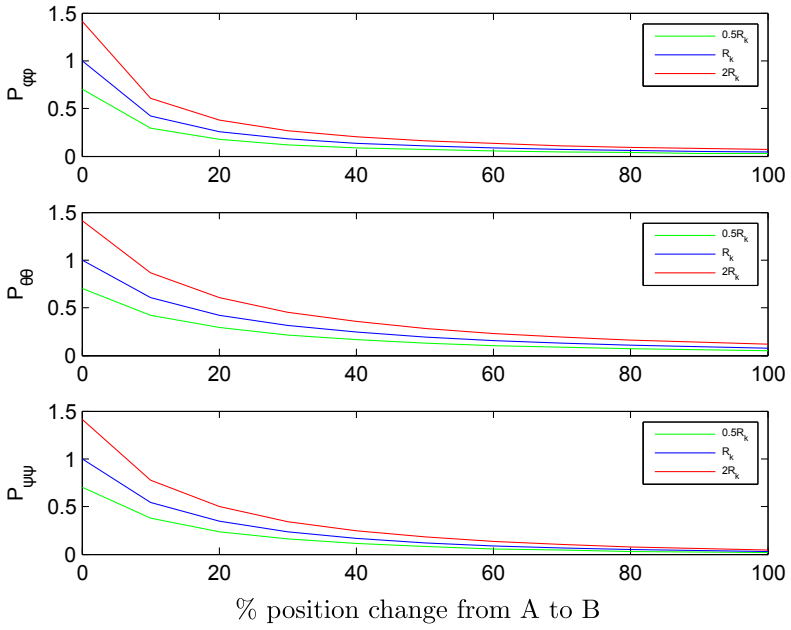

(b) Attitude error covariance fractional change

Figure 5.7 – The change in error covariance as a function of the % distance moved from IR configuration A to B as a fraction of the nominal error covariance at configuration A [Non Dimentional]

5.3.3 Optical - Stereoscopic

Once calculated in a separate subsystem the 3D coordinate acts as the measurement, very similar to the DGPS position measurement. The analysis of the associated measurement Jacobian is also the same the RB-DGPS position measurement with the change in measurement directly dependent on a change in relative aircraft position, and dependent on the change in

attitude as a function of the marker position relative to the tanker CG. From this one would expect the change in position and attitude error covariance to be similar to Figure 5.4. This is however not the case. Accompanying the coordinate transform from 2D monocular to 3D stereoscopic position measurements is a measurement covariance transform facilitated by the Unscented Transform as seen in Appendix C. This transform takes the effect of the change in relative aircraft states as well as marker position into account. As a result the effect of changes in the beacon position on the error covariance when using a stereoscopic configuration are much very similar to the monocular configuration results seen Figure 5.7 where an increase in the Y and Z position of the beacons affect the accuracy of the relative X and attitude estimates, and the relative X distance between the beacon and the sensors affects the accuracy of all the state estimates.

5.3.4 Boom

The measurement equations and resulting Jacobian can be evaluated as follows,

$$\boldsymbol{y} = \begin{bmatrix} \delta l \\ \delta\sigma \\ \delta\chi \end{bmatrix} = - \begin{bmatrix} l_0 \\ \sigma_0 \\ \chi_0 \end{bmatrix} + \begin{bmatrix} \|\boldsymbol{p}_t^{FR/BJ}\| \\ \sin^{-1}\left(\frac{\sqrt{(z_T^{FR/BJ})^2+(y_T^{FR/BJ})^2}}{\|\boldsymbol{p}_t^{FR/BJ}\|}\right) \\ \cos^{-1}\left(\frac{z_T^{FR/BJ}}{\sqrt{(z_T^{FR/BJ})^2+(y_T^{FR/BJ})^2}}\right) \end{bmatrix}$$

$$\boldsymbol{H}_{Boom} = \begin{bmatrix} \frac{1}{2l}\left(2x\frac{\partial x}{\partial \boldsymbol{x}} + 2y\frac{\partial y}{\partial \boldsymbol{x}} + 2z\frac{\partial z}{\partial \boldsymbol{x}}\right) \\ \frac{-1}{l^2\sqrt{1-\frac{z^2+y^2}{l^2}}}\left(\frac{1}{2}l\left(z^2+y^2\right)^{-\frac{1}{2}}\left(2z\frac{\partial z}{\partial \boldsymbol{x}}\right) - \sqrt{z^2+y^2}\frac{\partial l}{\partial \boldsymbol{x}}\right) \\ \frac{-1}{(z^2+y^2)\sqrt{1-\frac{z^2}{z^2+y^2}}}\left(\sqrt{z^2+y^2}\frac{\partial z}{\partial \boldsymbol{x}} - \frac{1}{2}z(z^2+y^2)^{-\frac{1}{2}}(2z\frac{\partial z}{\partial \boldsymbol{x}} + 2y\frac{\partial y}{\partial \boldsymbol{x}})\right) \end{bmatrix} \tag{5.3.7}$$

These derivatives are far more complicated than their GPS and Monocular vision counterparts. Fortunately, an evaluation of the effect of variable parameters on the magnitude of the derivatives is not necessary as the boom configuration is fixed within the AAR scenario. With the other sensors there is large amount of configuration variability but the boom joint and fuel receptacle are at fixed locations, and once connected there is very little relative motion that can affect the derivatives. As such the evaluation of variable parameters on state estimation accuracy in connection with boom use will not be considered in this project.

5.4 Non-rigid wing effects

From the analysis in the previous section the general conclusion is that by moving the point of measurement further from the tanker CG the better the estimates of the attitude and relative angular rate will become. This conclusion, however, does not take into account the effect of a flexible wing and its contribution to the uncertainty associated with the measurement.

As the measurement equations use the position of either the roaming receivers (RB-DGPS) or the IR beacons (Optical) in a rigid frame, the added movement of these components due to wing deflection will serve to increase the measurement noise.

The measurement model for each of the components along the wing now becomes

$$\boldsymbol{y}_{GPS}^{ij} = \begin{bmatrix} \tilde{\boldsymbol{p}}_{RB_j}^{RR_i/BR_j} \\ \tilde{\boldsymbol{v}}_{RB_j}^{RR_i/BR_j} \end{bmatrix} = \begin{bmatrix} \boldsymbol{p}_{RB_j}^{RR_i/RB_j} \\ \boldsymbol{v}_{RB_j}^{RR_i/RB_j} \end{bmatrix} + \begin{bmatrix} v_p \\ v_v \end{bmatrix} + \begin{bmatrix} v_p^{wing}\left(\boldsymbol{p}_t^{RR_i/T}\right) \\ v_v^{wing}\left(\boldsymbol{p}_t^{RR_i/T}\right) \end{bmatrix} \tag{5.4.1}$$

and

$$\boldsymbol{y}_{Mono}^{ij} = \begin{bmatrix} \tilde{\boldsymbol{u}}^{B_i/C_j} \\ \tilde{\boldsymbol{v}}^{B_i/B_j} \end{bmatrix} = \begin{bmatrix} \boldsymbol{u}^{B_i/C_j} \\ \boldsymbol{v}^{B_i/B_j} \end{bmatrix} + \begin{bmatrix} v_u \\ v_v \end{bmatrix} + \begin{bmatrix} v_u^{wing}\left(\boldsymbol{p}_t^{B_i/T}\right) \\ v_v^{wing}\left(\boldsymbol{p}_t^{B_i/T}\right) \end{bmatrix} \tag{5.4.2}$$

where the additional noise terms are functions of the distance of the particular component along the wing. The equations that describe the wing deflection as a function of the distance from the CG are however exceedingly complex, where entire areas of research have been devoted to characterizing wing deflection profiles.

Even though it is well know that the wing will deflect which will result in additional measurement uncertainty, this analysis will assume that the wing profile is known and in this case, rigid. This assumption is substantiated through the assumption that the frequency of wing deflection is much less than that of the sensor measurement noise and as such can be separated. By using multiple sensors along the wing the resultant profile can be successfully estimated. The development of such a system is beyond the scope of this project however, and as such is left for future development.

5.5 Additional Measurements

The addition of sensors, resulting in additional measurements, will effect an increase in the accuracy of the state estimates signified by a smaller error covariance. There are however practical considerations to the addition of sensors such as the limit in available space for sensor placement, and the effective increase in state estimate accuracy due to the addition of sensors beyond a certain number.

The effect of additional measurement on the state estimates can be evaluated by adding sensors to a system in a simulated environment. The simulation scenario is shown in Appendix D. Note that the sensors, and as such the measurements are incremented by three, and that the error covariances are given as fractions of the 3-sensor error covariance with nominal measurement noise.

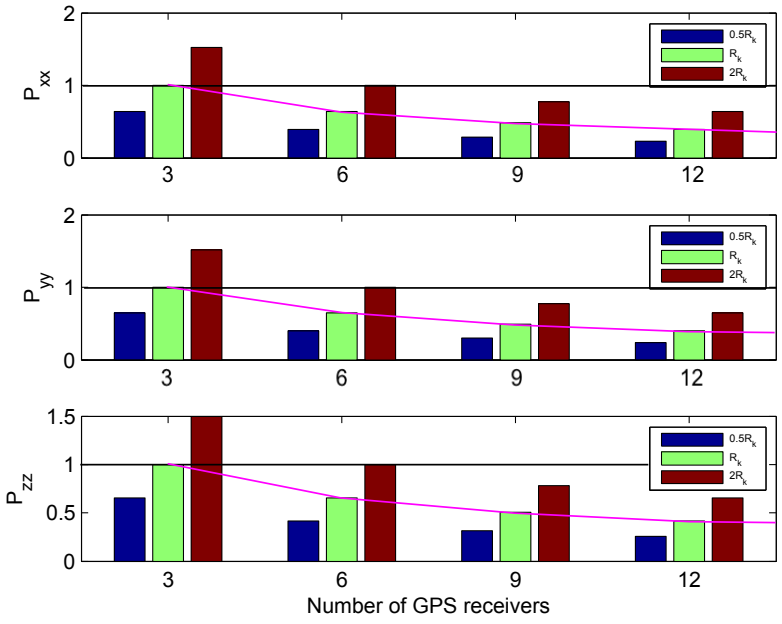

(a) Position error covariance fractional change

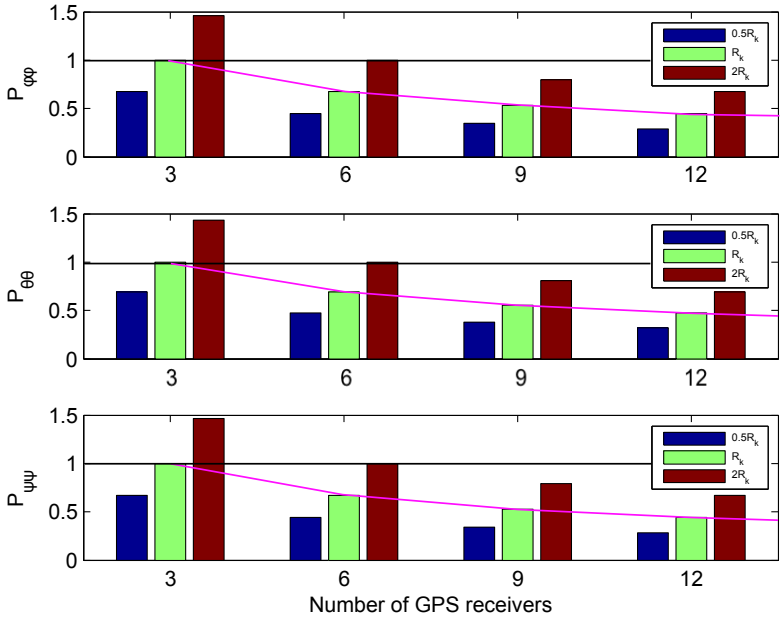

(b) Attitude error covariance fractional change

Figure 5.8 – The change in the position and attitude error covariances as a function the number of RB-DGPS roaming receivers of the tanker fuselage

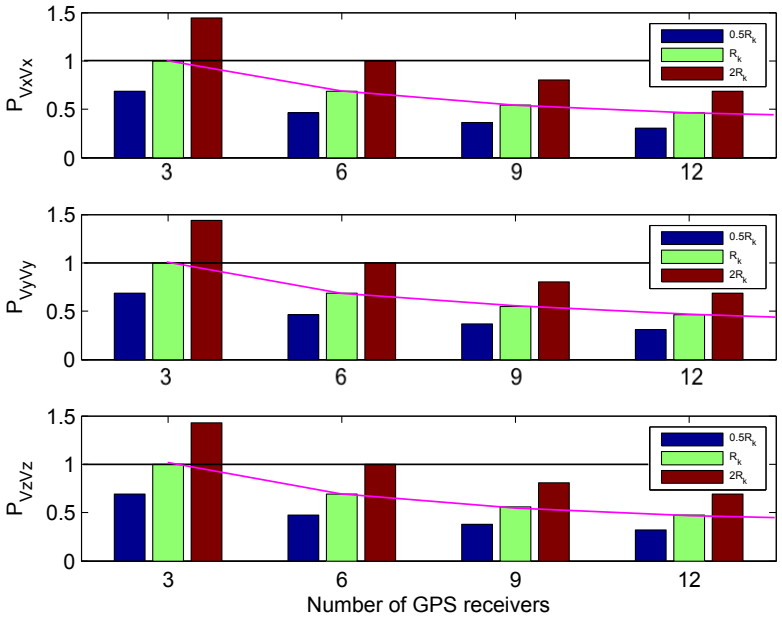

(a) Velocity error covariance fractional change

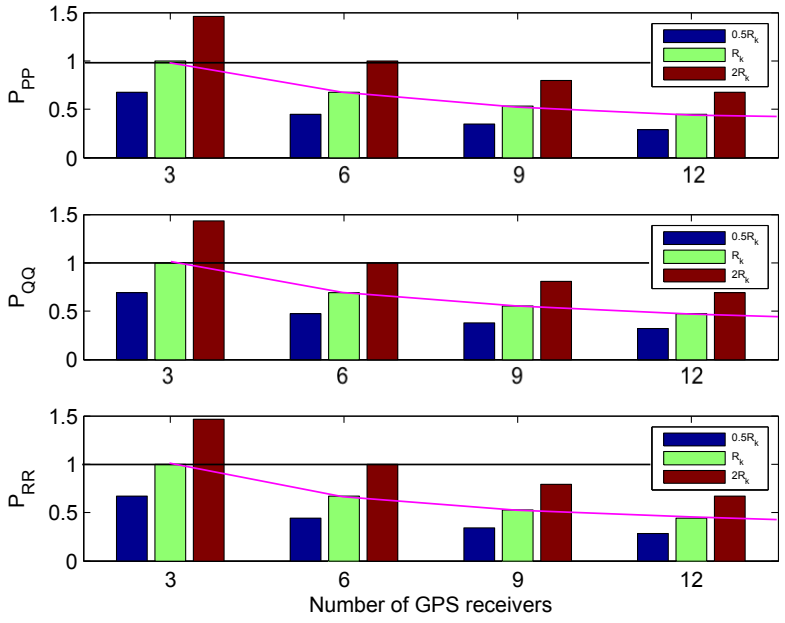

(b) Anular Velocity error covariance fractional change

Figure 5.9 – The change in linear and angular velocity error covariances as a function of the number of roaming GPS receivers

As expected, an increase in the number of measurements is accompanied by a decrease in the error covariance associated with all the states. Note that with the addition of each sensor the decrease in error covariance fraction is less, which is what is espected. It is also important to note the relationship between the effect of additional measurements, versus the effect of an increase in noise. As an example from Figure 5.8 in P_{xx} it can be seen that using nine roaming GPS receivers with sensor noise double that of the nominal value is equivalent to

three roaming GPS receivers with half the nominal noise. Insight such as this is useful in practice where trade-offs between the desired accuracy and situational constraints require careful consideration in choosing the placement and amount of sensor to be used in a final configuration.

A similar response is expected in the position and attitude states of both monocular and stereoscopic configurations. Minimal improvement in the velocity and angular velocity covariances due to the addition of optical vision measurements are expected as these measurement lack measurements directly related to these states.

5.6 Summary

As result of the sensitivity analysis all relevant parameters have been identified that effect a change in the state error covariance during either propagation or correction. Having been identified the effect of a change in each of these parameters has been characterized through an evaluation of the EKF Jacobian matrices. The resulting effects were also shown in simulation where it was shown that a change in particular parameters have a larger effect on the error covariance than others.

The main conclusions that can be drawn from the evaluations are that,

- The propagation of the error covariance is mainly dependent on the amount of noise present on the tanker and receiver acceleration and angular velocity measurements. Error propagation can be reduced by reducing IMU noise.
- An increase in the distance of either the GPS roaming receivers, or IR beacons from the tanker CG reduces the state estimate's sensitivity to noise and as such reduces the state error covariance. In the case of the optical sensors the distance of the beacons to the sensors also has a large impact on the estimation accuracy, with the distance preferably as small as possible.
- The wing deflection causes added uncertainty in the estimates value of the measurement, but will be assumed to be known.
- The addition of more RB-DGPS receivers or IR beacons will increase the accuracy with which the applicable states can be estimated.

With this knowledge the final simulation scenarios can be chosen for simulation. This occurs in the following section after which the configurations are used in full AAR simulation after which the resultant estimation error covariances are compared one another and to the criteria set in Chapter 2. If the minimum state accuracy criteria is not met, the insight into error

covariance improvement obtained in this chapter can be applied in choosing an improves sensor configuration.

Chapter 6

Simulation and results

This chapter represents the culmination of all the theory and insight presented in the preceding chapters. The objective is to simulate the various sensor configurations using both estimation algorithms in a realistic refueling scenario in order to evaluate the accuracy with which the state vector can be estimated. The resulting state estimate accuracy associated with each configuration, represented by the state error covariance, can be used to compare the performance between configurations and to evaluate each configuration's results with respect to the minimum accuracy criteria originally established in Chapter 2. Once the configurations have been evaluated suggestions can be made as to how state estimate accuracies can be improved upon with additional simulation to prove the hypothesis.

Leading up to simulation, the flight scenario is introduced where relevant relative and absolute aircraft states are shown allowing insight into the physical motion of the aircraft during the refueling procedure. After the flight scenario is set the sensor configurations are discussed, where the justification of sensor placement as well as a measure of the accuracy of the sensors in the form of noise covariances are provided.

The multitude of sensor configurations to be tested in simulation will results in too much information to be evaluated. For this reason the full simulation results of all configurations are not shown. Instead the full set of results will be shown of one particular configuration after which a section will follow with the summarised results of all the configurations. Note that the simulation results of each configuration as implemented on both the EFK and UKF is provided on the accompanying disk.

With the results of the sensor configurations easily interpreted, comments and conclusions can be drawn based on whether the configurations adhere to the minimum accuracy criteria which leads to suggestions of improvement and additional simulations.

6.1 Simulation Scenario

From Chapter 2 it is known that there are five stages of flight during a refueling procedure. Of these five the contact and refuel stages are of the highest importance as they correspond to the tightest control and estimation constraints. Of these two stages the contact stage, corresponding to the connect envelope, has the smallest margin in control and estimation error. As a result this stage has been chosen to evaluate the various sensor configurations and estimation algorithms in simulation.

The state estimation simulation is created by using the true relative and absolute states of the aircraft to generate the measurements produced by the sensors. These measurements are then corrupted by noise through the applicable sensor noise models and used as measurement and driving inputs to the EKF and UKF resulting in an estimate of the original states.

The true relative states between the aircraft are shown in Figures 6.1 to 6.4. These relative states have been obtained from a concurrent projects at Stellenbosch University, with focus on the control of the receiver aircraft fuel receptacle within the contact envelope.

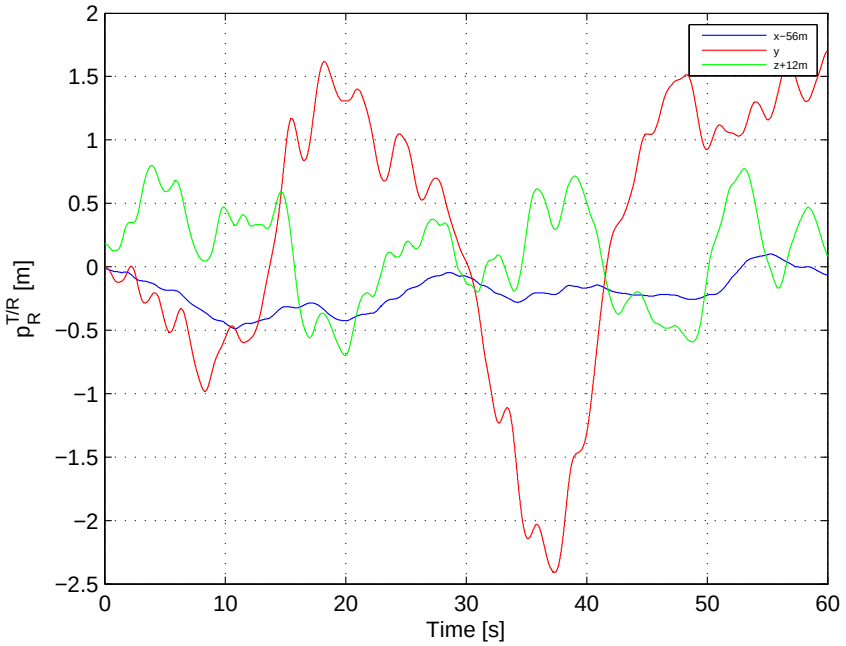

Figure 6.1 – True position of the tanker CG relative to the receiver CG coordinated in the receiver reference frame to be estimated

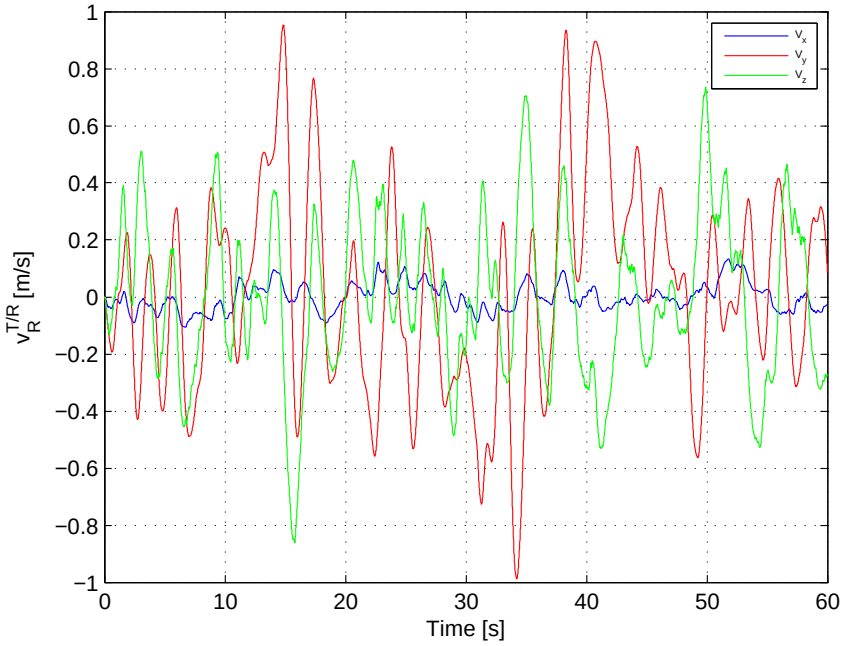

Figure 6.2 – True relative velocity between tanker and receiver CGs coordinated in the receiver reference frame to be estimated

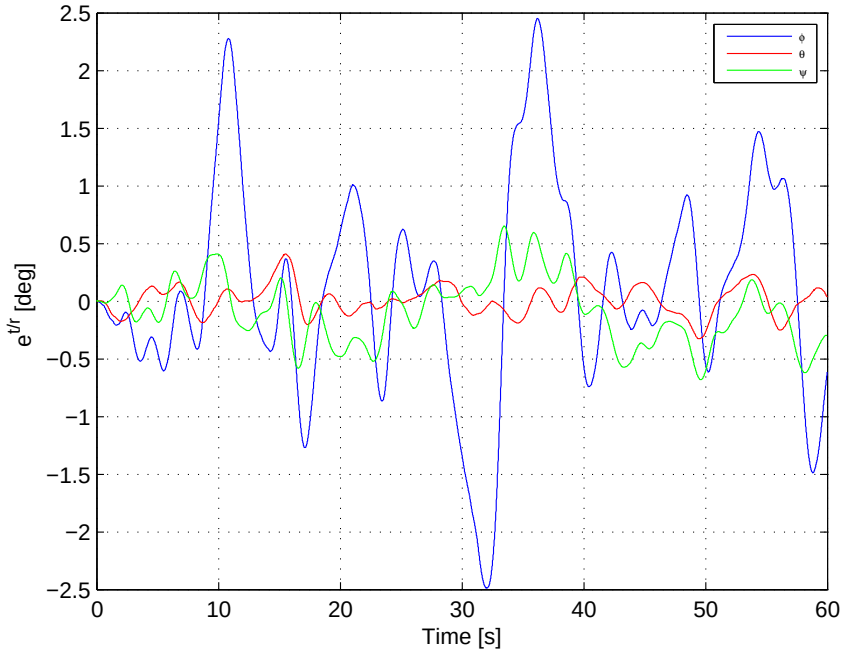

Figure 6.3 – Attitude of the tanker relative to the receiver in Euler angles

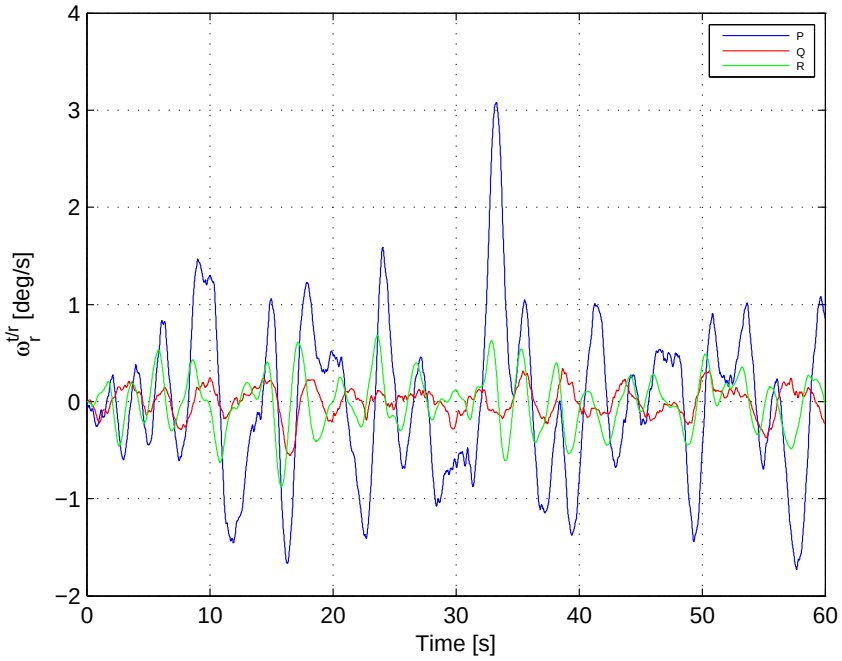

Figure 6.4 – Angular rate of the tanker body axis relative to the receiver coordinated in the tanker reference framse as to be estimated

In addition to the relative states, it is also useful to observe the states of the aircraft relative to a local NED reference frame. Since the receiver aircraft merely reacts to the motion of the tanker, showing its states are somewhat redundant. The tanker aircraft local NED velocity, attitude and body angular rates, defined in Appendix A, are shown in Figures 6.5 to 6.7.

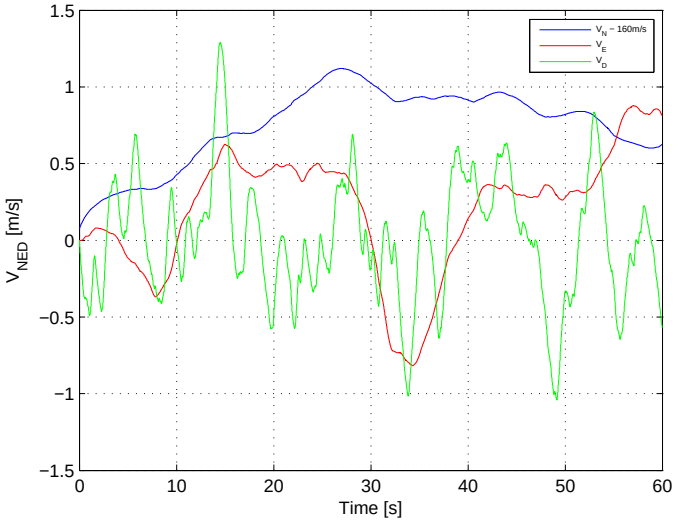

Figure 6.5 – Tanker velocity in the local NED reference frame

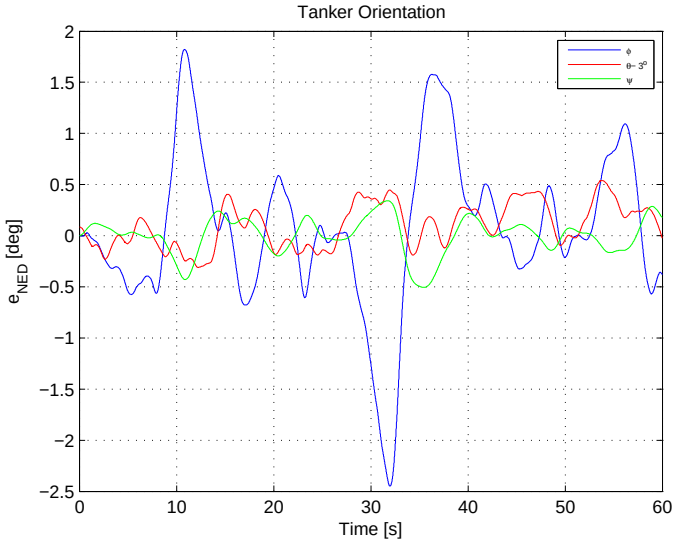

Figure 6.6 – Tanker attitude in the local NED reference frame

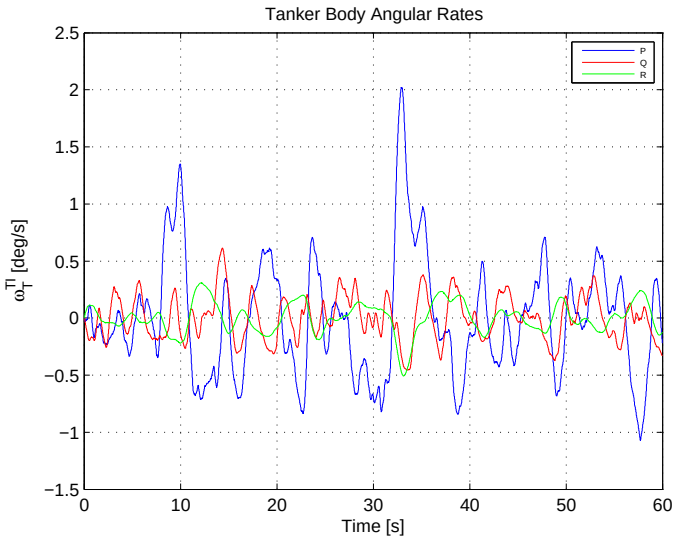

Figure 6.7 – Tanker velocity and attitude in the local NED reference frame as well as angular rates relative to inertial space

With the introduction of the true relative state between the aircraft as well as the states that have relevance on the motion of the tanker aircraft it is possible to move on to the state estimation simulation where it is first necessary to finalise the sensor configurations that will be implemented.

6.2 Sensor Configurations

The sensors available for use in AAR state estimation have been introduced in Chapter 2. These sensor can be combined in a large number of variations in order to obtain the necessary estimates. As it is impractical to test all configurations, twelve sensor configurations have

been set out to be to be implemented in combination with both the EKF and UKF.

The configurations are as follows:

- **Configuration 1** - Roaming Base DGPS only
- **Configuration 2** - Optical (Monocular Vision) only
- **Configuration 3** - Optical (Stereoscopic Vision) only
- **Configurations 4,5 & 6** - Roaming Base DGPS, Optical (Monocular Vision), Optical (Stereoscopic Vision) only, with the addition of the boom parameter measurements
- **Configurations 7,8 & 9** - Roaming Base DGPS, Optical (Monocular Vision), Optical (Stereoscopic Vision) only, with the addition of the IMU measurements
- **Configuration 10,11 & 12** - Roaming Base DGPS, Optical (Monocular Vision), Optical (Stereoscopic Vision) only, with the addition of the boom parameter and IMU measurements

Each configuration has been chosen to highlight the effectiveness with which a sensor type aids in state estimation, with the goal being to judge the relative advantage of utilizing a particular technology. The first three configurations will be referred to as the stand alone configurations as state estimation on these cases are solely dependent on a single type of sensor. Note that this does not mean that these are not multiple measurements, only that the measurement are limited to that of a sensor type. The additional configurations are aimed at evaluating the variable improvement in estimation with the addition of measurements such as the boom and the IMUs.

The consideration for the placement of each sensor on the receiver fuselage and accompanying marker on the tanker, as well as the quantity of each has been discussed in Chapter 5. The following is a summary of each of the considerations after which a graphical representation of the sensor placement is given in Figures 6.8 and 6.9. The exact placement of each component is given in Appendix D along with particular information on each sensor such as noise and update rate.

Optical : monocular and stereoscopic vision

- The placement of the sensors on the receiver fuselage must be as close to the infra-red beacons on the tanker as the field of view will allow.
- An increase in the distance of the The IR beacons from the tanker CG serves to increase the attitude and position estimates.
- All beacons intended to be viewed by a sensor must have line of sight (LOS) to the sensor.

- At least four (monocular) or three (stereoscopic) measurements must be obtained to achieve a unique solutions to the relative position and attitude estimates.
- When using stereoscopic vision only beacons in full view of both sensors will be utilised.

With these considerations in mind, five rear facing infra red emitting beacons where placed on the tanker. One on each wing and one on each of the rear extremities i.e, the rudder tip as well as elevator tips. Note that the beacons along the wings are not places at the wing tips. In Appendix D it is shown that the optical sensor's field of view does not allow the sensors to be placed on the wing extremities. If this configuration does not yield sufficiently accurate results, other considerations can be made in either the movement of the sensor to allow for beacon movement, or a sensor with a wider view range. It would also be possible to place more beacons on the tanker, but practically it is of little value as the current beacons already populate the critical areas that are visible from behind. A single optical sensor has been placed to the front of the receiver at such a point that the beacons fully populate its field of view at the AAR operating distance.

In the case of stereoscopic vision the same beacon configuration is used, with the single sensor replaced by a two sensors configuration which has each sensor at either side of the aircraft center line spaced 1m apart.

Roaming Base DGPS

- Placing the roaming GPS receivers further from the tanker CG serves to increase the attitude and angular velocity estimates.
- No line of sight is required but communication between base and rover must be maintained and the GPS antennas must have an unimpeded view of the sky.
- At least three position and velocity measurements must be obtained to achieve a solution the state estimates.

The placement of the RB-DGPS rovers and base requires a different approach to that of the optical senors. Due to the increased cost and complexity of using the RB-DGPS configuration only three rover modules are attached to the tanker fuselage, one on each wing, within the optimal zone, and the third to the rear of the aircraft. The position of the base station on the receiver aircraft does not affect the state estimates and as such has been placed arbitrarily near the receiver aircraft CG.

IMU and Boom

- The position of the boom joint and fuel receptacle are fixed warranting no placement consideration.

- The IMUs of either aircraft are typically not on the CG, but the simplification assumptions of Chapter 4 states that an inertial navigation system present on each aircraft compensates for this offset providing the body acceleration and angular velocity of each aircraft as an output to be used as driving input measurements to the process model.

Visual Representation

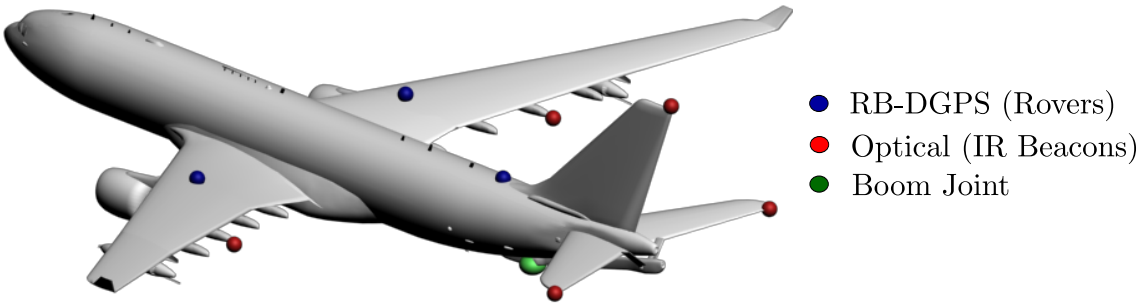

Figure 6.8 – Tanker aircraft with representation of the sensor layout applicable to the each of the sensor configurations

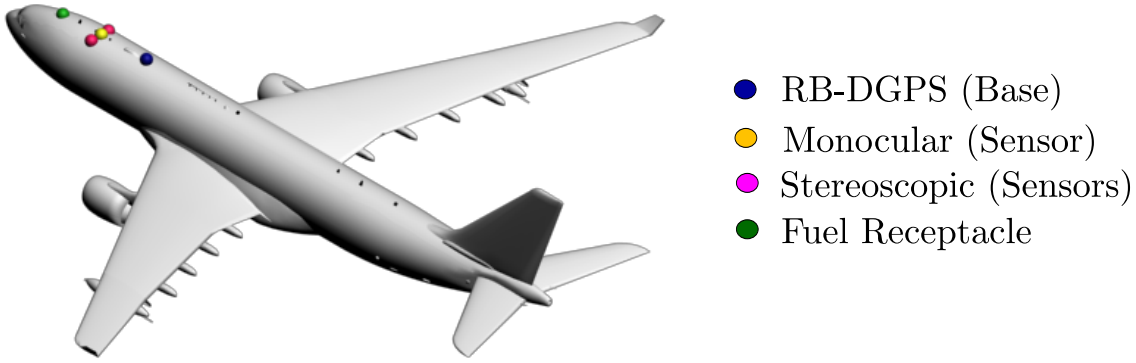

Figure 6.9 – Receiver aircraft with representation of the sensor layout applicable to the each of the sensor configurations

6.3 Results - Configuration 1 (Roaming Base-DGPS)

Having twelve sensor configurations implemented in two different estimation algorithms, each producing estimates for twelve states results in a large amount of information that must be effectively interpreted. For this reason the full interpretation of the results will be performed for one configuration, in this case the stand alone Roaming Base DGPS configuration, after which the subsequent section will contain only a summary of the results of all configurations.

6.3.1 State estimate error and the 3σ error bound

The results of implementing configuration 1 in the EKF can be seen in Figures 6.10 to 6.13 in which the difference in estimated and true relative position, velocity, attitude and angular rate, between the tanker and receiver CGs, can be seen.

The estimate error is also accompanied by its 3σ value, which is a standard statistical analysis tool providing a boundary for which the estimation error has a 99.7% likelihood of staying within.

A low- and high frequency variation in the 3σ magnitude can be observed from the results. The low frequency variation is primarily as a result of the adaptation of the process covariance which strongly effects the propagation of error covariance and the relationship between update and correction in the estimation algorithms. The high frequency variation corresponds to the frequency at which measurements are available. In the time between measurement the covariance increases as a result of pure propagation, with the innovation at measurement instances causing a sudden change in error covariance and as such the 3σ bound.

As a result of the inconsistent 3σ bound it is difficult to relate the performance of the configurations to one another. As a simple solution it was decided to use the average of the 3σ bound for the last 30 seconds of the simulation as an indication of the performance of the configuration.

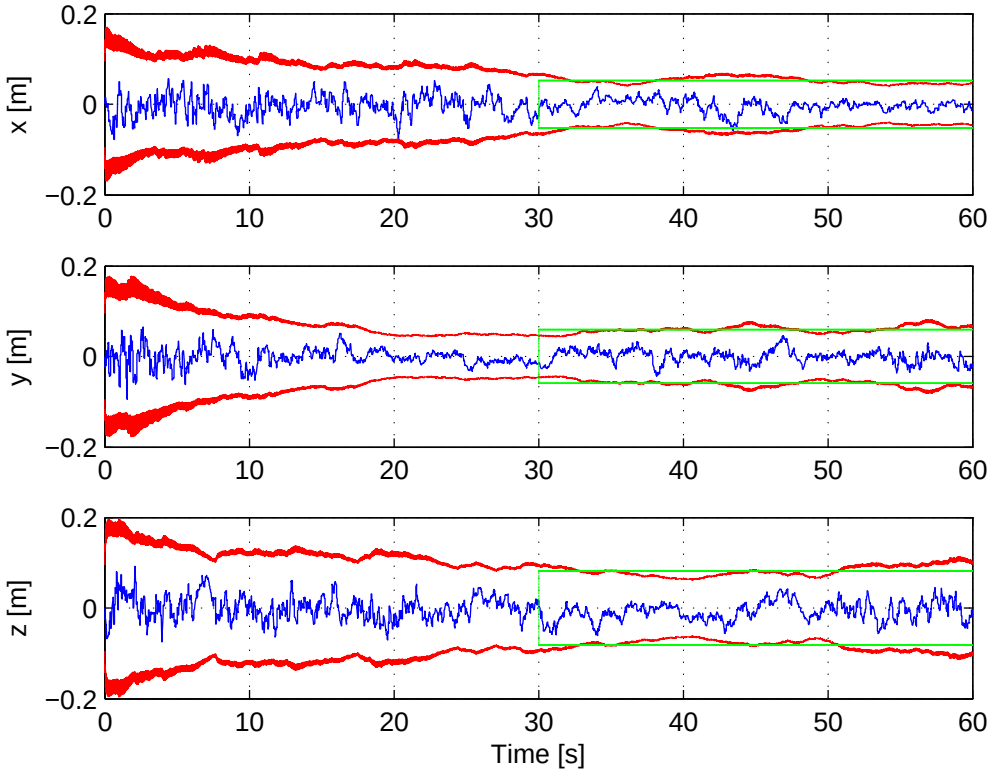

Figure 6.10 – Relative position estimate error, 3σ bound and average 3σ bound

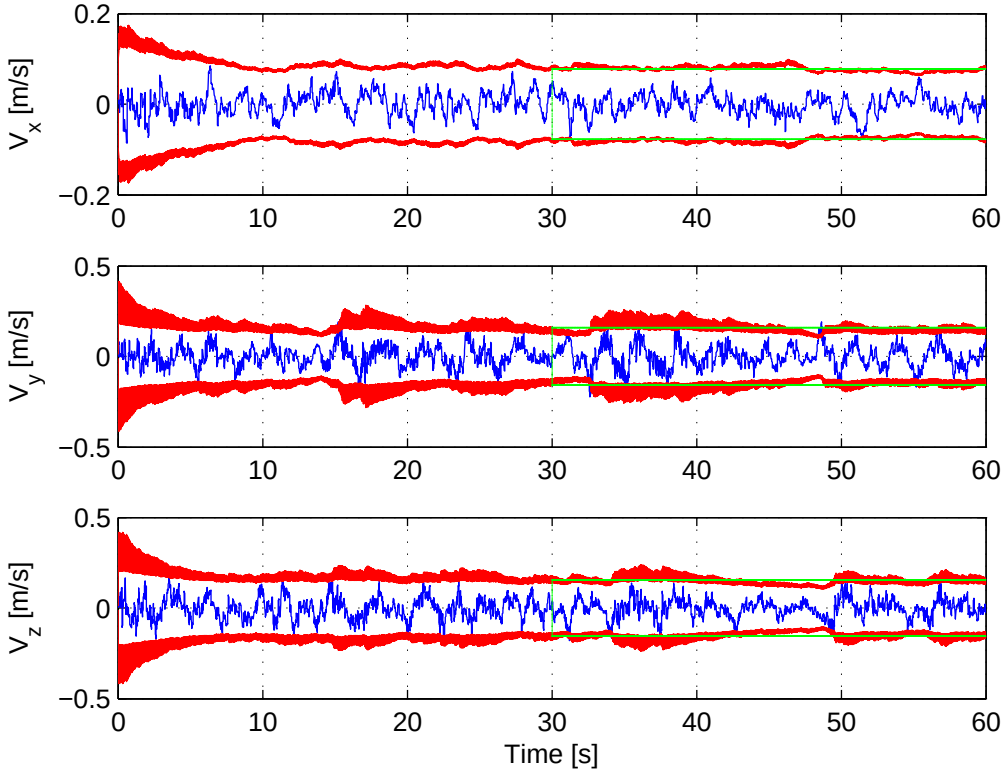

Figure 6.11 – Relative velocity estimate error, 3σ bound and average 3σ bound

This average will be represented by the height of the corresponding bar graph which can be related to the error limits established in Chapter 2, shown in Figure 6.14 .

From this it can be seen that configuration 1 falls within the required estimation accuracy limits for all states except relative pitch.

6.3.2 Percentage Control Envelope

In addition to evaluating the average 3σ of each of the configurations, each configuration will be given a *percentage of control envelope* rating.

Form Chapter 2 we can recall that the ultimate goal is to provide an estimate of the position and velocity states of the center of the control envelope relative to the fuel receptacle as accurately as possible. Since this cannot be done directly the relative aircraft states are estimated and used to reconstruct the required states. Having just obtained the estimates of the relative aircraft states, the error in these estimates will be used to evaluate the uncertainty in the position and velocity control input states. The state estimate 3σ results of each configuration will be used to construct a region of uncertainty in the control input, consistent with the downstream analysis presented in Chapter 2. The size of this control input uncertainty envelopes are compared to the size of the envelope in which control must be applied, and given a percentage rating depending on its relative size.

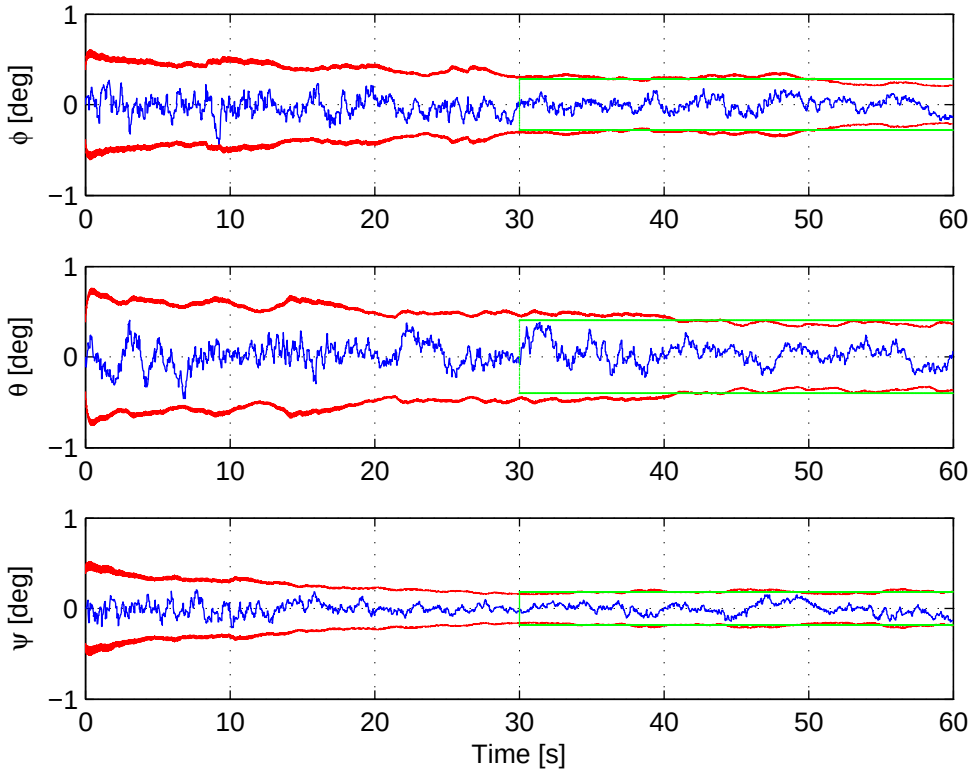

Figure 6.12 – Relative attitude estimate error, 3σ bound and average 3σ bound

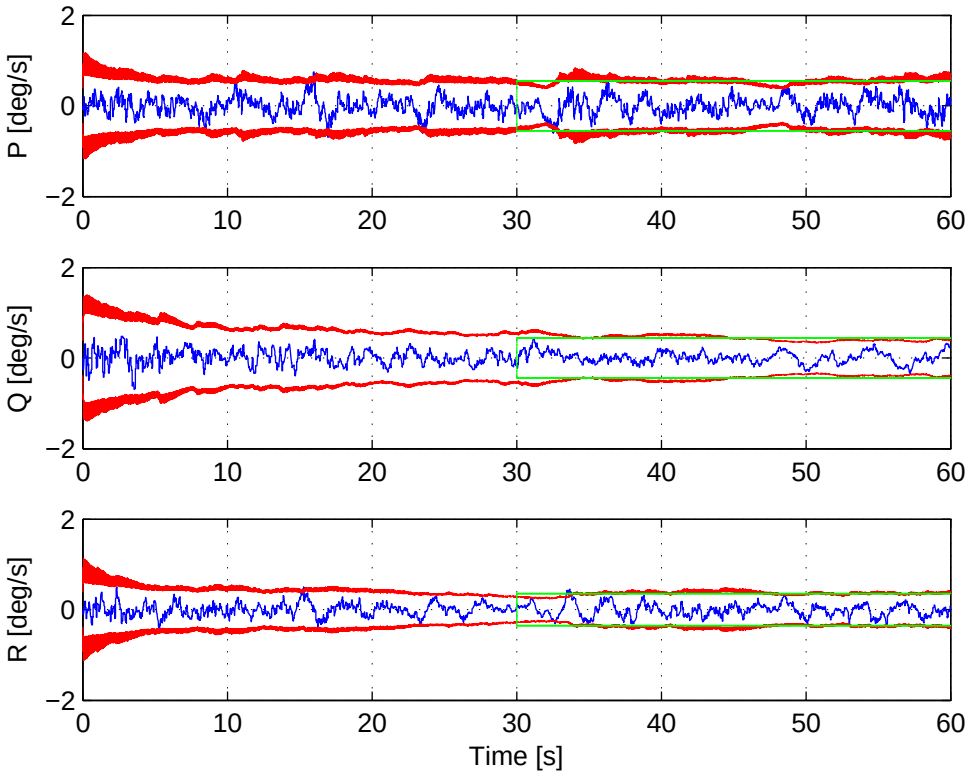

Figure 6.13 – Relative angular velocity estimate error, 3σ bound and average 3σ bound

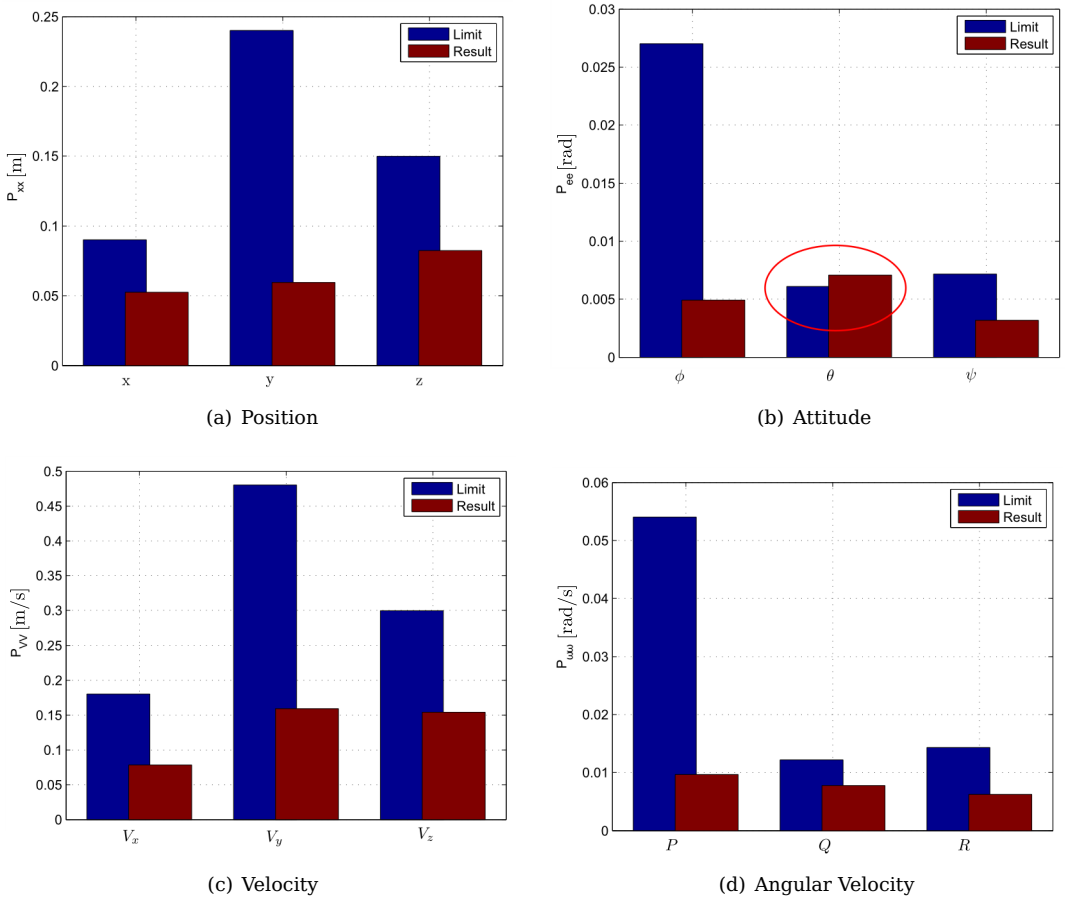

(a) Position (b) Attitude

(c) Velocity (d) Angular Velocity

Figure 6.14 – Averaged 3σ error in comparison to the minimum state estimate accuracy limits

Using the results of the current RB-DGPS configuration implemented in the EKF as an example, it is shown in Figure 6.15 that the area of uncertainty in the control input position obtained from the downstream equations of Chapter 2 is approximately 11% of the control encelope size.

This then indicates that the minimum criteria of 10% for position estimation is not met, and from Figure 6.14 it is clear to see that the accuracy with which relative pitch $\theta^{t/r}$ is estimated is not sufficient. As a result suggestions can be made to improve on the accuracy with which the state can be estimated. This is further discussed in the summary section that follows. A similar evaluation of the area of uncertainty associated with the control input velocity can aslo be performed using hte downstream equation in Chapter 2. The summary of this analysis for all configurations is shown later in the chapter.

6.3.3 Process Covariance Adaptation

As stated in Chapter 3, the measurement covariance is fixed and well known from the measurement noise characteristics of the sensors. The process noise, however, is much less known

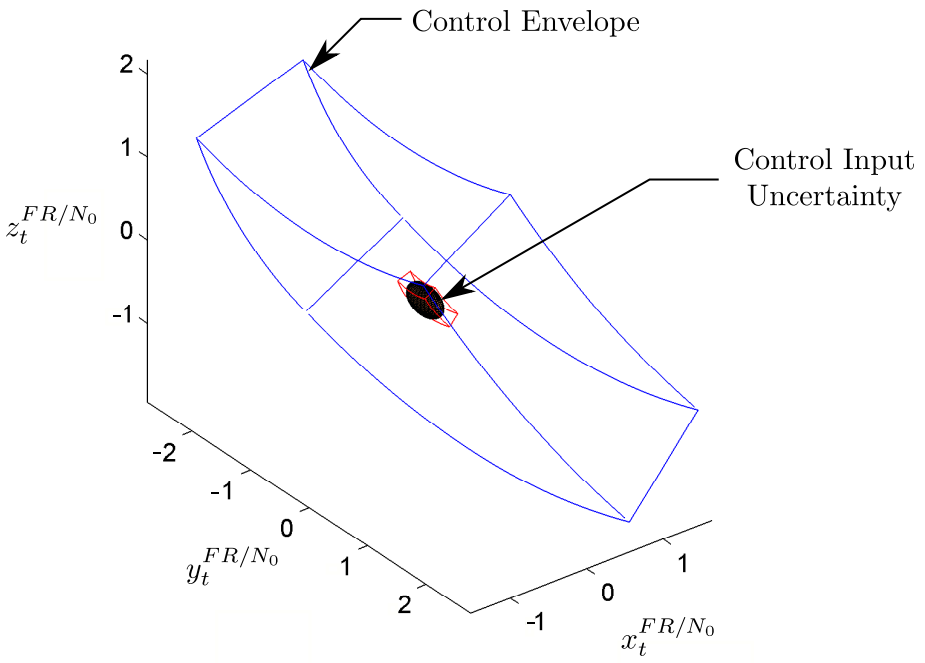

Figure 6.15 – Roaming Base DGPS percentage of control envelope

and is approximated to a constant value in typical applications through iteration. In order to work around the iterative covariance approach the process covariance is adapted based on the magnitude of measurement updates in relation to the expected covariance change allowing an *optimal* value for Q_k to be evaluated, which allows for modeling of all unknown and variable process noise effect.

The initial guess for Q_k is arbitrary and as such is chosen to be some value larger than the actual process covariance. In a system where no adaptation takes place, using a larger process covariance estimate than the true process covariance will result in too little confidence to be placed in the propagation of the states and too much confidence in the measurement update, typically resulting in a highly erratic state estimate which can be seen in the initial states estimation in Figures 6.10 to 6.13.

Process covariance is adapted and settles around some nominal value with sporadic fluctuations based on the magnitude of measurement errors at the particular time. The change in the process covariance can be seen in Figure 6.16 where the state estimate becomes less erratic when the process covariance becomes smaller until it settles at a nominal covariance.

The value of this adaptation can be seen in Figures 6.10 to 6.13, where the 3σ values of each state converge as the process covariance reaches a closer representation of its true value dictated by the function of the process covariance adaptation algorithm.

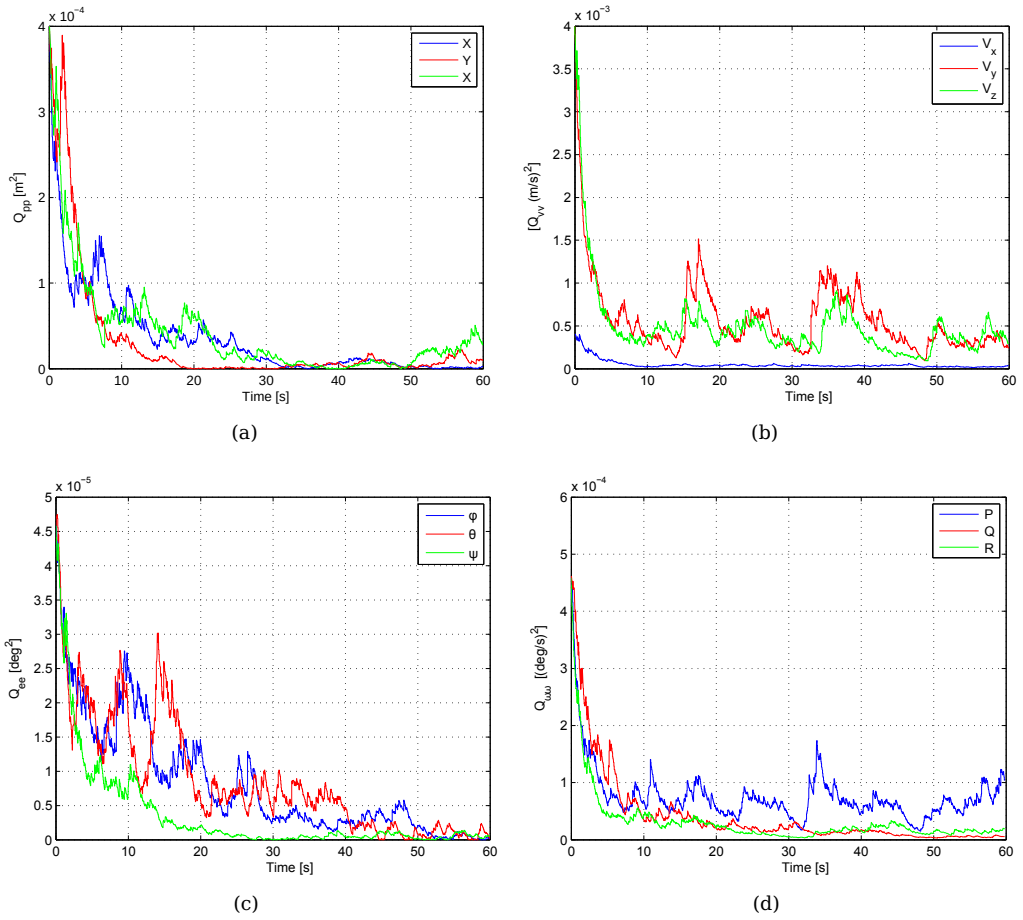

Figure 6.16 – The change in the process covariance associated with each of the states due to the process covariance adaptation

It is important to note that there is a significant difference in the process covariance adaptation of configuration 1, as opposed to that of configurations 2 and 3 where only optical measurement are present. In configurations where RB-DGPS measurements are present all 12 states are corrected based on measurement updates and as such the process covariance of all 12 states can be adapted. With the two optical configurations the measurements only have baring on the relative position and attitude states, and as such adaptation of the process noise covariance will only be applied for these states. This also then implies that process noise covariance for the velocity and angular rate states must be approximated and will stay constant for the duration of simulation. In these cases the values of the applicable process noise covariances have been tuned to resemble their optimal values.

6.3.4 EKF vs. UKF

Up to this point the simulation results of configuration one have been shown using the EKF estimation algorithm only. To evaluate all of the results regarding the simulation of configuration 1, the results shown to this point have to be repeated as the configurations are implemen-

ted in the UKF estimation algorithm. The interesting fact lies in the remarkable similarities between the results obtained from each of the algorithms, and as such these similarities will be highlighted in this section as to not be forced to repeatedly illustrate the similar results of both algorithms.

Again, in order to keep the illustration of the point as concise as possible, only the configuration 1 will be used to illustrate the similarities in estimation algorithm results, as an evaluation of each of the other configurations will result in the same conclusions.

The best way of illustrating the similarities between the state estimates produced by each of the algorithms is to show the state estimate error and 3σ bound adjacent to one another. Shown in Figure 6.17 the relative X distance and relative roll error estimates of the EKF and UKF, with the other states not shown as they exhibit the same behaviour.

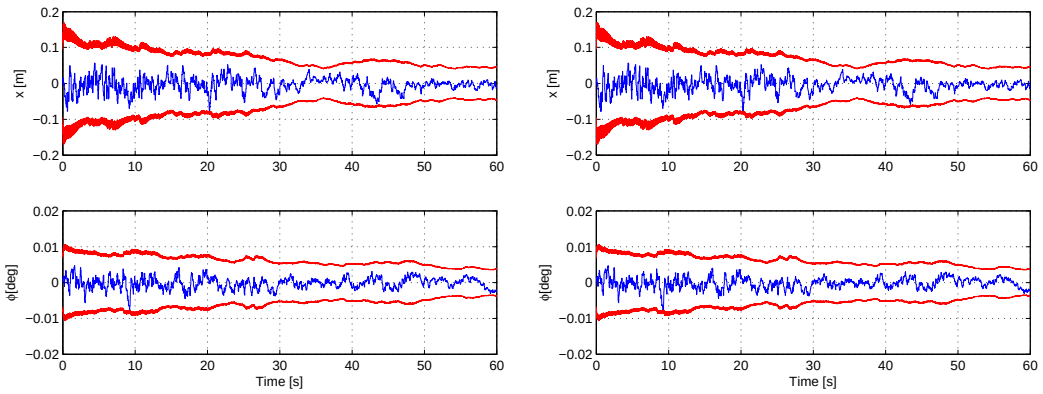

(a) EKF (b) UKF

Figure 6.17 – The relative x position and relative roll ϕ estimate error and 3σ bound for configuration 1 as evaluated in each of the estimation algorithms

To show that there is in fact a difference in the state estimates, the difference in the state estimate of the EKF and the UKF for the applicable states is shown in Figure 6.18.

An explanation for the high level of similarity in the results obtained from both these estimation algorithms can be found in a closer examination of the estimation strategy of each as well as the system of which the states are to be estimated.

Form Chapter 3 it is known that the Kalman Filter is used for optimal estimation of linear systems, with the EKF and UKF using the same Kalman Filter structure but different approximations in order to apply the filter to the non-linear estimation problem. In summary, the EKF linearizes the non-linear process and measurement models about the current state vector using a Taylor series expansion, with the UKF using a point cloud to approximate the probability distribution of the state vector which can the be transformed by the non-linear equations and averaged for state propagation

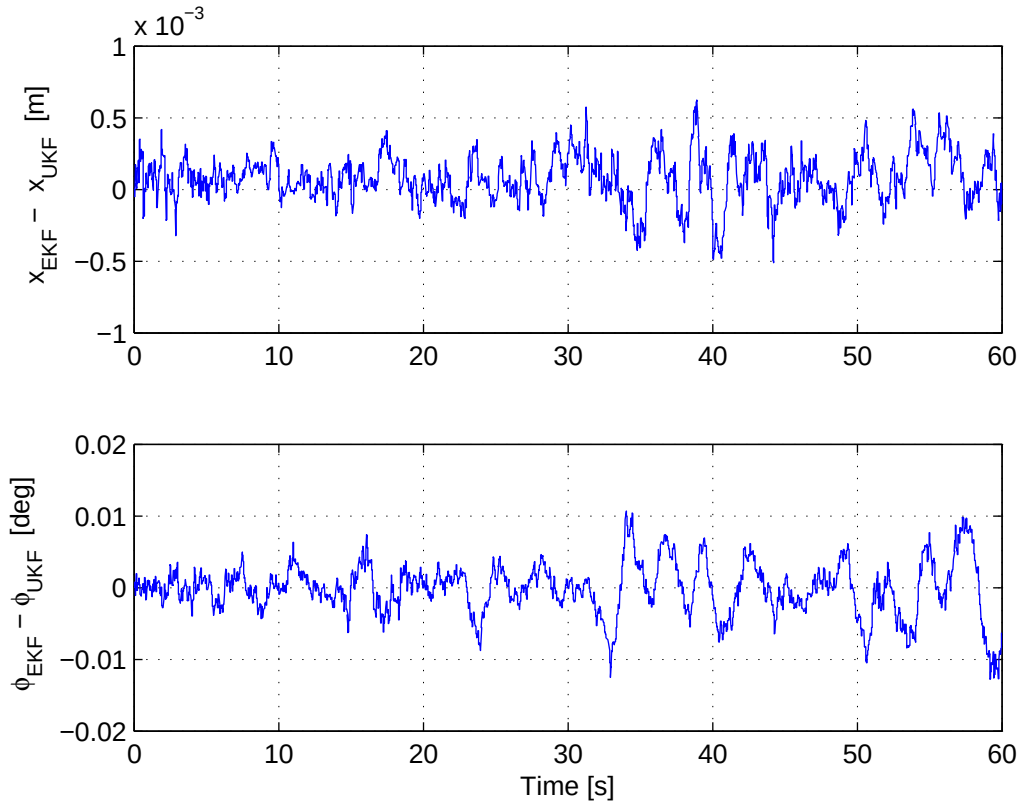

Figure 6.18 – The difference in the relative x position and relative roll ϕ estimate error resulting from each algorithm

The linearisation approach of the EKF is functional if the signal being estimated can be adequately approximated as linear between time steps. If the system proves to be sufficiently non-linear between time steps, the EKF has the potential to diverge. The UKF approach is stable in most non-linear application and will converge faster than the EKF under incorrect initial conditions. As such one would expect the UKF to produce the best result in the current non-linear state estimation simulation, however it has been found that even though the relative state estimation problem contains various non-linearities, none of them are severe enough within the rate of estimation to degrade the performance of the EKF notably beyond that of the UKF.

From this analysis it can bee seen that given reasonable initial state estimates, that there is no discernible difference between the use of either of the estimation algorithms, however for the reason of general robustness in estimation and the ease of practical implementation, where lengthy derivatives are not required, the use of the UKF is preferred.

6.4 Results - All Configuration Summary

Having shown the full results of configuration 1 the summarized results of all the configurations are presented in this section, with the detailed results of each configuration provided

on the attached disk. The average 3σ values for the twelve configurations are presented, split into four analyses for relative position, velocity, attitude and angular rate respectively after which an interpretation of the results, as well as recommendations on improvement are presented. The state accuracy results are then used to construct a *percentage of control envelope* rating for each of the configurations which is compared to the accuracy specifications of Chapter 2. Finally, the configurations that do not fall within the minimum accuracy criteria are refined using the insight gained in the individual state analysis and simulated to show the necessary improvements.

6.4.1 Relative Position

The relative performance comparisons of each sensor configuration with respect to the relative position estimates is shown in Figure 6.19. The following conclusions and recommendations can be made based on the results:

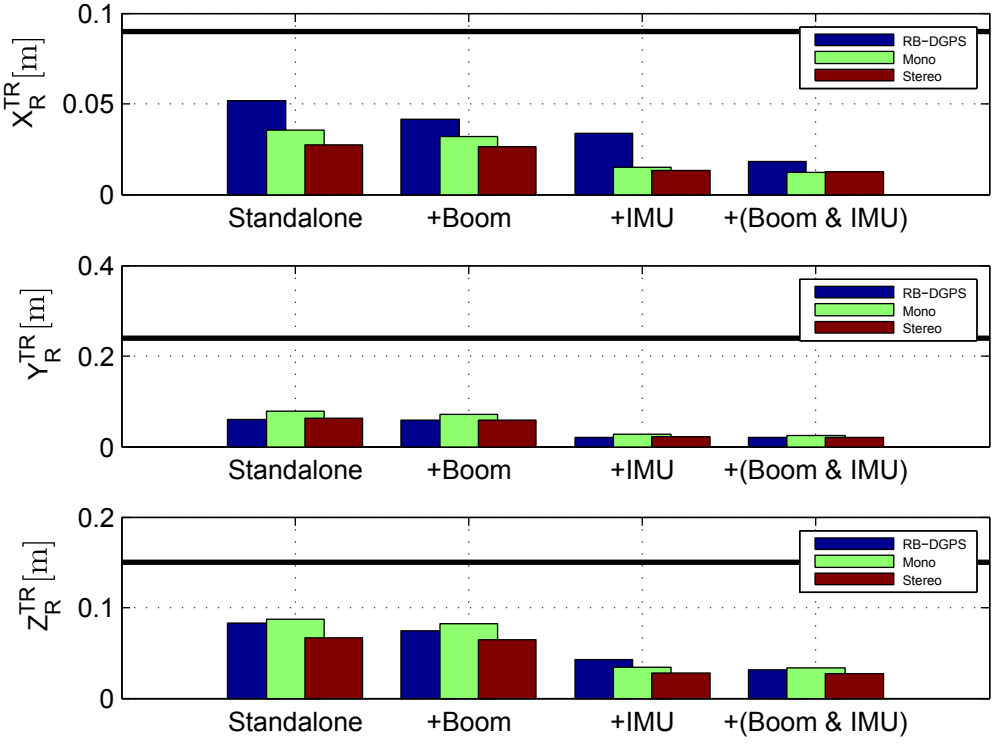

Figure 6.19 – Average 3σ error of the relative position state for all configurations implemented on the EKF

Conclusions

- All sensor configurations implemented fall within the minimum relative position accuracy criteria.

- The addition of the IMU and boom sensors to the stand alone optical and DGPS configurations improves on the 3σ error bound, with the IMU resulting in a larger improvement than that of the boom and the combined use of the IMU and boom producing overall better results.

- Of the configurations, those with an optical stereoscopic setup yield the most promising results. This configuration is expected to outperform its monocular counterpart. Interestingly enough it also outperforms the RB-DGPS which yields a higher average 3σ error bound due to the fact that the stereoscopic configuration makes use of five measurements where RB-DGPS uses only three as shown in Section 6.2.

Recommendation

- All the configurations fall within the allowable accuracy range. The sensors have been chosen to reflect that which can be commercially obtained and the configuration layout has been set for functionality and not necessarily to yield the most accurate result possible. Taking this into consideration there is no need to attempt to improve upon the current configurations for relative position estimation purposes. It is however possible to determine the effect that less accurate sensors will have on the state estimate accuracies. Due to the arbitrary nature of such a test, as well as the fact that the theoretical estimation accuracy variation as a function of noise variation has already been performed in Chapter 5, additional simulations regarding position estimates are deemed unnecessary.

6.4.2 Relative Velocity

The relative performance comparisons of each sensor configuration with respect to the relative velocity estimation are shown in Figure 6.20. The following conclusions and recommendations can be made based on the results:

Conclusions

- As expected the RB-DGPS configuration drastically outperforms the two optical configurations in terms of velocity estimation as it is the only configurations to use velocity measurement between points on the respective aircraft. The velocity estimates of the optical configurations are obtained as a result of the position estimates.

- The addition of the IMU yields the biggest improvement in velocity state estimates as the high accuracy accelerations and angular rates act as driving inputs to the estimator dramatically improves the confidence in state propagation and as such the accuracy of the position, velocity and attitude estimates.

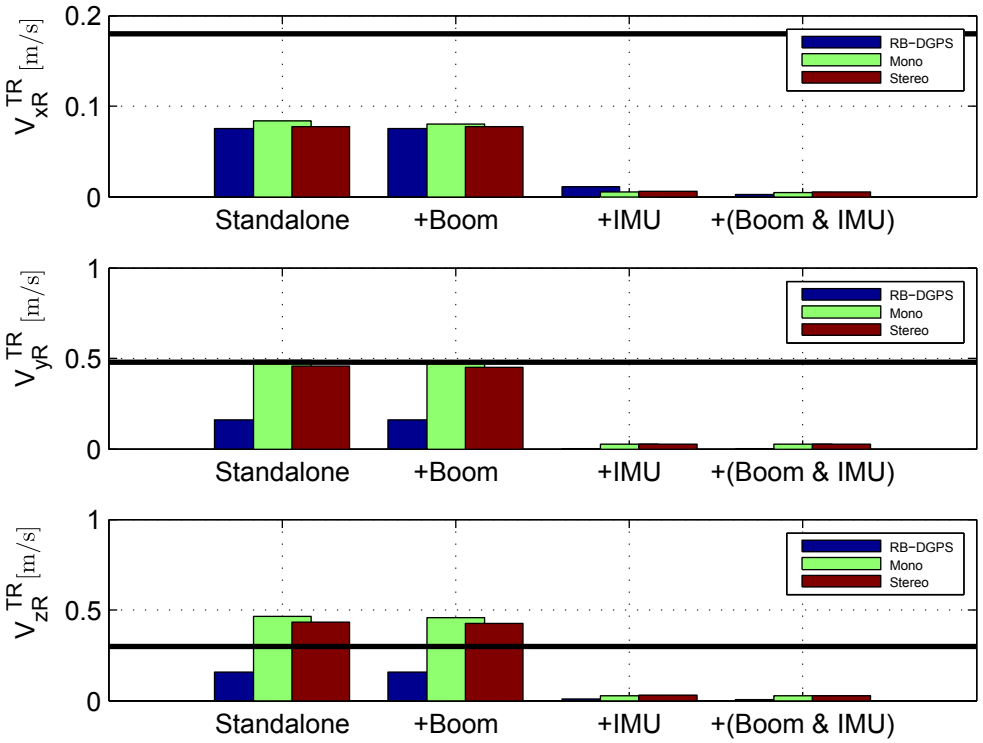

Figure 6.20 – Average 3σ error of the relative velocity state for all configurations implemented on the EKF

- The addition of the boom has little direct effect on the linear and angular velocity estimates as the measurements predominantly have relevance to the relative position and attitude states. Some effects can be expected due to the differentiation of these states, but have been found to be too small to consider relevant.

- The standalone configurations of optical monocular and stereoscopic vision, as well as the configurations corresponding to the addition of the boom measurement fail to meet the required 3σ accuracy criteria.

Recommendation

- Since there are configurations that do not meet the set requirements, improvements must be made to allow them to fall within the accuracy limits. The optical methods (monocular and stereoscopic) both fail to meet the minimum criteria since they both have a lack of higher order measurements. In these configurations the addition of either IMU or RB-DGPS would result in a velocity estimate improvement. As shown, the addition of the IMU driving inputs to the stand alone configurations already results in drastic improvements, thus the addition of RB-DGPS sensors to the optical configurations could prove to be useful.

6.4.3 Relative Attitude

The relative performance comparisons of each sensor configuration with respect to the relative attitude estimates are shown in Figure 6.21. The following conclusions and recommendations can be made based on the results:

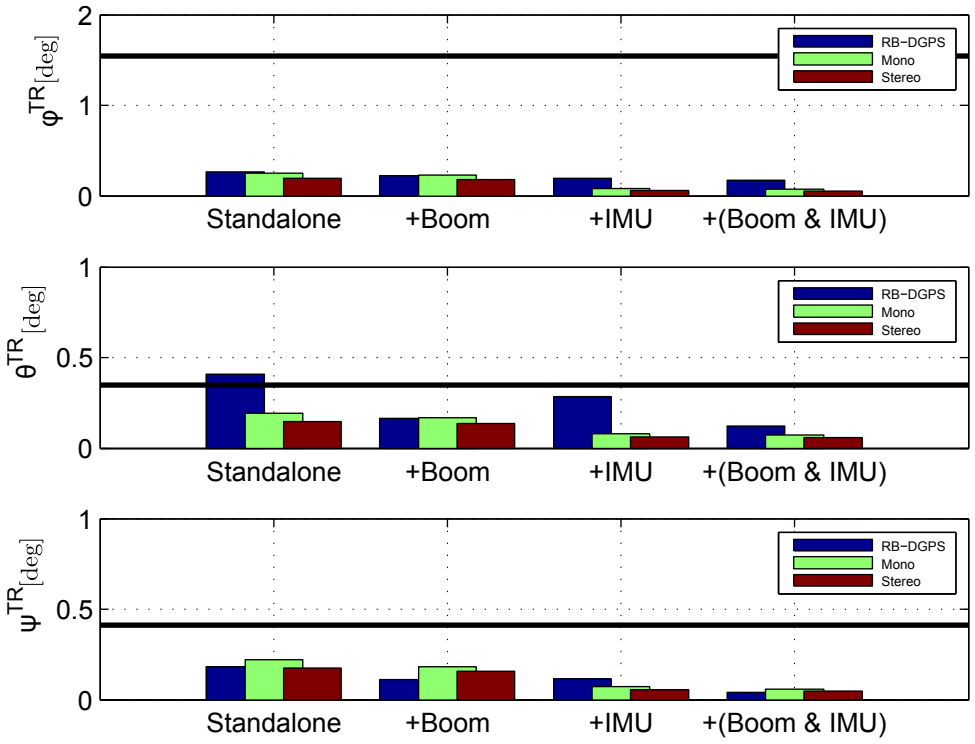

Figure 6.21 – Average 3σ error of the relative attitude state for all configurations implemented on the EKF

Conclusions

- The configurations that include the stereoscopic vision setup yield the most promising results. This configuration is expected to outperform its monocular counterpart, with the RB-DGPS yielding higher average 3σ error bound due to the fact that the stereoscopic configuration makes use of five measurements where RB-DGPS uses only three.
- The addition of the IMU driving inputs improve all standalone configuration accuracies since the addition of angular rate driving inputs drastically improve the confidence in attitude state propagation.
- The addition of the boom measurement improves upon all estimates, but most significantly on that of the relative pitch and yaw estimates, which is what is expected as a small error in those states result in larger errors in measurement estimates. This effect can particularly be seen in that of the pitch accuracy of the RB-DGPS. Since this configuration only has one measurement specifically pertaining to pitch as seen in Figure 6.8

the boom measurements include vital information on relative pitch which dramatically improves on the pitch estimates, even more than that of the IMU.

- As expected the addition of the boom and the IMU result in the highest level or attitude estimate accuracy.
- All configurations fall within the minimum accuracy criteria except for standalone RB-DGPS in pitch.

Recommendation

- From the insight gained in Chapter 5 there are various ways in which the insufficient accuracy of the RB-DGPS pitch can be improved upon. From the current simulation configurations it has been shown that the addition of the boom or IMU measurements result in sufficiently improved accuracy in pitch. An alternative to the addition of other sensors is the improvement of the setup of the current configuration. Currently the RB-DGPS only has three rover modules attached to the tanker fuselage, with only one having particular relevance to the pitch estimates. Improvement to the pitch estimates can be obtained by adding another roaming GPS receiver module to the front or rear of the aircraft, or by simply moving the current RB-DGPS roaming GPS receiver module further aft.

6.4.4 Relative angular rate

The relative performance comparisons of each sensor configuration with respect to the relative angular velocity estimation are shown in Figure 6.22. The following conclusions and recommendations can be made based on the results:

Conclusions

- As with the velocity estimates the RB-DGPS configurations drastically outperforms the two optical configurations in terms of angular velocity estimation as it is the only configurations to use velocity measurement between points on the respective aircraft. The angular velocity estimates of the optical configurations are obtained as a result of the attitude estimates.
- The addition of the IMU gyroscope measurements drastically improves on the relative angular rate state estimates as the relative angular rate is a direct function of the tanker and receiver angular rates as well as attitude.
- The addition of the boom has no effect on the linear or angular velocity estimates as the measurement only have bearing to the relative position and attitude states.

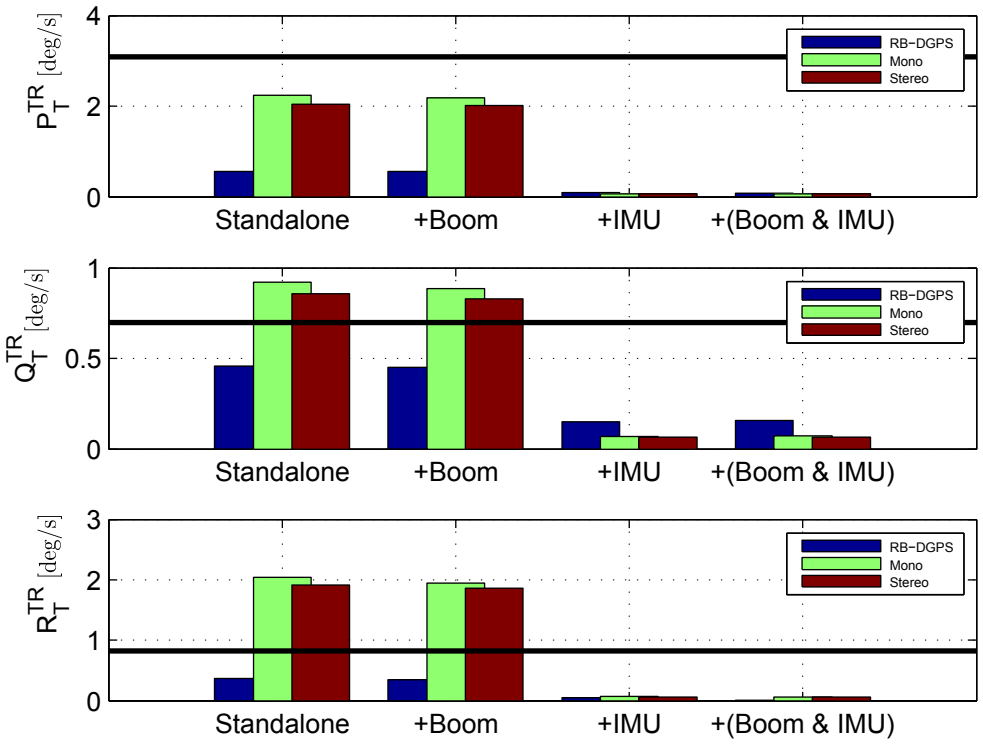

Figure 6.22 – Average 3 σ error of the relative angular velocity state for all configurations implemented on the EKF

- The standalone configurations of optical monocular and stereoscopic vision, as well as the configurations corresponding to the addition of the boom measurement fail to meet the required 3σ accuracy criteria in relative pitch and yaw rate.

Recommendation

- There are various ways in which the optical configurations can be improved upon to meet the minimum criteria. It has already been shown that the addition of an IMU is sufficient to improve the results. Alternatively, RB-DGPS can also be used to provide an improvement in velocity and angular rate measurements.

- Since the estimates of angular rate are dependent on the accuracy of the relative attitude, the improvement of attitude estimates will serve to improve the accuracy of the angular rates. An increase in the accuracy of attitude estimation can be achieved through adding more sensors, varying the particular sensor layout or improving on the noise characteristics of the sensors. This is, however, not a preferred method of improving on relative angular rate estimates as the current stand alone optical configurations cannot be improved upon without becoming impractical.

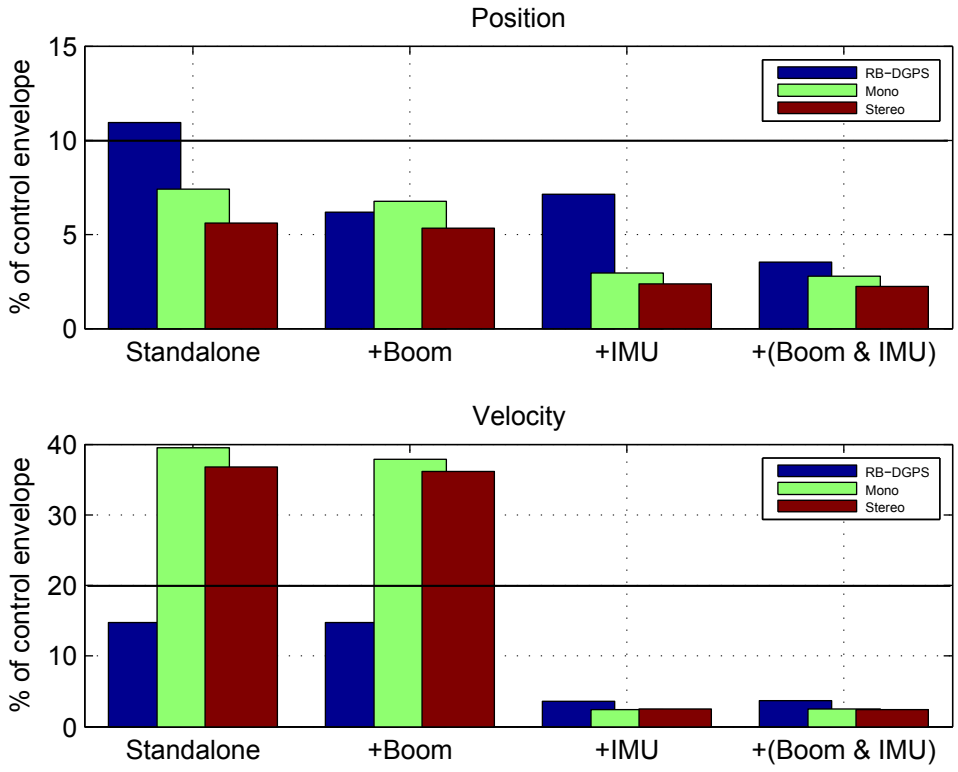

Figure 6.23 – Uncertainty in the resultant state estimates of the position and velocity of the control envelope center point relative to the fuel receptacle expressed as a *percentage of the envelope* in which control must be applied

6.5 Percentage of control envelope

Evaluating the 3σ bound of each of the states through all 12 configurations provides great insight into the strengths and weaknesses of each. It does not, however, provide a unified view of the effectiveness of a particular configuration in term of estimation accuracy. Having introduced just such an evaluation method earlier in the chapter, the *percentage of control envelope* ratings for all 12 configurations is shown in Figure 6.23.

From the *percentage of control envelope* rating the following conclusions can be drawn:

- All configurations, with the exception of RB-DGPS, fall within the specified constraints for relative position estimation.
- All configurations, with the exception of Optical Monocular and Stereoscopic, fall within the specified constraints for relative velocity and angular velocity estimation.
- The addition if the IMU dramatically increases the accuracy with which the states are estimated and in almost all cases results in the configuration with the highest level of accuracy.

Each of the original configurations have been tested and their resulting state estimate accuracies analysed providing an overview of the quality of the state estimates achievable with

commercially available sensors implemented through either the EKF or UKF in specific configurations. With the implementation of the original 12 configurations it has been found that some of the configuration do not meet the required accuracy criteria and some exceed the criteria. As such, additional simulation will aim to improve on the estimates of the problem states in order to have all configurations fall within the *percentage of control envelope* limits.

6.6 Additional Simulations

In this section two aspects of state estimation will be addressed in reflection of the results shown in the previous section. The first focuses on the required changes that must be made to configurations that do not meet the minimum accuracy criteria, and the second deals with the allowable simplifications that can be made to the configurations that exceed the minimum accuracy requirements.

6.6.1 Configuration Improvements

Roaming Base DGPS

With particular reference to Figure 6.21, it is clear that the state estimate error contributing the most to the inaccuracy of configuration 1 is that of relative pitch. From prior analysis it has been found that there is only one position measurement that has a particular effect on the pitch state estimate. The conclusion has been drawn that to improve upon the state estimate, either an additional measurement with relevance to the pitch state must be added, or the current measurement must be altered in some way as to improve on its contribution. From the configuration layout in Figure 6.8 the option to move the GPS rover on the tanker further aft seems like the easiest option which produces the results highlighted in Figure 6.25(a).

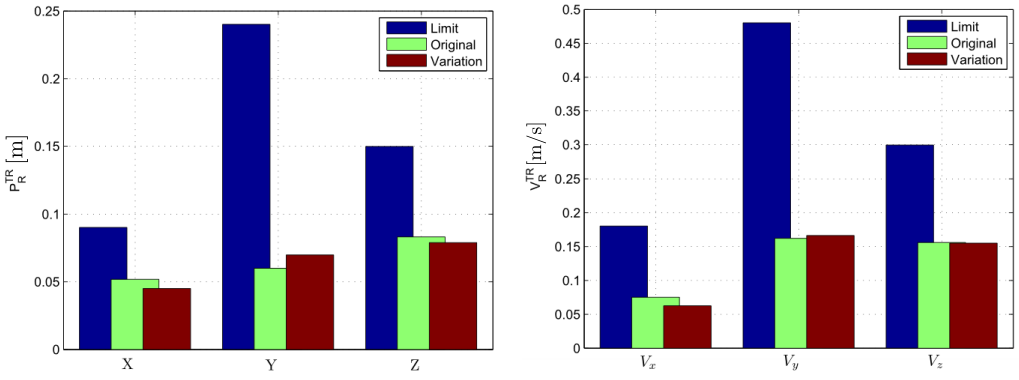

Figure 6.24 – The change in the average position and velocity 3σ associated with each of the states as a result of the improvement of configuration 1 - RB-DGPS

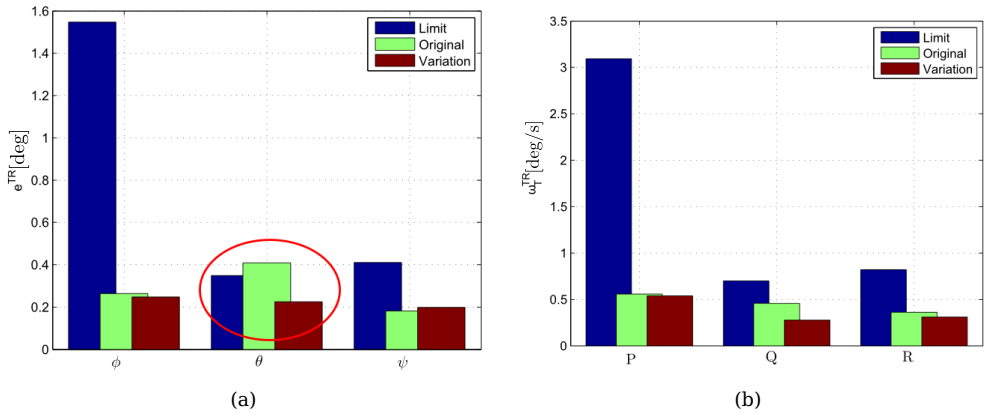

(a) (b)

Figure 6.25 – The change in the average attitude and angular velocity 3σ associated with each of the states as a result of the improvement of configuration 1 - RB-DGPS

This improvement is directly related to the improvement of the configurations *percentage on control envelope* rating which is improved to within the 10% range as seen in Figure 6.26.

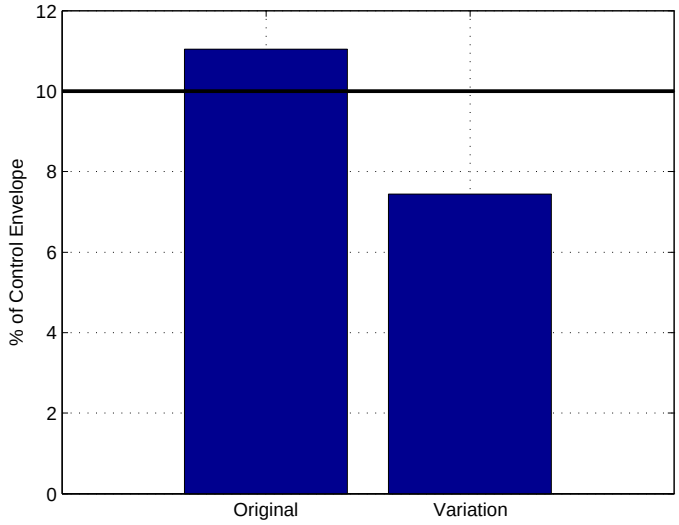

Figure 6.26 – Comparison between the percentage of control envelope rating between the original RB-DGPS configuration and the variation where one rover has been moved further to the tail

Optical Monocular and Stereoscopic

Form Figures 6.20 and 6.22 it is clear that the optical configurations are incapable of attaining the required accuracies in relative velocity and angular rate. The options for increasing the velocity accuracies of the optical configurations are to improve on the position estimates through the addition of more measurements, improve on position estimates through reduced measurement noise or the addition of sensors that provide measurements with relevance to the higher order states such as accelerations and velocities.

Since the measurement noise model for the optical sensor is related to high accuracy sensors, there is no sense in evaluating the effect of higher accuracy measurements from optical

sensors. Both monocular and stereoscopic configurations have five beacons attached to the tanker fuselage, which already populate most of the critical areas of the fuselage so there is also no sense in adding more measurements. From the original simulation the effect of adding higher order measurements such as aircraft IMUs have a dramatic improvement on the results. For this reason the last test is to evaluate the effect of RB-DGPS addition to the optical configurations as a means of improving velocity estimates. From the analysis in Chapter 5 it has been found that the position of the RB-DGPS will have no effect on the position and velocity estimates but will have an effect on attitude and angular rate. Since the two states requiring the largest improvement in angular rate accuracy are relative pitch and yaw rates the RB-DGPS sensor will be added to the tail of the tanker similar to that of the rover module attached to the rear of the tanker in the stand alone RB-DGPS section. The result of this is shown in Figures 6.27(b) and 6.28(b) where dramatic improvement in the state estimate accuracies in velocity and angular rate can be seen as a result of the addition of on RB-DGPS sensor to the rear of the aircraft.

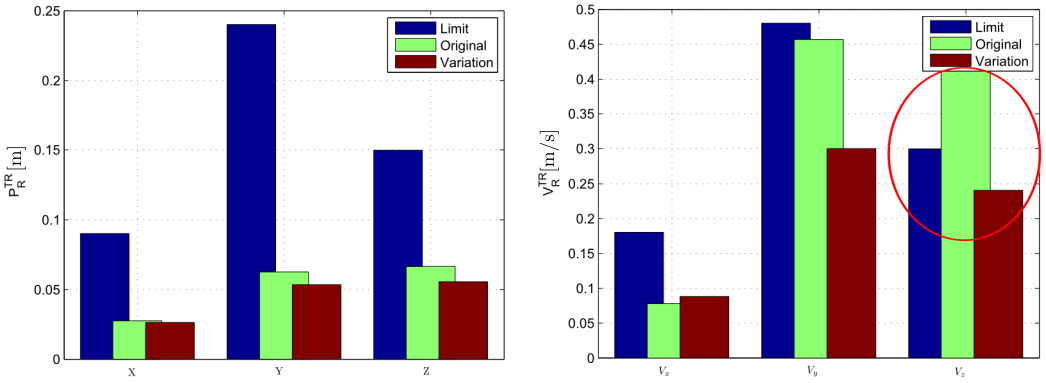

(a) (b)

Figure 6.27 – The change in the average position and velocity 3σ associated with each of the states as a result of the improvement of configuration 3 - Optical Steroscopic

This improvement in relative velocity and angular rate estimates is directly related to the improvement of the velocity *percentage of control envelope* rating of the optical configurations, which is improved to within the 20% range as seen inFigure 6.29.

All configurations now meet the minimum requirements for state estimation accuracy. There are various configurations that exceed the estimation criteria, but as the current configurations have been chosen to reflect what is practically possible there is little reason to test every possibility of less effective hardware or configurations. If such an analysis is in fact required, where the amount of sensors is limited and the accuracy of the measurement is also less than specified, the limited configuration parameters can be entered into the estimation configuration and the resulting accuracies evaluated.

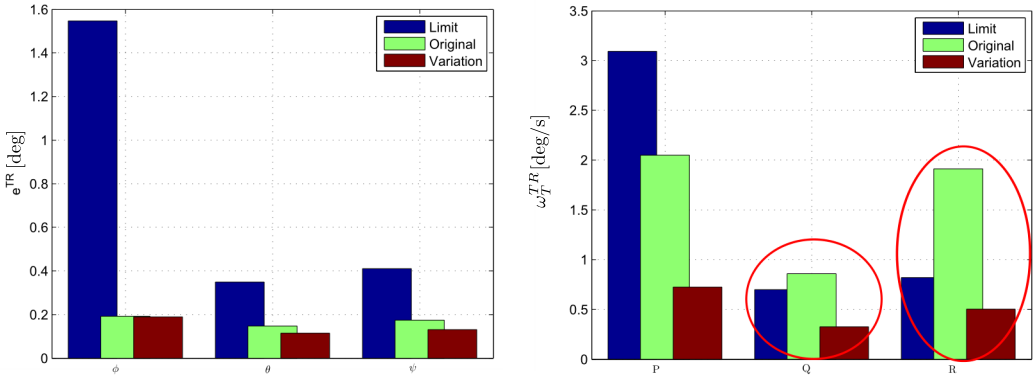

(a) (b)

Figure 6.28 – The change in the average attitude and angular velocity 3σ associated with each of the states as a result of the improvement of configuration 3 - Optical Stereoscopic

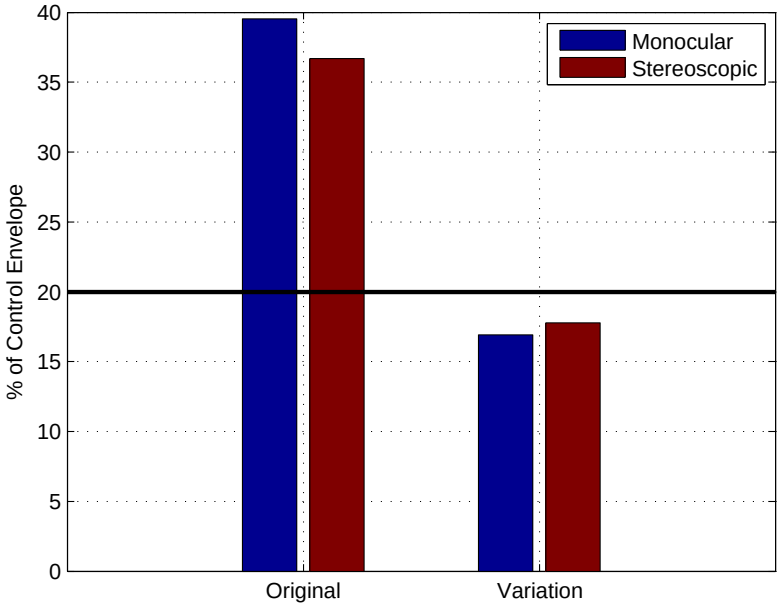

Figure 6.29 – Improvement in the *percentage of control envelope* of configurations 2 and 3 (Monosular and Steroscopic) with respect to the velocity control input due to configuration variation

6.7 Summary

In conclusion, the relative state estimation system has been tested using 12 configurations in conjunction with two estimation algorithms, in order to highlight the use of each of the sensors alone and in combination in a simulated AAR scenario. It has been shown that most of the configuration fall within the minimum specification for each state set in Chapter 2 even whilst being chosen for practicality rather than maximized accuracy. The state estimate accuracy results were related to a percentage of control envelope rating for both position and velocity providing a complete measure of the relative effectiveness of each. The configurations that did not meet the minimum criteria in both the individual state accuracy and *percentage of control*

envelope rating were analysed ,after which additional simulations showed that the minimum criteria could be achieved using the recommendations based on the theory of Chapter 5.

The following chapter will discuss final conclusions as well as recommendations for further analysis of the state estimation problem as it pertains to AAR.

Chapter 7

Conclusions and Recommendations

All of the phases in the design of the AAR estimation system have been undergone, with each of the preceding chapters focussing the development of a particular aspect of state estimation. As a summary, the objective of each of the chapters is listed,

- **Ch. 1** - Introduce the AAR scenario and the applicable state estimation problem through discussions on the motivation behind the project as well as previous work done. By using the single project goal of developing a state estimation system and a brief literature study in typical solutions a set of objectives was established setting the structure for the subsequent chapters.
- **Ch. 2** - Parameterise the state estimation problem through the definition of AAR specific considerations, such as the control input and estimation output requirements, estimation envelopes and minimum accuracy requirements. Provided an overview of each of the sensors as well as estimation algorithms that are considered.
- **Ch. 3** - Introduce the structure and fundamental function of each of the estimation algorithms accompanied by comparative examples to highlight the differences in estimation strategies.
- **Ch. 4** - Derivate the process and measurement models for use in the estimation algorithm structure. The process model describe the evolution of the state vector in time as a function of the states and control inputs, and the measurement model describes the relation between the measurement and the state vector.
- **Ch. 5** - Identify the parameters that effect a change in the propagation rate and correction magnitude of the state error covariance. The effect of a change in these parameters, such as sensor noise, sensor positioning and the number of measurements, is then related to change in error covariance allowing sensor configuration to be purposefully chosen for final simulation.

- **Ch. 6** - Simulate each of the configurations suggested in Chapter 2. First by finalisisng the sensor the simulation configurations based on the considerations of Chapter 5, and then implementing them through simulation of both the EKF and UKF. The full results of a single configurations is presented followed by the summarised results of all configurations. Conclusions are drawn based on the relative performance of each configuration, the performance with respect to the minimum criteria, and the difference in performance between estimation algorithms.

Each of the chapters provide their own summaries and conclusions based on the considerations made. The following is a summary of the most important conclusions made in each chapter.

- **Ch. 1**
  - Form the literature study it is clear that there is no unified solution to the relative state estimation problem as it applies to aircraft or spacecraft. As a result is was decided that the multiple configuration approach would be adopted where numerous sensor configuration variations would be tested on multiple estimation algorithms to evaluate the relative success with which the states can be estimated.
- **Ch. 2**
  - The accuracy with which the control input parameters are to be estimated is directly proportional to the size of the applicable control envelope. As a result the maximum allowable error, or uncertainty, in the control inputs are chosen to be 10% of the control envelope, for control position inputs, and 20% of the control envelope, for control velocity inputs. In order to satisfy the input requirements set by the control system the estimation state vector and associated minimum accuracy requirements are introduced and given physical constraints.
  - With five sensor posibilities available for use in the state estimation setup, 12 configurations are presented for simulation using each of the 3 estimation algorithms. The final setup is to be undergone in Chapter 6 after the considerations of Chapter 5.
- **Ch. 3**
  - All three estimation algorithms are applicable for use in AAR but due to the relatively small gain in the optimal nature of the state estimates through the use of the PF in comparison the complexity and demand in computational power it was decided to omit the PF from simulation until such a time where the neither the EKF nor the UKF could sufficiently contend with estimation of the non-linear system.

- The process covariance adaptation algorithm can be seamlessly integrated into each of the estimation algorithm structures.

- **Ch. 4**
  - When using the tanker and receiver aircraft IMUs, consideration must be given to the addition of Bias terms to the state vector as well as compensating for the offset of the IMU from the aircraft CG. In this evaluation, whoever, it is assumed that this is done by an independent system, and as such is omitted from the simulation.
  - In cases where the IMUs are present, the output of the IMU subsystems are used as the driving input measurement. When not present the measurements are assumed zero and the driving inputs are assumed to be white noise.
  - The use of quaternions can be successfully integrated in the general structure of the EKF and UKF through the use of the three-parameter error quaternion representation in the form of the vector of Modified Rodrigues Parameters.
  - The sensor models, especially in the case of the optical sensors cannot be fully described in simulation, and as such simplified models are presented where uncertainty in measurements are represented by additive white noise.

- **Ch. 5**
  - The noise associated with the tanker and receiver acceleration driving inputs most severely affect the propagation rate of the velocity error covariance and as such should be reduced to improve the accuracy of the position and velocity state estimates.
  - The noise associated with the tanker and receiver angular velocity driving inputs most severely affect the propagation rate of the attitude error covariance and as such should be reduced to improve the accuracy of the attitude state estimate.
  - An increase in the number of measurements serve to increase the accuracy with which the states can be estimated. The addition of RB-DGPS sensor will increase the accuracy of all states, with optical monocular and stereoscopic sensors only improving significantly on the position and attitude states. The IMU and boom measurement are omitted from the analysis as it is assumed that their configurations are fixed.
  - When using RB-DGPS, an increase in the distance of the roaming GPS antennas from the tanker CG serves to improve the attitude and angular velocity estimates.
  - When using optical monocular, or stereoscopic vision an increase in the distance of the IR beacons from the tanker CG serves to improve the attitude and relative X position estimates, where a decrease in the X distance between the beacon and the sensor serves to improve all the attitude and position estimates.

  - With the advantages of placing GPS antennas and IR beacons on the tanker extremities the fact that the wings are flexible, and that added uncertainty, is a prevalent concern. It is, however, assumed that the wing deflection can be sufficiently estimated due to the difference in magnitude and frequency of the white noise of the sensor and the deflection of the wing. As a result the subsequent analysis assumes a rigid wing.

- **Ch. 6**
  - Each of the sensor configurations are finalised based on the consideration of Chapter 5.
  - All configurations estimate the relative position to a sufficient accuracy.
  - Configuration 1, where only 3 RB-DGPS roaming receivers and one roaming base are used does not estimate the relative pitch to a sufficient accuracy. This can be solved by either adding a GPS antenna or moving the current one on the tail further aft, which is shown in simulation to sufficiently improve the relative pitch accuracy.
  - Configurations 2 and 3, where only monocular and stereoscopic sensors are used, do not reach the required accuracy in relative velocity and angular velocity states. The addition of sensors with higher order measurement, such as IMU or RB-DGPS dramatically improves the results.
  - Configurations that utilise both the aircraft IMUs yield the most accurate state estimates, with the addition of the boom only resulting in a noticeable improvement in the relative pitch and yaw state estimates of configurations where these states are not represented sufficiently.

From these conclusions various recommendations are presented for future research and development.

- In Chapter 4 the assumption is made that in independent subsystem allows compensation for both the IMU bias terms and the offset from the aircraft CG. Though this might be true in an AAR scenario, it might not be true in other applications, in which such a system can either be developed, or the full driving input models can be implemented in the estimation algorithms.
- In Chapter 4 the measurement models for the optical sensors are introduced with the assumptions that the effect of camera calibration uncertainty presents in the from of additive white noise. For more accurate simulation the calibration of optical sensors and the effect on the noise model can be further investigated.

- In Chapter 4 the assumption is also made that the deflection of the wing can be sufficiently estimated. The effect of this assumption has a large impact on the resultant sensor placement and state estimate accuracy. It is recommended that the validity of this assumption is tested in simulation through the further research into the estimation of wing deflection.

- Various improvements can be made on the fidelity of the simulation model, but in order to gain definitive results it is recommended that selected configuration be implemented in practice, where the sensor and noise models of simulation can be altered to reflect reality. The simulation can then be related to what is seen in practice to validate all the conclusions drawn in this project.

Appendix A

Vector Notation and Coordinate Frames

For clarity and consistency throughout this thesis it is important to define some basic concepts in term of notation since the solution to the state estimation problem relies heavily on the relative interaction between various reference frames and points of interest.

A.1 Reference frames

The choice of appropriate coordinate systems arise from various considerations. Typically there are certain coordinate systems in which a particular set of vectors makes sense. For navigation purposes it is typically necessary to relate aircraft position, velocity and orientation to the a reference frame fixed to the earth surface Earth, whereas for performance,control and stability purposes it is often required to relate the position and velocity of the aircraft relative to the atmosphere. In other chases coordinate system exist in which a vector is most naturally expressed. An aircraft thrust vector, for instance, would be considered fixed with respect to the aircraft body axis, or the acceleration experienced by and accelerometer always provides a measurement relative to an inertial axis. As such multiple reference frames are defined for used in the Thesis derivations.

All coordinate systems will be right handed and orthogonal designated by the symbol F. The coordinate system indicator is lower case and is intended to be a mnemonic for the name of the system, for example F_i will indicate the inertial reference frame. Unless otherwise stated lower chase letters indicate a coordinate systems, the corresponding upper case letters will indicate the origin of the reference frame such that the point I is the origin of F_i.

Axes of the system are labeled x, y, and z which correspond to unit vectors $\mathbf{i}$, $\mathbf{j}$, and $\mathbf{k}$ respectively and subscripted appropriately.

The following are the main coordinate systems of interest:

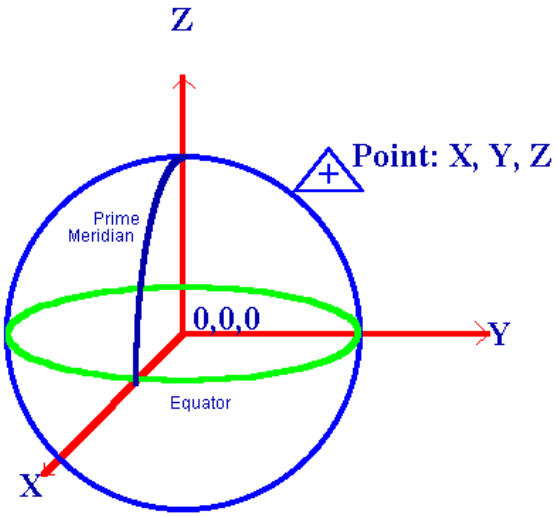

Figure A.1 – Earth Centered Earth Fixed

A.1.1 Inertial reference frame, F_i

The origin of the inertial reference frame may be any point that is completely unaccelerated, with its orientation usually irrelevant as long as it is fixed with respect to inertial space. For all intensive purposes the origin will be taken as the center of the Earth. The use of this axis system is limited to the derivation of the acceleration and angular rate vectors corresponding to the IMU measurements.

A.1.2 Local NED reference frame, F_l

For navigation purposes it is often required to represent the position, velocity and attitude of an object relative to a fixed coordinate frame on the surface on the earth. The local NED coordinate system has origin L at an arbitrary fixed point in the Earth's surface with the base vectors $\mathbf{i}_e$ pointing North, $\mathbf{j}_e$ pointing East and $\mathbf{z}_e$ pointing downwards to the center of the Earth. This reference frame is often also referred to as the NED reference frame.

A.1.3 Earth Centered Earth fixed reference frame, F_e

The Earth Centered Earth fixed reference frame is, as its name suggests, fixed to the rotation of the earth with reference frame at the Earth's. This reference frame is not of particular use in this thesis, and is merely referenced in the explanation of GPS function. As a result no further definition are provided.

A.1.4 Body-fixed reference frame, F_b

Body-fixed means that the origin and the base vectors of the coordinate system are fixed with respect to the nominal geometry of the aircraft in question. Typically the origin of the axis system B is set at the centre of mass (CM) of the aircraft. In cases where the CM of the aircraft varies, such as during fuel transfer application, the origin of the coordinate system can be fixed to a reference point on the fuselage. For the purposes of this thesis it is assumed that the CM is at a fixed known location of each aircraft.

The orientation of the axes can be seen in Figure A.2. Assuming that the aircraft has a plane of symmetry, the base vectors $\mathbf{i}_b$ and $\mathbf{k}_b$ lie in that plane of symmetry. $\mathbf{i}_b$ is chosen to point in the "forward" direction, where $\mathbf{k}_b$ is chosen pointing "downward". The base vector $\mathbf{j}_k$ completes the right handed axis system forming the lateral axis in the starboard direction.

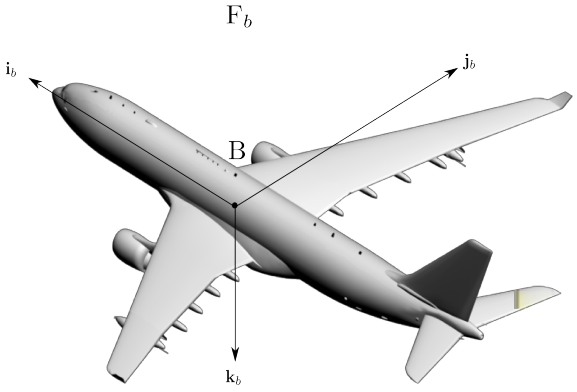

Figure A.2 – Body-Fixed Axis

It is important to note that there are two aircraft present in an AAR scenario and as such each will have a unique reference frame indicator with reference frame F_b describing a generic body-fixed axis system. The tanker and receiver reference frames are denoted by F_t and F_r, with origins T and R respectively.

A.1.5 Body-carried reference frame , F_c

The body-carried reference frame is similar to the body-fixed reference frame in the sense that its origin is fixed to the fuselage of the applicable aircraft. It differs though in its orientation, where it is free to rotate relative to the body-fixed axes as seen in Figure A.3. This coordinate system is principally used in describing components such as sensors or rotating parts on an aircraft. The difference in orientation relative to the aircraft body axis can be fixed or varied depending on the nature of the component.

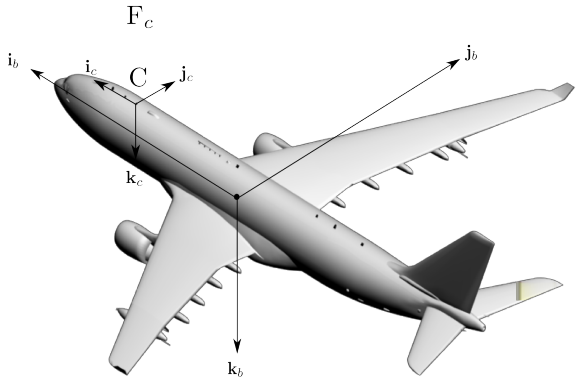

Figure A.3 – Body-Carried Axis

A with the the body-fixed coordinate system, there are multiple coordinate systems, typically corresponding to sensors, that fall under its description. As such the subscript c is replaced with a mnemonic for the particular component such as F_{o_i} indicating the coordinate system corresponding to the optical sensor i.

A.2 Vector Notation

A vector is an abstract geometrical object that has both magnitude and direction. It exists independently of any coordinate system. The vectors used here are Euclidean vectors that exist in three-dimensional space.

Commonly used vector symbols are

- $\boldsymbol{p}$ - Position
- $\boldsymbol{v}$ - Linear velocity
- $\boldsymbol{a}$ - Linear acceleration
- $\boldsymbol{e}, \boldsymbol{q}$ - Orientation represented by either Euler angles or quaternions
- $\boldsymbol{\omega}$ - Angular velocity
- $\boldsymbol{\alpha}$ - Angular acceleration

where vectors will be denoted by bold lower case letters or symbols.

How a particular vector is defined is dependent on the information it has relevance to. The following aspects must be taken into account when establishing vector notation:

- Position, velocity and acceleration vectors require the two points to which the vector has relevance to be specified

- Orientation, angular velocity and angular acceleration require the two reference frames to which the vector has relevance to be specified

Taking this into account the following notational conventions are used:

- A right superscript will be used to designate the points or reference frames relevant in the particular vector and will be divided by the symbol ”/” meaning ”with respect to” or ”relative to”.
- A right subscript will specify the coordinate system, denoting an array of the components of that vector in the specified system.

Considering arbitrary reference frames F_a and F_b some examples are:

- $\boldsymbol{p}^{A/B}$,$\boldsymbol{v}^{A/B}$ and $\boldsymbol{a}^{A/B}$: Position, velocity and acceleration vector of the origin of F_a relative to the origin of F_b
- $\boldsymbol{e}^{b/a}$ and $\boldsymbol{q}^{b/a}$: The Euler angle and Quaternion vectors that describe the orientation of reference frame F_b relative to reference frame F_a.
- $\boldsymbol{\omega}^{a/b}$ and $\boldsymbol{\alpha}^{a/b}$: Angular velocity and acceleration of reference frame F_a relative to reference frame F_b

Vectors can exist as described, but to quantify them they must be represented in some coordinate system. Once defined, the vector can be represented in any coordinate system by placing the vector at the origin of the coordinate system and finding its components along the three base vectors $\mathbf{i}$,$\mathbf{j}$ and $\mathbf{k}$. Typically these components will be unique to a coordinate system unless two coordinate systems are parallel. Coordinating a vector into a particular reference frame adds the reference frame indicator to the vector definition as a subscript. Again considering arbitrary reference frames F_a and F_b some examples are:

- $\boldsymbol{p}_b^{A/B}$,$\boldsymbol{v}_b^{A/B}$ and $\boldsymbol{a}_b^{A/B}$: Position, velocity and acceleration vectors coordinated into reference frame F_b
- $\boldsymbol{\omega}_b^{A/B}$ and $\boldsymbol{\alpha}_b^{A/B}$: Angular velocity and acceleration vectors coordinated into reference frame F_b

It is often required for vectors coordinated in a particular reference frame to be expressed in another in which case a coordinate transformation is undergone. For the coordinate transformation to me made possible a rotation matrix is required. Both Euler angles and quaternions have such rotation matrices which are derived in Appendix B, which are indicated by the transformation matrix symbol $\mathbf{T}(\,\cdot\,)$, where $\mathbf{T}(\mathbf{e^{a/b}})$ and $\mathbf{T}(\mathbf{q^{a/b}})$ are the transformation

matrices for Euler angles and quaternions respectively. Note that coordinate transformation using quaternions can be done using an alternate method, but for simplicity this method will be used throughout.

Coordinating a vector represented in reference frame F_a to F_b is given by,

$$\boldsymbol{p}_b^{A/B} = \boldsymbol{T}\left(\boldsymbol{q}^{b/a}\right)\boldsymbol{p}_a^{A/B} \tag{A.2.1}$$

where the inverse relation achieved through

$$\begin{aligned} \boldsymbol{p}_a^{A/B} &= \boldsymbol{T}\left(\boldsymbol{q}^{b/a}\right)^T \boldsymbol{p}_b^{A/B} && \text{(A.2.2)} \\ &= \boldsymbol{T}\left(\boldsymbol{q}^{a/b}\right)\boldsymbol{p}_b^{A/B} && \text{(A.2.3)} \\ & && \text{(A.2.4)} \end{aligned}$$

for a more detailed explanation to additional aspects such as the vector derivatives refer to [47]

Appendix B

Attitude Representations

In Autonomous Airborne Refueling (AAR), as with most relative navigation applications, a representation for the orientations of object relative to another is of great relevance. In this project two attitude representation are proposed in the form of Euler angles and quaternions. These attitude representation facilitate the transformation of vectors between reference frames through the coordinate transformation matrix $\boldsymbol{T}(\cdot)$. The following sections are devoted the introduction of two relevant attitude representations in reference to rotations between arbitrary reference frames F_a and F_b. The derivations are adapted from considerations in [47] .

B.1 Euler angles

The philosophy behind Euler angles is to use three angles and a predefined order of rotation to describe the attitude of axis system F_b with respect to axis system F_a. The Euler 3-2-1 sequence is most commonly used. To describe the attitude of B relative to A , begin with a temporary axis system F_{b_0} coinciding with F_a and carry out the following sequence of rotations in order,

- Yaw F_{b_0} through the angle ψ positively about the vector $\mathbf{k}_{b_0}$. Denote this new axis system F_{b_1} .
- Pitch F_{b_1} through the angle θ positively about the vector $\mathbf{j}_{b_1}$. Denote this new axis system F_{b_2}.
- Roll F_{b_2} through the angle ψ positively about the vector $\mathbf{i}_{b_2}$. Denote this new axis system F_b.

The Euler angles attitude parameters are thus concisely defined by the ordered set

$$\boldsymbol{e}^{b/a} = \{\phi, \theta, \psi\} \tag{B.1.1}$$

Euler angle representation is related to the coordinate transformation matrix $\mathbf{T}(\,\cdot\,)$ though the sequential rotations of the unit vectors which can be written as,

$$\boldsymbol{T}\left(\boldsymbol{e}^{a/b}\right) = \begin{bmatrix} 1 & 0 & 0 \\ 0 & \cos(\phi) & \sin(\phi) \\ 0 & -\sin(\phi) & \cos(\phi) \end{bmatrix} \begin{bmatrix} \cos(\theta) & 0 & -\sin(\theta) \\ 0 & 1 & 0 \\ \sin(\theta) & 0 & \cos(\theta) \end{bmatrix} \begin{bmatrix} \cos(\psi) & \sin(\psi) & 0 \\ -\sin(\psi) & \cos(\psi) & 0 \\ 0 & 0 & 1 \end{bmatrix} \tag{B.1.2}$$

which can be used to transform vectors coordinated in reference frame F_a to F_b through,

$$\boldsymbol{p}_a^{b/a} = \boldsymbol{T}\left(\boldsymbol{e}^{a/b}\right)\boldsymbol{p}_b^{b/a} \tag{B.1.3}$$

where the inverse transformation is possible through either an alternate Euler angle definition, or by using the inverse transformation matrix, which is equal to its transponent,

$$\begin{aligned} \boldsymbol{p}_b^{b/a} &= \boldsymbol{T}\left(\boldsymbol{e}^{b/a}\right)\boldsymbol{p}_a^{b/a} && \text{(B.1.4)} \\ &= \boldsymbol{T}\left(\boldsymbol{e}^{a/b}\right)^T\boldsymbol{p}_a^{b/a} && \text{(B.1.5)} \end{aligned}$$

The time rate of change of the Euler angles can be related to coordinates of the angular velocity vector in axis system F_b through,

$$\begin{aligned} \boldsymbol{\omega}^{b/a} &= \dot{\phi}\boldsymbol{i}_{\boldsymbol{\phi}} + \dot{\theta}\boldsymbol{j}_{\boldsymbol{\theta}} + \dot{\psi}\boldsymbol{k}_{\boldsymbol{\psi}} && \text{(B.1.6)} \\ &= \dot{\phi}\mathbf{i}_{b_2} + \dot{\theta}\mathbf{j}_{b_1} + \dot{\psi}\mathbf{k}_{b_0} && \text{(B.1.7)} \end{aligned}$$

where $\boldsymbol{i}_{\boldsymbol{\phi}}$, $\boldsymbol{j}_{\boldsymbol{\theta}}$ and $\boldsymbol{k}_{\boldsymbol{\psi}}$ are the unit vectors about which the respective Euler angle rotations occur. Coordinating all of the vectors into axis system F_b gives,

$$\boldsymbol{\omega}_b^{b/a} = \begin{bmatrix} 1 & 0 & \sin(\theta) \\ 0 & \cos(\phi) & \cos(\theta)\sin(\phi) \\ 0 & -\sin(\phi) & \cos(\theta)\cos(\phi) \end{bmatrix} \begin{bmatrix} \dot{\phi} \\ \dot{\theta} \\ \dot{\psi} \end{bmatrix} \tag{B.1.8}$$

where the inverse relation yields the Euler angle kinematic equation,

$$\begin{bmatrix} \dot{\phi} \\ \dot{\theta} \\ \dot{\psi} \end{bmatrix} = \begin{bmatrix} 1 & \sin(\phi)\tan(\theta) & \cos(\phi)\tan(\theta) \\ 0 & \cos(\phi) & -\sin(\phi) \\ 0 & \sin(\phi)\sec(\theta) & \cos(\psi)\sec(\theta) \end{bmatrix} \boldsymbol{\omega}_b^{b/a} \tag{B.1.9}$$

which is subject to the constraint $|\theta| \neq \frac{\pi}{2}$.

B.2 Quaternions

The philosophy behind quaternions is based on Euler's theorem which states that the orientation of axis system F_b relative to F_b can be uniquely described by rotating F_b from F_b about a vector $\hat{\mathbf{e}}$ through a rotation angle ϑ.

For mathematical singularity reasons, the quaternion parameters are defined to be,

$$\boldsymbol{q}^{a/b} = \begin{bmatrix} \boldsymbol{q}_{13}^{a/b} \\ q_4^{a/b} \end{bmatrix} = \begin{bmatrix} \hat{\mathbf{e}} \sin \frac{\vartheta}{2} \\ \cos \frac{\vartheta}{2} \end{bmatrix} \tag{B.2.1}$$

where the quaternion is constrained by the relationship $\left(\boldsymbol{q}^{a/b}\right)^T \left(\boldsymbol{q}^{a/b}\right) = 1$. The coordinate transformation matrix is related to the quaternion through,

$$\boldsymbol{T}\left(\boldsymbol{q}^{a/b}\right) = \Xi(\boldsymbol{q}^{a/b})^T \Psi(\boldsymbol{q}^{a/b}) \tag{B.2.2}$$

with,

$$\Xi(\boldsymbol{q}^{a/b}) = \begin{bmatrix} q_4^{a/b} I_{3\times 3} + [\boldsymbol{q}_{13}^{a/b}\times] \\ -\left(\boldsymbol{q}_{13}^{a/b}\right)^T \end{bmatrix} \tag{B.2.3}$$

$$\Psi(\boldsymbol{q}^{a/b}) = \begin{bmatrix} q_4^{a/b} I_{3\times 3} - [\boldsymbol{q}_{13}^{a/b}\times] \\ -\left(\boldsymbol{q}_{13}^{a/b}\right)^T \end{bmatrix} \tag{B.2.4}$$

where $[\boldsymbol{q}_{13}^{a/b}\times]$ is the cross product, or skew-symmetric matrix representation of the vector. This is used to transform vectors coordinated in reference frame F_a to F_b through,

$$\boldsymbol{p}_a^{b/a} = \boldsymbol{T}\left(\boldsymbol{q}^{a/b}\right) \boldsymbol{p}_b^{b/a} \tag{B.2.5}$$

The quaternion kinematic equation is given by,

$$\dot{\boldsymbol{q}}^{a/b} = \frac{1}{2}\Xi(\boldsymbol{q}^{a/b})\boldsymbol{\omega}_b^{b/a} \tag{B.2.6}$$

$$= \frac{1}{2}\Omega(\boldsymbol{\omega}_b^{b/a})\boldsymbol{q}^{a/b} \tag{B.2.7}$$

where

$$\Omega(\boldsymbol{\omega}_b^{b/a}) = \begin{bmatrix} -[\boldsymbol{\omega}_b^{b/a}\times] & \boldsymbol{\omega}_b^{b/a} \\ -(\boldsymbol{\omega}_b^{b/a})^T & 0 \end{bmatrix} \tag{B.2.8}$$

Some useful identities are give by

$$\begin{bmatrix} \boldsymbol{\omega}_b^{b/a} \\ 0 \end{bmatrix} \otimes \boldsymbol{q}^{a/b} = \Omega(\boldsymbol{\omega}_b^{b/a})\boldsymbol{q}^{a/b} \tag{B.2.9}$$

$$\boldsymbol{q}^{a/b} \otimes \begin{bmatrix} \boldsymbol{\omega}_b^{b/a} \\ 0 \end{bmatrix} = \Gamma(\boldsymbol{\omega}_b^{b/a})\boldsymbol{q}^{a/b} \tag{B.2.10}$$

where

$$\Gamma(\boldsymbol{\omega}_b^{b/a}) = \begin{bmatrix} [\boldsymbol{\omega}_b^{b/a}\times] & \boldsymbol{\omega}_b^{b/a} \\ -(\boldsymbol{\omega}_b^{b/a})^T & 0 \end{bmatrix} \tag{B.2.11}$$

and $\otimes$ is defined as the quaternion multiplied. Much more can be said in terms of quaternions, with particular reference to ease with which successive rotations can be achieve. For a more detailed discussion see [48].

Appendix C

Stereoscopic Vision Measurement Transformation

In Chapter 4 the stereoscopic vision measurment model is introduced. The principle of this measurement configuration lies in the fact that the 2D monocular measurement of a single beacon obtained from two, or more, optical sensors along with the known sensor positions in the receiver reference can be used to evaluate the relative 3D position vector of the beacon relative to the receier.

Since both the beacon position as well as the associated measurement variance is required the Unscented Transform is used to transform the 2D measurements and covariances.

Using the measured 2D parameters as the base vector,

$$\boldsymbol{x} = \begin{bmatrix} \boldsymbol{u}^{B_i/C_1} & \boldsymbol{v}^{B_i/C_1} & \boldsymbol{u}^{B_i/C_2} & \boldsymbol{v}^{B_i/C_2} \end{bmatrix}^T \tag{C.0.1}$$

and the measurement covariances

$$P_{xx} = R_{2D} = \begin{bmatrix} \sigma_{\boldsymbol{u}^{B_i/C_1}} & 0 & 0 & 0 \\ 0 & \sigma_{\boldsymbol{v}^{B_i/C_1}} & 0 & 0 \\ 0 & 0 & \sigma_{\boldsymbol{u}^{B_i/C_2}} & 0 \\ 0 & 0 & 0 & \sigma_{\boldsymbol{v}^{B_i/C_2}} \end{bmatrix} \tag{C.0.2}$$

Subsequently a *sigma point* vector can be established using the base vector and covariances,

$$\mathbf{X} = \begin{bmatrix} \boldsymbol{x} & \vdots & \boldsymbol{x} + \sqrt{(n+\lambda)P_{xx}} & \vdots & \boldsymbol{x} - sqrt(n+\lambda)P_{xx} \end{bmatrix} \tag{C.0.3}$$

where $n = 4$ and $\lambda = 0.1$ in accordance with the derivations in Chapter 3. The associated weights are also shown to be

$$W_m^0 = \frac{\lambda}{(n+\lambda)} \tag{C.0.4}$$

$$W_m^i = \frac{1}{2(n+\lambda)}, \quad i = 1, 2, \cdots, 2n \tag{C.0.5}$$

The *sigma point* vectors are transformed by 2D to 3D coordinate transformation equations,

$$\mathbf{Y}(i) = f(\mathbf{X}(i)) \tag{C.0.6}$$

$$z_r^{B_i/R} = z_r^{B_i/C_1} + z_r^{C_1/R} = \frac{1}{\frac{f^{C_1}}{u^{B_i/C_1}} - \frac{f^{C_1}}{u^{B_i/C_1}}} \left(x_r^{C_1/C_2} - \frac{f^{C_1} z_r^{C_1/C_2}}{u^{B_i/C_1}} \right) + z_r^{C_1/R} \tag{C.0.7}$$

$$y_r^{B_i/R} = y_r^{B_i/C_1} + y_r^{C_1/R} = \frac{1}{\frac{f^{C_1}}{v^{B_i/C_1}} - \frac{f^{C_1}}{v^{B_i/C_1}}} \left(x_r^{C_1/C_2} - \frac{f^{C_1} y_r^{C_1/C_2}}{v^{B_i/C_1}} \right) + y_r^{C_1/R} \tag{C.0.8}$$

$$x_r^{B_i/R} = x_r^{B_i/C_1} + x_r^{C_1/R} = \frac{1}{2} \left(\frac{f^{C_1} z_r^{B_i/C_1}}{u^{B_i/C_1}} + \frac{f^{C_1} y_r^{B_i/C_1}}{v^{B_i/C_1}} \right) + x_r^{C_1/R} \tag{C.0.9}$$

or

$$z_r^{B_i/R} = z_r^{B_i/C_2} + z_r^{C_2/R} = \frac{1}{\frac{f^{C_2}}{u^{B_i/C_2}} - \frac{f^{C_2}}{u^{B_i/C_2}}} \left(x_r^{C_2/C_1} - \frac{f^{C_2} z_r^{C_2/C_1}}{u^{B_i/C_2}} \right) + z_r^{C_2/R} \tag{C.0.10}$$

$$y_r^{B_i/R} = y_r^{B_i/C_2} + y_r^{C_2/R} = \frac{1}{\frac{f^{C_2}}{v^{B_i/C_2}} - \frac{f^{C_2}}{v^{B_i/C_2}}} \left(x_r^{C_2/C_1} - \frac{f^{C_2} y_r^{C_2/C_1}}{v^{B_i/C_2}} \right) + y_r^{C_2/R} \tag{C.0.11}$$

$$x_r^{B_i/R} = x_r^{B_i/C_2} + x_r^{C_2/R} = \frac{1}{2} \left(\frac{f^{C_2} z_r^{B_i/C_2}}{u^{B_i/C_2}} + \frac{f^{C_2} y_r^{B_i/C_2}}{v^{B_i/C_2}} \right) + x_r^{C_2/R} \tag{C.0.12}$$

after which the transformed vectors are averaged and the covariance evaluated which yields the desired output,

$$\tilde{\boldsymbol{p}}_r^{B_i/R} = \hat{\boldsymbol{y}} = \sum_{i=0}^{2n} W_m^i \mathbf{Y}(i) \tag{C.0.13}$$

$$R_{3D} = P_{yy} = \sum_{i=0}^{2n} W_m^i (\mathbf{Y}(i) - \hat{\boldsymbol{y}})(\mathbf{Y}(i) - \hat{\boldsymbol{y}})^T \tag{C.0.14}$$

Appendix D

Simulation Configurations

In Chapters 5 and 6 numerous simulations are performed to either illustrate the effect of a particular change in estimation configurations or to evaluate the resultant estimation accuracies of the finalised sensor configurations. The particulars of these simulation such as sensor positioning, sensor noise covariances and the true value of the states are given here to fully provide perspective to the results and allow them to be recreated.

D.1 The tanker and receiver aircraft

For realistic simulation it is important that the applicable sensors be places on the respective aircraft at locations consistent with reality. For this reason a diagram of the aircraft is provided.

Typically, the location of a component on an object is given with respect to the center of gravity CG, but as this location is not necessarily fixed a more appropriate reference point is chosen to by the nose of the aircraft. As a result the aircraft CG in these simulation is chosen to be,

Table D.1 – Aircraft CG relative to the aircraft nose

Aircraft	Variable	Value
Tanker	$\boldsymbol{p}_t^{CG/N}$	$[-(24.955 + 0.3 \times \text{AMC}) \quad 0 \quad 1.0445]^T$
Receiver	$\boldsymbol{p}_r^{CG/N}$	$[-(24.955 + 0.3 \times \text{AMC}) \quad 0 \quad 1.0445]^T$

where the point N signifies the aircraft nose and AMC in known as the Aerodynamic Mean Cord. All subsequent sensor positions are also indicated with respect to the aircraft nose.

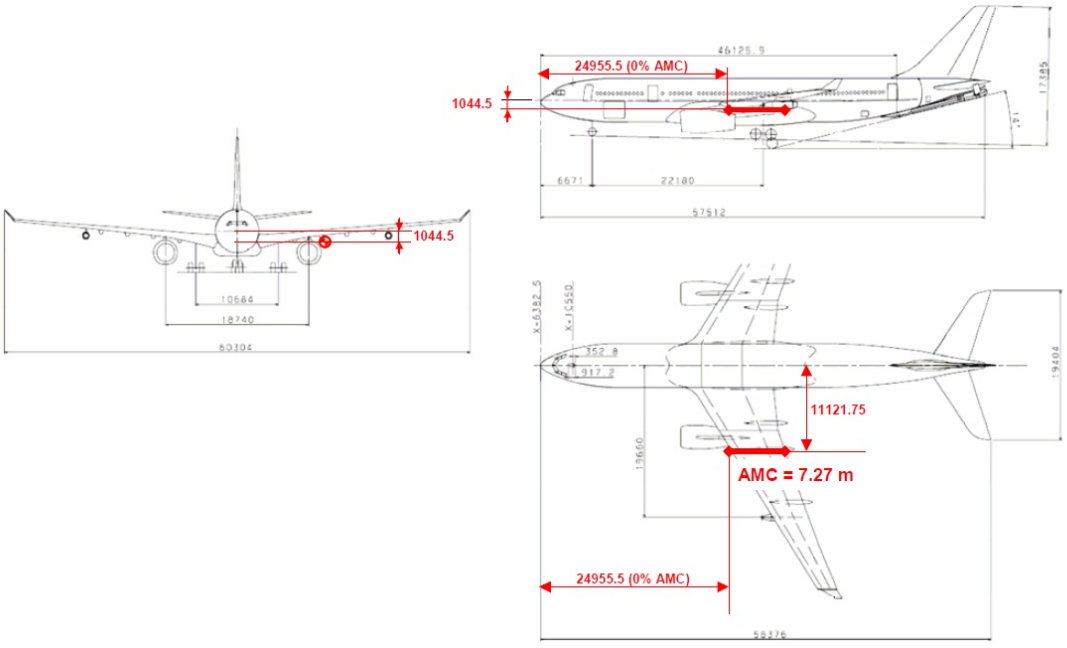

Figure D.1 – A330-200 MRTT Dimentions

D.2 Sensor noise covariance

Throughout the simulations in this thesis the driving input measurements and sensor measurement are assumed to have nominal values which are consistent which nose value of products that can either be purchased or developed. From Chapter 4 one can notice that even in cases where the noise of a particular sensor or driving input is increased to illustrate the effect, it is alway represented as a multiple or fraction of the nominal values. In this section these nominal noise parameters along with their references are provided.

D.2.1 Inertial Measurement Unit

In Chapter 4 the use of IMU are discussed, where the specific force and angular velocity measurement act as driving inputs to the process equations. The assumption is also made that there are independent systems that estimate the parameters that affect influence these measurement such as bias terms as well as increased specific force measurement due to sensor offset from the aircraft CG. The resultant output of such systems are the body acceleration and angular velocity of the applicable aircraft relative to inertial space. It is difficult to assume the amount of noise and uncertainty associated with these outputs and as such the noise associated with a commercial IMU will be used with the assumption that the sensor is on the aircraft CG and has no bias in specific force or angular rate measurement.

The IMU specifications obtained from [49] are shown to be

Range	±100°/sec	±175°/sec	±325°/sec	±2 g's	±6 g's	±10 g's
Bias (Over Temp.)	<0.03°/sec *2σ*			<1.0mg	<1.0mg *1σ*	<1.5mg
Bias (In Run Stability)	8°/hour *1σ*			0.02mg	0.04mg *1σ*	0.08mg
Scale Factor Error %	≤0.08% *(over temperature) 1σ*					
Resolution	0.002°	0.0025° /sec	0.003°	0.02mg	0.05mg	0.06mg
Angle Random Walk	0.0035°	0.005° /sec/√Hz *1σ*	0.006°	0.04mg	0.1mg /√Hz *1σ*	0.12mg
Alignment	1mrad *1σ*					
G-Sensitivity	<0.01°/sec/g *1σ*					
Self Test On	Δ 8°/s ± 4 °/s	Δ 8°/s ± 4 °/s	Δ 8°/s ± 4 °/s	Δ 0.25 ±0.12g	Δ 0.2 ±0.12g	Δ 1.25 ±0.75g
	Logic 1 = 3V to 5V at Pin 9					
Temp Range Operating:	-40°C to +85°C					
Non-Operating:	-55°C to +100°C					
Bandwidth	140 Hz, double-pole					
Temp Sensors	6 Internal Temperature Sensors					

Figure D.2 – IMU Specifications

where the angle random walk can be used to evaluate the standard deviation of the noise based on the sample frequency of 100Hz,

$$\sigma_{\boldsymbol{a}_t^{T/I}} = \frac{0.04 \times 9.81}{1000}\sqrt{100} \tag{D.2.1}$$

$$= 0.00394\frac{m}{s^2} \tag{D.2.2}$$

$$\sigma_{\boldsymbol{\omega}_{t/r}^{T?R/I}} = \frac{0.00035 \times \pi}{180}\sqrt{100} \tag{D.2.3}$$

$$= 6.1 \times 10^{-5}\frac{rad}{s} \tag{D.2.4}$$

D.3 Roaming Base Differential GPS

Roaming GPS receiver are places on the tanker with a roaming base on the receiver aircraft. In the introduction of RB-DGPS is it explained that the signals received by the roaming receivers are relayed to the roaming base which uses an internal estimation algorithm to produce the relative position and velocity measurements. This method is presented in theory in [3]. The NovAtel GPS on which our noise values are based implements this strategy in reverse, where the base station sends out its correction to the roaming receivers. It is assumes that either way, the same accuracies can be obtained. From the Novatel-OEMV1G datasheet [4]

$$\sigma_{\boldsymbol{p}_{t/r}^{RR/RB}} = 0.02m \tag{D.3.1}$$

$$\sigma_{\boldsymbol{v}_{t/r}^{RR/RB}} = 0.03\frac{m}{s} \tag{D.3.2}$$

Horizontal Position Accuracy (RMS)[2]	Single Point L1	1.5 m	Single Point L1	1.5 m	Single Point L1	1.5 m
	SBAS[1]	0.6 m	SBAS	10.6 m	Single Point L1/L2	1.2 m
	DGPS	0.4 m	DGPS	0.4 m	SBAS[1]	0.6 m
	OmniSTAR VBS[2]	0.6 m	RT-20[3]	0.2 m	DGPS	0.4 m
	RT-20[3]	0.2 m	RT-2 L1TE[4]	2 cm+1 ppm	RT-20[3]	0.2 m
					RT-2™	1 cm+1 ppm

Time to First Fix	
Cold Start[5]	60 s
Hot Start[6]	35 s
Time Accuracy[7]	20 ns RMS
Velocity Accuracy	0.03 m/s RMS
Velocity[8]	515 m/s

Figure D.3 – RB-DGPS Secifications

D.3.1 Optical - Monocular and Stereoscopic

Choosing the measurement noise for the optical sensors is not as straight forward as with the other sensors as it is not purpose built to provide the measurements required in this project. Form the introduction of the optical sensors and subsequent measurement model derivation in Chapters 2 and 4 we know that the 2D measurement are obtained though the averages lit pixels that correspond to the projection of the IR beacon light on the focal plane of the image sensor. The variation in the pixel that are lit is a function of how well the ambient light can be filtered out as well as the number of pixels. Without providing a full analysis it is assumed that an optical camera such as in [50] is used with a resolution of 1024×1024 is used with a refresh rate of 10Hz and a half angle FOV angle of 30^o.

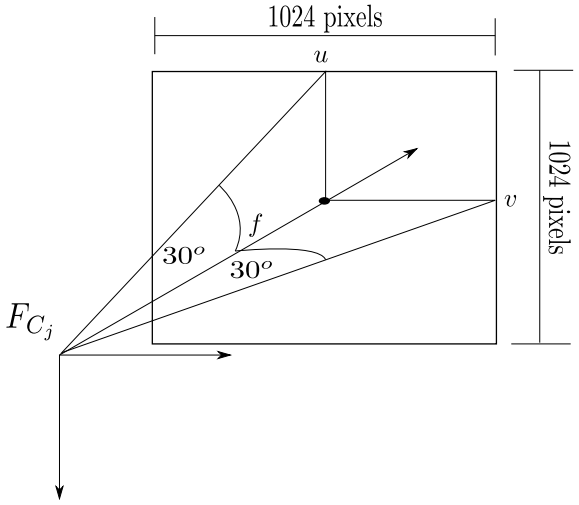

Figure D.4 – Representtion of optical sensor used in simulation

$$\begin{bmatrix} \sigma_{\boldsymbol{u}^{B_j/C_i}} \\ \sigma_{\boldsymbol{v}^{B_j/C_i}} \end{bmatrix} = \begin{bmatrix} 1\text{pix} \\ 1\text{pix} \end{bmatrix} \tag{D.3.3}$$

D.3.2 Boom parameters

The nominal values for the boom parameters are give as,

Table D.2 – Boom parameter nominal values

Variable	Value
l	15.25
σ	35
χ	0

The limits that correspond to each of the envelopes are given as as,

Table D.3 – Boom parameter limits - connect envelope

Variable	Value
δl	$\pm$0.7m
$\delta\sigma$	$\pm 7^0$
$\delta\chi$	$\pm 7.5^0$

Table D.4 – Boom parameter limits - disconnect envelope

Variable	Value
δl	$\pm$2.25m
$\delta\sigma$	$\pm 13^0$
$\delta\chi$	$\pm 12.5^0$

The length of the boom as well as the angular deflections of the universal joint can be measured in a multitude of ways. The design of the measurement system does not fall within the scope of this projects. As a result the following assumptions is made in terms of the magnitude of measurement noise,

$$\sigma_l = 0.001 \text{ m} \tag{D.3.4}$$

$$\sigma_\sigma = 0.01 \text{ deg} \tag{D.3.5}$$

$$\sigma_\chi = 0.01 \text{ deg} \tag{D.3.6}$$

D.4 Error covariance propagation - Chapater 5

In this simulation the increase in error covariance due to propagation is shown as a function of time.It is assumed that the driving input measurement are present but no observation measurement. The IMUs are assumed to be on the aircraft CGs

with their associated noises consistent with the noise rating from Section D.2.

Table D.5 – Assumed IMU location relative to the aircraft nose

Aircraft	Variable	Value
Tanker	$\boldsymbol{p}_t^{IMU/N}$	$[-(24.955 + 0.3 \times \text{AMC}) \quad 0 \quad 1.0445]^T$
Receiver	$\boldsymbol{p}_r^{IMU/N}$	$[-(24.955 + 0.3 \times \text{AMC}) \quad 0 \quad 1.0445]^T$

The relative states between the aircraft during simulation are constant and given as,

$$\boldsymbol{p}_r^{T/R} = \begin{bmatrix} 50 \\ 0 \\ -10 \end{bmatrix} \quad \boldsymbol{v}_r^{T/R} = \begin{bmatrix} 0 \\ 0 \\ 0 \end{bmatrix} \quad \boldsymbol{e}^{t/r} = \begin{bmatrix} 0 \\ 0 \\ 0 \end{bmatrix} \quad \boldsymbol{\omega}_t^{t/r} = \begin{bmatrix} 0 \\ 0 \\ 0 \end{bmatrix}$$

with the initial error covariance estimate chosen to be zero $P_0 = \mathbf{0}$. Variations in these terms are indicated the the relevant simulation.

D.5 Error covariance correction - Chapter 5

In this simulation the change in error covariance, as a function of sensor configuration parameters such as measurement noise, sensor placement and the number of sensors, is evaluated. In the simulation it is assumed that there are no driving input measurements. The sensors situated on the receiver reference frame are given as

Table D.6 – Sensor configuration for the receiver aircraft used in the error covariance correction simulation

Aircraft	Sensor	Variable	Value
Receiver	Monocular	$\boldsymbol{p}_r^{C_1/N}$	$[24.955 + 0.3\text{AMC} \quad 0 \quad 1.0445]^T$
	Stereo 1	$\boldsymbol{p}_r^{C_1/N}$	$[24.955 + 0.3\text{AMC} \quad -0.25 \quad 1.0445]^T$
	Stereo 2	$\boldsymbol{p}_r^{C_2/N}$	$[24.955 + 0.3\text{AMC} \quad 0.25 \quad 1.0445]^T$
	Roaming GPS Base	$\boldsymbol{p}_r^{RR/N}$	$[24.955 + 0.3\text{AMC} \quad 0 \quad 1.0445]^T$

In the simulation it is shown that the sensors on the tanker aircraft are moved from a configuration A

Table D.7 – Sensor Configuration A used in the sensitivity analysis simulations

Aircraft	Sensor	Variable	Value
Tanker	Beacon 1	$\boldsymbol{p}_t^{B_1/N}$	$[-32 \quad 2 \quad 1]^T$
	Beacon 2	$\boldsymbol{p}_t^{B_2/N}$	$[-32 \quad -2 \quad 1]^T$
	Beacon 3	$\boldsymbol{p}_t^{B_3/N}$	$[-35 \quad 0 \quad 2]^T$
	Roaming GPS Receiver 1	$\boldsymbol{p}_t^{RR_1/N}$	$[27.1 \quad 2 \quad 0]^T$
	Roaming GPS Receiver 2	$\boldsymbol{p}_t^{RR_2/N}$	$[27.1 \quad -2 \quad 0]^T$
	Roaming GPS Receiver 3	$\boldsymbol{p}_t^{RR_3/N}$	$[28.1 \quad 0 \quad -2]^T$

to a configuration B

Table D.8 – Sensor Configuration B used in the sensitivity analysis simulations

Aircraft	Sensor	Variable	Value
Tanker	Beacon 1	$\boldsymbol{p}_t^{B_1/N}$	$[-36 \quad 30 \quad -1]^T$
	Beacon 2	$\boldsymbol{p}_t^{B_2/N}$	$[-36 \quad -30 \quad -1]^T$
	Beacon 3	$\boldsymbol{p}_t^{B_3/N}$	$[-57 \quad 0 \quad -1]^T$
	Roaming GPS Receiver 1	$\boldsymbol{p}_t^{RR_1/N}$	$[-35 \quad 30 \quad -1]^T$
	Roaming GPS Receiver 2	$\boldsymbol{p}_t^{RR_2/N}$	$[-35 \quad -30 \quad -1]^T$
	Roaming GPS Receiver 3	$\boldsymbol{p}_t^{RR_3/N}$	$[-45 \quad 0 \quad -2]^T$

The relative states between the aircraft during simulation are constant and given as,

$$\boldsymbol{p}_r^{T/R} = \begin{bmatrix} 50 \\ 0 \\ -10 \end{bmatrix} \quad \boldsymbol{v}_r^{T/R} = \begin{bmatrix} 0 \\ 0 \\ 0 \end{bmatrix} \quad \boldsymbol{e}^{t/r} = \begin{bmatrix} 0 \\ 0 \\ 0 \end{bmatrix} \quad \boldsymbol{\omega}_t^{t/r} = \begin{bmatrix} 0 \\ 0 \\ 0 \end{bmatrix}$$

The nominal process and noise covariances are consistent with the noise rating from Section D.2.

D.6 Final Simulation - Chapter 6

In the final simulation all 12 sensor configurations implemented. From the considerations of Chapter 5 along with the practical consideration of sensor placement the final sensor setup is shown to be

Table D.9 – Final simulation - Receiver Aircraft sensor configuration

Aircraft	Sensor	Variable	Value
Tanker	Mono	$\boldsymbol{p}_t^{C_1/N}$	$[-(24.955 + 0.3\text{AMC}) \quad 0 \quad 1.0445]^T$
	Stereo 1	$\boldsymbol{p}_t^{C_1/N}$	$[-(24.955 + 0.3\text{AMC}) \quad -0.25 \quad 1.0445]^T$
	Stereo 2	$\boldsymbol{p}_t^{C_2/N}$	$[-(24.955 + 0.3\text{AMC}) \quad 0.25 \quad 1.0445]^T$
	Roaming GPS Base 1	$\boldsymbol{p}_t^{RB_1/N}$	$[-(24.955 + 0.3\text{AMC}) \quad 0.25 \quad 1.0445]^T$
	IMU	$\boldsymbol{p}_t^{IMU/N}$	$[-(24.955 + 0.3\text{AMC}) \quad 0.25 \quad 1.0445]^T$
	Boom Joint	$\boldsymbol{p}_t^{FR/N}$	$[-46.12 \quad 0 \quad 1.5]^T$

Table D.10 – Final simulation - Tanker Aircraft sensor configuration

Aircraft	Sensor	Variable	Value
Receiver	Beacon 1	$\boldsymbol{p}_t^{B_1/N}$	$[-32.5 \quad 20 \quad 0]^T$
	Beacon 2	$\boldsymbol{p}_t^{B_2/N}$	$[-32.5 \quad -20 \quad 0]^T$
	Beacon 3	$\boldsymbol{p}_t^{B_3/N}$	$[-56.375 \quad 7.25 \quad -2.5]^T$
	Beacon 4	$\boldsymbol{p}_t^{B_4/N}$	$[-56.375 \quad -7.25 \quad -2.5]^T$
	Beacon 5	$\boldsymbol{p}_t^{B_5/N}$	$[-56.375 \quad 0 \quad -10]^T$
	Roaming GPS Receiver 1	$\boldsymbol{p}_t^{RR_1/N}$	$[-30 \quad 15 \quad 0]^T$
	Roaming GPS Receiver 2	$\boldsymbol{p}_t^{RR_2/N}$	$[-30 \quad -15 \quad 0]^T$
	Roaming GPS Receiver 3	$\boldsymbol{p}_t^{RR_3/N}$	$[-45 \quad 0 \quad -2.5]^T$
	IMU	$\boldsymbol{p}_t^{IMU/N}$	$[-(24.955 + 0.3\text{AMC}) \quad 0.25 \quad 10.445]^T$
	Fuel Receptacle	$\boldsymbol{p}_t^{FR/N}$	$[4.2 \quad 0 \quad -2.25]^T$

The progression of the true relative states are shown in Chapter 6, with the noise parameters of each sensor consistent with the noise rating from Section D.2.

Bibliography

[1] October 2011.
Available at: http://www.cslu.ogi.edu/nsel/ukf/node6.html

[2] Gauvain, J.: Definition of an autonomous air-to-air refueling mode for the a330 mrtt during receiver's phases. Tech. Rep., Airbus, 2006.

[3] F.D.Busse: *Precise Formation-State Estimation In Low Earth Orbit Using Carrier Differential GPS*. Ph.D. thesis, Stanford University, 2003.

[4] Novatel-oemv1g gnss receiver. October 2011.
Available at: http://www.novatel.com/products/gnss-receivers/oem-receiver-boards/oemv-receivers/#

[5] E.A.Olsen, Park, C. and How, J.: 3d formation flight using differential carrier-phase gps sensors, September 1998. Presented at the Institute of Navigation GPS Meeting, Nashville, TN.

[6] Montenbruck, O., Lightsey, E.G., Ebinuma, T. and Leung, S.: A differential gps system for spacecraft proximity operation. In: *International ESA Conference on Guidance, Navigation and Control Systems*. 2002.

[7] Farrell, J., Givargis, T. and Barth, M.: Real-time differential carrier phase gps-aided ins. *IEEE Trnasactions on Control Systems Technology*, vol. 8, pp. 709–721, 2000.

[8] of Air Traffic Controllers' Association, I.F.: A beginner's guide to gnss in europe, August 1999. Document prepared by EVP Europe.

[9] Du, J.-Y.: *Vision Based navigation system for autonomous proximity operations: and experimental and analytical study*. Ph.D. thesis, Texas A&M University, 2004.

[10] Bowers, R.: *Estimation Algorithm for Autonomous Aerial Refueling using a Vision-Based Relative Navigation System*. Master's thesis, Texas A&M University, August, 2005.

[11] Mati, R.: Vision-based autonomous probe and drogue aerial refueling, 2006.

[12] Kelsey, J.: Vision-based relative pose estimation for autonomous rendezvous and docking. Tech. Rep., Scientific Systems Company, Inc., 2002.

[13] Langelaan, J.: *State Estimation for Autonomous Flight in Cluttered Environments*. Ph.D. thesis, Stanford University, March 2006.

[14] de Jager, A.: *The design and implementation of vision-based autonomous rotorcraft landing*. Master's thesis, Stellenbosch University, 2011.

[15] Visser, B.: *Die presisie landing van Šn onbemande vliegtuig*. Master's thesis, Stellenbosch University, 2009.

[16] Alonso, R., Crassidis, J. and Junkins, J.: Vision based relative navigation for formation flying of spacecraft. *American Institute of Aeronautics and Astronautics*, vol. 4439, 2000.

[17] Mienie, D.: *Autonomous Docking for a Satellite Pair Using Monocular Vision*. Master's thesis, Stellenbosch University, 2008.

[18] Andersen, C.M.: *Three Degree of Freedom Compliant Motion Control For Robotic Aircraft Refueling*. Master's thesis, Aeronautical Engineering, Air Force Institute of Technology, Wright-Patterson, Ohio, 1990.

[19] Bennett, R.A.: *Brightness Invariant Port Recognition For Robotic Aircraft Refueling*. Master's thesis, Air Force Institute of Technology, Wright-Patterson, Ohio, 1990.

[20] Shipman, R.P.: *Visual Servoing For Autonomous Aircraft Refueling*. Master's thesis, Air Force Institute of Technology, Wright-Patterson, Ohio, 1989.

[21] Doebbler, J. and Valasek, J.: Boom and receptacle autonomous air refueling using visual snake optical sensor. *Journal of Guidance Control and dynamics*, vol. 30, 2007.

[22] Fosbury, A. and Junkins, J.: Relative navigation of air vehicles.

[23] Junkins, J., Crassidis, J., Fosbury, A., Kim, S. and Cheng, Y.: Kalman filtering for relative spacecraft attitude and position estimation. *American Institute of Aeronautics and Astronautics*.

[24] Lippiello, V., Siciliano, B. and Villani, L.: Adaptive extended kalman filtering for visual motion estimation of 3d objects. *Control Engineering Practice*, vol. 15, pp. 123–134, 2007.

[25] Mammarella, M., Campa, G., Napolitano, M., Fravolini, M., Gu, Y. and Perhinschi, M.: Machine vision/gps integration using ekf for the uav aerial refueling problem. *Systems, man, and cybernetics*, vol. 38, pp. 791–801, 2008.

[26] X.Wang, Cui, N. and Guo, J.: Huber-based unscented filtering ant its application ot vision-based relative navigation. *IET Radar, sonar and Navigation*, vol. 4, pp. 134–141, 2009.

[27] Cheon, Y. and Kim, J.: Unscented filtering in a unit quaternion space for spacecraft attitude estimation, 2007. 1-4244-0755-9/07.

[28] Cheng, Y. and Crassidis, J.: Particle filtering of attitude estimation using a minimal local-error representation.

[29] Julier, S. and Uhlman, J.: Unscented filtering and non-linear estimation. In: *IEEE*, vol. 92. 2004.

[30] Mohamed, A. and Schwarz, K.: Adaptive kalman filtering for ins/gps. *Journal f Geodesy*, vol. 73, pp. 193–203, 1999.

[31] Shi, Y., Han, C. and Liang, Y.: Adaptive ukf for target tracking with unknown process noise statistics. In: *12th International Conference on Information Fusion*. 2009.

[32] Lui, J. and Lu, M.: An adaptive ukf filtering algorithm for gps position estimation.

[33] Pourtakdoust, S. and Asl, H.G.: An adaptive unscented kalman filter for quaternion-based oerientation estimation. *Aircraft Engineering and Aerospace Technology : An International Journal*, vol. 79/5, pp. 485–493, 2007.

[34] Ross, S., Pachter, M. and Jacques, D.: Auonomous aerial refueling based on the tanker reference frame. *IEEEAC*, vol. 1415, 2005.

[35] Dibley, P., Allen, M. and Nabaa, N.: Autonomous airborne refueling demonstration, phase i flight-test results, December 2007. NASA/TM-2007-214632.

[36] Williamson, W.: An instrumentation system applied to formation flight. *IEEE Transaction on Control Systems Technology*, vol. 15, pp. 75–85, 2007.

[37] Bergman, N.: *Recursive Bayesian Estimation: Navigation and Tracking Applications*. Ph.D. thesis, Linkĺoping University, 1999.

[38] Crassidis, J. and Markley, F.: Unscented filtering for spacecraft attitude estimation. *American Institute of Aeronautics and Astronautics*.

[39] Simon, D.: *Optimal State Estimation : Kalman, Hinf and Non-Linear Approaches*. John Wiley & sons, INC.,Pubication, 2006.

[40] Terejanu, G.: Unscented kalman filter tutorial. Department of Computer Science and Engineering, University of Buffalo, Buffalo, NY14260.

[41] Julier, S., Uhlman, J. and Durrant-Whyte, H.: A new method for the nonlinear transformation of means and covariances. *IEEE Transaction on Automatic Control*, vol. 45(3), pp. 477–482, 2000.

[42] Lee, D.-J.: *Nonlinear Bayesian Filtering with Applications to estimation and Navigation*. Ph.D. thesis, Texas A&M University, 2005.

[43] Maybeck, P.: *Stochastic Models, Estimation, and Control*, vol. 2. Academic Press, 1972.

[44] Goh, S.: *Unscented Filtering for Relative Attitude and Aposition Estimation*. Master's thesis, State University of New York at Buffalo, 2007.

[45] Markley, F., Crassidis, J. and Cheng, Y.: Nonlinear attitude filtering methods. *American Institute of Aeronautics and Astronautics*.

[46] Markley, F.: Attitude error representations for kalman filtering.

[47] Peddle, I.: *Acceleration Based Manoeuvre Flight Control System for Unmanned Aerial Vehicles*. Ph.D. thesis, Stellenbosch University, 2008.

[48] Sola, J.: Quaternion. Kinematics for the error-state KF, February 2010.

[49] MRM 30 Analog IMU.
Available at: `http://www.gladiatortechnologies.com/DATASHEET/MRM30_AnalogIMU_datasheet_Rev042511.pdf`

[50] October 2011.
Available at: `http://www.ptgrey.com/products/fireflymv/fireflymv.pdf`